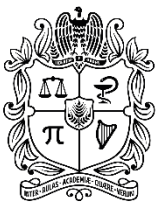

UNIVERSIDAD
NACIONAL
DE COLOMBIA

Noise Reduction in Phase Maps from Digital Holographic Microscopy

Carlos Andrés Buitrago Duque

Universidad Nacional de Colombia
Facultad de Ciencias, Escuela de Física
Medellín, Colombia
2020

Noise Reduction in Phase Maps from Digital Holographic Microscopy

Reducción de Ruido en Mapas de Fase de Microscopía Holográfica Digital

Carlos Andrés Buitrago Duque

Thesis presented as a partial requirement to qualify for the title of:

Magister en Ciencias - Física

Advisor:

Jorge Iván García Sucerquia, Ph.D.

Research field:

Digital Holographic Microscopy

Research group:

Optics and Optodigital Processing

Universidad Nacional de Colombia

Facultad de Ciencias, Escuela de Física

Medellín, Colombia

2020

To those who walked before, for the path they left. And to those who follow behind, hoping the new trails allow them to travel further beyond.

Acknowledgments

The results presented in this document, and all the ones that had to be left out, are the outcome of two years of work and academic development that could not be pursued alone. In the process, I had the opportunity of sharing, learning, and collaborating with a numerous amount of people whose contribution to the achievement of the proposed objectives is inmensurable and must not go unaccounted for. Among them, my deepest gratitude is to professor Jorge Garcia-Sucerquia, whose role as an advisor was always dutifully fulfilled and who was always willing to offer its guidance on both the academic and the human difficulties, and to my family, for their unconditional support and affection during every single step in the process.

My sincere gratitude is also extended to professor Ana Doblas and the graduate student Raúl Castañeda from the Department of Electrical and Computer Engineering of The University of Memphis, for the productive research collaborations and fruitful joint work. Additionally, to professor Oscar Arnache Olmos from the Solid State research group of the Universidad de Antioquia, and professor Mauricio Arroyave Franco and the graduate student Javier Hernández Higuita from the Applied Electromagnetism research group of the Universidad EAFIT; for their selfless availability and willingness to promptly welcome the use of their equipment and facilities in the development of the required experiments.

Special gratitude must also be directed to the Science Faculty of the Universidad Nacional de Colombia, for the use of the Optics laboratory, the fruitful discussions and academic courses that were partaken with the members of its faculty, and the approved travel grants that allowed the participation in the international conferences. Similarly, to the OSA and SPIE societies, for their professional development support and allowing the creation of networking connections with academic peers from across the globe.

Finally, I am deeply grateful to the members of the Optics and Optodigital Processing research group, both past and present, for their previous works set solid support to the presented results. I hope that our future developments find this work to be similarly useful.

Resumen

La Microscopía Holográfica Digital (DHM) es una técnica que ha permitido la medición cuantitativa de las diferencias de fase que los objetos microscópicos introducen en una iluminación coherente. Esta técnica, sin embargo, sufre de la presencia de ruido coherente; este infortunado efecto de la iluminación coherente tiene efectos perjudiciales sobre el poder de resolución y la precisión de las mediciones realizadas, obstaculizando la amplia adopción de tecnologías basadas en DHM. Por lo tanto, el desarrollo de DHM y su efectiva implementación en aplicaciones de imágenes cuantitativas de fase está altamente relacionado con el desarrollo de métodos de reducción de ruido robustos que puedan compensar adecuadamente esta limitación.

En la presente tesis de maestría, se proponen e implementan estrategias de reducción de ruido que puedan ser aplicadas a mapas de fase cuantitativos obtenidos numéricamente en microscopía holográfica digital. Para lograrlo, se realizó una revisión del estado del arte de las técnicas existentes para reducción de ruido en mapas de fase, identificando que, si bien existen extensas fuentes literarias que abordar el problema de ruido en holografía digital, la mayoría están orientadas hacia información de intensidad; además, las pocas que están optimizadas para reducción de ruido en fase han sido principalmente empleadas en objetos macroscópicos, por lo que no han sido consideradas las condiciones experimentales específicas de DHM. Bajo esta idea, nuevas técnicas de reducción de ruido que se adaptan a las condiciones experimentales específicas de DHM son propuestas, su factibilidad es estudiada en modelaciones numéricas y resultados experimentales, y sus límites de aplicación establecidos con métricas previamente reportadas en la literatura especializada.

Los resultados fueron consolidados en 9 manuscritos sometidos a revistas indexadas de circulación internacional, 7 de estos ya publicados, y 6 presentaciones en eventos internacionales. Estos productos constituyen el núcleo de la presente tesis.

Palabras clave: Ruido coherente, Microscopía Holográfica Digital, Imágenes Cuantitativas de fase

Abstract

Digital Holographic Microscopy (DHM) is a technique that has allowed the quantitative measurement of the phase delays that microscopic samples introduce into a coherent illumination. The technique, however, suffers from the presence of coherent noise; this deleterious effect of coherent illumination has detrimental results for the resolution power and accuracy of the measured information, hindering the widespread adoption of DHM-based technologies. Therefore, the advancement of DHM and its effective implementation in Quantitative Phase Imaging applications is highly linked to the development of robust denoising methods that can adequately compensate for this limitation.

In this Master's thesis, the proposal and implementation of noise reduction strategies that can be applied to quantitative phase maps numerically obtained from Digital Holographic Microscopy are sought. To achieve so, a review of the state-of-the-art in existing phase-map denoising methodologies was done, finding that, while extensive literature sources that tackle the problem of noise in digital holography exist, most are focused on intensity information; meanwhile, the few that are optimized for phase denoising have been mostly used in macroscopic objects thus failing to consider the experimental conditions of DHM. Under this understanding, new denoising methodologies adapted to the specific experimental conditions of DHM are explored, its feasibility verified on both numerically modeled and experimental results, and their application limits established with previously reported metrics from the existing literature.

The results were reported on 9 manuscripts submitted to indexed journals of international circulation, 7 of them already published, and 6 presentations in international conferences. These products constitute the core of the present thesis.

Keywords: Coherent noise, Digital Holographic Microscopy, Quantitative Phase Imaging

Content

List of figures

Pág.

Introduction

Microscopy is a highly versatile tool with interdisciplinary applications in many fields, being of uttermost importance in biological research and biomedical diagnosis under the “seeing is believing” paradigm. Since the invention of the optical microscope, a non-stop evolution and refinement of the technique has been pursued, with researchers all across the globe developing approaches to increase the resolution, enhance the contrast, and gain access to new information [1]. One of such advances, which has been receiving increasing attention in the past decades, is the ability to access the phase-delays introduced by a sample on a propagating wavefront [2,3]. When an object is coherently illuminated, the amplitude of the scattered wave is proportional to either the transmittance or reflectance of the sample, while its phase encodes the optical path-length changes introduced by the object [4]. In the case of reflective samples, the phase differences are related to the height-map of the object, while, for transmissive samples, these changes are related to both the topography of the object and its refraction index distribution. In the latter case, which is the common situation for biological specimens, this information can be directly related to parameters of analytical interest like cell mass, volume, and surface area [5]. Therefore, the development of microscopy techniques able to retrieve the phase information has been an active area of research, with a special interest in being able to quantify the resulting phase differences.

Digital Holographic Microscopy (DHM) is a coherent imaging technique that allows the label-free observation of optically translucent samples and the quantitative measurement of their induced optical path length changes. Its implementation is composed of two main stages: the hologram recording in a digital format, and its subsequent numerical reconstruction. Since Gabor’s original conception of the analog version of this technique [6], multiple alternative ways to execute each of the stages have been proposed [7]; each with its own advantages or disadvantages for a given application case. Nonetheless, most of these approaches can be usually grouped according to their common defining

characteristics. In the scope of this thesis, a classification based on the need, or lack thereof, of a lens-based imaging system during the recording stage is considered.

DHM's ability to retrieve the complex field information of a sample has been shown to be useful in a wide range of areas, including the analysis of microorganisms [8], biomedical parameters [9,10], fluid dynamics [11], material sciences [12], metrology [13–15], among many others. In these applications, and any other DHM-based solution, due to the direct connection between the phase delay and the commonly required analysis parameters, having an accurate and precise quantitative measurement of the optical path change is a key condition. However, being a coherent imaging technique, DHM is subject to the deleterious effects of coherent noise, usually known as speckle [16]. Speckle noise, which is inherited from the roughness that most real-world materials present on the optical scale, can ruin the information retrieval from coherent imaging systems affecting the resulting phase measurements in different ways, with a loss in resolution being one of the most deleterious for microscopy applications [17].

The speckle effects and the derived difficulties of its presence have been a central study topic in other disciplines like ultrasound imaging [18,19], synthetic aperture radar [20,21], optical coherence tomography [22,23], optical astronomy [24,25], and optical holography [26]. Digital Holography (DH) has also seen a wide range of denoising proposals, either as numerical processing methods to be applied over the reconstructed information [27–29], as physical modifications to the hologram recording system [30,31], or as a combination of both [32–34]. Despite the applicability of most of these strategies to DHM, their driving applications in DH have set their main focus in the denoising of intensity information; additionally, while some methods have also been explicitly proposed for phase-map denoising [35,36], most are designed for fringe-pattern configurations, where the main noise issue in the phase-maps is the high-spatial-frequency alterations in the useful phase-data that reduces the effectivity of the unwrapping procedures [37,38]. Therefore, there is an unsatisfied need to explicitly evaluate the existing phase denoising techniques under DHM experimental conditions and to propose new methods specifically designed for such architectures.

In this Master's thesis, the proposal, evaluation, and implementation of noise reduction strategies for phase-maps obtained from digital holographic microscopy was reached. To

achieve it, the following objectives were completed: i) Review the state-of-the-art in phase-maps noise reduction techniques, ii) Implement new phase-maps noise reduction methodologies that fit the experimental conditions imposed by digital holographic microscopy architectures, iii) Verify the feasibility of the proposed strategies in numerical models and experimental results, and iv) Study the applicability limits based on the evaluation of their performance with metrics previously reported in peer-reviewed literature.

The following chapters present a brief introduction and contextualization to each research topic associated with this thesis. Chapter 1 introduces the conceptual background and state-of-the-art for the content of the next chapters. Chapter 2 presents a non-speckle approach to the denoising of phase maps retrieved from digital holographic microscopy, by optimizing the information retrieval of both lens-based and lensless architectures. Chapter 3 illustrates the development and implementation of two numerical denoising techniques based on the manipulation of the retrieved complex field. Chapter 4 presents an optical denoising technique whose implementation is based on the engineering and control of the pupil function in the imaging system during the recording stage. Finally, Chapter 5 concludes with the main results achieved, and the perspectives of future work that can be derived from them.

Despite this traditional chapter distribution, the main core of the present thesis is constituted by the following works which, having been peer-reviewed and published in journals of international circulation with high-quality standards and strict editorial policies, represent a tangible contribution to the scientific advancement of the objective research field. These 9 papers are attached at the end of this text and referenced in their associated chapter:

- *"Non-approximated Rayleigh–Sommerfeld diffraction integral: advantages and disadvantages in the propagation of complex wave fields,"* Applied Optics **58**, G11-G18 (2019) [39]
- *"Phase-shifting digital holographic microscopy with an iterative blind reconstruction algorithm,"* Applied Optics **58**, G311-G317 (2019) [40]
- *"Realistic modeling of digital holographic microscopy,"* Optical Engineering **59**(10), 102418 (2020) [41]
- *"Single-shot pseudostochastic speckle noise reduction in numerical complex-valued wavefields,"* Optical Engineering **59**(7), 073107 (2020) [42]

- *"Sizing calibration in digital lensless holographic microscopy via iterative Talbot self-imaging,"* Optics and Lasers in Engineering, **134**, 106176 (2020) [43]
- *"Fast-iterative blind phase-shifting digital holographic microscopy using two images,"* Applied Optics **59**, G7469-7476 (2020) [44]
- *"Pointwise phasor tuning for single-shot speckle noise reduction in phase wave fields,"* Optics and Lasers in Engineering, **137**, 106365 (2020) [45]
- *"Physical pupil manipulation for speckle reduction in digital holographic microscopy,"* Heliyon, **7**, e06098 (2021) [46]
- *"Open-source, Cost-effective, Portable, 3D-printed Digital Lensless Holographic Microscope,"* Applied Optics **60**, A205-A214 (2021) [47]

Additionally, the most significant results were presented in scientific conferences of international scope in the form of both oral and poster presentations as follows:

- "*Evaluation of Non-Approximated Numerical Calculation of the Diffraction Integral,*" in Digital Holography and Three-Dimensional Imaging Topical Meeting, Bordeaux France, 2019 [48]
    - **Winner of Best Student Poster Award.**
- "*Denoising Phase Maps of Digital Holographic Microscopy by Complex Tuning*," in Digital Holography and Three-Dimensional Imaging, Bordeaux France, 2019 [49]
- *"Blind phase-shifting digital holographic microscopy using an iterative approach,"* Three-Dimensional Imaging, Visualization, and Display, Digital Forum, 2020 [50]
- *"Fast-iterative bling reconstruction algorithms for accurate quantitative phase images in phase-shifting digital holographic microscopy,"* Imaging and Applied Optics Congress (Online), Washington DC United States, 2020 [51]
- *"Iterative Talbot Self-Imaging Calibration for Sizing in Digital Lensless Holographic Microscopy,"* Imaging and Applied Optics Congress (Online), Washington DC United States, 2020 [52]
    - **Best Student Paper Award Finalist.**
- *"Speckle Reduction in Digital Holographic Microscopy by Physical Manipulation of the Pupil Function,"* Imaging and Applied Optics Congress (Online), Washington DC United States, 2020 [53]

The knowledge acquired throughout the development of this Master's thesis was used to help the formation and induction to academia of multiple undergraduate students; namely, by directly helping the undergraduate courses of "Workshop II: Mechanical Design",

“Mechanical Physics”, “Optical Instrumentation”, and “Physics of Electricity and Magnetism”, for one semester each; by having an active involvement in the Optic’s Student Chapter (CEO – UNCM) as an acting officer to both SPIE[1] and OSA[2]; and by mentoring the work of four undergraduate Engineering Physics students in their participation in the Optics and Optodigital Processing research group. Finally, this knowledge was also used in a short research stance in Centro de Investigaciones en Óptica, Mexico, developing a project for the application of Digital Holographic Interferometry to the Measurement of Non-Visible Impact Damage on Ballistic Panels, and the formulation of six research projects before national and international institutions, with the role of co-investigator, to further develop the results achieved in this thesis and complete their integration with the current advancements in the research program of the Optics and Optodigital Processing group.

[1] The International Society for Optics and Photonics (https://spie.org/)
[2] The Optical Society (https://www.osa.org/)

1. Digital Holographic Microscopy

Digital Holographic Microscopy (DHM) is one of the principal modern applications of Digital Holography (DH), which allows the label-free observation of optically translucent samples and the quantitative measurement of their induced optical path length changes. The direct access to both phase and amplitude profiles of a sample gives DHM the possibility of making Quantitative Phase Imaging (QPI), which proves particularly powerful in a wide range of disciplines. While some previous microscopy techniques like Dark-Field [54], Phase-Contrast [2], and Differential Interference Contrast Microscopy [55], had provided indirect access to the phase information for some decades, DHM introduced the novel ability to quantitively measure those phase shifts non-invasively with subwavelength axial accuracy [56,57]. This capability, supported by the additional versatilities of the digital world that allow a numerical-extended depth of focus and the computational processing of the complex-valued wavefield, have constituted DHM as a highly attractive microscopy technique.

Like any other DH technique, DHM can be thought of as a two-step imaging process, whose main stages are commonly known as recording and reconstruction; while the first occurs physically, the second is strictly numerical [58]. The recording stage specifics differ between the multiple available architectures of DHM, but any basic setup consists of an illumination source, an interferometric configuration with microscopic imaging optics, and a digitizing sensor [7]. The intensity distribution recorded by the sensor, so forth referred to as the hologram $H(x,y)$, is the amplitude superposition between the Object Wave $O(x,y)$ and the Reference Wave $R(x,y)$ [59]

$$H(x,y) = |O(x,y) + R(x,y)|^2. \tag{1.1}$$

The former is given by the interaction of the sample and the illumination which, gathering the object's information, propagates through the imaging system to the sensor plane;

meanwhile, the latter is an unperturbed version of the illumination that travels directly to the recording device. As both the object and reference waves are complex-valued, Eq. 1.1 is expanded as

$$H(x,y) = \underbrace{|O(x,y)|^2 + |R(x,y)|^2}_{\mathbf{DC}} + \underbrace{O(x,y)R^*(x,y)}_{\mathbf{+1}} + \underbrace{O^*(x,y)R(x,y)}_{\mathbf{-1}} \tag{1.2}$$

where the superscript $*$ represents the complex conjugate.

In Eq. 1.2, the first two terms to the right are real quantities and, thus, their sum is commonly known as the DC or zeroth diffraction order; similarly, the next two terms are known as the $+1$ and -1 diffraction orders, as they carry the complex-valued object information mixed with the reference wave and are thus associated with the real and virtual images of the object [60]. The distribution of these terms in the spatial-frequency spectrum is defined by the interference angle between the object and reference waves, and can be used to distinguish between in-line holography [61] and off-axis holography [57]. As seen in **Fig. 1-1**, the former presents a complete superposition of the diffraction orders, while the latter is characterized by their total separation in the spatial-frequency spectrum.

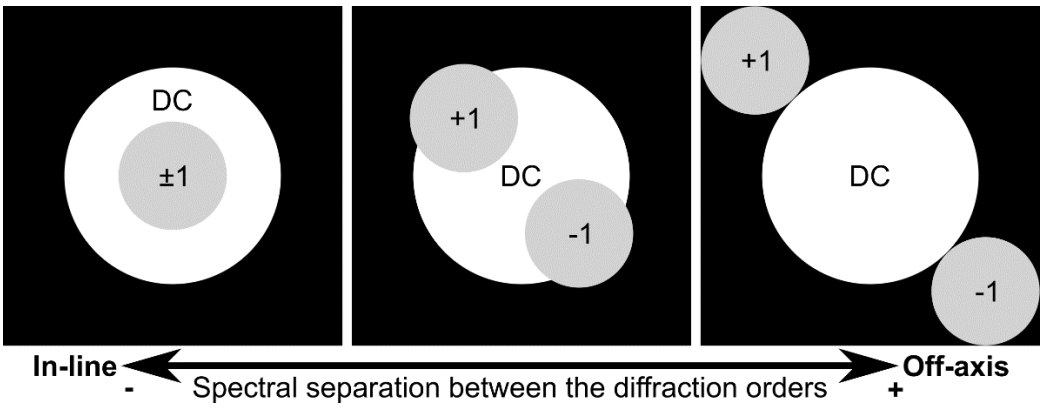

Fig. 1-1 Possible spectral separations between the hologram's diffraction orders. From a complete superposition of in-line holography, in the left, to their total separation in off-axis holography, in the right.

The reconstruction stage, which may occur in whichever computing device receives the sensor's digital output, is the numerical processing required to recover the complex-valued wavefield diffracted by the object that was carried by the Object Wave and codified into the interference pattern. The required calculations to achieve an effective reconstruction depend on the selected recording setup; however, most configurations involve a

computational equivalent of the diffraction process to recover the complex-valued field and a filtering process to remove the DC term and complex conjugate of the object [62]. The spectral distribution in off-axis setups allows a numerical separation of the orders to be pursued with a direct spatial filter, achieving a reconstruction of the object information without the presence of neither the DC term nor the conjugated image [63]; however, managing this configuration needs careful and precise alignment of the optical components, and incurs in a considerable reduction of the available space-bandwidth product that could reduce the maximum achievable resolution of the system [64]. In-line and slightly-off-axis configurations ease the system's alignment requirements and ensure that the information is diffraction-limited, such that the resolution limit of the DHM system equals that of the imaging system without penalties derived from the numerical processing; however, the total or partial superposition of the diffraction orders forces the use of more sophisticated and computationally-intensive reconstruction techniques [65–67] to obtain the object information without the detrimental presence of the DC order or the conjugated image (also known as the "twin image") [68].

As stated before, the specific details of the recording and reconstruction stages are determined by the selected DHM architecture and operation mode. Among the ample range of setups that are available in the literature, multiple classifications can be made based on their common defining characteristics. Some of these groupings are based, for instance, in the spectral separation of the diffraction orders (as presented above), the interferometric principle used, or the required reconstruction approach; in no way are these, or most other classifications, exclusive between them, as most are somewhat overlapped. In the scope of this work, a distinction is made over the use, or lack thereof, of a lens-based imaging system during the recording stage, because this classification eases the recognition of the possible noise sources in phase-maps retrieved from each architecture. Two DHM variants will thus be distinguished: lens-based DHM, and lensless DHM.

1.1 Lens-based Digital Holographic Microscopy

The implementation of a traditional lens-based system for image formation in a Digital Holographic Microscope is the most common configuration. In their conventional form, the setup can be done by either introducing an optical microscope configuration into the object arm of an interferometer or by adding an interferometric path into an existing optical

microscope with coherent illumination. As stated before, any DHM setup has an illumination source, an interferometric configuration with microscopic imaging optics, and a digitizing sensor. When a laser is selected as the illumination source for lens-based DHM, steady interference patterns can be achieved in almost any interferometric configuration; however, the selection of the specific setup is given by the desired application case, with the Mach-Zehnder and Michelson interferometers being the main candidates. The former is particularly convenient for transmissive samples, while the latter is preferable when dealing with reflective or opaque objects. In either case, the object arm is modified by introducing the imaging system of an optical microscope; namely, a Microscope Objective (MO) and a Tube Lens (TL). The resulting configurations are illustrated in **Fig. 1-2**, with panel (a) showing a Mach-Zehnder-based transmission DHM, and panel (b) a Michelson-based reflection DHM.

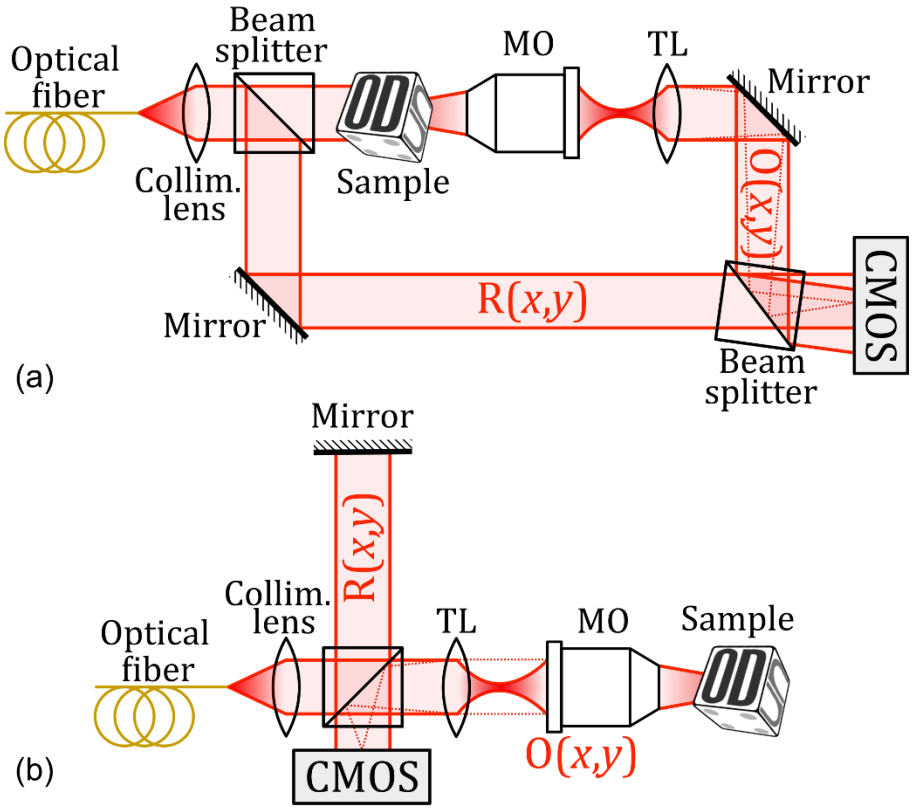

Fig. 1-2 Common architectures of DHM created by inserting an optical microscope into the object arm of an interferometer. (a) Transmission setup based on a Mach-Zehnder interferometer. (b) Reflection setup based on a Michelson interferometer.

In either case, the behavior of the optical microscope introduced in the object arm may be studied as an imaging system linear in the complex amplitude to determine its image formation properties. To do so, the simplified representation shown in **Fig. 1-3** is used: the MO is represented by a thin lens with a pupil of known transmittance $P(x', y')$ in its back focal plane, and the TL is approximated as a thin lens. While the numerical refocusing properties of digital holography would allow the recording to be done at any distance after the TL, keeping the object at a sharp focus in the sensor plane (as would be done in a conventional microscope) can significantly speed up the reconstruction process because no further propagation of the numerically retrieved complex wavefield is needed. Under this configuration, known as image-plane holography [69], a sample placed in the front focal plane of the MO would be sharply imaged into the sensor plane at the back focal plane of the TL. Therefore, the only distance left to optimize is the separation d between the MO pupil and the TL. In a conventional microscope, the distance d can be arbitrarily large if the MO is infinity-corrected; however, it has been shown that, while no noticeable changes in intensity occur, the phase information is severely affected [70]. Therefore, special caution must be taken during the microscope configuration for the quantitative phase imaging purposes of DHM.

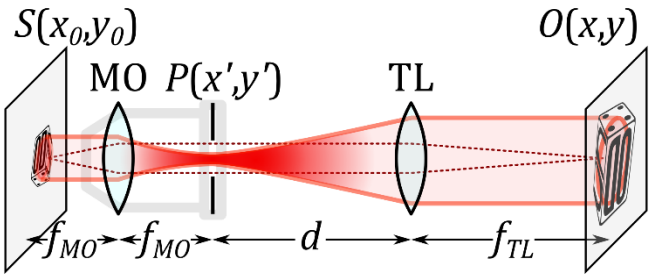

Fig. 1-3 Simplified representation of the imaging system of an optical microscope. To compensate for the spherical phase aberration, the MO and the TL must be set up in a telecentric-afocal configuration such that $d = f_{TL}$

To inspect the system's imaging properties, an ABCD-matrix-based diffraction analysis can be done. Initially, the propagation of the optical field emitted by the sample $S(x, y)$ to the pupil plane is represented as [60]

$$\begin{bmatrix} 1 & f_{MO} \\ 0 & 1 \end{bmatrix} \begin{bmatrix} 1 & 0 \\ -1/f_{MO} & 1 \end{bmatrix} \begin{bmatrix} 1 & f_{MO} \\ 0 & 1 \end{bmatrix} = \begin{bmatrix} 0 & f_{MO} \\ -1/f_{MO} & 0 \end{bmatrix}, \tag{1.3}$$

where f_{MO} is the focal length of the MO. By introducing the parameters from Eq. 1.3 into the diffraction equation written in terms of matrix optics [71], the functional form of the complex field at the pupil plane is shown to be

$$\begin{aligned} U_P(x',y') &= \frac{i}{\lambda f_{MO}} e^{i\frac{2\pi}{\lambda}2f_{MO}} \iint_{-\infty}^{\infty} S(x_0,y_0) e^0 e^{-i\frac{2\pi}{\lambda f_{MO}}(x_0x'+y_0y')} dx_0 dy_0 \\ U_P(x',y') &= \frac{i}{\lambda f_{MO}} e^{i\frac{2\pi}{\lambda}2f_{MO}} \mathcal{F}\{S(x_0,y_0)\}|_{f_y=y'/\lambda f_{MO}}^{f_x=x'/\lambda f_{MO}} \end{aligned} \tag{1.4}$$

with $\mathcal{F}\{\ \}$ being the Fourier Transform operator and λ the illumination wavelength. The resulting field in Eq. 1.4 then interacts with the pupil function $P(x',y')$ and propagates through the second half of the imaging system represented by

$$\begin{bmatrix} 1 & f_{TL} \\ 0 & 1 \end{bmatrix} \begin{bmatrix} 1 & 0 \\ -1/f_{TL} & 1 \end{bmatrix} \begin{bmatrix} 1 & d \\ 0 & 1 \end{bmatrix} = \begin{bmatrix} 0 & f_{TL} \\ -1/f_{TL} & 1-d/f_{TL} \end{bmatrix}, \tag{1.5}$$

where f_{TL} is the focal length of the TL. The complex field that reaches the image plane $O(x,y)$ is thus

$$O(x,y) = \frac{i}{\lambda f_{TL}} e^{i\frac{2\pi}{\lambda}(d+f_{TL})} e^{i\frac{2\pi}{\lambda}\frac{f_{TL}-d}{2f_{TL}^2}(x^2+y^2)} \iint_{-\infty}^{\infty} U_P(x',y') P(x',y') e^{-i\frac{2\pi}{\lambda f_{TL}}(x'x+y'y)} dx' dy'$$

$$O(x,y) = \frac{i}{\lambda f_{TL}} e^{i\frac{2\pi}{\lambda}(d+f_{TL})} e^{i\frac{2\pi}{\lambda}\frac{f_{TL}-d}{2f_{TL}^2}(x^2+y^2)} \mathcal{F}\{U_P(x',y')P(x',y')\}|_{f_y=y/\lambda f_{TL}}^{f_x=x/\lambda f_{TL}}. \tag{1.6}$$

Using Eq. 1.4 to rewrite the Fourier transform of $U_P(x',y')$ yields

$$\mathcal{F}\{U_P(x',y')\} = \mathcal{F}\left\{\frac{i}{\lambda f_{MO}} e^{i\frac{2\pi}{\lambda}2f_{MO}} \mathcal{F}\{S(x_0,y_0)\}|_{f_y=y'/\lambda f_{MO}}^{f_x=x'/\lambda f_{MO}}\right\}\Big|_{f_y=y/\lambda f_{TL}}^{f_x=x/\lambda f_{TL}}.$$

$$\mathcal{F}\{U_P(x',y')\} = i|\lambda f_{MO}| e^{i\frac{2\pi}{\lambda}2f_{MO}} S\left(\frac{x}{M},\frac{y}{M}\right), \tag{1.7}$$

with $M = -f_{TL}/f_{MO}$ being the effective magnification of the imaging system. By inserting Eq. 1.7 into Eq. 1.6, using the convolution theorem to replace $\mathcal{F}\{U_P(x',y')P(x',y')\}$ by $\mathcal{F}\{\mathcal{F}\{U_P(x',y')\} \otimes \mathcal{F}\{P(x',y')\}\}$, and doing some algebraic manipulation, the final form for the complex field at the output of the imaging system is found to be

$$O(x,y) = \frac{1}{M} e^{i\frac{2\pi}{\lambda}(d+f_{TL}+2f_{MO})} e^{i\frac{\pi(f_{TL}-d)}{\lambda f_{TL}^2}(x^2+y^2)} \left[S\left(\frac{x}{M},\frac{y}{M}\right) \otimes \tilde{P}\left(\frac{x}{\lambda f_{TL}},\frac{y}{\lambda f_{TL}}\right)\right], \tag{1.8}$$

where $\tilde{P}\left(\frac{x}{\lambda f_{TL}}, \frac{y}{\lambda f_{TL}}\right)$ is the Fourier transform of the pupil $P(x', y')$.

In Eq. 1.8, the term $e^{i\frac{2\pi}{\lambda}(d+f_{TL}+2f_{MO})}$ is a constant phase shift that does not affect the overall behavior of the field and $1/M$ is an amplitude-only factor; the term $e^{i\frac{\pi(f_{TL}-d)}{\lambda f_{TL}^2}(x^2+y^2)}$, however, introduces a spherical phase aberration into the field [72] that turns the microscope into a shift-variant system. The quadratic factor can be numerically compensated [73], but even negligible differences in this process can induce significative errors in the phase measurements [70]. Nonetheless, from a closer inspection to the exponent values, the aberration can be removed if $d = f_{TL}$; that is, if the MO and TL are setup in an afocal-telecentric configuration. If this condition is met, the system becomes shift-invariant and the aberration is completely removed by purely-optical means [74]; furthermore, it has been shown this configuration optimizes the use of the spatial-frequency domain [64].

Therefore, when an image-plane afocal-telecentric DHM configuration is used, the Object Wave $O(x, y)$ that reaches the digital detector and coherently interferes with the Reference Wave $R(x, y)$ to form the hologram $H(x, y)$ is

$$O(x, y) = \frac{1}{|M|}\left[S\left(\frac{x}{M}, \frac{y}{M}\right) \otimes \tilde{P}\left(\frac{x}{\lambda f_{TL}}, \frac{y}{\lambda f_{TL}}\right)\right], \tag{1.9}$$

where

$$\tilde{P}\left(\frac{x}{\lambda f_{TL}}, \frac{y}{\lambda f_{TL}}\right) = \iint_{-\infty}^{\infty} P(x', y') e^{-i\frac{2\pi}{\lambda f_{TL}}(x'x+y'y)} dx' dy'. \tag{1.10}$$

That is, a geometrical image of the sample scaled with the microscope's lateral magnification M, composed by light spots whose size, position, and shape are controlled by the pupil function $P(x', y')$.

The hologram $H(x, y)$ can then be reconstructed by any appropriate interferometry method [75]. Particularly, for an off-axis diffraction-limited configuration, this can be achieved by direct filtering in the spatial-frequencies spectrum [63,76], and, if operating under the above-described conditions, no further propagation nor aberration compensation would be

needed. From the numerically reconstructed complex object field $O'(x,y)$, either the intensity

$$I(x,y) = |O'(x,y)|^2 = (\mathrm{Re}\{O'(x,y)\})^2 + (\mathrm{Im}\{O'(x,y)\})^2, \tag{1.11}$$

or phase

$$\phi(x,y) = \mathrm{atan2}\left\{\frac{\mathrm{Im}\{O'(x,y)\}}{\mathrm{Re}\{O'(x,y)\}}\right\}, \tag{1.12}$$

can be computed, with $\mathrm{Re}\{\ \}$ and $\mathrm{Im}\{\ \}$ being the real and imaginary components of the complex field, respectively, and the function $\mathrm{atan2}\{\ \}$ being the arc-tangent function with a modulo 2π output.

From a phase-map retrieved using Eq. 1.12 further properties of the object can be retrieved. In the case of reflective samples, the phase differences are related to the height-map of the object, while, for transmissive samples, these changes are related to both the topography of the object and its refraction index distribution. Both relations are illustrated in **Fig. 1-4**. Therefore, these properties can be measured using the widely known relations [56,75]

$$\Delta\phi_{ref} = \frac{\Delta h\,\pi}{\lambda} \tag{1.13}$$

for reflection imaging, and

$$\Delta\phi_{tra} = \frac{2\pi}{\lambda}\Delta h\,(n_{obj} - n_{med}) \tag{1.14}$$

for transmission samples. In these equations, $\Delta\phi$ is the measured phase delay and Δh the height difference of a feature in the sample, while n_{obj} and n_{med} are the refraction indices of the imaged object and surrounding medium, respectively.

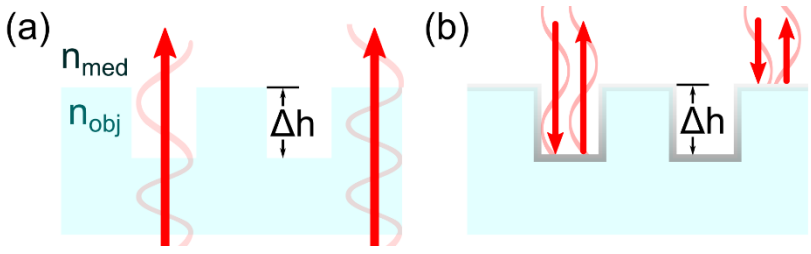

Fig. 1-4. Phase delays introduced by the optical-path difference for the illumination interacting with a (a) transmissive (b) reflective object.

1.1.1 Noise in Lens-based Digital Holographic Microscopy

As shown above, the versatility of lens-based DHM setups allows the pursual of optimized recording configurations; under such conditions, the possible noise-artifacts sources are reduced. For instance, when an image-plane DHM is working in a diffraction-limited afocal-telecentric regime, the reconstruction stage can ideally recover the full object information, as described by Eq. 1.9, without penalties derived from the numerical processing. With the elimination of the need for a numerical refocusing of the sample's information and the purely-optical compensation of the spherical aberration, the main source of noise in the recovered information is thus the coherent digital imaging process itself.

Eq. 1.9 shows that the Object Wave $O(x,y)$ is a composition of the sample information $S(x,y)$, scaled with the microscope's lateral magnification M, by light spots whose size, position, and shape are controlled by the pupil function $P(x',y')$. Therefore, the reconstructed information of an ideal object would only be limited by the pupil function and the resolution capability would be that of the diffraction limit of the system. However, most real-world materials have a noticeable and almost random roughness in the optical scale [17]; when a sample, either transmissive or reflective, is coherently illuminated, each small difference in the surface roughness induces a phase delay that randomly contributes to the observed field. Altogether, the interference of all these random additions after being processed by the imaging system, produces a random high-contrast fine-scale granular pattern atop of the object information, as illustrated in **Fig. 1-5**.

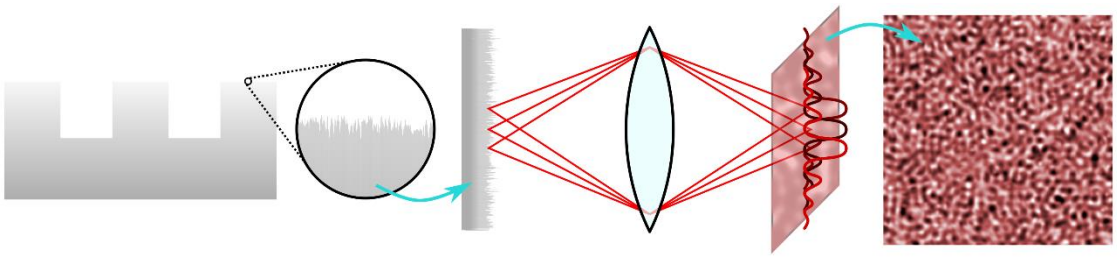

Fig. 1-5. Origin of speckle-noise in a coherent imaging system: the roughness of real-world materials is comparable with the optical wavelengths, thus inducing random phase-delays that interfere in the image plane.

This phenomenon, now known as "Speckle", was identified and reported quickly after the introduction of the first commercially-available lasers [77,78]. Since then, its reduction or

suppression has been an active area of research transversal to many imaging disciplines like ultrasound imaging [18,19], synthetic aperture radar [20,21], optical coherence tomography [22,23], optical astronomy [24,25], and optical holography [26]. In the optical domain, the most complete analyses of speckle's statistical behavior have been published by J. W. Goodman [16,17,79] and J. C. Dainty [80]. While these works consider the complex nature of the diffractive phenomena that produce the speckle pattern, the descriptions are mostly directed towards intensity information, given that it is the only physical parameter that can be measured in the imaging process. Nonetheless, for the intent of the present Master´s thesis, it must be highlighted that the speckle noise affects the quality of the whole reconstructed field, leading to degraded information on both amplitude and phase reconstructions, even as indirect measurements. To this effect, the following remarks are extracted from [16], which is the most up-to-date reference in speckle theory. To avoid unnecessary duplicity of information, the reader is referred to this work if a complete derivation of these statements is needed.

As stated before, speckle noise is originated by the addition of a numerous amount of randomly-phased contributions originating from a coherently illuminated material, whose roughness randomly places scatterers in or over the sample. This process can be understood as a random-phasor sum, where each scatterer contributes with a phasor addition over an area of the image plane determined by the conditions of the imaging system. This interpretation of the speckle nature allows a treatment based on the random-walk statistics as long as three assumptions are made; namely, as stated by J. W. Goodman representing each phasor contribution as $A_n e^{i\phi_n}$ [16]:

> "1. The amplitudes A_n and phases ϕ_n are statistically independent of A_m and ϕ_m provided that $n \neq m$. That is, knowledge of the values of the amplitude and/or phase of one of the component phasors conveys no knowledge about the amplitude and/or phase of another component phasor.
>
> 2. For any n, A_n and ϕ_n are statistically independent of each other. That is, knowledge of the phase of a component phasor conveys no knowledge of the value of the amplitude of that same phasor, and vice versa.
>
> 3. The phases ϕ_m are uniformly distributed on the interval $(-\pi, \pi)$. That is, all values of phase are equally likely."

From these assumptions, the widely known intensity probability density distribution for “fully developed” speckle is shown to be

$$p_I(I) = \left(\frac{1}{\bar{I}}\right) \exp\left(-\frac{I}{\bar{I}}\right), \tag{1.15}$$

with $\bar{I}$ being the mean intensity value, which corresponds to a negative exponential distribution. It is worth noting that, for this to be applicable, the third assumption sets a uniform probability distribution for the phase as

$$p_\phi(\phi) = \frac{1}{2\pi} \; \forall \; \phi \in (-\pi, \pi). \tag{1.16}$$

The intensity distribution in Eq. 1.15 sets the standard deviation σ_I as equal to the mean $\bar{I}$; thus, the two commonly used parameters of speckle contrast C and signal-to-noise ratio S/N are left equal to unity. The speckle contrast $C = \sigma_I/\bar{I}$ is a measure of the intensity fluctuations in the speckle pattern in comparison to the average intensity, while its inverse, the signal-to-noise ratio $S/N = \bar{I}/\sigma_I$, measures the reciprocal relation. A fully developed speckle can thus severely degrade the image formation, as the level of the fluctuations would be comparable to the average value.

In some cases, however, the speckles cannot be fully resolved in the image plane; such a situation corresponds to “partially developed” speckles, in which the consecutive grains are partially averaged during the image formation. The probability distribution for this case becomes highly convoluted and is usually classified by the starting value of the speckle contrast, with the probability density function evolving from the inverse negative-exponential for $C = 1$ to a Gaussian-like distribution as C approaches 0 [35]. Consequently, this case redefines the random-phasors assumed phase from a uniform distribution to a zero-mean Gaussian random variable with a standard deviation σ_ϕ. Contrary to the previous description, this implies that a non-zero intensity always exists, such that as C approaches 0, a residual Gaussian noise is left.

Aside from the just described coherent noise, lens-based DHM could have an additional noise source derived from the recording medium itself. The use of a digital camera introduces a kind of noise that is present in all photonic light-sensing systems: a mix of photonic noise, electronic noise, and quantization noise. However, it has been shown that

the quantization noise, in general, does not have a high dependence with the object distribution [81] and that, even so, the resulting affectation to the image quality can be treated under the same denoising techniques that speckle noise [82]. It was also shown that the most prominent of these noises is the photonic noise [83], but its effect is only particularly deleterious in low-light recording conditions [84] which falls out of the scope of the present work.

1.2 Digital Lensless Holographic Microscopy

The holographic method, as originally conceived by D. Gabor [6,85], was meant to replace the low-quality magnetic lenses used in electron microscopy by a “perfect” lens: free-space propagation of a spherical wave produced by a point source. Spatial coherence is ensured with the radiation emanating from a single point in space, while the diverging behavior of the spherical wave ensures a natural magnification on the propagation. Under this idea, illustrated in **Fig. 1-6**, the illumination complex amplitude, A_{ref}, produced from the point-source propagates towards the recording screen, with a small part of it, A_{scat}, being scattered by an object placed in its path at a distance z. At the screen, which is located at a distance L from the source, the impinging amplitude is thus the superposition of the illuminating amplitude and the wave scattered by the object; that is

$$A(x,y) = A_{ref}(x,y) + A_{scat}(x,y), \tag{1.17}$$

such that the recorded intensity becomes

$$\begin{aligned} I(x,y) &= |A(x,y)|^2 \\ &= \left|A_{ref}\right|^2 + |A_{scat}|^2 + \left[A_{ref}A_{scat}^* + A_{scat}A_{ref}^*\right]. \end{aligned} \tag{1.18}$$

The relation between Eq. 1.2 and Eq. 1.18 can be immediately drawn, as this last one is the expression of holographic diffraction [6] which constituted the basis of holography.

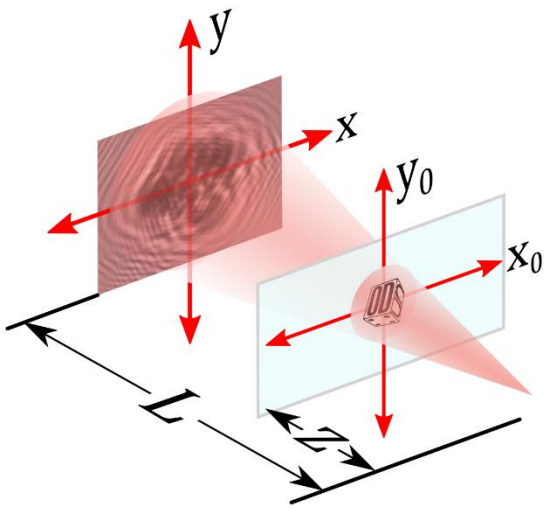

Fig. 1-6. Gabor's holography proposal. A point-source of spherical waves illuminates an object placed at a distance z, projecting a holographic diffraction pattern at a distance L from the source.

At its conception, Gabor's idea could not be implemented due to the then existing limitations in computational power, which hindered the reconstruction stage required to recover the sample's information from the hologram. With the invention of the laser, the holographic principle was promptly brought to the optical realm, where the implementation of off-axis configurations allowed to circumvent the computation limitations at the cost of bulkier and more complex setups for the recording stage. However, with the ever-increasing computational power and development of new optimized reconstruction algorithms [62], the last decades have seen a reemergence of spherical-wavefront lensless DHM with increasing interest as an alternative to do phase-imaging with a reduced hardware cost.

The simplest implementation of this technique is known as Digital Lensless Holographic Microscopy (DLHM) [86]. It was stated before that any DHM setup has an illumination source, an interferometric configuration with microscopic imaging optics, and a digitizing sensor. For DLHM, following Gabor's idea, the illumination is a point-source capable of emitting spherical waves; while in its most common implementation this is achieved by focalizing a laser into a pinhole with a diameter in the order of the illumination wavelength λ, the use of alternative sources like Optical Pickup Units [87], engineered optical fibers [88], gradient-index lenses [89], aspheric lenses [90], and Light-Emitting Diodes [91], have also been reported. In all the previous cases, the Numerical Aperture (NA) is the critical parameter as it determines the effective resolution of the system [92,93], as given by

$$\Delta r \geq \frac{\lambda}{2\,NA}, \tag{1.19}$$

where Δr is the minimum distance between to point objects that can be resolved by the DLHM system. The role of the digitizing sensor is usually played by a digital camera, either CMOS or CCD, and the interferometric configuration is given by the holographic diffraction described in Eq. 1.18 using the free-space propagation of the spherical wave, rather than lenses, as the magnifying imaging optics.

Unlike lens-based DHM, in which the experimental setup can be optimized to ensure the hassle-free reconstruction of the Object Wave, the hardware simplicity of DLHM comes at the expense of a demanding computational process to recover the sample's information. The reconstruction stage is the backward diffraction process of the stored hologram using the reference wave as the carrier; from the theory of optical wave propagation, this stage is thus given by the Kirchhoff-Fresnel transform [60,94]:

$$O'(\overrightarrow{r_0}) = \int_{screen} \widetilde{H}(\vec{r}) A_{ref}(\vec{r}) \frac{\exp\left\{-i\frac{2\pi}{\lambda}|\vec{r} - \overrightarrow{r_0}|\right\}}{|\vec{r} - \overrightarrow{r_0}|} \chi(\vec{r}) d\vec{r}\,, \tag{1.20}$$

where $\vec{r}$ and $\overrightarrow{r_0}$ are the position vectors from the source to the recording plane and sample plane, respectively, $\chi(\vec{r})$ is the inclination factor, and $A_{ref}(\vec{r})$ is the complex amplitude of the illuminating wave. Here, $\widetilde{H}(\vec{r}) = I(\vec{r}) - \left|A_{ref}(\vec{r})\right|^2$ is known as the contrast hologram [86] and its use, rather than $I(\vec{r})$ directly, can remove undesired flaws in the illumination or camera that may appear during the hologram recording [95]; this subtraction, while optional, can be easily achieved by taking an intensity recording without any sample present, or, in some cases, by applying a high-pass filter on the hologram [96].

The use of a point-source of spherical waves located in such a way that the recording device remains perpendicular to the optical axis, sets

$$A_{ref}(\vec{r}) = \frac{1}{|\vec{r}|}\exp\left\{-i\frac{2\pi}{\lambda}|\vec{r}|\right\}, \tag{1.21}$$

and

$$\chi(\vec{r}) = -\frac{i}{2\lambda}\left(1 + \frac{L}{|\vec{r}|}\right). \tag{1.22}$$

Replacing Eq. 1.21 and 1.22 into Eq. 1.20 leads to

$$O'(\overrightarrow{r_0}) = -\frac{i}{2\lambda}\int_S \widetilde{H}(\vec{r})\frac{1}{|\vec{r}|}\exp\left\{-i\frac{2\pi}{\lambda}|\vec{r}|\right\}\frac{\exp\left\{-i\frac{2\pi}{\lambda}|\vec{r}-\overrightarrow{r_0}|\right\}}{|\vec{r}-\overrightarrow{r_0}|}\left(1+\frac{L}{|\vec{r}|}\right)d\vec{r}\,, \tag{1.23}$$

where, if the contrast hologram is used,

$$\widetilde{H}(\vec{r}) = A_{ref}(\vec{r})A^*_{scat}(\vec{r}) + A_{scat}(\vec{r})A^*_{ref}(\vec{r})\,, \tag{1.24}$$

due to $\left|A_{ref}(\vec{r})\right|^2$ being numerically subtracted, and $|A_{scat}|^2$ being negligible as an operational condition of the technique [6]. While Eq. 1.23 is written for the reconstruction of the information at the sample plane, it can be likewise computed for any other plane by changing the vector $\overrightarrow{r_0}$ to whichever position is of interest; this allows, for instance, the rendering of the 3D structure of the sample if sufficiently transparent, and the analysis of the whole illumination volume from a single hologram.

A direct calculation of Eq. 1.23 has a high computationally complexity, and the traditional Fourier-transform-based numerical scalar diffraction algorithms [97] do not satisfy the experimental conditions of DLHM due to the high-NAs involved and the need to independently manipulate the output window size. As stated before, this impasse hindered the viable implementation of this technology until a suitable algorithm was developed [98]; however, this method, which assumes that the distance from the point-source to the sample is many times less than to the screen, has been now highly optimized [96,99] and even implemented at video-rate speeds [100].

Eq. 1.24 shows that, unlike lens-based DHM, the reconstructed information from DLHM will have the simultaneous presence of both the real and virtual images of the sample. While this “twin-image” problem is a common nuisance for other in-line holographic techniques, the use of a spherical illumination highly alleviates its detrimental effects in a DLHM configuration. When the object is reconstructed, the in-focus position of the conjugated image would be symmetrically located at the opposite side of the point-source location; as the distance between the sample and the source is typically many times the wavelength,

the twin image would be highly-defocused contributing only an almost-uniform background addition [95]. Thus, despite being present in the object reconstruction, the conjugated image effect is not as detrimental as the one found in plane-wave in-line holographic configurations.

From the reconstructed complex wave amplitude $O'(x_0, y_0)$, both the intensity and phase of the object can be therefore computed with the same relations presented for lens-based DHM in Eq. 1.11 and 1.12. While some claims arguing that DLHM is not capable of producing phase images can be found in the literature, it has been widely proven otherwise [95,96,101]; furthermore, an ample discussion of the phase recovery process and quantitative phase imaging with DLHM is available in [102].

For a more in-detail treatment of the experimental implementation of DLHM, its imaging properties, and some common applications, the reader is referred to [95].

1.2.1 Noise in Digital Lensless Holographic Microscopy

The hardware simplicity of DLHM architectures significantly reduces the possible noise sources during the recording stage; additionally, with only a point-source of spherical waves and a digital camera, the physical setup lacks the imaging system structure that was previously used to recognize speckle formation in lens-based DHM. This does not mean that the speckle formation is absent in DLHM; rather, its full development is shared with the reconstruction stage. While the image-plane configuration of lens-based DHM allowed a description in terms of the full imaging system to be pursued in the reconstruction stage, the image formation properties of DLHM are forcefully divided between the two stages.

On one hand, the intensity that impinges into the recording device after the holographic diffraction process may be understood as a free-space speckle formation process in the camera plane [17], assuming that it is directly produced by the optical roughness of the sample; however, as the objects that fulfill DLHM's weak-scattering condition do not significantly modify the incident illumination [6], the random phase delays of the scatterers are expected to be narrowly distributed in a zero-mean Gaussian, thus only slightly contributing to the speckle formation in the recording screen. On the other hand, as the reconstruction process numerically emulates the free-space diffraction, the recovered

complex field would have gone through an imaging process equivalent to the one achieved by the lens-based system; as such, the imaging-system-driven speckle formation process [17] should still be appliable for the recovered information. In this case, however, there is not an easily-controllable pupil function that characterizes the speckle grain's size, position, and shape; instead, the point spread function of the system is simultaneously determined by both the recording and reconstruction parameters [103].

Another common source of undesired noise in DLHM configurations is the presence of imperfections (including dust particles, scratches, and defects) in the illumination source, the digital camera, or even the medium surrounding the sample, and the appearance of multiple reflections in the illumination volume [104]. The linearity of the holographic diffraction principle in the complex amplitude, which supports the DLHM ability to recover phase information [95], causes the imperfections to project a diffraction pattern that is added to the desired information during the recording; however, that same linearity allows some of these unwanted additions to be promptly removed with the use of the contrast hologram of the scene [103]. The reflections, however, cannot be so easily accounted for; the glass slide used in the preparation of the samples, the protection elements of the recording sensor, and even the external surface of the illumination source, may act as reflection spots which, if the coherence of the source is high enough, will produce parasitic fringes in the hologram that affect the reconstructed information [105].

Finally, the recording device itself can also be a noise source. However, as this kind of noise is of technical nature, and thus directly related to the photonic device rather than the microscope configuration, the same considerations stated for lens-based DHM can be made.

1.3 Existing noise reduction methodologies

The severe degradation that noise introduces into coherent imaging techniques has limited their applicability in some fields. In the case of DHM, its full-field, noninvasive, dynamic, high-sensitivity quantitative imaging capabilities on both amplitude and phase of microscopic objects, while attractive for many disciplines, have been hindered by the noise sources identified in the previous subsections; among them, the multiplicative coherent noise, commonly known as speckle, is the most deleterious one as it adds ambiguity to the

measurements and may deteriorate the resolution of the system. Therefore, the development of noise reduction or suppression methodologies is of primordial interest for most researchers in the field.

By understanding the possible noise sources in DHM architectures, and the physical processes that drive them, three kinds of denoising methods can be envisioned: i) those based on the engineering of the illumination source, modifying its coherence properties, ii) those that rely upon modifications or optimizations to the recording stage, and iii) those that reduce the noise effects by numerically processing the reconstructed information. While some of the most successful denoising methods reported to date are hybrid methods that do not fully comply with only one category [33,34], their individual steps can surely be fully classified into one.

Due to the uncountable amount of work that has been devoted to speckle and the ever-increasing number of research publications related to these methods, multiple review works have been published with the most successful approaches for a given technique. In Digital Holography, recent and complete compilations of speckle denoising methods are available in [106,107], one of them having been published in the first months of 2020; additionally, a comprehensive study of the suppression of other inaccuracy sources can be found in [108], and quantitative evaluations of the effects of noise reduction in phase images in [35,109]. Below, some of the denoising methods with higher applicability to DHM experimental conditions are briefly presented and referenced. As a detailed description of each method would fall beyond the scope of the present work, and the existing reviews are considerably updated, the reader is referred to the aforementioned literature for this intent.

1.3.1 Engineering of the illumination source

Given that most of the noises identified in the past sections are consequences of the high levels of coherence given by traditional laser sources, one of the first ideas to reduce its incidence was to eliminate the coherence requirement altogether. Following this idea, the incoherent-imaging capabilities of many coherent techniques have been tested to determine how much of the illumination coherence, either temporal or spatial, can be removed without completely losing the valuable properties of the technique.

For holography-based techniques, early reports showed that the coherence requirement could be partially relaxed while still retaining most of its interferometric capabilities [110]; these were later confirmed and expanded for digital holography setups and their additional sampling restraints [111]. The first partially-coherent implementation in lens-based DHM successfully used LED illuminations, with a mix of carefully-aligned spatial and color filters to reduce the coherent noise while still retaining the numerical refocusing capability [112]; recently, this technique was also improved to provide color images and demonstrate the phase reconstruction capabilities [113].

The filtering, and thus alignment, requirements of this first proposal were later partially alleviated by the introduction of a diffuser-based setup, which aimed to reduce the spatial coherence of a common laser source [114]. In this configuration, the laser light is focused on a rotating diffuser, and the transmitted light is then collimated and used as the illumination source of a traditional lens-based DHM setup. The random roughness of the illuminated area of the diffuser and its rotation create a speckle field that constantly changes. As such, the illumination that is passed to the DHM system follows a random-phased imaging process analogous to the one described for the noise formation in lens-based DHM; the net result of this time-varying decorrelations being a reduction of the spatial coherence. The degree of decorrelation is controlled by the illuminated area of the diffuser, which can be tuned, in turn, by altering the positions of the focusing and collimating lenses, resembling a Koehler illuminator from conventional microscopy [115]. The feasibility of this implementation has been widely proven successful in multiple application areas, including accurate quantitative phase imaging [116–118]; and while its use commonly requires multiple recordings to compensate for the speckle-field additions, if an exact knowledge of the implemented diffuser's statistical properties is available, it can be used to reduce possible spatial resolution losses [119]. An alternative variation of this approach, which considers the use of a highly-incoherent source instead of a laser and the introduction of a diffraction grating in the reference path, has reported impressive results even with phase imaging [120].

Another option for reducing the coherence during the recording is the introduction of "random lasers" [121], which have been slowly adopted during the past decade; these new lasers with reduced spatial coherence have also allowed the development of DHM-based approaches under similar configurations to those of the lens-based setups [122]. However,

these laser sources have a high entry-point price and require especial implementation cautions that limit their applicability for the moment.

Finally, for DLHM setups, a coherence reduction approach can be especially effective due to the small operational distances and weak-scattering objects employed in the technique. Particularly, given the simplicity of the DLHM configuration, a replacement of the laser source by LED illumination has been conducted, showing significant improvements in both speckle and parasitic-reflections noise at the cost of spatial resolution [105,123]. The resulting implementations were shown to retain the desired holographic properties, and have even been explored in the recovery of color information [124]. However, while the literature currently has mathematical descriptions of Quantitative Phase Imaging under partially-coherent illumination [125], and some of the mentioned references for lens-based DHM have shown experimental results of phase-maps with reduced coherence under similar implementations, no works could be found that explicitly deal with the incidence of coherence reduction on DLHM phase reconstructions.

1.3.2 Optical denoising methods

In general, the source-engineering noise reduction methods decrease the achievable focal depth and demand a very precise adjustment between the Object and Reference waves optical paths to ensure the required interference [108], thus increasing the alignment difficulty. An alternative approach that keeps the signal of interest highly correlated during the recording while still achieving a decorrelation of the noise, is the time multiplexing of the holograms with changing noise patterns; that is, repeatedly capturing the same scene with multiple realizations of the noise and averaging the results. These kinds of approaches, also known as “multi-look” methods, rely on the introduction of noise diversity between recordings (each one being a “look”) by a wide arrange of methods.

One of the most adopted approaches to introduce the required diversity into the recordings involves the insertion of a moving diffuser into the light path in an equivalent setup to the one described in the previous subsection. In this case, however, the averaging occurs incoherently over the reconstruction of the multiple recordings taken for different positions of the diffuser [34,126,127]. While this technique has been mostly implemented in digital

holography for large objects, it has also been implemented as part of hybrid methods with promising results in DHM [33], including the improvement of phase information.

The noise variations between the recordings can also be produced by inducing small changes into any of the multiple parameters that control coherent noise formation [16], at the expense of adding complexity to the setup and alignment of the system. For instance, this can be achieved by slightly changing the angle of the illumination [128,129], recording device [30,130], or even the imaged object [131,132]; it can also be done by using different wavelengths [133,134] or polarizations [31,135] in the illumination, or by introducing moving transmission masks in its path [136–138]. In all these cases, after the N "looks" have been recorded, their reconstructions must be averaged; this is straightforwardly done as [106]

$$\boldsymbol{A} = \frac{1}{N}\sum_{i=1}^{N} \boldsymbol{A}_i \,, \tag{1.25}$$

where $\boldsymbol{A}_i$ is the reconstruction of the i-th hologram, in either intensity of phase, as given by Eq. 1.11 or 1.12.

The operational principle of noise reduction by the averaging of multiple decorrelated speckle patters is commonly described in terms of the speckle contrast C [16]. It has been shown that, if N fully uncorrelated speckle patterns are averaged, the resulting contrast will decrease as $1/\sqrt{N}$ [80]. Nonetheless, most existing approaches to introduce noise decorrelation between shots cannot ensure fully uncorrelated noise patterns; as such, the effective degree of speckle contrast reduction achievable by the presented methods can only approximate this trend. Furthermore, by the asymptotic behavior of the ideal trend, one can see beforehand that any multi-look method reaches a saturation point above which adding new "looks" would not cause further improvement [30].

The main drivers of the denoising performance of multi-look methods are, thus, the available number of "looks" to be averaged and the achievable noise decorrelation degree between them (up to the aforementioned saturation point). Consequently, their use becomes limited to the ability to produce multiple recordings with changing noise over an unchanging scene, severely limiting their use in the observation of dynamical processes which are of common interest in biological applications. Furthermore, as the superposition of the multiple reconstructions must be made incoherently [16], the information of the

amplitude and phase becomes decorrelated, hindering the possibility of effectively manipulating a denoised version of the complex field [139]. Regarding this last drawback, an alternative encoding method to Eq. 1.25 was recently proposed as [140]

$$\boldsymbol{A} = \frac{1}{N}\left(N! \prod_{i=1}^{N} \boldsymbol{A}_i\right)^{1/N}, \tag{1.26}$$

but its implementation has been mostly exploited in numerical denoising methods, and its applicability in DHM experimental conditions has not yet been explored enough in the available literature.

1.3.3 Numerical denoising methods

A final alternative approach to reduce coherent noise is the implementation of numerical denoising methods. These techniques, which are applied to the reconstructed information, allow the noise suppression to be pursued without any modification to the recording setup; as such, most are single-shot methods, highly suitable for dynamic processes, and appliable to previously recorded holograms. Additionally, these methods can be designed for denoising either the hologram directly (thus preserving the coherence between amplitude and phase) or a single reconstruction of any kind (as described for the optical denoising methods).

The high versatility that the digital world provides, added to the modern strengthened interest in digital image processing across many fields, has led to a copious and ever-increasing amount of numerical denoising methods, algorithms, and strategies. While a complete mapping of all the numerical denoising techniques that have been proposed for Digital Holography would represent a Herculean task, a review of the most relevant and successful ones can be found in [106] while a comprehensive overview with more detailed descriptions is available in [107] and the supplementary information of [106]. Nonetheless, most of the existing methods can be grouped by the kind of numerical processing approach implemented; namely, those that emulate the optical multi-look techniques, those that operate over the spatial domain, those that operate over a transform domain, and those based on deep-learning. From this perspective, a brief description of each of the proposed categories is presented below, referencing its main representatives in the current state-of-the-art.

A first intuitive approach to numerical denoising implementations is the creation of digital equivalents of the optical multi-look methods presented in the previous subsection. The most relevant advances in this regard have been presented by analogs to the multiple illumination or recording angles method and the moving transmittance mask method. The first has been achieved by resampling and then averaging the reconstructions of non-image-plane holograms, either randomly [28], with a non-overlapping window [141], or with a shifting and overlapping window [142]. Meanwhile, the second was achieved by a similar sampling window but acting on the Fourier spectrum rather than the spatial distribution of the hologram [27]. Unlike their optical counterparts, the use of these methods does cause a loss in spatial resolution.

Another approach for denoising speckle-affected information is the use of filters over the spatial domain; that is, directly over the reconstructed amplitude or phase. Most of the available options that fall into this category were not designed for Digital Holography; rather, they have been adapted from other disciplines. Among the multiple available filters, the following are the most common ones. Initially, from those that act locally (over each pixel while considering its vicinity): the Mean, Median and Wiener filters, which are typical in image processing [143]; the Lee filter [144], which is based in pixel-wise statistics [145]; and the Frost filter [146], which optimizes the minimum standard error and introduces the consideration of the noise being multiplicative. And from those that act non-locally: the Non-Local-Mean filter [147], which uses a Bayesian framework to extend the Mean filter from additive noise to multiplicative noise; and a filter based on the anisotropic diffusion model [148], which was recently adapted to DHM phase imaging with great results [149].

While spatial-domain filters have shown promising results, they deal with a limited ability to achieve effective speckle denoising due to the multiplicative nature of this noise. As this difficulty has also been previously recognized in other fields with different noise sources, a set of alternative methods that transform the information into other domains where the signal and the noise might be more easily separated, have been developed. Some of the most common representatives of these kinds of approaches, consequently named transform-domain methods, are: Fourier-transform-based methods [150,151], typically implemented via a Fast Fourier Transform, and whose most successful implementation is the Windowed Fourier Transform filter (WFT2F) which was specifically designed for fringe

patterns [152,153]; Wavelet-transform-based methods [154,155]; sparsity-based methods, which work without any prior estimation of the noise statistics and whose most prominent implementation in digital holography is SPADEDH [139]; and transformation methods based non-local statistics, from which Block-Matching and 3D filtering (BM3D) [156] and the Homomorphic filter [157] are the most successful implementations.

Almost all the methods from the aforementioned categories are dependent on a set of parameters whose exact values to ensure the best possible outcome are not easy to determine. The deep-learning-based methods try to surpass this limitation by implementing Deep-Learning strategies and Convolutional Neural Networks that allow the automatic extraction of the best possible parameters in an indirect way. This sort of approaches commonly implement indirectly some of the already mentioned methods, and they have shown promising results for coherent noise during the past couple of years [158–161].

From the great number of referenced methods, the analysis conducted in [35,109] allows the determination of the methods that produce the best results in Digital Holography reconstructions. In these works, it was concluded that the current bleeding-edge in numerical speckle denoising is set by BM3D [162], which has even led to the development of a hybrid method with optical multiplexing to achieve almost-speckle-free information in large objects [34]; however, in the case of phase reconstructions, WFT2F [152] achieved the best results in terms of the standard output error, despite being surpassed by BM3D when complicated features were present. These two techniques (WFT2F and BM3D) will be therefore implemented and used as base-line for the new speckle denoising methods proposed in this Master thesis.

Finally, it must be highlighted that, as reported by the latest reviews of denoising methods for Digital Holography [106], very few of the existing numerical denoising strategies are specifically suited for digital holography; rather, most have been adapted to it. Consequently, there is a current need for a deep investigation in noise suppression techniques that operate simultaneously and efficiently on both amplitude and phase. Currently, the closest approaches to such a task are the sparsity-based methods like SPADEDH [139,163] and a generalization of BM3D to the complex domain [164,165].

As a summary: noise reduction methods based on the engineering of the illumination source can be the most effective but introduce complexities on the recording setup that not all applications may tolerate; optical denoising methods offer a denoising alternative without compromising the spatial resolution, but come at the expense of added complexity to the setup and the need to record multiple holograms for a single final image; and digital denoising methods can be single-shot and do not require any modifications to the existing setups, but its noise reduction capacity almost always causes a loss of spatial resolution. The trade-offs of each approach must thus be considered according to the particular needs of each application case. Furthermore, while the speckle denoising research field might seem saturated, the state-of-the-art suggest that research regarding new denoising strategies suited for the reconstructed complex field of DHM must be pursued with high interest. In this pursual, WFT2F and BM3D should be used as the comparison points due to their current category as the state-of-the-art techniques for speckle denoising.

2. Suppression of non-speckle noise and numerical artifacts

As identified above, the highly deleterious effects of coherent noise in Digital Holographic Microscopy (DHM) include the introduction of ambiguity to the measurements and a notorious degradation of the image visual quality. However, it was also presented that, in the search for an effective suppression method, one common consequence is a reduction of the spatial resolution of the system. Given that in any microscopy technique the spatial resolution is one of the parameters of uttermost importance, the possible benefits of denoising with any collateral affectation to it must be carefully weighed before the application of such a technique. Therefore, before the proposal or implementation of any denoising technique, it must be ensured that the microscopy setup is adequately characterized and optimized, such that any other non-speckle affectation to the imaging properties of the system are either suppressed beforehand or easily identified. Consequently, in this chapter, the characterization and calibration of the DHM architectures are sought, ensuring the suppression of non-speckle noise and numerical artifacts derived from the reconstruction stage in both lens-based DHM and Digital Lensless Holographic Microscopy (DLHM).

2.1 Optimizations for Lens-based DHM

From the brief description of speckle-noise generation in a lens-based DHM that was presented in section 1.1.1, it can be seen that to have a full overview and accurate knowledge of the noise behavior and imaging capabilities of the system, one must consider a wide set of parameters that characterize the microscope. Namely, the system is defined by the illumination wavelength, the microscope's objective numerical aperture and magnification, the focal length of the tube lens, the angle between the reference and object waves, and the discretization parameters set by the recording device.

Having a realistic representation of DHM, to accurately predict the noise behavior and imaging capabilities of the system, allows the straightforward determination and tuning of the best-case experimental conditions that should be reached. After recognizing such a scenario, the noise that is inherent to the technique can be easily distinguished from the technical noise derived from the misalignment of the setup or inherited from the numerical processing of the information. The system can then be tuned to comply as closely as possible with the theoretical prediction, ensuring that the setup parameters are optimal, and recognizing any losses as derived from the denoising strategies to be proposed. Furthermore, such a modeling approach would allow the production of accurate numerical noise representations to be used in the evaluation of the proposed strategies.

The described need for a realistic representation of lens-based DHM was met with the work reported in the following manuscript, attached at the end of this text:

"Realistic modeling of digital holographic microscopy," Optical Engineering **59**(10), 102418 (2020) [41]

Having the platform for realistically representing a lens-based DHM, an experimental dual-mode setup (that is, one capable of working in both transmission and reflection mode) was designed and implemented following the schematic in panel (a) of **Fig. 2-1**.

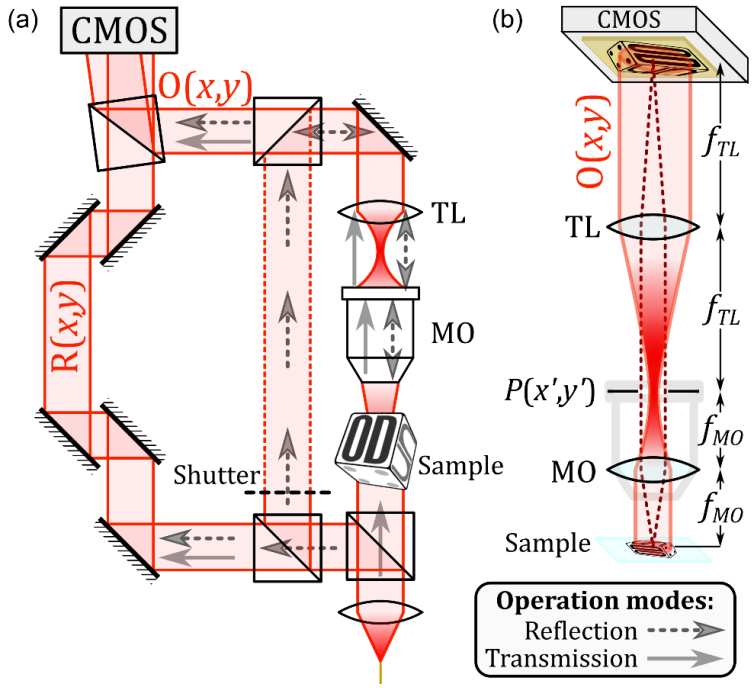

Fig. 2-1. Design of a dual-mode implementation of lens-based DHM. (a) General design. (b) Afocal-telecentric configuration of the microscope optics in the object arm.

As seen in panel (b) of **Fig. 2-1**, the microscope in the object arm was set up in an afocal-telecentric configuration, ensuring the full compensation of the spherical phase aberration since the recording, and reducing the required processing of the phase maps [74].

An example of the achieved phase imaging capabilities is presented in **Fig. 2-2**. The microscope operates with an illumination wavelength of 533 nm, a MO of 10X/0.25, and a CMOS camera of 2048 x 2048 pixels of 3.4 µm side length. The hologram of a star test target made of acrylate polymer over glass is presented in panel (a), where the inset shows the Shannon-limited fringes. In panel (b), the Fourier Spectrum of the hologram shows the complete separation of the diffraction orders that characterizes an off-axis configuration. Panels (c) and (d) show the amplitude and phase reconstructions, respectively; as the object is a phase-pure sample, the amplitude is mostly a noise field while the phase carries the object's information. The insets in these last panels show the resulting high-frequency speckle noise in a background area.

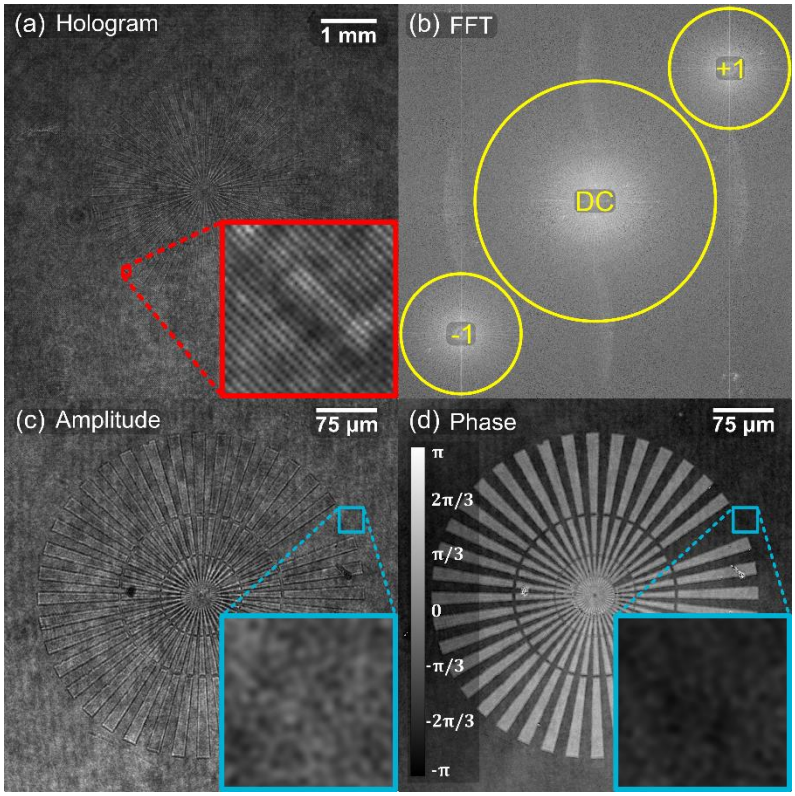

Fig. 2-2. Illustrative experimental result from a dual-mode implementation of lens-based DHM operating in transmission mode. (a) Hologram of phase benchmarking test, and an inset showing the interference fringes. (b) Fourier Spectrum of the hologram. (c/d) Amplitude/Phase reconstruction using +1 order. The insets in panels (c) and (d) show the resulting speckle noise in a background area.

Panel (b) of **Fig. 2-2** suggests that the configuration is using almost completely the available space-bandwidth of the sensor. Indeed, using the realistic DHM model [41], the results can be directly associated with a diffraction-limited configuration, and explicit computation of the maximum allowable NA for the system [64] yields

$$NA \leq \frac{(0.533\ \mu\text{m})\ (10)}{\sqrt{2}\left(\sqrt{2}+3\right)\ (3.4\ \mu\text{m})} \approx 0.251. \tag{2.1}$$

This calculation is underwhelming, as an NA ≤ 0.25 is highly restrictive for a microscopy configuration as it severely limits the achievable resolution. Such difficulty was promptly verified by changing the imaging sensor to another CMOS camera whose pixel side length is 5.2 µm, as illustrated in **Fig. 2-3**. In panel (a), the hologram of the reflective lithographic sample, selected to portray the dual-mode-imaging capability, shows the Shannon-limited fringes; however, the Fourier Spectrum in panel (b) shows that it is not possible to reach a diffraction-limited configuration: the diffraction orders, bounded by red circles, are partially overlapped between them and wrapped around the spectrum.

Using the same process as in Eq. 2.1, the maximum permissible NA for the configuration with the alternative sensor yields

$$NA \leq \frac{(0.533\ \mu\text{m})\ (10)}{\sqrt{2}\left(\sqrt{2}+3\right)\ (5.2\ \mu\text{m})} \approx 0.164, \tag{2.2}$$

thus confirming that the available space-bandwidth with this camera cannot adequately sample the full spatial-frequency components that the 10x/0.25 MO provides. Consequently, a reconstruction by direct spatial filtering must be considered inappropriate; the yellow circle in panel (b) of **Fig. 2-3** shows the filter used for the reconstruction in amplitude and phase, in panels (c) and (d) respectively, taken over the +1 order. While the reconstructions are free of the anomalous presence of the other diffraction orders and the spherical aberration, the reduced filter size produces significative losses in resolution; this can be seen from the insets in the reconstructions, where the speckle noise in the background is composed by grains of bigger size than those of **Fig. 2-2** despite using the same optical imaging system.

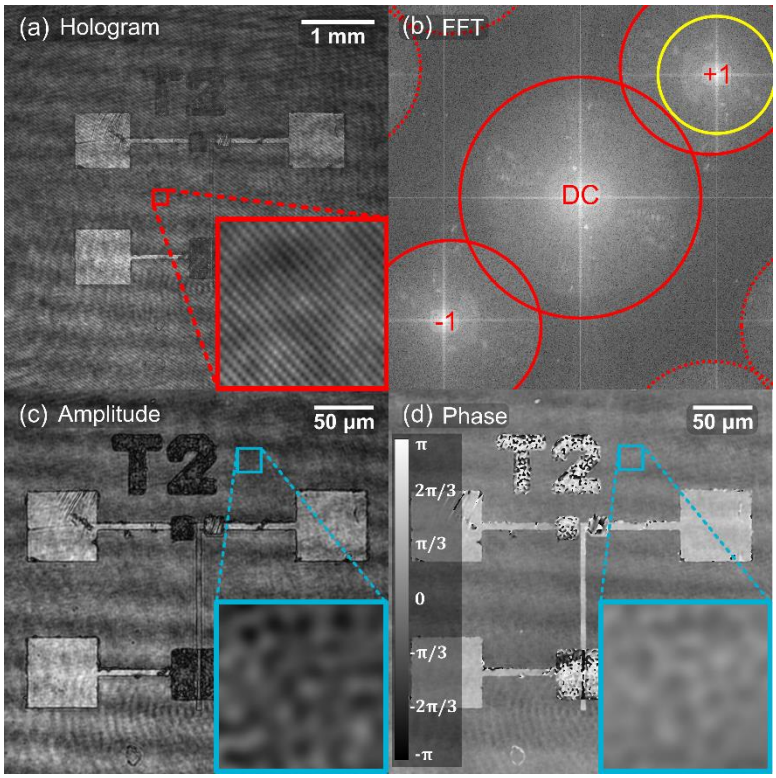

Fig. 2-3. Illustrative experimental result from a dual-mode implementation of lens-based DHM operating in reflection mode. (a) Hologram of a reflective lithographic sample and an inset showing the interference fringes. (b) Fourier Spectrum of the hologram. (c/d) Amplitude/Phase reconstruction using the yellow circle in panel (b). The insets in panels (c) and (d) show the resulting speckle noise in a background area.

For the subsequent analysis of speckle denoising proposals, and being able to appraise the drawbacks from their implementation, it is of uttermost importance to have an accurate representation of the system's resolution capability. To achieve so, the aforementioned conditions would limit the analysis to small magnifications and the use of the higher-end sensor. This is an unacceptable restriction to the desired application cases and calls for an alternative solution.

Despite the robust and minimum-processing approach that the off-axis architecture provides, an alternative to increasing the maximum allowable NA of the system is the implementation of phase-shifting reconstruction techniques on a slightly-off-axis configuration. **Fig. 2-4** shows a phase-shifting reconstruction of the same sample imaged in the off-axis from **Fig. 2-2** but using the lower-end sensor from **Fig. 2-3**. In panels (a) and (c) of **Fig. 2-4**, two holograms, recorded in slightly-off-axis configuration with a π-shift between them, are shown; the large period of the fringes shows that the interference angle

is small when compared to the previous off-axis results. Panel (b) shows the Fourier Spectrum of the hologram from panel (a); as expected, the three diffraction orders are almost completely overlapped. Finally, panel (d) shows the phase reconstruction of the object. It can be immediately verified from the inset, taken from the center of the test, that the reconstructed information using the phase-shifting approach has the same resolution as the off-axis diffraction-limited case.

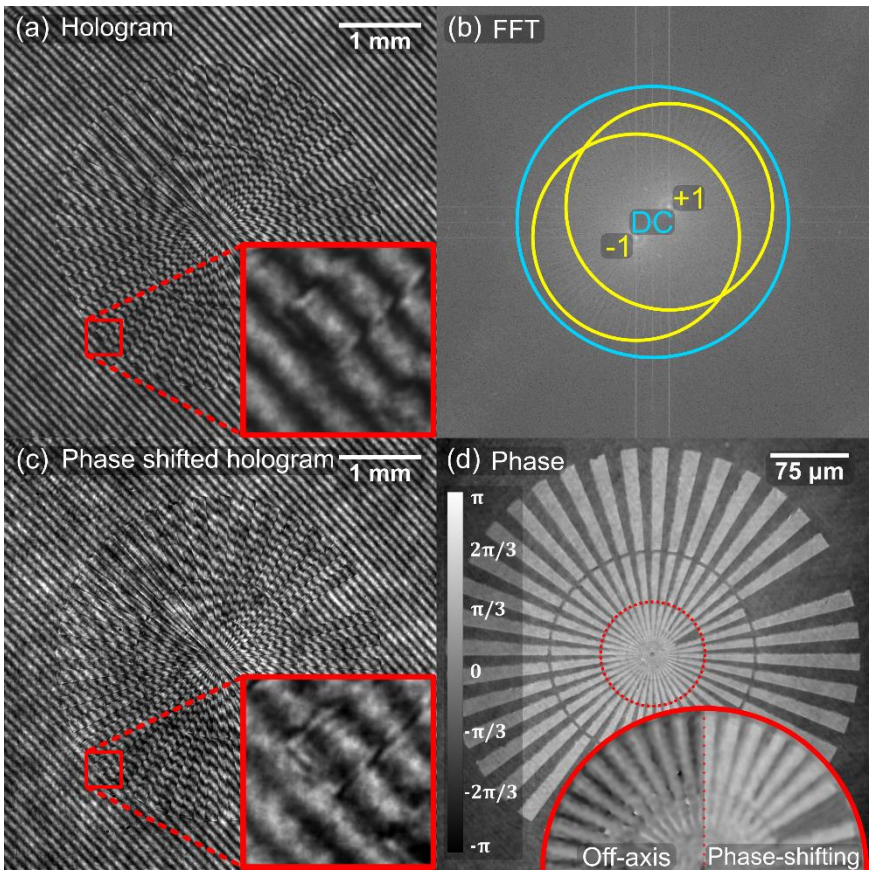

Fig. 2-4. Phase-shifting DHM from a slightly-off-axis configuration in transmission mode. (a) Hologram of a phase benchmarking test. (b) Fourier Spectrum of the hologram with high overlap between the diffraction orders. (c) A phase-shifted hologram. (d) Phase reconstruction using the +1 order; the inset compares the center of the test from this reconstruction to the off-axis diffraction-limited case.

It is thus seen that phase-shifting techniques allow surpassing the limited NA values of the off-axis configuration; additionally, they represent an easier alignment and thus higher-temporal stability. However, their implementation forces the acquisition of multiple holograms with well-defined and known phase-shifts which, in turn, tends to increase the setup complexity. To keep the high-throughput of the off-axis configuration that allows the

implementation of DHM into dynamical processes, alternative phase-shifting algorithms that require fewer input holograms are required. Furthermore, to ease the added complexity to the setup that is required to ensure that the induced phase-shifts are known and controlled, alternative approaches where this requirement is relaxed are also needed.

The described need for alternative phase-shifting DHM algorithms with a reduced number of input images and a waived need to precisely know and control the phase-shift between holograms was met with the work reported in the following manuscripts, attached at the end of this text:

- *"Phase-shifting digital holographic microscopy with an iterative blind reconstruction algorithm,"* Applied Optics **58**, G311-G317 (2019) [40]
- *"Fast-iterative blind phase-shifting digital holographic microscopy using two images,"* Applied Optics **59**, G7469-7476 (2020) [44]

Additionally, these works were presented in the following conferences:

- *"Blind phase-shifting digital holographic microscopy using an iterative approach,"* Three-Dimensional Imaging, Visualization, and Display, Digital Forum, 2020 [50]
- "*Fast-iterative bling reconstruction algorithms for accurate quantitative phase images in phase-shifting digital holographic microscopy,"* Imaging and Applied Optics Congress (Online), Washington DC United States, 2020 [51]

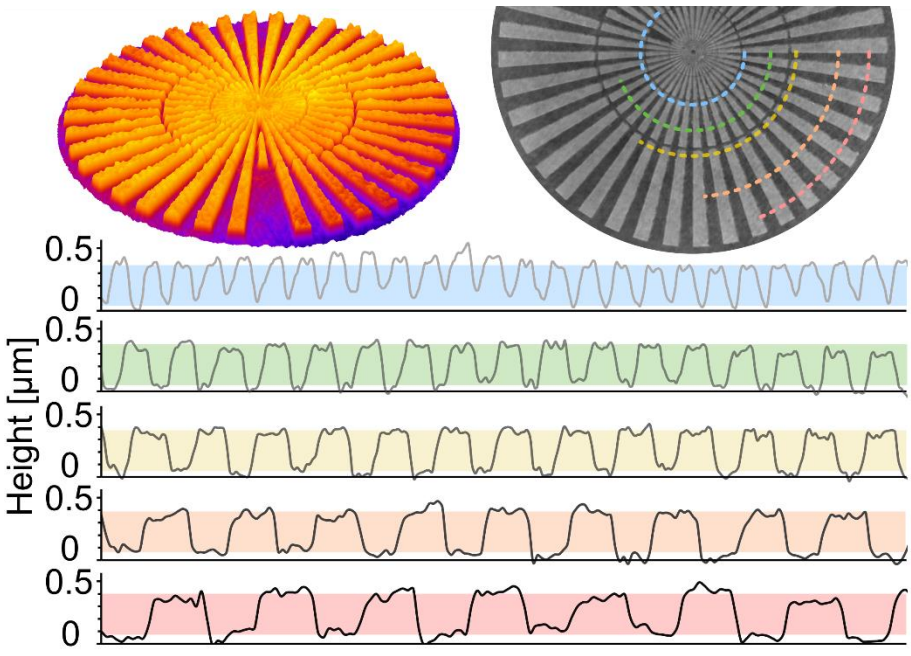

Fig. 2-5. Phase-map reconstruction accuracy using the phase-shifting method proposed in [40]. The size of the color bars in the plots marks the theoretical height of the target's features.

Fig. 2-5 shows a result obtained with the phase-shifting method proposed in [40] for a height-calibrated star test target. The height profiles, taken at different spatial-frequency ranges of the object, were compared to the nominal value reported by the manufacturer. Each plot is bounded by a colored bar that shows the calibrated height. The good agreement between the reconstructed information and the theoretical expectation, at all the spatial-frequencies ranges, proves that the developed blind reconstruction algorithm with a reduced number of input images achieves the desired accurate and high-quality retrieval of phase-maps from DHM.

The proposed optimizations in this section allow the lens-based DHM to operate in an ample range of sizes and magnifications, either in an off-axis or a slightly-off-axis regime, with reduced time penalties, without the need of introducing additional complexity to the setup, and ensuring that the recovered information is diffraction-limited. Knowing that the reconstructed phase information accurately reflects the imaging capabilities of the system, added to the developed realistic simulation platform, will allow the precise distinction between the information degradation induced by coherent-noise during the imaging process and the possible negative influence of the proposed noise reduction techniques.

2.2 Optimizations for DLHM

While the architecture of DLHM is significantly simpler than its lens-based counterpart, a wide set of parameters must also be considered during the analysis of its imaging properties. Namely: the illumination wavelength, the distance from the point-source to the sample (z) and the screen (L, which defines the curvature radius of the impinging wavefront), the numerical aperture of the source, and the discrete parameters of the recording device. A recent publication from the Optics and Optodigital Processing research group proposed an ImageJ-based [166] platform for the simulation and numerical processing of a DLHM system [96]; while this work does not explicitly consider the speckle formation phenomena, the platform developed for lens-based DHM [41] can produce a transmittance distribution with realistic optical roughness that could be then used as the input for the simulation, yielding a realistic simulation platform for DLHM.

Having a platform for realistically representing a DLHM system, from which the same optimization procedures described for lens-based DHM are applicable, an experimental

DLHM was implemented by focusing the light of a 405 nm laser diode onto a pinhole of 500 nm in diameter and using a CMOS camera with 2048 x 2048 pixels with 6 µm of side length to record the resulting diffraction patterns. The recorded information was transferred to a mid-range laptop, equipped with the aforementioned processing platform [96], for the subsequent reconstructions. This setup is illustrated in **Fig. 2-6**.

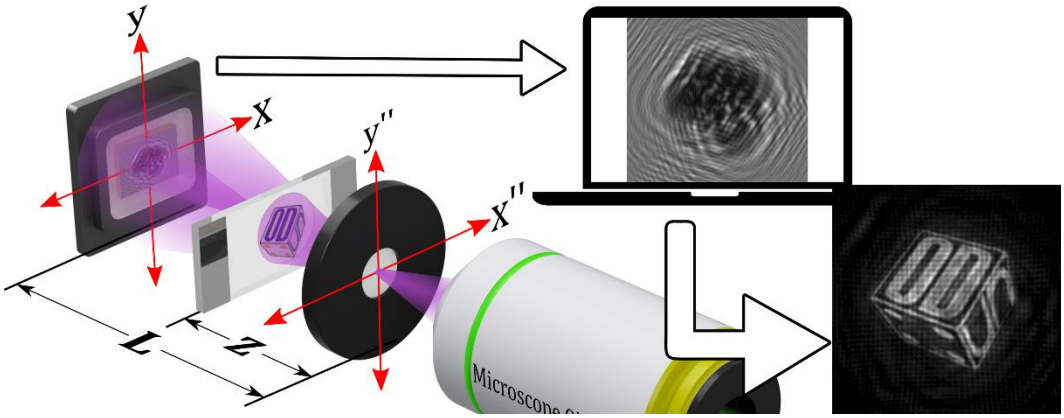

Fig. 2-6. DLHM setup where the spherical illumination is done by focusing laser light into a pinhole.

As stated before, accurate representation and characterization of the full resolution capabilities of the system are of uttermost importance. Due to the simple experimental setup of the resulting DLHM architecture, and following the descriptions from section 1.2, two main limitations are identified: the approximations introduced by the existing reconstruction algorithms, which may induce numerical artifacts in the recovered information, and the accurate knowledge of the experimental parameters used during the recording of the hologram. These limitations were thus addressed.

Firstly, the remarkable reduction in computational complexity that the state-of-the-art reconstruction algorithms achieve is attributed to their implementation with Fast Fourier Transforms (FFT) [167]. However, the use of such computational approaches requires the introduction of approximations to the diffraction integral to ensure that the backpropagation can be written in terms of a convolution, which, in turn, may be approximated to a discrete FFT. When such approximations are made, the propagation is limited to a defined application range due to the discretization of the kernels, and numerical artifacts may be introduced as a result of the truncation of the Fourier series. These limitations have been previously shown to produce significant deviations in the recovered phase information in

traditional propagation techniques, even inside the commonly-accepted application ranges [168]. Particularly, for the Kirchhoff-Helmholtz reconstruction algorithm, which is implemented by the aforementioned processing platform [96], a detailed analysis of the required approximations and the associated resolution limitations (and how to overcome them) is presented in [95].

These limitations are almost unavoidable. Any optimized calculation of the diffraction process must involve some sort of approximation to avoid dealing with the direct computation of the double integral. Nonetheless, if an accurate representation is desired as a reference to identify these possible noise sources, such an implementation must be achieved. Rather than reducing the computational complexity of the direct and non-approximated calculation of the diffraction integral, a full implementation with reduced execution time is sought. To achieve it, the linearity of Eq. 1.20 can be exploited to parallelize the computation of each reconstruction point using a general-purpose computing on Graphical Processing Units (GPGPU) paradigm in CUDA [169].

The described need for complete and non-approximated calculation of the diffraction integral in technologically-attractive times was met with the work reported in the following manuscript, attached at the end of this text:

"Non-approximated Rayleigh–Sommerfeld diffraction integral: advantages and disadvantages in the propagation of complex wave fields," Applied Optics **58**, G11-G18 (2019) [39]

Additionally, this work was presented in the following conference:

"*Evaluation of Non-Approximated Numerical Calculation of the Diffraction Integral,*" in Digital Holography and Three-Dimensional Imaging Topical Meeting, Bordeaux France, 2019 [48]

- **Winner of Best Student Poster Award.**

Having the possibility of reconstructing accurately, and without approximations, the object information, allows the immediate identification of numerical artifacts derived from the approximated reconstruction process. However, the exactness of the recovered information will also be determined by the accurate knowledge of the setup parameters; the numerical reconstruction, in any of its implementations, requires the input of the illumination wavelength, the distance between the point-source and the recording plane (L), the distance between the point-source and the sample (z), and the dimensions of the digital sensor. From these parameters, the illumination wavelength and the sensor information are

usually clearly defined from the manufacturer's information, and the distance z can be changed as needed during the reconstruction thanks to the numerical refocusing capabilities of holographic techniques. Conversely, the distance L must be measured from the experimental setup, often requiring a mechanical intervention of a measuring tool in the configuration; this is undesirable, when not impossible, due to the small operating distances and the sensible surfaces of the optical components involved.

As the selection of the distance L sets the curvature radius of the spherical-wave carrier during the reconstruction process, even small differences may produce significant alterations to the recovered information. Indeed, it was previously reported that an inadequate measurement of the illumination distance results in both a scale change in the reconstructed information and a loss of spatial resolution [170]. Therefore, a method to accurately calibrate the illumination distance without its physical measurement in the setup would ensure a risk-free determination of the complete set of parameters required for the operation of the DLHM, leading to reconstructions without numerical artifacts.

The described need for a calibration method for DLHM that ensures the sizing of the reconstructed information and prevents any loss in resolution from an inadequate selection of the reconstructed parameters was met with the work reported in the following manuscript, attached at the end of this text:

"Sizing calibration in digital lensless holographic microscopy via iterative Talbot self-imaging," Optics and Lasers in Engineering, **134**, 106176 (2020) [43]

Additionally, this work was presented in the following conference:

"Iterative Talbot Self-Imaging Calibration for Sizing in Digital Lensless Holographic Microscopy," Imaging and Applied Optics Congress (Online), Washington DC United States, 2020 [52]

- **Best Student Paper Award Finalist.**

The designed calibration technique offers a higher sensibility to changes in the distance L than the existing calibration method [170], waives the need for a refocusing step during the process as it is calculated axially over the intensity distribution, and allows the implementation of the non-approximated reconstruction algorithm [39] without time penalties because it operates over a single point in the reconstruction plane.

Thus, having developed a non-approximated propagation strategy and a robust calibration method for the microscope parameters, the DLHM configuration can be used to achieve reconstructed information, including phase maps, free from numerical artifacts. Furthermore, the ability to achieve these optimized reconstructions allows the straightforward identification of numerical artifacts that may appear while using the traditional reconstruction strategies; thus, the effects that any denoising proposal may have over the object information, either in resolution or visual quality, can be accurately inspected in DLHM.

Finally, as a clear indication of the feasibility and effectiveness of the proposed strategies, they were implemented in the phase-map reconstruction of multiple holograms acquired with the most cost-effective DLHM setup reported to date, shown in **Fig. 2-7**. The system, which costs less than US$ 55, was designed and assembled in a coordinated effort with the undergraduate students from the Optics and Optodigital Processing research group. All the associated information was reported in the following manuscript, attached at the end of this text:

"Open-source, Cost-effective, Portable, 3D-printed Digital Lensless Holographic Microscope," Applied Optics **60**, A205-A214 (2021) [47]

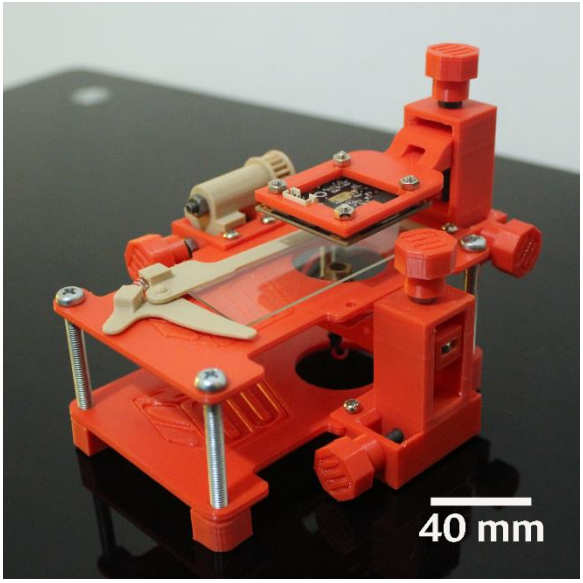

Fig. 2-7. Physical assembly of the most cost-effective DLHM setup reported to date.

2.3 Summary of core works for the chapter

In summary, the attached manuscripts that constitute the core of this chapter are:

- *"Realistic modeling of digital holographic microscopy,"* Optical Engineering **59**(10), 102418 (2020) [41]
- *"Phase-shifting digital holographic microscopy with an iterative blind reconstruction algorithm,"* Applied Optics **58**, G311-G317 (2019) [40]
- *“Fast-iterative blind phase-shifting digital holographic microscopy using two images,”* Applied Optics **59**, G7469-7476 (2020) [44]
- *"Non-approximated Rayleigh–Sommerfeld diffraction integral: advantages and disadvantages in the propagation of complex wave fields,"* Applied Optics **58**, G11-G18 (2019) [39]
- *“Sizing calibration in digital lensless holographic microscopy via iterative Talbot self-imaging,”* Optics and Lasers in Engineering, **134**, 106176 (2020) [43]
- *“Open-source, Cost-effective, Portable, 3D-printed Digital Lensless Holographic Microscope,”* Applied Optics **60**, A205-A214 (2021) [47]

Which were additionally presented in the following conferences:

- “*Evaluation of Non-Approximated Numerical Calculation of the Diffraction Integral,*” in Digital Holography and Three-Dimensional Imaging Topical Meeting, Bordeaux France, 2019 [48]
    - **Winner of Best Student Poster Award.**
- *“Blind phase-shifting digital holographic microscopy using an iterative approach,”* Three-Dimensional Imaging, Visualization, and Display, Digital Forum, 2020 [50]
- *“Fast-iterative bling reconstruction algorithms for accurate quantitative phase images in phase-shifting digital holographic microscopy,”* Imaging and Applied Optics Congress (Online), Washington DC United States, 2020 [51]
- *“Iterative Talbot Self-Imaging Calibration for Sizing in Digital Lensless Holographic Microscopy,”* Imaging and Applied Optics Congress (Online), Washington DC United States, 2020 [52]
    - **Best Student Paper Award Finalist.**

3. Phase noise reduction by numerical manipulation of complex fields

In the previous chapters, a characterization of the coherent noise sources in Digital Holographic Microscopy (DHM) was made, later supported by the development of a realistic modeling platform for the specific experimental conditions of the technique; additionally, several optimizations to the reconstruction process were proposed to ensure that the recovered information is free of numerical artifacts and most non-speckle noise is dutifully removed. Having that ample understanding of the speckle noise incidence in DHM setups, and the capability to accurately distinguish its deleterious effects from technical affectations, new denoising methods, that fit the particular experimental conditions that DHM sets, can be proposed and evaluated.

It has been stated that the use of DHM techniques allows the numerical reconstruction of both the amplitude and phase information of a microscopic sample. As such, the full complex field information can be gathered and manipulated in a controlled way after the reconstruction. This feature allows the envision of noise-reduction techniques based on the direct processing of the retrieved complex field, allowing a numerical single-shot implementation of optical multi-look denoising approaches.

In previous work from the Optics and Optodigital Processing research group, a single-shot pseudostochastic denoising procedure was proposed following this idea [171]. Despite achieving promising preliminary results, the physical description and overall understanding of the denoising behavior were incomplete, preventing its full implementation. From the consolidated understanding of coherent noise that has been developed, this proposal is revisited and supplemented; the result was two novel numerical noise reduction methods, whose development, testing, and report, is summarized in this chapter.

As discussed in the description of the speckle-noise generation under coherent illumination, the roughness of the sample introduces random phase delays at each emission point of the object, leading to interferences that form the recorded speckle grains at the detector plane. Therefore, the recovered phase information $\phi(x,y)$ must be understood as a superposition of a deterministic and a random portion; the former being the information of the sample itself, and the latter being inherited from the speckle noise. From this perspective, the noise decorrelation used by optical multi-look denoising techniques can be emulated in the numerical phase maps if a controlled introduction of variations into the random portion of the phase is achieved.

A numerically retrieved complex-valued wavefield $\psi(x,y)$ can be expressed at any point (x,y) as

$$\begin{aligned} \psi(x,y) &= A(x,y)\exp[i\,\phi(x,y)] \\ \psi(x,y) &= \mathrm{Re}[\psi(x,y)] + i\,\mathrm{Im}[\psi(x,y)] \end{aligned} \tag{3.1}$$

with $A(x,y)$ and $\phi(x,y)$ being the amplitude and phase, respectively, and $\mathrm{Re}[\,]$ and $\mathrm{Im}[\,]$ the real and imaginary components of the complex field. In general, the amplitude is independent of the phase, and the real component is independent of the imaginary one; however, each pair is connected to the other as given by

$$\begin{aligned} A(x,y) &= |\psi(x,y)| = \sqrt{(\mathrm{Re}\{\psi(x,y)\})^2 + (\mathrm{Im}\{\psi(x,y)\})^2}, \\ \phi(x,y) &= \mathrm{atan}\left\{\frac{\mathrm{Im}\{\psi(x,y)\}}{\mathrm{Re}\{\psi(x,y)\}}\right\}, \end{aligned} \tag{3.2}$$

and,

$$\begin{aligned} \mathrm{Re}[\psi(x,y)] &= A(x,y)\cos\big(\phi(x,y)\big) \\ \mathrm{Im}[\psi(x,y)] &= A(x,y)\sin\big(\phi(x,y)\big). \end{aligned} \tag{3.3}$$

Eq. 3.3 shows that the phase information is completely coded into both the Real and Imaginary components of the complex-valued field. Taking advantage of the complex nature of the digitally retrieved field, the generation of the decorrelated noise fields can be pursued by preserving the information into one of these components, while the other is numerically altered; for instance, the imaginary component could be kept intact while pseudo-speckle realizations are added to the real component. The new fields can then be

reconstructed in either phase or amplitude and averaged to produce a synthetic reconstruction with reduced coherent noise. Unlike the optical methods, where the variations may induce large decorrelations between noise realizations, working over a single hologram imposes a reduced range to the achievable decorrelation degree; nonetheless, this limitation is partially alleviated by the effortless generation of multiple noise realizations in the computational approach.

The described idea of coherent denoising using pseudo-speckle realizations over the retrieved complex wavefield was developed in the work reported in the following manuscript, attached at the end of this text:

"Single-shot pseudostochastic speckle noise reduction in numerical complex-valued wavefields," Optical Engineering **59**(7), 073107 (2020) [42]

The reported development and testing of the method implemented the setup in **Fig. 2-1**, with the improvements discussed in section 2.1, to achieve high-quality reconstructions of both transmissive and reflective samples. The recovered phase maps, aside from the improved visual quality, were demonstrated (by comparison to a calibrated stylus profilometer) to provide accurate axial measurements with uncertainties consistent with the interferometric capabilities in the order of $\lambda/100$ [172].

However, it was discussed in section 1.3.2 that one of the main drawbacks of optical multi-look techniques is the loss of correlation between in the denoised amplitude and phase information; indeed, as the averaging must be understood as an incoherent superposition [16], the result is not a denoised field but, rather, denoised information extracted and processed from a noisy complex field. Consequently, with the method being a numerical emulation of such approaches, the denoised information cannot be effectively subjected to wave-propagation procedures [139]. To overcome this limitation, an alternative strategy that operates over the complex field rather than the extracted information is needed.

Under the same understanding that motivated the above-presented method, a denoising algorithm that directly modifies the complex field was envisioned. The proposed additions to one of the complex components of the noisy field can be alternatively understood from their effect on the phasor representation of the field. Any given position (x_0, y_0) of the noisy field $\psi(x, y)$ can be represented by a phasor Ψ_i with a phase value of ϕ; when the random

component is added, the phasor is slightly shifted from its initial position in the complex plane, producing a new phasor Ψ_o with phase value ϕ_o. This process, illustrated in **Fig. 3-1**, can occur in a pointwise manner as each position can be independently manipulated. Therefore, if each phasor is iteratively and randomly shifted, a quality-driven tuning of the phasor representation of the overall field can be pursued; the desired effect is to reduce the local noise-induced additive phase incidence while preserving the sample information.

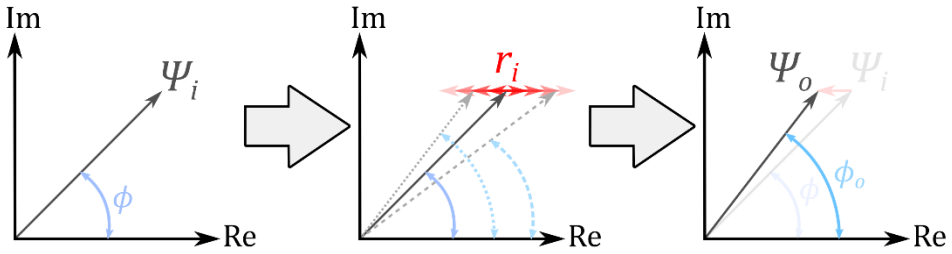

Fig. 3-1. Phasor tuning: To the input phasor Ψ_i of known phase ϕ a small randomly-generated real component r_i is added, producing a new phasor Ψ_o with a new phase value ϕ_o.

A significant caveat is immediately identified for such a proposal: As the tuning process causes a fluctuation of the phase values with the random phasor movements, any existing high-frequency phase wrappings are at risk of becoming significantly distorted in the output phase map. This limitation is mostly alleviated by the intended application of the method to DHM; most objects of interest, due to their microscopic scale, generally display few wrappings of low frequencies. Nonetheless, if an object has sharp features with wrapping-inducing size differences, the use of this method may be hindered.

For the quality-driven intent to work, a metric of the speckle incidence needs to be evaluated at each iteration. From the state-of-the-art revision, a well-documented compendium of the existing denoising performance metrics with high applicability to phase maps was found in [35]; however, for the application cases considered in that work, the preservation of the phase-wrapping positions was of primordial interest. Due to the intended application of the method to phase maps from DHM, and the aforementioned limitation in high-frequency phase wrappings, the best performance was achieved with the speckle contrast [79], redefined for the phase maps as

$$C_\phi = \frac{\sigma_P}{\bar{P}}. \tag{3.4}$$

In Eq. 3.4, σ_P is the standard deviation and $\bar{P}$ the average of the phase values of a given analysis region, such that the presented relation measures the ratio of the phase fluctuations to the mean value of the region. Therefore, this parameter was implemented as the control metric of the method, by evaluating its evolution in an ideally-uniform background region.

The described method for coherent denoising using a pointwise phasor tuning of the wavefield, and considering the speckle contrast as control metric for the quality-guided evolution, was reported in the following manuscript, attached at the end of this text:

"Pointwise phasor tuning for single-shot speckle noise reduction in phase wave fields," Optics and Lasers in Engineering, **137**, 106365 (2020) [45]

Additionally, this work was presented in the following conference:

"*Denoising Phase Maps of Digital Holographic Microscopy by Complex Tuning*," in Digital Holography and Three-Dimensional Imaging, Bordeaux France, 2019 [49]

As shown in the published manuscript, the proposed method achieves notorious improvements, both visually appraised and quantitatively established by the speckle contrast reduction. Furthermore, as the review in section 1.3.3 showed that the best performance with numerical denoising approaches was achieved with the BM3D [162] and WFT2F [153] methods, the results were compared against these existing implementations, showing that similar results can be achieved without additional times penalties in the convergence times.

The results of the two proposed methods are illustrated in **Fig. 3-2**, with panels (a) and (b) showing the application of the pseudostochastic denoising method [42] over the height-map of a USAF 1951 test target, and panels (c) and (d) the denoising results of the pointwise phasor tuning method [45] over the phase map of a Drosophila Melanogaster's thin head-section with intricated internal structures. Both methods achieve a notorious enhancement of the visual quality and a reduction in the ambiguity of the measurements introduced by speckle noise in the phase-maps. While the feasibility tests from these applications were done in a lens-based DHM architecture, they are not restricted to this technique; on the contrary, as the operation principle of the methods is supported by the

numerical manipulation of the complex-valued wavefield, they could be straightforwardly implemented in phase-maps recovered from lensless DHM architectures.

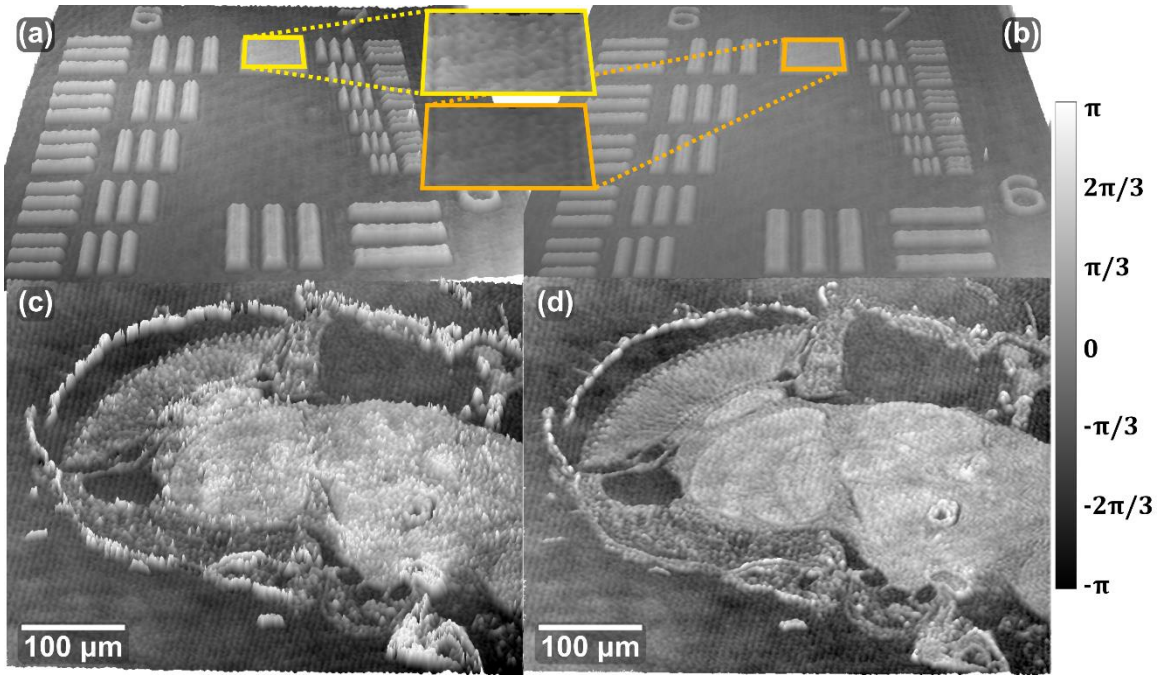

Fig. 3-2. Experimental DHM phase maps before/after applying the noise suppression procedure: (a/b) Pseudostochastic denoising [42]. (c/d) Pointwise phasor tuning [45].

3.1 Summary of core works for the chapter

In summary, two novel numerical speckle-noise reduction methods, particularly suited for DHM experimental conditions, were developed and tested in the denoising of phase-maps extracted from both numerically-generated and experimental complex-valued wavefields. The applicability of the methods was evaluated using the traditional metric of speckle contrast, and their performance was compared against the current state-of-the-art denoising algorithms. The attached manuscripts that constitute the core of this chapter are:

- *"Single-shot pseudostochastic speckle noise reduction in numerical complex-valued wavefields,"* Optical Engineering **59**(7), 073107 (2020) [42]
- *"Pointwise phasor tuning for single-shot speckle noise reduction in phase wave fields,"* Optics and Lasers in Engineering, **137**, 106365 (2020) [45]

Which were also presented in the following conference:

- "*Denoising Phase Maps of Digital Holographic Microscopy by Complex Tuning*," in Digital Holography and Three-Dimensional Imaging, Bordeaux France, 2019 [49]

4. Phase noise reduction by control of the imaging system properties

The chapter 3 summarized the proposal of two numerical denoising methods, supported by the ability of Digital Holographic Microscopy (DHM) to numerically recover the complex-valued information from the field scattered by the object and an understanding of the speckle formation process in the imaging system. Being of numerical nature, these methods operate in the reconstruction stage. However, the developed understanding of the imaging system properties also allows to envision denoising procedures that operate in the recording stage if careful control of the system properties is achieved. This same idea is followed by the “multi-look” denoising approaches, briefly presented in section 1.3.2, by introducing slight changes into one or several of the recording parameters to achieve decorrelated noise patterns between the “looks”, whose resulting reconstructions can be later incoherently averaged to reduce the noise influence.

Among the multiple strategies that have been reported in the existing literature to create the noise decorrelation required by multi-look approaches, the ones based on the insertion of a moving transmission mask in the illumination path usually have the lowest affectation to the setup complexity. The operation principle of these methods can be readily understood from the speckle-formation description and Eq. 1.9. As stated in the previous chapters, the latter can be read as the composition of the scaled geometrical image of the object by a set of light spots whose size, position, and shape are controlled by those same parameters of the pupil function. Thus, the introduction of any modification to the pupil function changes the light spots that compose the object wave at the recording plane, consequently changing the noise pattern. Therefore, in this chapter, the fine control of the imaging system properties conferred by the pupil function is exploited for the development of speckle denoising methods that suits the experimental conditions of DHM.

While the most common denoising methods based on a moving mask use a random distribution [136,137,173] to achieve changes in all position, shape, and size in a single implementation, the method can equally work with changes in only one of these parameters. This latter approach was widely explored, for instance, in analog holography using a traditional circular aperture with controlled movement during the reconstruction stage [138,174–177]. In digital holography similar implementations have been proposed but, owing to the versatility of the digital world, most have been of numerical nature. In those cases, one common way to achieve the spatial-filtering effect that changes the noise patterns, has been the resampling of the hologram in the spatial domain [28,142,178,179]; however, this approach cannot be used in an image-plane configuration like the one searched and optimized in this work. Alternatively, a discrete spatial-filtering can be done in the Fourier plane [27] by digitally emulating a 4-f processor with a moving window of fixed size in the intermediate plane [60]; this approach, illustrated in **Fig. 4-1**, was proposed as a numerical implementation of an optical multi-look technique (see 1.3.2) and, thus, implements an incoherent superposition of the resulting intensities to retrieve a synthetic denoised one.

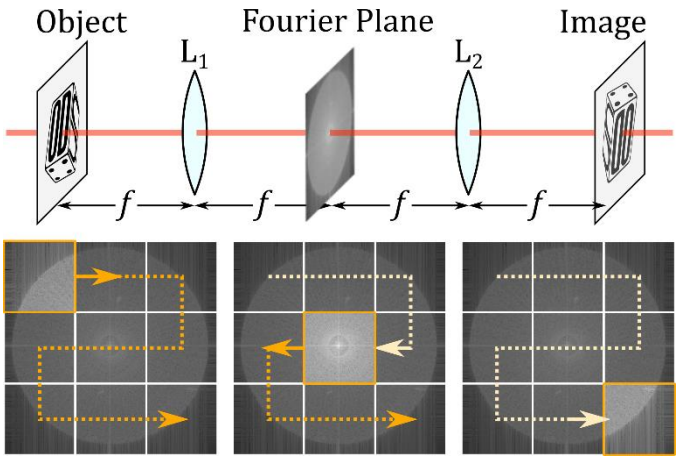

Fig. 4-1. Digital emulation of the moving mask optical multi-look denoising procedure by introducing a moving window in the Fourier plane of a digital 4-f processor. This method was proposed in [27].

Given the ample success that has been reported in the use of resampling-based procedures for speckle reduction in digital holography [28,34], it is reasonable to expect that such benefits can be brought to the denoising of phase maps obtained from DHM. However, as shown in **Fig. 4-2**, the application of the method reported in [27] over the phase

reconstruction of a phase-only Star Test Target proves otherwise. While panels (a) and (b), which respectively illustrate the intensity reconstruction before and after the method application, show a partial smoothing of the speckle noise, the reconstructed phase-map of the sample, in panel (c), is almost unrecognizable in panel (d) after the denoising procedure. This application considered only 9 window positions, which explains the timid reduction achieved in the intensity, but highlights the immediate emergence of the disastrous phase distortion.

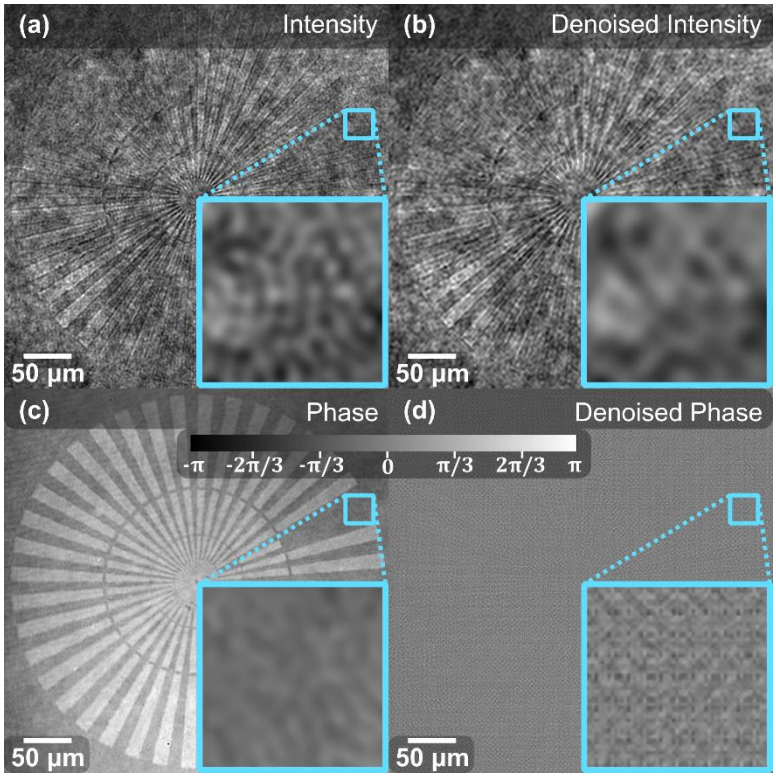

Fig. 4-2. Experimental results of the denoising method reported in [27]. While the intensity reconstruction achieves a partial improvement, the phase map is rendered useless.

To understand the cause for this undesired and catastrophic distortion of the phase information when the discrete Fourier filtering process is applied, an experimental implementation of the optical technique that the method emulates was sought. For this intent, the lens-based DHM setup illustrated in **Fig. 2-1** becomes particularly handy. As seen from panel (b) of that figure, the afocal-telecentric architecture of the microscope optics in the object arm can serve the same optical purpose than the 4-f processor in **Fig. 4-1**, but with a non-unitary magnification given by the focal difference between the two

lenses. Therefore, the object arm of the microscope can be modified with the insertion of a moving aperture in the pupil plane of the MO-TL imaging configuration, to manipulate the effective pupil function of the recorded object wave. This small modification to the recording stage, illustrated in **Fig. 4-3**, can be achieved without significantly increasing the complexity of the system by using, for instance, an x-y displacement mount and an iris diaphragm.

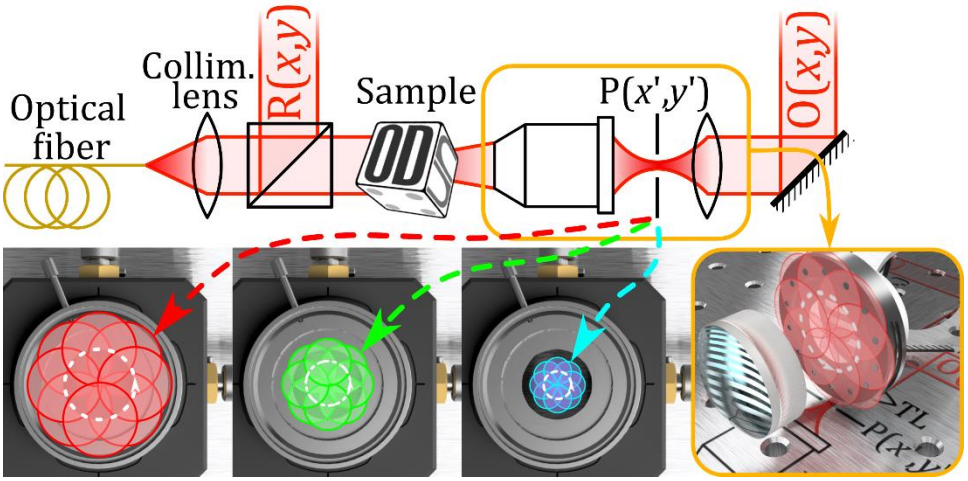

Fig. 4-3. Experimental object-arm design with variable pupil function $P(x', y')$. A movable aperture is introduced atop of the fixed pupil of the system and displaced between successive exposures to generate a decorrelation in the noise fields.

With the proposed configuration, the effective pupil function of the imaging system will keep its circular shape, but both its size and position can be independently controlled. Using the realistic DHM modeling platform [41], a prediction of the denoising performance was made, as summarized in **Fig. 4-4**. The yellow-bounded regions in the background of the original, panel (a), and denoised, panel (b), phase-maps were used to compute the signal-to-noise-ratio (SNR) and the speckle contrast (see Eq. 3.4) at each of the 3 considered cases; namely, the aperture was reduced to 80%, 50%, and 30% of the original pupil radius and displaced radially 95% of its resulting radius to 8 different angular positions. The results are shown in panels (d), (e), and (f), respectively, for the central region of the test. Additionally, when these panels are compared with panel (c), which shows the same central region on the original noisy phase-map, a reduction in the resolution power of the imaging system is seen, due to the rejection of the higher spatial frequencies when the pupil size is reduced, as can be expected.

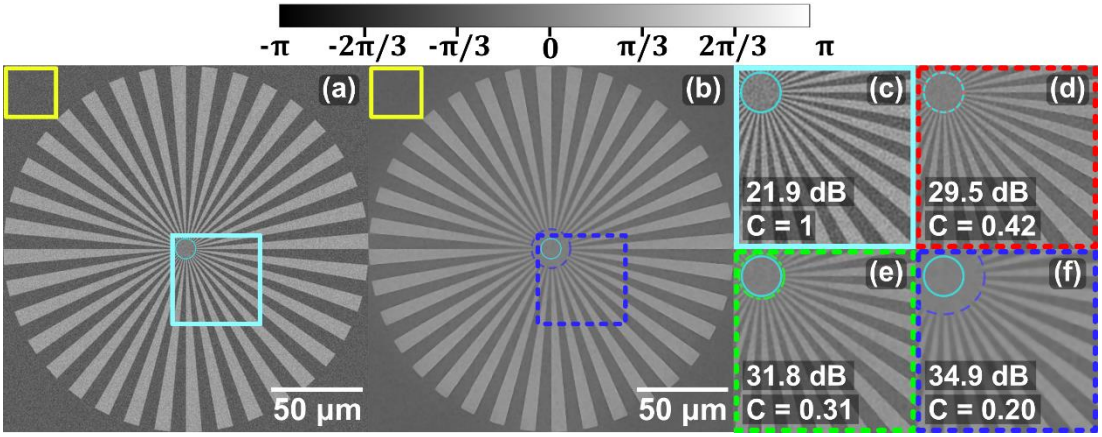

Fig. 4-4. Numerical simulation of phase-map optical multi-look denoising by changing the pupil function in the object arm. (a/b) Star test target before/after denoising. (c) Close-up in the center region of the noisy phase-map. (d/e/f) Close-up in the center region of denoised phase-maps using an displaced aperture with 80% / 50% / 30% of the original diameter.

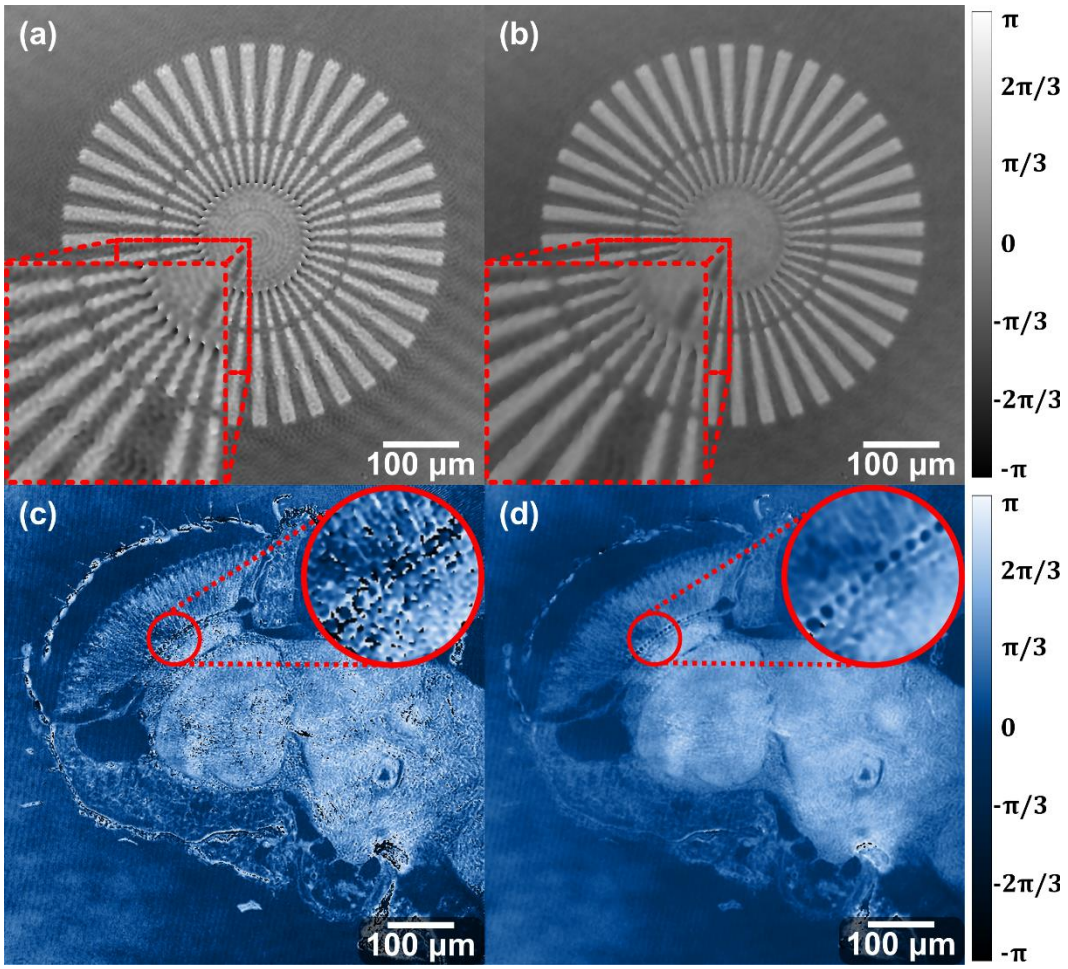

Fig. 4-5. Denoising of phase-maps from DHM by averaging the reconstructions from 8 holograms acquired with different positions of the pupil function in the object arm. (a/b) Star test target before/after denoising. (c/d) Thin head section from a Drosophila Melanogaster fly before/after denoising.

Having numerically verified that the proposed configuration can achieve an effective reduction of the coherent noise distortions in phase-maps recovered from DHM, the method was experimentally implemented. The results in **Fig. 4-5**, achieved by averaging 8 positions of an aperture reduced to 50% of its original size and displaced to 95% of the resulting radius, show a significant enhancement of the visual quality in phase-maps from both a standard benchmarking test, in panels (a) and (b), and a biological sample with intricated internal structures, in panels (c) and (d).

The full development and implementation of the above-described denoising procedure, supported in the physical manipulation of the pupil function of the imaging system in the object arm of a DHM setup, was reported in the following manuscript, attached at the end of this text:

"Physical pupil manipulation for speckle reduction in digital holographic microscopy," Heliyon, **7**, e06098 (2021) [46]

Additionally, this work was presented in the following conference:

"Speckle Reduction in Digital Holographic Microscopy by Physical Manipulation of the Pupil Function," Imaging and Applied Optics Congress (Online), Washington DC United States, 2020 [53]

Despite the low-complexity modifications to the setup that the proposed method requires, the optical multi-look approach limits its applicability in dynamic processes due to the need of recording multiple holograms of an unchanging scene. Thus, the results showing great promising from the experimental implementation of this denoising procedure based on the manipulation of the pupil function are an additional motivation; if the conditions that limited the applicability of the discrete Fourier filtering method [27] in phase-maps are identified, they can be overcome to propose a numerical emulation of the method. Furthermore, if such an implementation was achieved, the method could be extended to phase maps obtained in lensless DHM (DLHM), where a physical version is not feasible but a numerical emulation could be readily implemented.

Due to the time constraints of the present Master thesis, such ideas could not be fully developed. Nonetheless, some preliminary and greatly promising results were achieved in this regard. A complete study in this line is left as future work that can promptly follow from the information recorded in this thesis.

4.1 Summary of core works for the chapter

In summary, an optical multi-look denoising method that operates in the recording stage of DHM was proposed with a minimal incidence on the complexity of the system, and whose development, characterization, and results can be found in the attached manuscript that constitutes the core of this chapter:

- *"Physical pupil manipulation for speckle reduction in digital holographic microscopy,"* Heliyon, **7**, e06098 (2021) [46]

which was also presented in the following conference:

- *"Speckle Reduction in Digital Holographic Microscopy by Physical Manipulation of the Pupil Function,"* Imaging and Applied Optics Congress (Online), Washington DC United States, 2020 [53]

5. Conclusions and future work

5.1 Conclusions

The main results of this Master thesis can be summarized as follows:

Initially, both the lens-based and lensless architectures of DHM were optimized to ensure their complete characterization, the suppression of the non-speckle noise sources, and preventing the introduction of numerical aberrations during the reconstruction stage. For the lens-based DHM architectures, a realistic modeling platform was developed, allowing the precise distinction between the information degradation induced by coherent-noise during the imaging process and the possible negative influence of the proposed noise reduction strategies. Additionally, two new reconstruction methods for phase-shifting DHM were developed; these methods require a reduced number of input images and remove the need to precisely know and control the phase-shift between holograms, while still achieving the reconstruction of accurate and high-quality phase maps. These optimizations allowed the architecture to operate in an ample range of sizes and magnifications, either in an off-axis or a slightly-off-axis regime, with reduced time penalties, without the need of introducing additional complexity to the setup, and ensuring that the recovered information was diffraction-limited. For the lensless DHM architectures, a non-approximated propagation strategy and a robust calibration method for the microscope parameters were developed; with these optimizations, the DLHM configuration was be used to achieve reconstructed information, including phase maps, free from numerical artifacts or resolution losses derived from the numerical processing of the hologram.

The ability to achieve optimized reconstructions in both architectures allowed the straightforward identification of numerical artifacts that could appear while using traditional reconstruction strategies, and ensured that the reconstructed phase information accurately reflects the imaging capabilities of the system. Therefore, the effects that the denoising

proposals had over the object information, either in resolution or visual quality, could be accurately inspected. With these optimizations, three novel speckle-noise reduction methods were proposed; two numerical denoising methods, and one optical multi-look approach.

The proposed numerical denoising methods are supported in the ability of DHM to access and numerically manipulate the complex-valued field retrieved from the object. The first proposal consisted in the digital emulation of an optical multi-look approach, by numerically generating pseudo-speckle fields into the wavefield whose reconstructions were later incoherently averaged. The second proposal made iterative alterations to the complex-valued wavefield to locally tune the phasor value in a quality-driven optimization. The applicability of the methods was evaluated on both numerically-generated and experimental complex-valued wavefields. The performance of the proposed methods was evaluated using the traditional metrics of speckle contrast and signal-to-noise ratio, and their performance was compared against the current state-of-the-art denoising algorithms BM3D and WFT2F.

Finally, an optical multi-look denoising method that operates in the recording stage of DHM was proposed. The method is supported on the controlled manipulation of the imaging system properties that can be achieved by changing the size and position of the pupil function. The implemented strategy, whose performance was also quantified with the traditional denoising metrics of speckle contrast and signal-to-noise-ratio, allowed the achieving of enhanced visual quality in the phase maps with a minimal incidence on the complexity of the system.

All of these results evidence the achievement of the objective of proposing, evaluating, and implementing noise reduction strategies for phase maps obtained from digital holographic microscopy. The review of the state-of-the-art in phase-maps noise reduction techniques supported the identified need for the development of such techniques. This necessity was then satisfied with the implementation of new noise reduction methodologies for phase maps, ensuring their fit to the experimental conditions imposed by digital holographic microscopy architectures. The feasibility of the proposed methods was verified in numerical models and experimental results, and their applicability limits were studied based on the evaluation of their performance with metrics previously reported in peer-reviewed literature.

5.2 Future work perspectives

The results achieved in this Master thesis paved a great part of the road in the field of noise reduction in phase maps, and also pointed towards the following research that can be further developed:

1. Following the open-source paradigm that the Optics and Optodigital Processing research group has maintained over the past years, the realistic modeling platform [41] must be consolidated as an easily accessible software. To achieve this, and ensure its integration with the existing suite of DHM software solutions [96,180], the platform can be incorporated into an ImageJ plugin [166].

2. During the development and experimental set up of the lens-based DHM architecture that operates in both transmission and reflection mode (see **Fig. 2-1**), a set of optomechanical and alignment optimizations were done. These additions allowed the obtention of a stable system that produces accurate reconstructions with minimal post-processing requirements, and at a reduced cost when compared to the commercial DHM systems. As the complete design and alignment procedure are useful to any other researcher in the field, they must be compiled and reported on a laboratory note.

3. The reconstruction of the lens based DHM holograms under the optimized setup could be done with a significantly reduced computational effort. To ease the recording and expand the usability of the setup, a software that allowed the video-rate live reconstruction of the information in either amplitude, intensity, or phase was designed and implemented. This software must be integrated into the existing suite of DHM software solutions [96,180] by incorporating its functionality into an ImageJ plugin [166].

4. The developed phase-shifting algorithms [40,44] ease the setup complexity requirement for this kind of DHM architectures without a significant time penalty. However, to further expand their applicability (for instance, to high-speed interferometry), the parallelization of their execution can be sought under the GPGPU paradigm [169]. Additionally, the algorithm that only requires two input images [44] can be used to simplify the multi-camera design proposed in [181] into a single Mach-Zender setup with two cameras of simultaneous acquisition.

5. The non-approximated propagation algorithm [39], which implements the full Rayleigh-Sommerfeld diffraction integral, should be adapted and incorporated into the existing numerical propagation suite, JDiffraction [182], developed and maintained by the Optics and Optodigital Processing Group, to ensure its open-accessibility.

6. The sizing calibration method for DLHM based on the Talbot self-imaging effect [43], should be adapted and incorporated into the existing DLHM reconstruction software [96], which is developed and maintained by the Optics and Optodigital Processing Group. Additionally, a non-iterative alternative can be sought to reduce the computational effort and execution times of the calibration.

7. The proposed digital denoising methods based on the numerical manipulation of the retrieved complex-valued field [42,45] were explicitly tested in phase-maps from lens-based DHM; as their operation is fully-digital, their applicability in DLHM can also be explored.

8. The optical multi-look denoising method based on the physical manipulation of the pupil has limited usability in dynamic processes. To increase its applicability, the conditions that limited the use in phase maps of the discrete Fourier filtering method [27] must be identified and overcome, in order to propose a numerical emulation of the proposed method. Furthermore, such an implementation can also be extended to phase maps obtained in DLHM.

A. Appendix: Core manuscripts

Below are attached the nine manuscripts that represent the core of the present thesis. They are presented in the format in which each was submitted to the corresponding journal, and ordered by their mention in the main text; namely:

Chapter 2: Suppression of non-speckle noise and numerical artifacts

- *"Realistic modeling of digital holographic microscopy,"* Optical Engineering **59**(10), 102418 (2020) [41]
- *"Phase-shifting digital holographic microscopy with an iterative blind reconstruction algorithm,"* Applied Optics **58**, G311-G317 (2019) [40]
- *“Fast-iterative blind phase-shifting digital holographic microscopy using two images,”* Applied Optics **59**, G7469-7476 (2020) [44]
- *"Non-approximated Rayleigh–Sommerfeld diffraction integral: advantages and disadvantages in the propagation of complex wave fields,"* Applied Optics **58**, G11-G18 (2019) [39]
- *“Sizing calibration in digital lensless holographic microscopy via iterative Talbot self-imaging,”* Optics and Lasers in Engineering, **134**, 106176 (2020) [43]
- *“Open-source, Cost-effective, Portable, 3D-printed Digital Lensless Holographic Microscope,”* Applied Optics **60**, A205-A214 (2021) [47]

Chapter 3: Phase noise reduction by numerical manipulation of complex fields

- *"Single-shot pseudostochastic speckle noise reduction in numerical complex-valued wavefields,"* Optical Engineering **59**(7), 073107 (2020) [42]
- *“Pointwise phasor tuning for single-shot speckle noise reduction in phase wave fields,”* Optics and Lasers in Engineering, **137**, 106365 (2020) [45]

Chapter 4: Phase noise reduction by control of the imaging system properties

- *“Physical pupil manipulation for speckle reduction in digital holographic microscopy,”* Heliyon, **7**, e06098 (2021) [46]

References

[1] Milestones in light microscopy. Nat Cell Biol 2009;11:1165–1165. https://doi.org/10.1038/ncb1009-1165.

[2] Zernike F. Phase contrast, a new method for the microscopic observation of transparent objects. Physica 1942;9:686–98. https://doi.org/10.1016/S0031-8914(42)80035-X.

[3] Zernike F. Phase contrast, a new method for the microscopic observation of transparent objects part II. Physica 1942;9:974–86. https://doi.org/10.1016/S0031-8914(42)80079-8.

[4] Kemper B, von Bally G. Digital holographic microscopy for live cell applications and technical inspection. Appl Opt 2008;47:A52. https://doi.org/10.1364/AO.47.000A52.

[5] Beuthan J, Minet O, Helfmann J, Herrig M, Müller G. The spatial variation of the refractive index in biological cells. Phys Med Biol 1995;41. https://doi.org/10.1088/0031-9155/41/3/002.

[6] Gabor D. A New Microscopic Principle. Nature 1948;161:777–778.

[7] Kim MK. Digital Holographic Microscopy. Springer; 2011.

[8] Mölder A, Sebesta M, Gustafsson M, Gisselson L, Gjörloff Wingren A, Alm K. Non-invasive, label-free cell counting and quantitative analysis of adherent cells using digital holography. J Microsc 2008;232:240–7. https://doi.org/10.1111/j.1365-2818.2008.02095.x.

[9] Popescu G. Quantitative phase imaging of cells and tissues. McGraw Hill Professional; 2011.

[10] Park YK, Depeursinge C, Popescu G. Quantitative phase imaging in biomedicine. Nat Photonics 2018;12:578–89. https://doi.org/10.1038/s41566-018-0253-x.

[11] Boucherit S, Bouamama L, Benchickh H, Lenoir J-M, Simoëns S. Three-dimensional solid particle positions in a flow via multiangle off-axis digital holography. Opt Lett 2008;33:2095. https://doi.org/10.1364/OL.33.002095.

[12] Makarchuk S, Beyer N, Gaiddon C, Grange W, Hébraud P. Holographic Traction

Force Microscopy. Sci Rep 2018;8:3038. https://doi.org/10.1038/s41598-018-21206-2.

[13] Charrière F, Kühn J, Colomb T, Montfort F, Cuche E, Emery Y, et al. Characterization of microlenses by digital holographic microscopy. Appl Opt 2006;45:829. https://doi.org/10.1364/AO.45.000829.

[14] Coppola G, Ferraro P, Iodice M, Nicola S De, Finizio A, Grilli S. A digital holographic microscope for complete characterization of microelectromechanical systems. Meas Sci Technol 2004;15:529–39. https://doi.org/10.1088/0957-0233/15/3/005.

[15] Depeursinge CD, Marian AM, Montfort F, Colomb T, Charrière F, Kühn J, et al. Digital Holographic Microscopy (DHM) applied to Optical Metrology: A resolution enhanced imaging technology applied to inspection of microscopic devices with subwavelength resolution. Fringe 2005, Berlin/Heidelberg: Springer-Verlag; n.d., p. 308–14. https://doi.org/10.1007/3-540-29303-5_41.

[16] Goodman JW. Speckle Phenomena in Optics: Theory and Applications, Second Edition. Second Ed. SPIE; 2020. https://doi.org/10.1117/3.2548484.

[17] Goodman JW. Some fundamental properties of speckle. J Opt Soc Am 1976;66:1145. https://doi.org/10.1364/JOSA.66.001145.

[18] Tay PC, Garson CD, Acton ST, Hossack JA. Ultrasound Despeckling for Contrast Enhancement. IEEE Trans Image Process 2010;19:1847–60. https://doi.org/10.1109/TIP.2010.2044962.

[19] Mateo JL, Fernández-Caballero A. Finding out general tendencies in speckle noise reduction in ultrasound images. Expert Syst Appl 2009;36:7786–97. https://doi.org/10.1016/j.eswa.2008.11.029.

[20] Jong-Sen Lee, Grunes MR, de Grandi G. Polarimetric SAR speckle filtering and its implication for classification. IEEE Trans Geosci Remote Sens 1999;37:2363–73. https://doi.org/10.1109/36.789635.

[21] Lee JS, Jurkevich L, Dewaele P, Wambacq P, Oosterlinck A. Speckle filtering of synthetic aperture radar images: A review. Remote Sens Rev 1994;8:313–40. https://doi.org/10.1080/02757259409532206.

[22] Bouma BE, Tearney GJ. Handbook of Optical Coherence Tomography. New York: Marcel Dekker; 2002.

[23] Schmitt JM, Xiang SH, Yung KM. Speckle in Optical Coherence Tomography. J Biomed Opt 1999;4:95. https://doi.org/10.1117/1.429925.

[24] Roddier F. V The Effects of Atmospheric Turbulence in Optical Astronomy, 1981, p. 281–376. https://doi.org/10.1016/S0079-6638(08)70204-X.

[25] Michael CR, Byron MW. Imaging Through Turbulence. CRC Press; 2018. https://doi.org/10.1201/9780203751282.

[26] Caulfield HJ. Special Problems: Speckle. Handb. Opt. Hologr., 1979, p. 367–71.

[27] Maycock J, Hennelly BM, McDonald JB, Castro A, Naughton TJ, Frauel Y, et al. Reduction of speckle in digital holography by discrete Fourier filtering. J Opt Soc Am A 2007;24:1617–22. https://doi.org/10.1364/JOSAA.24.001617.

[28] Bianco V, Paturzo M, Memmolo P, Finizio A, Ferraro P, Javidi B. Random resampling masks: a non-Bayesian one-shot strategy for noise reduction in digital holography. Opt Lett 2013;38:619–21. https://doi.org/10.1364/OL.38.000619.

[29] Haouat M, Garcia-Sucerquia J, Kellou A, Picart P. Reduction of speckle noise in holographic images using spatial jittering in numerical reconstructions. Opt Lett 2017;42:1047–50. https://doi.org/10.1364/OL.42.001047.

[30] Baumbach T, Kolenovic E, Kebbel V, Jüptner W. Improvement of accuracy in digital holography by use of multiple holograms. Appl Opt 2006;45:6077. https://doi.org/10.1364/AO.45.006077.

[31] Rong L, Xiao W, Pan F, Liu S, Li R. Speckle noise reduction in digital holography by use of multiple polarization holograms. Chinese Opt Lett 2010;8:653–5. https://doi.org/10.3788/COL20100807.0653.

[32] Le Clerc F, Gross M, Collot L. Synthetic-aperture experiment in the visible with on-axis digital heterodyne holography. Opt Lett 2001;26:1550–2. https://doi.org/10.1364/OL.26.001550.

[33] Park Y, Choi W, Yaqoob Z, Dasari R, Badizadegan K, Feld MS. Speckle-field digital holographic microscopy. Opt Express 2009;17:12285–92. https://doi.org/10.1364/OE.17.012285.

[34] Bianco V, Memmolo P, Paturzo M, Finizio A, Javidi B, Ferraro P. Quasi noise-free digital holography. Light Sci Appl 2016;5:e16142–e16142. https://doi.org/10.1038/lsa.2016.142.

[35] Montresor S, Picart P. Quantitative appraisal for noise reduction in digital holographic phase imaging. Opt Express 2016;24:14322. https://doi.org/10.1364/OE.24.014322.

[36] Kemao Q, Wang H, Gao W. Windowed Fourier transform for fringe pattern analysis: Theoretical analyses. Appl Opt 2008;47:5408–19. https://doi.org/10.1364/AO.47.005408.

[37] Ghiglia DC, Pritt MD. Two-Dimensional Phase Unwrapping: Theory, Algorithms, and Software. First. Wiley-Interscience; 1998.

[38] Poittevin J, Picart P, Gautier F, Pezerat C. Quality assessment of combined quantization-shot-noise-induced decorrelation noise in high-speed digital holographic metrology. Opt Express 2015;23:30917. https://doi.org/10.1364/OE.23.030917.

[39] Buitrago-Duque C, Garcia-Sucerquia J. Non-approximated Rayleigh–Sommerfeld diffraction integral: advantages and disadvantages in the propagation of complex wave fields. Appl Opt 2019;58:G11. https://doi.org/10.1364/ao.58.000g11.

[40] Doblas A, Buitrago-Duque C, Robinson A, Garcia-Sucerquia J. Phase-shifting digital holographic microscopy with an iterative blind reconstruction algorithm. Appl Opt 2019;58:G311. https://doi.org/10.1364/AO.58.00G311.

[41] Buitrago-Duque C, Garcia-Sucerquia J. Realistic modeling of digital holographic microscopy. Opt Eng 2020;59:1. https://doi.org/10.1117/1.OE.59.10.102418.

[42] Buitrago-Duque C, Castañeda R, Garcia-Sucerquia J. Single-shot pseudostochastic speckle noise reduction in numerical complex-valued wavefields. Opt Eng 2020;59:1. https://doi.org/10.1117/1.OE.59.7.073107.

[43] Buitrago-Duque C, Garcia-Sucerquia J. Sizing calibration in digital lensless holographic microscopy via iterative Talbot self-imaging. Opt Lasers Eng 2020;134:106176. https://doi.org/10.1016/j.optlaseng.2020.106176.

[44] Castañeda R, Buitrago-Duque C, Garcia-Sucerquia J, Doblas A. Fast-iterative blind phase-shifting digital holographic microscopy using two images. Appl Opt 2020;59:7469. https://doi.org/10.1364/AO.398352.

[45] Buitrago-Duque C, Castañeda R, Garcia-Sucerquia J. Pointwise phasor tuning for single-shot speckle noise reduction in phase wave fields. Opt Lasers Eng 2021;137:106365. https://doi.org/10.1016/j.optlaseng.2020.106365.

[46] Buitrago-Duque C, Garcia-Sucerquia J. Physical pupil manipulation for speckle reduction in digital holographic microscopy. Heliyon 2021;7:e06098. https://doi.org/10.1016/j.heliyon.2021.e06098.

[47] Tobon-Maya H, Zapata-Valencia S, Zora-Guzmán E, Buitrago-Duque C, Garcia-Sucerquia J. Open-source, cost-effective, portable, 3D-printed digital lensless holographic microscope. Appl Opt 2021;60:A205. https://doi.org/10.1364/AO.405605.

[48] Buitrago-Duque C, Garcia-Sucerquia J. Evaluation of Non-Approximated Numerical Calculation of the Diffraction Integral. Digit. Hologr. Three-Dimensional Imaging 2019, Washington, D.C.: OSA; 2019, p. W3A.12. https://doi.org/10.1364/DH.2019.W3A.12.

[49] Buitrago-Duque C, Castañeda R, Garcia-Sucerquia J. Denoising Phase Maps of Digital Holographic Microscopy by Complex Tuning. Digit. Hologr. Three-Dimensional Imaging 2019, Washington, D.C.: OSA; 2019, p. Th3A.15. https://doi.org/10.1364/DH.2019.Th3A.15.

[50] Doblas A, Robinson A, Buitrago-Duque C, Garcia-Sucerquia J. Blind phase-shifting digital holographic microscopy using an iterative approach (Conference Presentation). Three-Dimensional Imaging, Vis. Disp. 2020, 2020, p. 114020D. https://doi.org/10.1117/12.2555093.

[51] Castaneda R, Buitrago C, Garcia-Sucerquia J, Robinson A, Doblas A. Fast-iterative blind reconstruction algorithms for accurate quantitative phase images in phase-shifting digital holographic microscopy. Imaging Appl. Opt. Congr., Washington, D.C.: OSA; 2020, p. HTh5D.3. https://doi.org/10.1364/DH.2020.HTh5D.3.

[52] Buitrago-Duque C, Garcia-Sucerquia J. Iterative Talbot Self-Imaging Calibration for Sizing in Digital Lensless Holographic Microscopy. Imaging Appl. Opt. Congr., Washington, D.C.: OSA; 2020, p. HW3C.5. https://doi.org/10.1364/DH.2020.HW3C.5.

[53] Buitrago-Duque C, Garcia-Sucerquia J. Speckle Reduction in Digital Holographic Microscopy by Physical Manipulation of the Pupil Function. Imaging Appl. Opt. Congr., Washington, D.C.: OSA; 2020, p. HTh5D.5.

https://doi.org/10.1364/DH.2020.HTh5D.5.

[54] Pluta M, Maksymilian P. Advanced light microscopy. Amsterdam: Elsevier; 1988.

[55] Lang W. Nomarski differential interference-contrast microscopy. 1968.

[56] Marquet P, Rappaz B, Magistretti PJ, Cuche E, Emery Y, Colomb T, et al. Digital holographic microscopy: a noninvasive contrast imaging technique allowing quantitative visualization of living cells with subwavelength axial accuracy. Opt Lett 2005;30:468.

[57] Cuche E, Marquet P, Depeursinge C. Simultaneous amplitude-contrast and quantitative phase-contrast microscopy by numerical reconstruction of Fresnel off-axis holograms. Appl Opt 1999;38:6994. https://doi.org/10.1364/AO.38.006994.

[58] Picart P, Leval J. General theoretical formulation of image formation in digital Fresnel holography. J Opt Soc Am A 2008;25:1744–61. https://doi.org/10.1364/JOSAA.25.001744.

[59] Schnars U, Jueptner WPO. Digital Holography. Berlin Heidelberg: Springer-Verlag; 2005.

[60] Goodman JW. Introduction to Fourier Optics. 4th ed. W. H. Freeman; 2017.

[61] Xu L. Properties of digital holography based on in-line configuration. Opt Eng 2000;39:3214. https://doi.org/10.1117/1.1327503.

[62] Poon T-C, Liu J-P. Introduction to Modern Digital Holography. Cambridge University Press; 2014.

[63] Cuche E, Marquet P, Depeursinge C. Spatial filtering for zero-order and twin-image elimination in digital off-axis holography. Appl Opt 2000;39:4070–5. https://doi.org/10.1364/AO.39.004070.

[64] Sánchez-Ortiga E, Doblas A, Saavedra G, Martínez-Corral M, Garcia-Sucerquia J. Off-axis digital holographic microscopy: practical design parameters for operating at diffraction limit. Appl Opt 2014;53:2058. https://doi.org/10.1364/AO.53.002058.

[65] Latychevskaia T, Fink H-W. Solution to the Twin Image Problem in Holography. Phys Rev Lett 2007;98:233901. https://doi.org/10.1103/PhysRevLett.98.233901.

[66] Goodwin EP, Wyant JC. Field Guide to Interferometric Optical Testing. SPIE; 2009. https://doi.org/10.1117/3.702897.

[67] Creath K. V Phase-Measurement Interferometry Techniques. Prog. Opt., 1988, p. 349–93. https://doi.org/10.1016/S0079-6638(08)70178-1.

[68] Guizar-Sicairos M, Fienup JR. Understanding the twin-image problem in phase retrieval. J Opt Soc Am A 2012;29:2367. https://doi.org/10.1364/JOSAA.29.002367.

[69] Brandt GB. Image Plane Holography 1969;8:1421–9. https://doi.org/10.1364/AO.8.001421.

[70] Doblas A, Sánchez-Ortiga E, Martínez-Corral M, Saavedra G, Andrés P, Garcia-Sucerquia J. Shift-variant digital holographic microscopy: inaccuracies in quantitative phase imaging. Opt Lett 2013;38:1352–4. https://doi.org/10.1364/OL.38.001352.

[71] Collins SAJ. Lens-System Diffraction Integral Written in Terms of Matrix Optics. J Opt Soc Am 1970;60:1168–77. https://doi.org/10.1364/JOSA.60.001168.

[72] Sánchez-Ortiga E, Doblas A, Martínez-Corral M, Saavedra G, Garcia-Sucerquia J. Aberration compensation for objective phase curvature in phase holographic microscopy: comment. Opt Lett 2014;39:417. https://doi.org/10.1364/OL.39.000417.

[73] Seo KW, Choi YS, Seo ES, Lee SJ. Aberration compensation for objective phase curvature in phase holographic microscopy. Opt Lett 2012;37:4976–8. https://doi.org/10.1364/OL.37.004976.

[74] Sánchez-Ortiga E, Ferraro P, Martínez-Corral M, Saavedra G, Doblas A. Digital holographic microscopy with pure-optical spherical phase compensation. J Opt Soc Am A Opt Image Sci Vis 2011;28:1410–7. https://doi.org/10.1364/JOSAA.28.001410.

[75] Kreis T. Handbook of Holographic Interferometry: Optical and Digital Methods. Weinheim: WILEY-VCH GmbH & Co; 2005.

[76] Takeda M, Ina H, Kobayashi S. Fourier-transform method of fringe-pattern analysis for computer-based topography and interferometry. J Opt Soc Am 1982;72:156. https://doi.org/10.1364/JOSA.72.000156.

[77] Oliver BM. Sparkling spots and random diffraction. Proc IEEE 1963;51:220–1. https://doi.org/10.1109/PROC.1963.1686.

[78] Goodman JW. Statistical properties of laser sparkle patterns. 1963.

[79] Goodman JW. Statistical optics. John Wiley & Sons; 2015.

[80] Dainty JC. Laser speckle and related phenomena. Springer science & business Media; 2013.

[81] Mills GA, Yamaguchi I. Effects of quantization in phase-shifting digital holography. Appl Opt 2005;44:1216. https://doi.org/10.1364/AO.44.001216.

[82] Pandey N, Hennelly B. Quantization noise and its reduction in lensless Fourier digital holography. Appl Opt 2011;50:B58. https://doi.org/10.1364/AO.50.000B58.

[83] Lesaffre M, Verrier N, Gross M. Noise and signal scaling factors in digital holography in weak illumination: relationship with shot noise. Appl Opt 2013;52:A81. https://doi.org/10.1364/AO.52.000A81.

[84] Gross M, Atlan M, Absil E. Noise and aliases in off-axis and phase-shifting holography. Appl Opt 2008;47:1757. https://doi.org/10.1364/AO.47.001757.

[85] Gabor D. Microscopy by reconstructed wave-fronts. Procedings R Soc London 1949;197:454–87. https://doi.org/10.1038/166399b0.

[86] Garcia-Sucerquia J, Xu W, Jericho SK, Klages P, Jericho MH, Kreuzer HJ. Digital in-line holographic microscopy. Appl Opt 2006;45:836. https://doi.org/10.1364/AO.45.000836.

[87] Hwu EE Te, Boisen A. Hacking CD/DVD/Blu-ray for Biosensing. ACS Sensors 2018. https://doi.org/10.1021/acssensors.8b00340.

[88] Patiño-Jurado B, Botero-Cadavid JF, Garcia-Sucerquia J. Optical Fiber Point-Source for Digital Lensless Holographic Microscopy. J Light Technol 2019;37:5660–6. https://doi.org/10.1109/JLT.2019.2921307.

[89] Serabyn E, Liewer K, Lindensmith C, Wallace K, Nadeau J. Compact, lensless digital holographic microscope for remote microbiology. Opt Express 2016;24:28540–8. https://doi.org/10.1364/OE.24.028540.

[90] Sanz M, Trusiak M, García J, Micó V. Variable zoom digital in-line holographic microscopy. Opt Lasers Eng 2020;127:105939. https://doi.org/https://doi.org/10.1016/j.optlaseng.2019.105939.

[91] Repetto L, Piano E, Pontiggia C. Lensless digital holographic microscope with light-emitting diode illumination. Opt Lett 2004;29:1132. https://doi.org/10.1364/OL.29.001132.

[92] Garcia-Sucerquia J, Xu W, Jericho SKK, Jericho MHH, Klages P, Kreuzer HJJ. Resolution power in digital in-line holography. Proc. SPIE - Int. Soc. Opt. Eng., vol.

6027 I, 2006. https://doi.org/10.1117/12.668213.

[93] Patiño-Jurado B. Fiber optics point-source for digital lensless holographic microscopy. Universidad Nacional de Colombia, 2019.

[94] Schnars U, J ptner WPO. Digital recording and numerical reconstruction of holograms. Meas Sci Technol 2002;13:R85–101. https://doi.org/10.1088/0957-0233/13/9/201.

[95] Jericho MH, Jürgen Kreuzer H. Point Source Digital In-Line Holographic Microscopy Digital In-Line Holographic Microscopy, 2011, p. 3–30. https://doi.org/10.1007/978-3-642-15813-1_1.

[96] Trujillo C, Piedrahita-Quintero P, Garcia-Sucerquia J. Digital lensless holographic microscopy: numerical simulation and reconstruction with ImageJ. Appl Opt 2020;59:5788–95. https://doi.org/10.1364/AO.395672.

[97] Ersoy OK. Diffraction, Fourier Optics and Imaging. Hoboken, NJ, USA: John Wiley & Sons, Inc.; 2007. https://doi.org/10.1002/0470085002.

[98] Kreuzer HJ. Holographic microscope and method of hologram reconstruction. US. Patent 6411406 (Canadian patent CA 2376395), 2002.

[99] Restrepo JF, Garcia-Sucerquia J. Magnified reconstruction of digitally recorded holograms by Fresnel-Bluestein transform. Appl Opt 2010;49:6430–5. https://doi.org/10.1364/AO.49.006430.

[100] Trujillo CA, Restrepo JF, Garcia-Sucerquia J. Real time numerical reconstruction of digitally recorded holograms in digital in-line holographic microscopy by using a graphics processing unit. Photonics Lett Pol 2010;2:177–9. https://doi.org/10.4302/photon. lett. pl.v2i4.166.

[101] Patiño-Jurado B, Botero-Cadavid JF, Garcia-Sucerquia J. Cone-shaped optical fiber tip for cost-effective digital lensless holographic microscopy. Appl Opt 2020;59:2969–75. https://doi.org/10.1364/ao.384208.

[102] Piedrahita-Quintero P. Métodos de cuantificación de fase a partir de mediciones de intensidad en microscopía holográfica digital sin lentes. Universidad Nacional de Colombia, 2018.

[103] Kreuzer HJ, Nakamura K, Wierzbicki A, Fink HW, Schmid H. Theory of the point source electron microscope. Ultramicroscopy 1992;45:381–403.

https://doi.org/10.1016/0304-3991(92)90150-I.

[104] Meng H, Anderson WL, Hussain F, Liu DD. Intrinsic speckle noise in in-line particle holography. J Opt Soc Am A 1993;10:2046. https://doi.org/10.1364/JOSAA.10.002046.

[105] Garcia-Sucerquia J. Noise reduction in digital lensless holographic microscopy by engineering the light from a light-emitting diode. Appl Opt 2013;52:A232–9. https://doi.org/10.1364/AO.52.00A232.

[106] Bianco V, Memmolo P, Leo M, Montresor S, Distante C, Paturzo M, et al. Strategies for reducing speckle noise in digital holography. Light Sci Appl 2018;7:48. https://doi.org/10.1038/s41377-018-0050-9.

[107] Kumar M, Tounsi Y, Kaur K, Nassim A, Mandoza-Santoyo F, Matoba O. Speckle denoising techniques in imaging systems. J Opt 2020;22:063001. https://doi.org/10.1088/2040-8986/ab8b7f.

[108] Liu Y, Wang Z, Huang J. Recent Progress on Aberration Compensation and Coherent Noise Suppression in Digital Holography. Appl Sci 2018;8:444. https://doi.org/10.3390/app8030444.

[109] Montrésor S, Memmolo P, Bianco V, Ferraro P, Picart P. Comparative study of multi-look processing for phase map de-noising in digital Fresnel holographic interferometry. J Opt Soc Am A 2019;36:A59. https://doi.org/10.1364/josaa.36.000a59.

[110] Mottier FM, Dändliker R, Ineichen B. Relaxation of the Coherence Requirements in Holography. Appl Opt 1973;12:243. https://doi.org/10.1364/AO.12.000243.

[111] Claus D, Iliescu D, Rodenburg JM. Coherence requirement in digital holography. Appl Opt 2013;52:A326. https://doi.org/10.1364/AO.52.00A326.

[112] Dubois F, Joannes L, Legros J-C. Improved three-dimensional imaging with a digital holography microscope with a source of partial spatial coherence. Appl Opt 1999;38:7085. https://doi.org/10.1364/AO.38.007085.

[113] Dubois F, Yourassowsky C. Full off-axis red-green-blue digital holographic microscope with LED illumination. Opt Lett 2012;37:2190. https://doi.org/10.1364/OL.37.002190.

[114] Dubois F, Novella Requena M-L, Minetti C, Monnom O, Istasse E. Partial spatial coherence effects in digital holographic microscopy with a laser source. Appl Opt

2004;43:1131. https://doi.org/10.1364/AO.43.001131.

[115] Koehler A. New Method of Illumination for Photomicrographical Purposes. J R Microsc Soc 1894;14:261–2.

[116] Martínez-León L, Pedrini G, Osten W. Applications of short-coherence digital holography in microscopy. Appl Opt 2005;44:3977. https://doi.org/10.1364/AO.44.003977.

[117] Dubois F, Callens N, Yourassowsky C, Hoyos M, Kurowski P, Monnom O. Digital holographic microscopy with reduced spatial coherence for three-dimensional particle flow analysis. Appl Opt 2006;45:864. https://doi.org/10.1364/AO.45.000864.

[118] El Mallahi A, Minetti C, Dubois F. Automated three-dimensional detection and classification of living organisms using digital holographic microscopy with partial spatial coherent source: application to the monitoring of drinking water resources. Appl Opt 2013;52:A68. https://doi.org/10.1364/AO.52.000A68.

[119] Funamizu H, Uozumi J, Aizu Y. Enhancement of spatial resolution in digital holographic microscopy using the spatial correlation properties of speckle patterns. OSA Contin 2019;2:1822. https://doi.org/10.1364/OSAC.2.001822.

[120] Choi Y, Yang TD, Lee KJ, Choi W. Full-field and single-shot quantitative phase microscopy using dynamic speckle illumination. Opt Lett 2011;36:2465. https://doi.org/10.1364/OL.36.002465.

[121] Redding B, Choma MA, Cao H. Spatial coherence of random laser emission. Opt Lett 2011;36:3404. https://doi.org/10.1364/OL.36.003404.

[122] Slabý T, Kolman P, Dostál Z, Antoš M, Lošťák M, Chmelík R. Off-axis setup taking full advantage of incoherent illumination in coherence-controlled holographic microscope. Opt Express 2013;21:14747. https://doi.org/10.1364/OE.21.014747.

[123] Pitkäaho T, Niemelä M, Pitkäkangas V. Partially coherent digital in-line holographic microscopy in characterization of a microscopic target. Appl Opt 2014;53:3233. https://doi.org/10.1364/AO.53.003233.

[124] Garcia-Sucerquia J. Color digital lensless holographic microscopy: laser versus LED illumination. Appl Opt 2016;55:6649. https://doi.org/10.1364/AO.55.006649.

[125] Nguyen TH, Edwards C, Goddard LL, Popescu G. Quantitative phase imaging with

partially coherent illumination. Opt Lett 2014;39:5511. https://doi.org/10.1364/OL.39.005511.

[126] Garcia-Sucerquia J, Ramírez JH, Castaneda R, Herrera-Ramírez J, Castaneda R. Incoherent recovering of the spatial resolution in digital holography. Opt Commun 2006;260:62–7. https://doi.org/10.1016/j.optcom.2005.10.003.

[127] Kubota S, Goodman JW. Very efficient speckle contrast reduction realized by moving diffuser device. Appl Opt 2010;49:4385. https://doi.org/10.1364/AO.49.004385.

[128] Kang X. Speckle noise reduction in digital holography by multiple holograms. Opt Eng 2007;46:115801. https://doi.org/10.1117/1.2802060.

[129] Su T-W, Isikman SO, Bishara W, Tseng D, Erlinger A, Ozcan A. Multi-angle lensless digital holography for depth resolved imaging on a chip. Opt Express 2010;18:9690. https://doi.org/10.1364/OE.18.009690.

[130] Pan F, Xiao W, Liu S, Rong L. Coherent noise reduction in digital holographic microscopy by laterally shifting camera. Opt Commun 2013;292:68–72. https://doi.org/10.1016/j.optcom.2012.11.091.

[131] Pan F, Xiao W, Liu S, Wang F, Rong L, Li R. Coherent noise reduction in digital holographic phase contrast microscopy by slightly shifting object. Opt Express 2011;19:3862–9. https://doi.org/10.1364/OE.19.003862.

[132] Herrera-Ramirez J, Hincapie-Zuluaga DA, Garcia-Sucerquia J. Speckle noise reduction in digital holography by slightly rotating the object. Opt Eng 2016;55:121714. https://doi.org/10.1117/1.OE.55.12.121714.

[133] Nomura T, Okamura M, Nitanai E, Numata T. Image quality improvement of digital holography by superposition of reconstructed images obtained by multiple wavelengths. Appl Opt 2008;47:D38. https://doi.org/10.1364/AO.47.000D38.

[134] Jiang H, Zhao J, Di J. Digital color holographic recording and reconstruction using synthetic aperture and multiple reference waves. Opt Commun 2012;285:3046–9. https://doi.org/10.1016/j.optcom.2012.02.076.

[135] Brozeit A, Burke J, Helmers H, Sagehorn H, Schuh R. Noise reduction in electronic speckle pattern interferometry fringes by merging orthogonally polarised speckle fields. Opt Laser Technol 1998;30:325–9. https://doi.org/10.1016/S0030-3992(98)00060-7.

[136] Matsumura M. Speckle Noise Reduction by Random Phase Shifters. Appl Opt 1975;14:660. https://doi.org/10.1364/AO.14.000660.

[137] Yu FTS, Wang EY. Speckle Reduction in Holography by Means of Random Spatial Sampling. Appl Opt 1973;12:1656. https://doi.org/10.1364/AO.12.001656.

[138] Hariharan P, Hegedus ZS. Reduction of speckle in coherent imaging by spatial frequency sampling. Opt Acta (Lond) 1974;21:345–56. https://doi.org/10.1080/713818900.

[139] Memmolo P, Esnaola I, Finizio A, Paturzo M, Ferraro P, Tulino AM. SPADEDH: a sparsity-based denoising method of digital holograms without knowing the noise statistics. Opt Express 2012;20:17250. https://doi.org/10.1364/OE.20.017250.

[140] Memmolo P, Bianco V, Paturzo M, Javidi B, Netti PA, Ferraro P. Encoding multiple holograms for speckle-noise reduction in optical display. Opt Express 2014;22:25768. https://doi.org/10.1364/oe.22.025768.

[141] Garcia-Sucerquia J, Ramírez JAH, Prieto DV. Reduction of speckle noise in digital holography by using digital image processing. Optik (Stuttg) 2005;116:44–8. https://doi.org/10.1016/j.ijleo.2004.12.004.

[142] Fukuoka T, Mori Y, Nomura T. Speckle Reduction by Spatial-Domain Mask in Digital Holography. J Disp Technol 2016;12:315–22. https://doi.org/10.1109/JDT.2015.2479646.

[143] Gonzalez RC, Woods RE. Digital Image Processing. Prentice Hall; 2002.

[144] Lee J-S. Digital Image Enhancement and Noise Filtering by Use of Local Statistics. IEEE Trans Pattern Anal Mach Intell 1980;PAMI-2:165–8. https://doi.org/10.1109/TPAMI.1980.4766994.

[145] Leo M, Distante C, Paturzo M, Memmolo P, Locatelli M, Pugliese E, et al. Automatic Digital Hologram Denoising by Spatiotemporal Analysis of Pixel-Wise Statistics. J Disp Technol 2013;9:904–9. https://doi.org/10.1109/JDT.2013.2268936.

[146] Frost VS, Stiles JA, Shanmugan KS, Holtzman JC. A Model for Radar Images and Its Application to Adaptive Digital Filtering of Multiplicative Noise. IEEE Trans Pattern Anal Mach Intell 1982;PAMI-4:157–66. https://doi.org/10.1109/TPAMI.1982.4767223.

[147] Coupe P, Hellier P, Kervrann C, Barillot C. Nonlocal means-based speckle filtering for ultrasound images. IEEE Trans Image Process 2009;18:2221–9. https://doi.org/10.1109/TIP.2009.2024064.

[148] Gerig G, Kubler O, Kikinis R, Jolesz FA. Nonlinear anisotropic filtering of MRI data. IEEE Trans Med Imaging 1992;11:221–32. https://doi.org/10.1109/42.141646.

[149] Wu Y, Cheng H, Wen Y, Chen X, Wang Y. Coherent noise reduction of phase images in digital holographic microscopy based on the adaptive anisotropic diffusion. Appl Opt 2018;57:5364. https://doi.org/10.1364/AO.57.005364.

[150] Kerr D, Santoyo FM, Tyrer JR. Manipulation of the Fourier Components of Speckle Fringe Patterns as Part of an Interferometric Analysis Process. J Mod Opt 1989;36:195–203. https://doi.org/10.1080/09500348914550241.

[151] Varman P, Wykes C. Smoothing of speckle and moire fringes by computer processing. Opt Lasers Eng 1982;3:87–100. https://doi.org/10.1016/0143-8166(82)90002-1.

[152] Kemao Q. Windowed Fourier transform for fringe pattern analysis. Appl Opt 2004;43:2695–702. https://doi.org/10.1364/AO.43.002695.

[153] Kemao Q. Two-dimensional windowed Fourier transform for fringe pattern analysis: Principles, applications and implementations. Opt Lasers Eng 2007;45:304–17. https://doi.org/10.1016/j.optlaseng.2005.10.012.

[154] Hua Xie, Pierce LE, Ulaby FT. SAR speckle reduction using wavelet denoising and Markov random field modeling. IEEE Trans Geosci Remote Sens 2002;40:2196–212. https://doi.org/10.1109/TGRS.2002.802473.

[155] Mallat SG. A wavelet tour of signal processing. 2nd ed. San Diego: Academic Press; 1999.

[156] Dabov K, Foi A, Katkovnik V, Egiazarian K. Image Denoising by Sparse 3-D Transform-Domain Collaborative Filtering. IEEE Trans Image Process 2007;16:2080–95. https://doi.org/10.1109/TIP.2007.901238.

[157] Cai X. Reduction of speckle noise in the reconstructed image of digital holography. Optik (Stuttg) 2010;121:394–9. https://doi.org/10.1016/j.ijleo.2008.07.026.

[158] Hao F, Tang C, Xu M, Lei Z. Batch denoising of ESPI fringe patterns based on convolutional neural network. Appl Opt 2019;58:3338. https://doi.org/10.1364/AO.58.003338.

[159] Wang P, Zhang H, Patel VM. SAR Image Despeckling Using a Convolutional Neural Network. IEEE Signal Process Lett 2017;24:1763–7. https://doi.org/10.1109/LSP.2017.2758203.

[160] Yan K, Yu Y, Huang C, Sui L, Qian K, Asundi A. Fringe pattern denoising based on deep learning. Opt Commun 2019;437:148–52. https://doi.org/10.1016/j.optcom.2018.12.058.

[161] Moon I, Jaferzadeh K, Kim Y, Javidi B. Noise-free quantitative phase imaging in Gabor holography with conditional generative adversarial network. Opt Express 2020;28:26284. https://doi.org/10.1364/OE.398528.

[162] Dabov K, Foi A, Katkovnik V, Egiazarian K. Image denoising with block-matching and 3D filtering. In: Dougherty ER, Astola JT, Egiazarian KO, Nasrabadi NM, Rizvi SA, editors., 2006, p. 606414. https://doi.org/10.1117/12.643267.

[163] Memmolo P, Iannone M, Ventre M, Netti PA, Finizio A, Paturzo M, et al. Quantitative phase maps denoising of long holographic sequences by using SPADEDH algorithm. Appl Opt 2013;52:1453. https://doi.org/10.1364/AO.52.001453.

[164] Katkovnik V, Egiazarian K. Sparse phase imaging based on complex domain nonlocal BM3D techniques. Digit Signal Process 2017;63:72–85. https://doi.org/10.1016/j.dsp.2017.01.002.

[165] Katkovnik V, Ponomarenko M, Egiazarian K. Sparse approximations in complex domain based on BM3D modeling. Signal Processing 2017;141:96–108. https://doi.org/10.1016/j.sigpro.2017.05.032.

[166] Schneider CA, Rasband WS, Eliceiri KW. NIH Image to ImageJ: 25 years of image analysis. Nat Methods 2012;9:671–5. https://doi.org/10.1038/nmeth.2089.

[167] Li J, Picart P. Calculating Diffraction by Fast Fourier Transform. Digit Hologr 2012:77–114. https://doi.org/10.1002/9781118562567.ch3.

[168] Castañeda R, Toro W, Garcia-Sucerquia J. Evaluation of the limits of application for numerical diffraction methods based on basic optics concepts. Optik (Stuttg) 2015;126:5963–70. https://doi.org/10.1016/j.ijleo.2015.08.109.

[169] Trujillo C, Garcia-Sucerquia J. Graphics Processing Units: More than the pathway to realistic video-games. Dyna 2011;78:164–72.

[170] Riesenberg R, Kanka M. Self-calibrating lensless inline-holographic microscopy by a sample holder with reference structures. Opt Lett 2014. https://doi.org/10.1364/ol.39.005236.

[171] Castañeda Quintero RA. Levantamiento topográfico de estructuras microscópicas opacas mediante técnicas cuantitativas de fase en microscopía holográfica digital. Universidad Nacional de Colombia, 2017.

[172] Malacara D, Servín M, Malacara Z. Interferogram Analysis For Optical Testing, Second Edition. CRC Press; 2005. https://doi.org/10.1201/9781420027273.

[173] Hariharan P, Hegedus ZS. Reduction of speckle in coherent imaging by spatial frequency sampling - II. Random spatial frequency sampling. Opt Acta (Lond) 1974;21:683–95. https://doi.org/10.1080/713818950.

[174] Dainty JCC, Welford WTT. Reduction of speckle in image plane hologram reconstruction by moving pupils. Opt Commun 1971;3:289–94. https://doi.org/10.1016/0030-4018(71)90088-5.

[175] Kawagoe Y, Takai N, Asakura T. Speckle reduction by a rotating aperture at the fourier transform plane. Opt Lasers Eng 1982;3:197–218. https://doi.org/10.1016/0143-8166(82)90022-7.

[176] Lewis RW. Speckle Reduction by Spatial Sampling. Opt Eng 1976;15:274–5. https://doi.org/10.1117/12.7971965.

[177] Welford WTT. Time-averaged images produced by optical systems with time-varying pupils. Opt Commun 1971;4:275–8. https://doi.org/10.1016/0030-4018(71)90148-9.

[178] Hincapie D, Herrera-Ramírez J, Garcia-Sucerquia J. Single-shot speckle reduction in numerical reconstruction of digitally recorded holograms. Opt Lett 2015;40:1623–6. https://doi.org/10.1364/OL.40.001623.

[179] Zhang W, Cao L, Zhang H, Zhang H, Han C, Jin G, et al. Quantitative study on a resampling mask method for speckle reduction with amplitude superposition. Appl Opt 2017;56:F205. https://doi.org/10.1364/ao.56.00f205.

[180] Piedrahita-Quintero P, Garcia-Sucerquia J. Off-axis digital holography simulation in ImageJ. Opt - Int J Light Electron Opt 2017;140:626–33. https://doi.org/https://doi.org/10.1016/j.ijleo.2017.04.091.

[181] Trujillo C, Garcia-Sucerquia J. Phase-shifting digital holographic microscopy by

using a multi-camera setup. Opt Lett 2017;42:4841–4. https://doi.org/10.1364/OL.42.004841.

[182] Piedrahita-Quintero P, Trujillo C, Garcia-Sucerquia J. JDiffraction: A GPGPU-accelerated JAVA library for numerical propagation of scalar wave fields. Comput Phys Commun 2017;214:128–39. https://doi.org/10.1016/j.cpc.2016.12.016.

Realistic modeling of digital holographic microscopy

Carlos Buitrago-Duque and Jorge Garcia-Sucerquia*
Universidad Nacional de Colombia Sede Medellín, School of Physics,
Medellín, Colombia

Abstract. A self-contained platform for realistic modeling of digital holographic microscopy (DHM) is presented. Amplitude and phase samples, imaged in different architectures, can be modeled to produce numerical DHM holograms that include all the parameters that are present in real experiments, providing an accessible way for newcomers to have a first approach to this research field. The platform is based on considering the imaging arm of the DHM that produces the object wave as the result of the convolution process between the geometrical-optics image prediction of the sample with the point spread function introduced by diffraction. The DHM hologram is produced by the amplitude superposition of complex-valued object wave with a reference wave of arbitrary description. The sampling of the analytically produced DHM holograms is set from the input discretized image according to the specifications of the digital camera aimed to be used. The feasibility of the realistic platform is exemplified by contrasting the wrong results of a nonrealistic simulation with experimental results to show the need for using a complete realistic simulation like the one presented; further applications of the platform to numerical modeling speckle noise reduction over samples with controlled levels of roughness, and phase-shifting DHM techniques, are included. [DOI: 10.1117/1.OE.59.10.102418]

Keywords: digital holographic microscopy; numerical modeling; phase shifting; diffraction limit.

Paper 191504SS received Oct. 26, 2019; accepted for publication Mar. 17, 2020; published online Apr. 2, 2020.

1 Introduction

Numerical modeling plays an important role in almost all the branches of knowledge from social sciences[1] to pure science and technology.[2] For example, in the latter, it provides the opportunity of forecasting the results of very complex experiments and it leads to the design and evaluation of the performance of new developments. In particular, in low-resources settings, numerical modeling is perhaps the only way to access to cutting-edge-technology, which plays a fundamental role in the education processes at every level and becomes their sole possible way to approach many research areas.

In the realm of the optical sciences, different commercial programming platforms, such as MATLAB®, COMSOL Multiphysics®, and Mathematica®, along with open-source environments of development, such as Java,[3] python[4] and ImageJ,[5–7] have been utilized for numerical modeling. For any chosen development tool, one of the most important features that whichever numerical modeling has to accomplish is to be as close as possible to the real experiment. In wave optics,[8,9] particularly in the case of coherent imaging,[10] the management of the causes and the effects of the coherent noise on the performance of the system must be treated with extreme care. A remarkable example of how this approach has to be done is presented by Professor Picart's group[11,12]; in these works, realistic modeling of phase imaging in digital holography has been presented with the aim of studying different strategies of reducing the inherited noise from the coherent illumination. Notwithstanding several groups have developed strategies for numerical modeling applicable to the field of digital holography,[6,7,11,13–15] up to the best knowledge of the authors, there is no available tool to realistically model digital holographic microscopy (DHM). In this work, a self-contained platform for realistic modeling of DHM

*Address all correspondence to Jorge Garcia-Sucerquia, E-mail: jigarcia@unal.edu.co

0091-3286/2020/$28.00

is presented; the geometrical as well as the physical optics properties of the imaging system, such as magnification and numerical aperture (NA) of the imaging system, the sampling of the produced hologram by the discretized digital recording camera, the effects of the roughness of the imaged sample, and optimized utilization of the space bandwidth, are considered. Even though the methods utilized in the present contribution can be found spread in the specialized literature, this work presents all the compiled parameters and conditions that must be taken into account to do a realistic numerical modeling of DHM, including all those that determine the performance of real experiments. This work is aimed to provide to the readers, especially to newcomers to the field, the needed information about considering surface roughness, magnification, and NA of the imaging system, tilt angle of the reference wave and digital camera, to obtain numerical models of DHM holograms that closely resemble those that could be recorded in a physical experiment. This contribution may be especially worthwhile for readers from low-resource settings to have a first approach to DHM. A contrast between the wrong results derived from a nonrealistic DHM simulation and experimental results is presented to show the need for using a complete realistic modeling of DHM as the one proposed in this work. Applications to phase-shifting DHM and coherent noise reduction by multiple speckle realizations superposition are presented to show the feasibility of the realistic modeling of DHM.

2 Modeling of Digital Holographic Microscopy

DHM merges the imaging capabilities of microscopy and holography.[16–19] The most striking feature of this merging is a label-free imaging architecture that can see transparent specimens at the micrometer-sized range. To reach this feature, a regular optical microscope architecture, composed of a microscope objective (MO) and a tube lens (TL), is modified with the insertion of an additional arm of illumination that produces the reference wave $[R(x,y)]$. The arm composed of the MO and the TL produces a complex-valued wavefield, named object wave $[O(x,y)]$. See Fig. 1 for an illustration of a DHM operating in transmission mode.

The sample is illuminated by a coherent light source, conventionally a laser, such that the $R(x,y)$ and $O(x,y)$ waves have the possibility of being superimposed in amplitude over the surface of a digital recording camera. The intensity recorded by the camera is known as a hologram $H(x,y)$ and is therefore given by[19,20]

$$H(x,y) = |R(x,y) + O(x,y)|^2. \tag{1}$$

In Eq. (1), $R(x,y) = A_R(x,y)e^{i\varphi_R(x,y)}$ is the explicit form of the complex-valued amplitude of the reference wave, being $A_R(x,y)$ and $\varphi_R(x,y)$ its amplitude and phase, respectively; similarly, the complex-valued object wave has the explicit form $O(x,y) = A_O(x,y)e^{i\varphi_O(x,y)}$.

2.1 *Modeling of the Object Wave*

As the complex-valued object wave is the result of the imaging process from the sample plane to the recording camera, it deserves further analysis. The modeling can be thought to consider the DHM operating in transmission[21,22] or reflection mode[21,23]; in the quoted references, the reader can find a detailed description of the imaging system for each case. However, in either operating

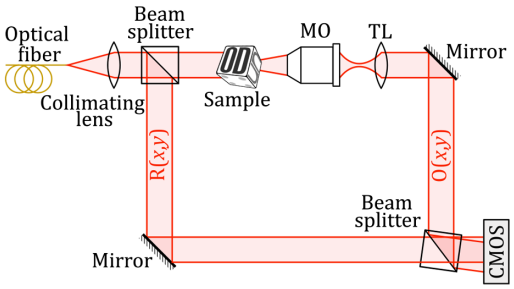

Fig. 1 Illustration of a digital holographic microscope operating in transmission mode.

mode, the imaging system of the DHM, set up in telecentric-afocal[24–26] regimen, produces a complex-valued object wave given by the convolution process between the geometrical-optics image prediction of the sample $1/|M|O_s()$ with the point spread function introduced by the diffraction effects $\tilde{h}()$, namely[20]

$$O(x,y) = \frac{1}{|M|} O_s\left(\frac{x}{M}, \frac{y}{M}\right) \otimes \tilde{h}\left(\frac{x}{\lambda f_{\mathrm{TL}}}, \frac{y}{\lambda f_{\mathrm{TL}}}\right). \tag{2}$$

In Eq. (2), $M = -f_{\mathrm{TL}}/f_{\mathrm{MO}}$ is the overall magnification of the microscope given by the focal lengths of the TL and the MO, respectively. O_s is the complex wavefield at the sample plane and $\tilde{h}(x,y)$ is the Fraunhofer diffraction pattern of the pupil function $P(x',y')$ of the microscope:

$$\tilde{h}\left(\frac{x}{\lambda f_{\mathrm{TL}}}, \frac{y}{\lambda f_{\mathrm{TL}}}\right) = \int_{-\infty}^{\infty}\int_{-\infty}^{\infty} P(x',y') \exp\left[-i\frac{2\pi}{\lambda f_{TL}}(x'x + y'y)\right] \mathrm{d}x'\,\mathrm{d}y'. \tag{3}$$

According to the convolution theorem,[20] the complex-valued object wave in Eq. (2) can be computed as the product of the Fourier transform of the geometrical image of the complex wavefield at the sample plane $1/|M|O_s()$ times the diffraction effects of the imaging system $\tilde{h}()$; as for these calculations, analytical Fourier transforms are computed by means of fast Fourier transforms (FFTs).[27,28]

Equations (2) and (3) play a key role in the performance of the realistic modeling of the DHM. The modeling of the geometrical image of the complex wavefield at the sample plane O_s gives a set of three opportunities. (i) Initially, in the analytical expression of O_s, the amplitude and phase of the ideal sample are coded. For instance, a pure phase object is modeled with a unitary amplitude and the given phase representing it; the latter can be the result of the topography and index of refraction for a transmissive object or the height for a reflective one. (ii) Over the just computed O_s, any sort of deviation from the ideal phase of the sample can be added. A direct example of it is the introduction of different levels of roughness that the real objects exhibit, which are extra phase terms added to the ideal one. (iii) The size of the pixels of the recording camera $\Delta P \times \Delta Q$ defines the discretization of the sample plane via the geometrical magnification of imaging system M:

$$\Delta P' \times \Delta Q' = \frac{\Delta P}{M} \times \frac{\Delta Q}{M}. \tag{4}$$

Once the size of the pixels at the sample plane is defined, and considering that Eq. (2) cast into FFTs is utilized for the computation of the complex-valued object wave, the number of pixels at the sample plane equals those of the recording camera $P \times Q$. Consequently, the available field-of-view (FOV) for the modeled DHM along the x- and y-directions is given by

$$\mathrm{FOV}_x \times \mathrm{FOV}_y = \frac{P\Delta P}{M} \times \frac{Q\Delta Q}{M}. \tag{5}$$

The discretization of the realistic modeling here presented is based on the specification of the digital recording camera. Such specifications are transferred to the sample plane via the geometrical magnification of imaging system M to define the pixel size at the said plane and, therefore, the available FOV along each direction.

To complete the modeling of the complex-valued object wave in Eq. (2), the computation of the diffraction effects, namely the impulse response of the imaging system, has to be performed. As stated in Eq. (3), such impulse response is the Fraunhofer diffraction pattern of the pupil function. This simple, yet effective and accurate, approach allows the inclusion of any complex-valued shape for the pupil function; it gives the opportunity of evaluating, for instance, the results of engineered pupil functions aimed to enhance the resolution of the microscope and/or to understand the effects of given optical aberrations on the performance of the DHM.[29–31]

The computed complex-valued object wave is produced over the image plane of the imaging system. If a reference wave is superposed on such an object wave, an image plane DHM hologram[32,33] is generated. For digital recording cameras placed out of focus, the just computed object wave can be numerically propagated, for instance, via angular spectrum,[6,9] Fresnel transform,[6,34,35] or Fresnel–Bluestein method.[6,34,35] The superposition of a reference wave with this propagated object wave produces a new DHM hologram that must be propagated to obtain the in-focus reconstruction.

2.2 *Modeling of the Reference Wave*

For modeling purposes, both the amplitude and the phase of the reference wave $R(x,y) = A_R(x,y)e^{i\varphi_R(x,y)}$ are analytically generated. This feature allows the production of any type of reference waves;[36] from the very simple plane wave with constant amplitude impinging perpendicular to the recording camera, namely $R(x,y) = A$, to any type of complex wavefronts, as, for instance, spherical reference waves that allow the study of the magnification in holography.[20,37] However, the inclusion of the discretization effects of the recording camera imposes the fulfillment of the sampling theorem at the imaging plane.[20] For illustration purposes, one can consider a plane wave as the reference one, with wave vector at $z = 0$ equal to $\mathbf{k} = 2\pi/\lambda(\cos\alpha\mathbf{U}_x + \cos\beta\mathbf{U}_y)$ being $\mathbf{U}_x$ and $\mathbf{U}_y$ unit vectors along x and y directions; from this expression for the reference wave, one can model an in-line geometry for the case $\alpha = \beta = 0$[38–40] or an off-axis geometry with $\alpha \neq 0$ and/or $\beta \neq 0$.[38,39] For the in-line geometry, the fulfillment of the sampling theorem is only associated with the maximum spatial frequency of the complex-valued object wave that can be recorded by the digital camera. However, in the case of the off-axis geometry, further analysis must be done. Because in the modeling considered in this work, the imaging system has been set up in telecentric-afocal regime, the computed complex-valued object wave is a plane wave.[22] Therefore, the DHM hologram can be understood as an amplitude superposition of two plane waves producing a fringe pattern with period $\Delta x = \frac{\lambda}{2\sin\alpha/2}$ and $\Delta y = \frac{\lambda}{2\sin\beta/2}$, along the x and y directions of the digital recording camera, in that order. The fulfillment of the sampling theorem imposes that at least 2 pixels record the period[36] of the interference fringes. Considering that for the commercially available cameras, the angles α and β are small enough for the approximation $\sin\bullet \approx \bullet$ to be valid, the maximum values for the angles that define that wave vector of the complex-valued reference wave are[36]

$$\alpha_{\max} = \frac{\lambda}{2\Delta P} \quad \text{and} \quad \beta_{\max} = \frac{\lambda}{2\Delta Q}. \tag{6}$$

The final consideration that must be taken into account for the modeling of the DHM holograms is the optimized use of the space bandwidth. While the full space bandwidth is available for allocating the frequency spectrum of the imaged sample in the in-line geometry, in the case of off-axis geometry, the three diffraction orders that compose the Fourier spectrum of the hologram have to be fitted in the space bandwidth. For simplicity of the analysis, one can consider a digital recording camera with an equal number of identical pixels. This consideration makes the space bandwidth square, setting its optimized use for a wave vector with equal angles with respect to x and y directions. For this configuration, with $\alpha = \beta = \phi$, there has been previously demonstrated that the NA of the MO and the magnification of the imaging system M have to fulfill the condition:[22,39]

$$\frac{NA}{M} \leq \frac{2\sqrt{2}\pi}{3}\sin\phi. \tag{7}$$

Equations (6) and (7) are merged to fully determine the angle that must exist between the object and reference waves in off-axis geometry to fulfill the sampling theorem and to make optimized use of the available space bandwidth:[22]

$$\sin^{-1}\left(\frac{3}{2\sqrt{2}\pi}\frac{\mathrm{NA}}{M}\right) \leq \phi \leq \frac{\lambda}{2\Delta P}. \tag{8}$$

2.3 *Reconstruction of Modeled DHM Holograms*

The modeled hologram is reconstructed with the appropriate method according to the type and the kind of the reference wave utilized;[19,36] multiple reconstruction methods are very well documented in the specialized literature.[19,36,37] For in-line geometry, phase-shifting reconstruction methods,[41] for instance, demand the modeling of holograms of the same sample with a relative phase shift of the reference wave; in the applications section, the method is illustrated with the reconstruction of a simulated phase map. For the off-axis geometry, the spatial filtering method, envisioned by Takeda et al.[42] and latter adapted to DHM[18] with further automatic methods to compensate the tilt effect introduced by the reference wave,[26] allows the recovering of the complex-valued object wave $O(x, y)$ at the recording plane. If the modeled hologram is an image-plane one,[32,33] from $O(x, y)$, the amplitude and phase can be computed. If the modeled hologram is an out-of-focus one, $O(x, y)$ has to be propagated to the in-focus plane prior to the computation of the amplitude and phase of the imaged sample.

For any case of the realistic modeling, the recovered complex-valued object wave $O(x, y)$ allows the computing of the phase of the image sample:

$$\varphi_O(x, y) = \tan^{-1} \frac{\mathrm{Im}\{O(x, y)\}}{\mathrm{Re}\{O(x, y)\}} \tag{9}$$

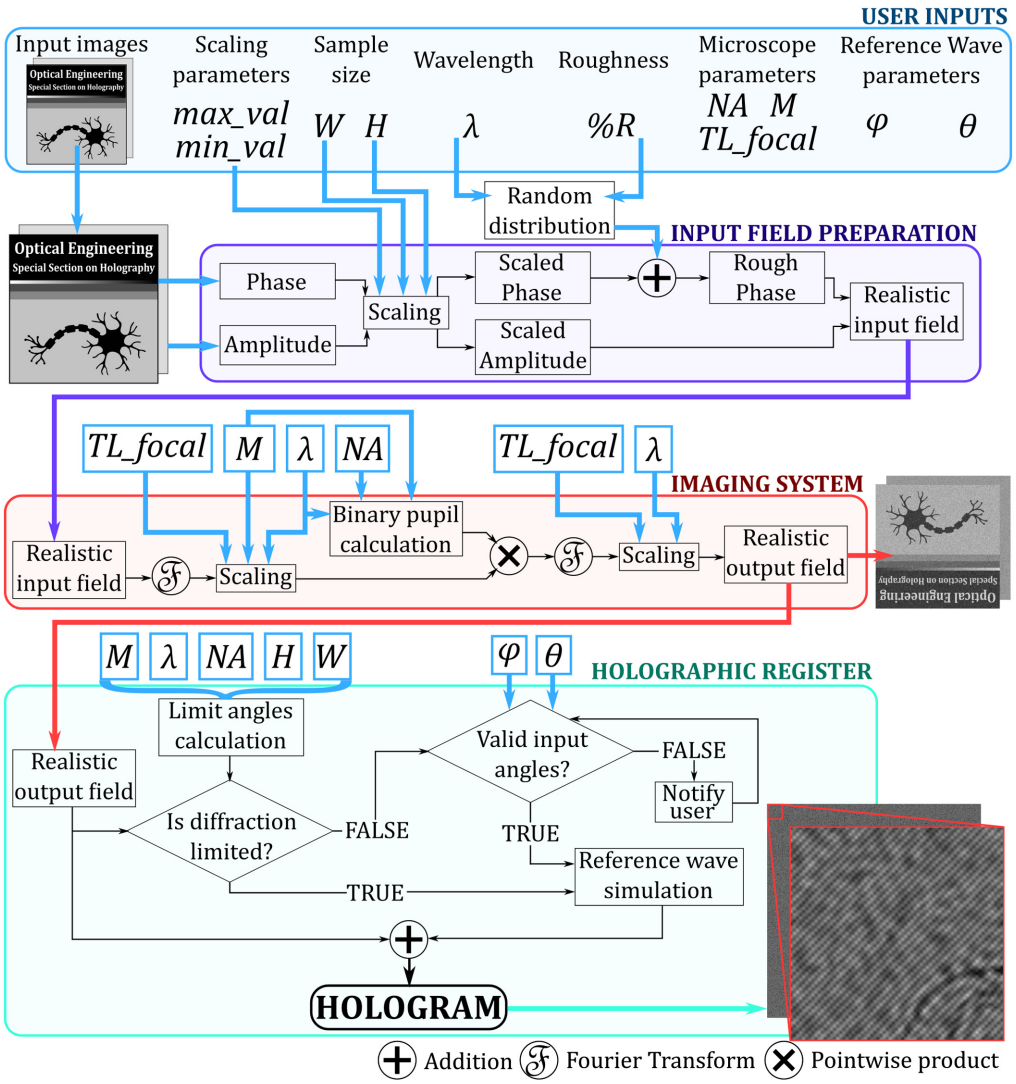

Fig. 2 Summary and flowchart of the realistic modeling platform.

or its amplitude

$$A_O(x,y) = O(x,y) \times O^*(x,y), \tag{10}$$

with * being the complex conjugate.

2.4 *Summary*

Figure 2 presents a summary, in the form of a flowchart, of the aforementioned steps required to achieve a realistic modeling of DHM. Aside from the information flow and processing steps, this diagram allows the quick identification of the relevant parameters, given as user inputs, and an easy following of their influence over each step of the modeling process; furthermore, these relations serve as a reference guide for the critical parameters involved in each experimental step of DHM.

3 Experimental Comparison of Nonrealistic and Realistic Modeling of DHM

According to the well-known literature in DHM,[19,21,32,37,43,44] one, especially newcomers to the field, could be tempted to model DHM as a direct amplitude superposition of a complex-valued reference wavefield with the corresponding object wavefield. In this regard, for the simplest approach, the reference wave is analytically modeled as $R(x,y) = A_R(x,y)e^{i\varphi_R(x,y)}$, and the object wave as the image of an object, corrupted with some sort of noise, and numerically diffracted toward the digital camera plane. A more elaborated modeling approach, yet not entirely realistic, could include an imaging system with wrongly estimated parameters that lead to results that do not appropriately simulate the experimental ones. To illustrate this scenario, the image-plane hologram[32,33] of a star test target is produced from an input image of 1200×1200 pixels corrupted with white Gaussian noise to 8 dB of signal-to-noise ratio and illuminated with a 533-nm wavelength; this sample is imaged through a system with a pupil of 8 mm in diameter and an effective magnification of 10×. Finally, the off-axis hologram is calculated for a digital camera with square pixels of 3.45-μm side length. Figure 3(a) shows the produced hologram with its corresponding Fourier spectrum in Fig. 3(b). From this latter panel, the wrong use of the space bandwidth is seen: the diffracted orders are overlapped, challenging the needed spatial filtering[42,45] for the hologram reconstruction whose result is shown in Fig. 3(c). According to this latter panel, the DHM is capable of fully resolving the whole set of spatial frequencies that compose the test target, as indicated by the blue-dashed circle at ~560 cycles/mm. This resolution power of the DHM is linked with a speckle size in the order of 4 μm, calculated from the autocorrelation[10,31] of the cyan-square bounded area in the background of panel (c); this same analysis area and its autocorrelation are shown in panel (d).

The panels of the second row of Fig. 3 show the results of experimentally imaging a real resolution star test target of 400 μm in diameter. The hologram, in panel (e), was recorded in a transmission DHM using a $10\times/0.25$ MO attached with a TL of 200-mm focal length, an illuminating wavelength of 533 nm, projected onto 1200×1200 square pixels of 3.45 μm of side length from a digital camera. In panel (f), the Fourier spectrum of the experimentally recorded DHM hologram is shown to fulfill the optimization parameters above stated according to Sánchez-Ortiga et al.[22] The diffracted orders show no overlapping while using the complete space bandwidth. In this setup, the reconstructed hologram shown in panel (g) indicates that the cutoff frequency of the real DHM is not enough to fully resolve the whole set of spatial frequencies that compose the star test target; the blurred-up white-circle bounded zone in the center of the target indicates the nonresolved set of spatial frequencies at around 250 cycles/mm, in comparison with the blue-dashed circle resolved in panel (c). The speckle size for the experiment is of the order of 16 μm. To understand the disagreement between the nonrealistic modeling and the experimental results, a realistic modeling in the proposed platform was performed; the corresponding results are presented in the third row of Fig. 3. Figure 3(i) presents the modeled hologram obtained when considering the $10\times/0.25$ MO and the TL with 200-mm focal length utilized in the experiment and the same wavelength of 533 nm. The Fourier

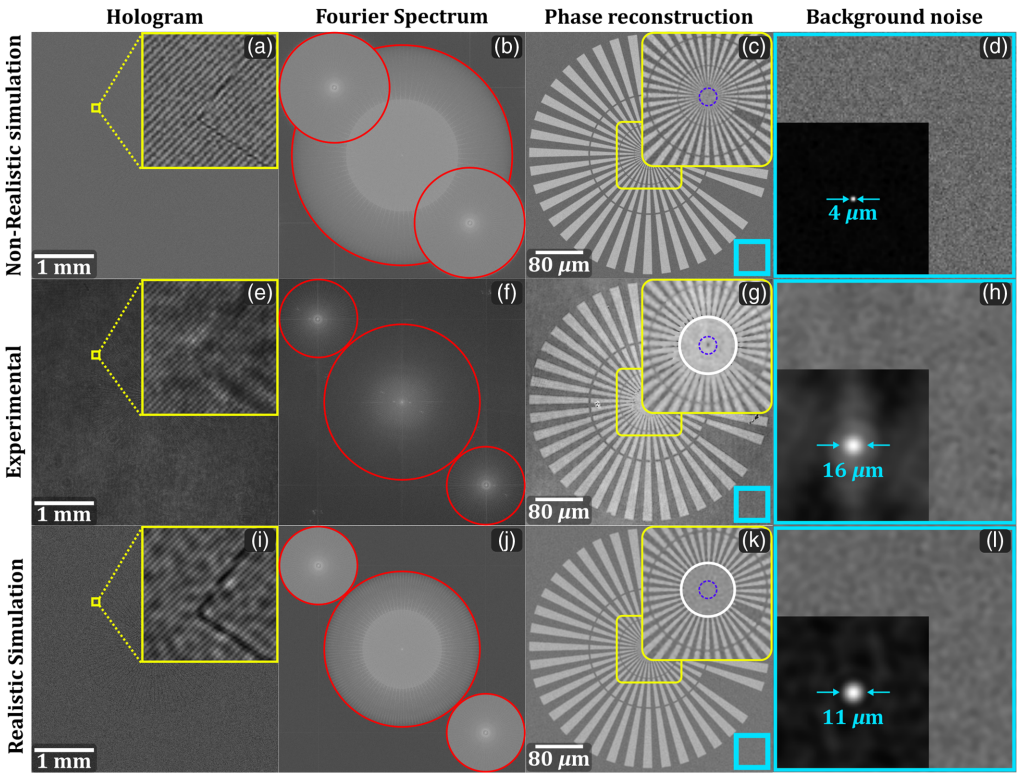

Fig. 3 Nonrealistic and realistic modeling in DHM versus experimental results for a star test target. (a)–(l) Top/middle/bottom row for nonrealistic modeling/experimental results/realistic modeling and first/second/third/fourth column for hologram/Fourier spectrum/phase reconstruction/speckle noise and size.

spectrum of the realistically modeled hologram shows the nonoverlapping of the diffracting orders that use the whole space bandwidth, showing high similarity to what is obtained in the real experiment. The corresponding hologram reconstruction in panel (k) shows the same white-circle-bounded blurred-up zone in the center of the target, indicating the similar lack of resolving power revealed in the experimental results; the calculated speckle size of 11 μm partially agrees with the size calculated for the experiment.

In summary, the oversight of the actual experimental physical parameters when performing a nonrealistic modeling of DHM could point to misleading results in comparison to the experimental equivalent. Conversely, the right use of those physical parameters in a realistic platform points to the right performance of the DHM setup, serving as forecasting for those with a physical setup at hand or as a real representation of the results for those that only have the numerical modeling to be initiated in the DHM field.

4 Applications

To test the feasibility and applicability of the described platform to achieve realistic models of DHM, two typical experiments have been simulated. Initially, a speckle noise reduction procedure in intensity reconstructions was done by averaging multiple realizations of the same amplitude object[46,47] imaged in an off-axis architecture and, secondly, a phase-shifting[41] reconstruction from three fully controlled holograms of a pure-phase object imaged in an in-line architecture. It is worth mentioning that the execution time of a given application is controlled by the required number of holograms. In strict terms of the proposed platform, a MATLAB implementation running on a single core of a 2.20 GHz CPU produces a single-realistic DHM hologram, once all the needed parameters are introduced, in ~200 ms.

4.1 *Noise Reduction in Modeled Digital Holographic Microscopy*

The use of coherent sources, which allows DHM to have steady interference patterns, comes at the cost of dealing with coherent noise, commonly known as speckle.[48] Speckle noise reduction is an active area of research, with multiple approaches to reduce its affectation on coherent imaging systems being constantly reported in the literature. Comprehensive reviews of the state-of-the-art of such methodologies can be found elsewhere.[11,12,49] To test the applicability of the proposed realistic modeling platform in speckle denoising, an averaging of intensity reconstructions from holograms recorded using multiple realizations of roughness over the same amplitude sample was done, as summarized in Fig. 4. Initially, an amplitude distribution with uniform phase was numerically modeled and taken to be the ideal sample information; the corresponding intensity distribution is shown in Fig. 4(a). To this ideal wavefield, a superficial roughness was introduced by adding Gaussian-distributed values, with mean in the order of $\lambda/3$, to the ideal phase distribution. The imaging system was taken to be composed of a $40\times/0.65$ MO, a TL with 200 mm of focal length, and a square sensor with a side length of 8 mm and 4 μm of pixel pitch. Consequently, the full available FOV in the sample plane was of 200 μm in both directions. Using an illumination wavelength of 405 nm, the object information was superposed in

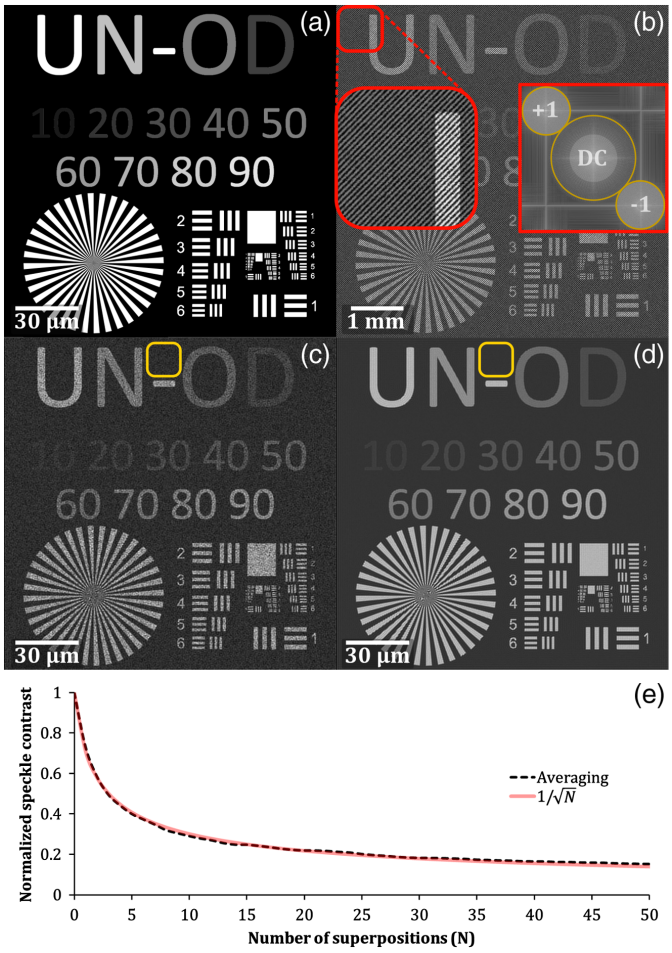

Fig. 4 Speckle noise reduction in intensity reconstructions by averaging multiple realizations of noisy holograms. (a) Ideal intensity distribution. (b) Realistically modeled hologram. The left inset shows a close-up of the interference fringes, while the right one presents the corresponding Fourier Spectrum. (c) Intensity reconstruction from the hologram in panel (b). (d) Intensity distribution obtained by averaging 50 reconstructions with uncorrelated speckle patterns. (e) Normalized speckle contrast evolution with the number of superpositions, measured inside the yellow-bounded region on panels (c) and (d).

amplitude with the reference wave, for which Eq. (8) sets the adequate tilting angles between 0.006 and 0.05 rad to achieve a diffraction-limited DHM hologram; the resulting hologram, using a tilt angle between the reference and object waves of 0.049 rad, is shown in Fig. 4(b). In the rightmost inset of this same panel, the corresponding Fourier spectrum is displayed; as desired, the diffraction orders are nonoverlapped and optimal usage of the space bandwidth is achieved illustrating the diffraction limit of the modeled DHM hologram. Panel (c) shows the intensity reconstruction of the hologram in panel (b), computed as described in Sec. 2.3 for off-axis architectures; in the reconstruction, the affectation produced by the speckle noise is evident. The process was recreated multiple times, randomly changing the roughness distribution to be introduced while keeping all other design parameters. By averaging these results, an overall reduction in the speckle noise is achieved; this can be seen in Fig. 4(d), in which the resulting intensity after averaging 50 independent realizations is shown. Panel (e) shows the evolution of the speckle contrast inside the yellow-bounded regions in panels (c) and (d), if the initial value is taken to be unitary. The speckle contrast measurement, $C = \overline{I}/\sigma_I$ being $\overline{I}$ the average intensity and σ_I its standard deviation,[48] follows the regular $1/\sqrt{N}$ law,[48] with N being the number of superimposed speckle realizations; this behavior was to be expected as, by changing the roughness distribution in every realization, each resulting intensity is ensured to have a unique speckle pattern completely uncorrelated to the other reconstructions.[48] Therefore, the simulated experiment is shown to adequately emulate the physical behavior of the experiment, both in the imaging process, and the speckle statistics associated with the coherent noise.

4.2 *Phase Shifting in Modeled Digital Holographic Microscopy*

Although off-axis DHM systems have a high versatility and applicability in dynamic processes due to the possibility of recovering the complex wavefield from a single-shot hologram, they require a careful alignment to achieve a diffraction-limited acquisition with nonoverlapping orders.[22,45] Thus, there are multiple applications in which the in-line architecture, which ensures effortless diffraction-limited imaging,[41,50] is of special interest. Its use, however, comes at the cost of having the three diffraction orders of the hologram overlapped in the Fourier domain; as such, the reconstruction process requires, for instance, the application of phase-shifting techniques to recover the object information without the presence of the other diffraction components.[41] Therefore, to appropriately model this technique, a set of holograms of the same sample but with known and controlled phase shifts in the reference wave are needed. To further test the realistic modeling platform, a phase-shifting experiment was simulated for a pure-phase object with values ranging between $-\pi/2$ and $\pi/2$ rad; that is, the ideal sample information was taken to be composed of a known phase distribution and unitary amplitude. A superficial roughness in the order of $\lambda/5$ was introduced to the sample by adding Gaussian-distributed values to the ideal phase. The resulting wavefield, considered to be illuminated with a wavelength of 405 nm, was then sharply imaged through a microscope composed of a $40\times/0.65$ objective and a TL with 200-mm focal length into a square sensor of 20-mm side length and 19.5-μm pixel pitch. With these parameters, the system has a resulting FOV in the sample plane of 500 μm in both directions, and a maximum admissible angle between the object and reference waves of 0.01 rad according to Eq. (6). In the sensor plane, the imaged wavefield of the object is superposed in amplitude with a plane reference wave tilted an angle of 0.001 rad; the resulting hologram is shown in Fig. 5(a). Using this initial hologram as the reference point, two additional holograms were identically generated except for the introduction of an additional phase shift in the reference wave of $\pi/2$ and $3\pi/2$ rad; the corresponding holograms are presented in Figs. 5(b) and 5(c), in that order. The respective phase shift can be seen in the inset zoomed-in areas of panels (a)–(c) and are further emphasized by the profile plot shown in panel (e), taken over the yellow line in those same three panels. Finally, Fig. 5(d) shows the reconstructed phase map obtained after applying a phase-shifting algorithm[51] to the three aforementioned holograms.

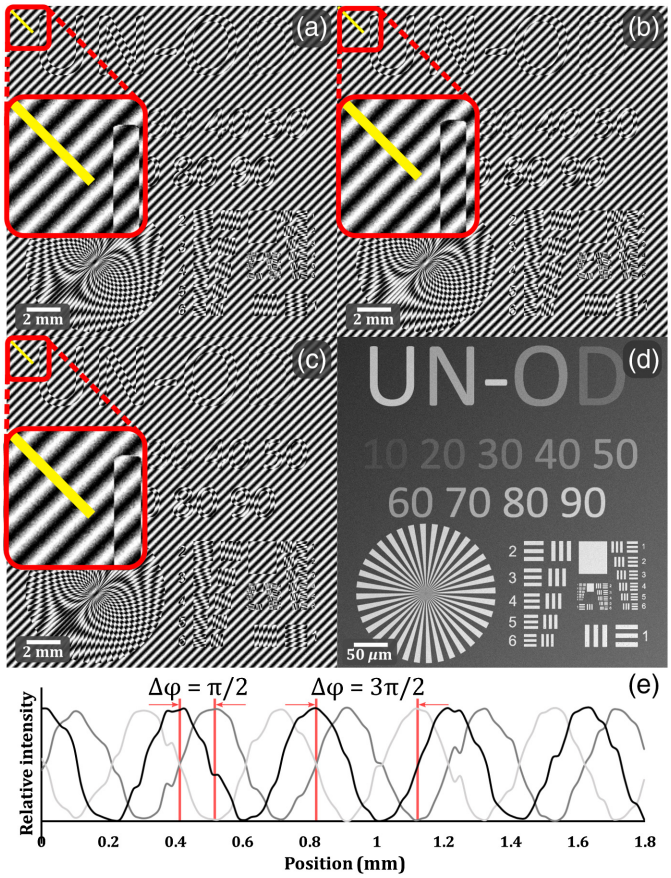

Fig. 5 Realistic modeling of phase-shifting in digital holographic microscopy. (a)–(c) The modeled holograms with a phase delay of 0, $\pi/2$, and $3\pi/2$ rad, respectively. (d) Reconstructed phase map. (e) Profile plot of the interference fringes over the yellow line in panels (a) through (c).

5 Conclusions

A self-contained platform for realistic modeling of DHM has been presented. Based on the underlying wave physical process that guides the retrieving of complex wavefields in DHM, an environment that allows the control of all the parameters that take place in the two stages of DHM has been presented. In the recording stage, the modeling starts by setting the sampling conditions of the input discretized image and the smoothness of the object in terms of fractions of the wavelength. The specifications of the digital recording camera, pixel size, and number of pixels, along with the knowledge of the geometric conditions of the imaging system, are utilized for mimicking the effect of using spatially discretized irradiance sensors; additionally, setting the smoothness provides the possibility of studying the effects of the object in the coherent noise present in DHM. Such smoothness is added to the input real image resembling the imaged sample as a phase function that turns the input image in a generic complex-valued sample; the latter characteristic enables the modeling of amplitude and/or phase objects. After the sample is modeled, it is imaged through the designed imaging system. Following the wave optics rules, the imaging process is simplified as the convolution operation between the geometrical-optics image prediction of the sample with the point spread function introduced by diffraction; in the former, the magnification of the imaging system is introduced, and, in the latter, the complex-valued pupil function is accounted for. These two features enable the modeling platform with the needed versatility to study, for instance, diverse effects on the resolution of the DHM in terms of engineered pupil functions. To complete the recording stage, the complex-valued imaged sample is superimposed in amplitude with a reference wave to produce the modeled hologram. As the reference wave is analytically produced, plane waves with different inclination angles, spherical waves, or any other thought reference wave can be utilized to produce the DHM hologram.

A contrast between the wrong results derived from a nonrealistic DHM simulation and equivalent experimental results has been presented to show the need for using a complete realistic modeling of DHM as the one proposed in this work. In this work, the feasibility of realistic modeling of DHM has been evaluated on modeling DHM holograms of amplitude and phase objects in both off-axis and in-line architectures; specifically, a typical speckle denoising strategy over intensity images with controlled level of roughness is shown in the former, and an application of phase-shifting techniques over pure-phase maps is presented for the latter. The results from the comparison with experimental results and those on both simulations show an adequate emulation of the physical properties of the experiments, validating the applicability of the proposed realistic modeling platform.

Acknowledgments

The present work was done thanks to the funding by Universidad Nacional de Colombia Sede Medellin. The authors declare no conflicts of interest associated with the present work.

References

1. C. Cioffi-Revilla, "Computational social science," *WIREs Comput. Stat.* **2**(3), 259–271 (2010).
2. M. Rappaz, "Numerical modeling in materials science and engineering," *Mater. Today* **6**(3), 53 (2003).
3. T. Mzoughi et al., "WebTOP: a 3D interactive system for teaching and learning optics," *Comput. Educ.* **49**(1), 110–129 (2007).
4. H. Ghalila et al., "Optics simulations: a Python workshop," *Proc. SPIE* **10452**, 1045218 (2017).
5. C. A. Schneider, W. S. Rasband, and K. W. Eliceiri, "NIH Image to ImageJ: 25 years of image analysis," *Nat. Methods* **9**(7), 671–675 (2012).
6. P. Piedrahita-Quintero, R. Castañeda, and J. Garcia-Sucerquia, "Numerical wave propagation in ImageJ," *Appl. Opt.* **54**(21), 6410–6415 (2015).
7. P. Piedrahita-Quintero and J. Garcia-Sucerquia, "Off-axis digital holography simulation in ImageJ," *Optik* **140**, 626–633 (2017).
8. E. Hecht, *Optics*, 4th ed., Addison-Wesley, Reading, Massachusetts (2001).
9. O. K. Ersoy, *Diffraction, Fourier Optics and Imaging*, Wiley Series in Pure and Applied Optics, John Wiley & Sons, Hobenken, New Jersey (2006).
10. J. W. Goodman, *Statistical Optics*, Wiley, New York (1985).
11. S. Montresor and P. Picart, "Quantitative appraisal for noise reduction in digital holographic phase imaging," *Opt. Express* **24**(13), 14322–14343 (2016).
12. V. Bianco et al., "Strategies for reducing speckle noise in digital holography," *Light Sci. Appl.* **7**(1), 48 (2018).
13. T. Shimobaba et al., "Computational wave optics library for C++: CWO++ library," *Comput. Phys. Commun.* **183**(5), 1124–1138 (2012).
14. P. Piedrahita-Quintero, C. Trujillo, and J. Garcia-Sucerquia, "JDiffraction: a GPGPU-accelerated JAVA library for numerical propagation of scalar wave fields," *Comput. Phys. Commun.* **214**, 128–139 (2017).
15. T. Nishitsuji et al., "Fast calculation of Fresnel diffraction calculation using AMD GPU and OpenCL," in *Digital Hologr. and Three-Dimensional Imaging*, Optical Society of America, DWC20 (2011).
16. E. Cuche, F. Bevilacqua, and C. Depeursinge, "Digital holography for quantitative phase-contrast imaging," *Opt. Lett.* **24**(5), 291–293 (1999).
17. S. Ulf and P. O. J. Werner, "Digital recording and numerical reconstruction of holograms," *Meas. Sci. Technol.* **13**(9), R85 (2002).
18. P. Picart, *New Techniques in Digital Holography*, ISTE Ltd. and John Wiley & Sons, Inc., New Jersey (2015).
19. M. K. Kim, *Digital Holographic Microscopy. Principles, Techniques, and Applications*, Springer Series in Optical Sciences, Springer, New York (2011).

20. J. W. Goodman, *Introduction to Fourier Optics*, 3rd ed., Roberts & Company Publishers, Greenwood Village (2005).
21. E. Cuche, P. Marquet, and C. Depeursinge, "Simultaneous amplitude-contrast and quantitative phase-contrast microscopy by numerical reconstruction of Fresnel off-axis holograms," *Appl. Opt.* **38**(34), 6994–7001 (1999).
22. E. Sánchez-Ortiga et al., "Off-axis digital holographic microscopy: practical design parameters for operating at diffraction limit," *Appl. Opt.* **53**(10), 2058–2066 (2014).
23. J. Garcia-Sucerquia and R. Castañeda, "3D topography of reflective samples by single-shot digital holographic microscopy (conference presentation)," *Proc. SPIE* **10666**, 106660V (2018).
24. E. Sánchez-Ortiga et al., "Digital holographic microscopy with pure-optical spherical phase compensation," *J. Opt. Soc. Am. A* **28**(7), 1410–1417 (2011).
25. A. Doblas et al., "Shift-variant digital holographic microscopy: inaccuracies in quantitative phase imaging," *Opt. Lett.* **38**(8), 1352–1354 (2013).
26. C. Trujillo et al., "Automatic full compensation of quantitative phase imaging in off-axis digital holographic microscopy," *Appl. Opt.* **55**(36), 10299–10306 (2016).
27. M. Frigo and S. G. Johnson, "FFTW: an adaptive software architecture for the FFT," in *Proc. IEEE Int. Conf. Acoust., Speech and Signal Process.*, Vol. 3, pp. 1381–1384 (1998).
28. R. P. Muffoletto, J. M. Tyler, and J. E. Tohline, "Shifted Fresnel diffraction for computational holography," *Opt. Express* **15**(9), 5631–5640 (2007).
29. M. K. Kim, "Principles and techniques of digital holographic microscopy," *SPIE Rev.* **1**(1), 018005 (2010).
30. P. Ferraro et al., "Compensation of the inherent wavefront curvature in digital holographic coherent microscopy for quantitative phase-contrast imaging," *Appl. Opt.* **42**(11), 1938–1946 (2003).
31. P. Picart and J. Leval, "General theoretical formulation of image formation in digital Fresnel holography: erratum," *J. Opt. Soc. Am. A* **25**(7), 1744–1761 (2008).
32. D. Carl et al., "Parameter-optimized digital holographic microscope for high-resolution living-cell analysis," *Appl. Opt.* **43**(36), 6536–6544 (2004).
33. P. Hariharan, *Optical Holography: Principles, Techniques, and Applications*, 2nd ed., Cambridge University Press, Cambridge (1996).
34. J. Li and P. Picart, "Calculating diffraction by fast Fourier transform," in *Digital Holography*, J. Li and P. Picart, Eds., pp. 77–114, John Wiley & Sons, Inc., New Jersey (2012).
35. J. F. Restrepo and J. Garcia-Sucerquia, "Magnified reconstruction of digitally recorded holograms by Fresnel-Bluestein transform," *Appl. Opt.* **49**(33), 6430–6435 (2010).
36. T. Kreis, *Handbook of Holographic Interferometry: Optical and Digital Methods*, Wiley-VCH Verlag Ed, Weinheim (2005).
37. P. Picart and J.-C. Li, *Digital Holography*, Wiley, New York (2012).
38. L. Xu et al., "Imaging analysis of digital holography," *Opt. Express* **13**(7), 2444–2452 (2005).
39. M. Karray, P. Slangen, and P. Picart, "Comparison between digital Fresnel holography and digital image-plane holography: the role of the imaging aperture," *Exp. Mech.* **52**(9), 1275–1286 (2012).
40. Y. Zhang et al., "Reconstruction of in-line digital holograms from two intensity measurements," *Opt. Lett.* **29**(15), 1787–1789 (2004).
41. T. Zhang and I. Yamaguchi, "Three-dimensional microscopy with phase-shifting digital holography," *Opt. Lett.* **23**(15), 1221–1223 (1998).
42. M. Takeda, H. Ina, and S. Kobayashi, "Fourier-transform method of fringe-pattern analysis for computer-based topography and interferometry," *J. Opt. Soc. Am.* **72**(1), 156–160 (1982).
43. B. Kemper and G. von Bally, "Digital holographic microscopy for live cell applications and technical inspection," *Appl. Opt.* **47**(4), A52–A61 (2008).
44. P. Bao et al., "Lensless phase microscopy using phase retrieval with multiple illumination wavelengths," *Appl. Opt.* **51**(22), 5486–5494 (2012).

45. E. Cuche, P. Marquet, and C. Depeursinge, "Spatial filtering for zero-order and twin-image elimination in digital off-axis holography," *Appl. Opt.* **39**(23), 4070–4075 (2000).
46. T. Baumbach et al., "Improvement of accuracy in digital holography by use of multiple holograms," *Appl. Opt.* **45**(24), 6077–6085 (2006).
47. J. Garcia-Sucerquia et al., "Incoherent recovering of the spatial resolution in digital holography," *Opt. Commun.* **260**(1), 62–67 (2006).
48. J. W. Goodman, "Some fundamental properties of speckle," *J. Opt. Soc. Am.* **66**(11), 1145–1150 (1976).
49. V. Bianco et al., "Quasi noise-free digital holography," *Light Sci. Appl.* **5**, e16142 (2016).
50. E. Tajahuerce and B. Javidi, "Encrypting three-dimensional information with digital holography," *Appl. Opt.* **39**(35), 6595–6601 (2000).
51. S. De Nicola et al., "Wavefront reconstruction of Fresnel off-axis holograms with compensation of aberrations by means of phase-shifting digital holography," *Opt. Lasers Eng.* **37**, 331–340 (2002).

Carlos Buitrago-Duque is a graduate student from the School of Physics of the Universidad Nacional de Colombia, Medellin, Colombia, where he also received his degree in engineering physics. His research interests include digital holography, computational modeling and numerical processing of physical systems, and optical metrology. He is a SPIE member.

Jorge Garcia-Sucerquia is an associate professor with the School of Physics, Universidad Nacional de Colombia, Medellin, Colombia, where he serves in the program of engineering physics. He received his BSc, MSc, and PhD degrees in physics from the Universidad de Antioquia, Medellin, Colombia. His research interests include digital holography, optical metrology, and optical coherence fields in which he is the author of more than 200 journal papers. He is a SPIE member.

Research Article Vol. 58, No. 34 / 1 December 2019 / Applied Optics G311

applied optics

Phase-shifting digital holographic microscopy with an iterative blind reconstruction algorithm

Ana Doblas,[1,*] Carlos Buitrago-Duque,[2] Aaron Robinson,[1] and Jorge Garcia-Sucerquia[2]

[1]Department of Electrical and Computer Engineering, The University of Memphis, Memphis, Tennessee 38152, USA
[2]School of Physics, Universidad Nacional de Colombia—Sede Medellin, A. A.: 3840, Medellin 050034, Colombia
*Corresponding author: adoblas@memphis.edu

Received 16 July 2019; revised 9 October 2019; accepted 14 October 2019; posted 14 October 2019 (Doc. ID 372731); published 12 November 2019

In phase-shifting digital holographic microscopy (PS-DHM), the reconstructed phase map is obtained after processing several holograms of the same scene with a phase shift between them. Most of the reconstruction algorithms in PS-DHM require an accurate and known phase shift between the recorded holograms. This requirement limits the applicability of the method. To ease the use of PS-DHM, this paper presents an iterative-blind phase shift extraction method based on demodulation of the different components of the recorded holograms. The method uses a DHM system operating in a slightly off-axis architecture. The proposed method uses three-frame holograms with arbitrary and unequal phase shifts between them and therefore eases the use of the PS-DHM. We believe both simulated and experimental results demonstrate the goodness and feasibility of the proposed technique.

https://doi.org/10.1364/AO.58.00G311

1. INTRODUCTION

Digital holographic microscopy (DHM) has been attracting increased interest among the biomedical and material science communities. The increased attention has rocketed DHM to one of the most rapidly emerging optical imaging modalities due to its ability to provide the complex amplitude distribution (e.g., amplitude and phase distributions) of a wave scattered by an object [1–4]. DHM systems, which are based on optical interferometry, record the interference pattern (e.g., hologram) generated between the scattered light from the sample, named the object wave, and a known reference wave. The angle between the reference and the object waves determines the DHM performance: off-axis versus in-line (also known as on-axis). The hallmark of off-axis DHM systems is that the complex amplitude distribution of an object wave can be reconstructed from a single hologram because the three components of the hologram are fully separable in the Fourier domain [5]. In slightly off-axis DHM systems, those three components, the real and conjugate images, and the zero-order term are partially overlapped. Nonetheless, those systems offer ease of the system's alignment and ensure that the reconstructed DHM images are diffraction-limited (e.g., the resolution limit of the DHM system is given by the resolution power of the imaging system with no penalty due to the numerical processing). The unique disadvantage of slightly off-axis DHM systems is that, as in-line systems, they require the acquisition of several phase-shifted holograms and the application of phase-shifting (PS) techniques [6–15] to reconstruct the desired object information with no presence of the zero-order component nor the conjugate image in the recovered information. Traditional PS algorithms reconstruct the complex object information using a well-known formula [6,7] based on the accurate knowledge of the phase shifts between the recorded holograms. Frequently this information is not accurately known, or the methods to produce the phase shifts are not accurate enough. The lack of accurate knowledge in the phase steps results in distorted reconstructed DHM images. Blind phase-shifting algorithms [8–15] have been investigated in PS-DHM systems by recording several phase-shifted holograms with unknown and arbitrary (e.g., no constant) phase steps. All these efforts have focused on iterative and noniterative computational approaches for blind PS-DHM systems using more than two phase-shifted holograms. The common principle of these approaches is the evaluation of an error function to determine the unknown phase steps in the phase-shifted holograms. Current disadvantages of the reported blind PS algorithms are the number of required phase-shifted frames, the prior knowledge of experimental parameters such as the background intensity or the modulation amplitude of the interferogram and/or the required computational time processing.

In this paper, we demonstrate a phase-shifted extraction method for a blind PS-DHM system that is based on the correct demodulation of the hologram spectrum. The proposed method only requires the acquisition of three-frame holograms with arbitrary and unequal phase shifts. There is no need of prior knowledge of the background, reference, nor any other parameter. This method applies to slightly off-axis DHM systems with a very small interference angle, resulting in a significant overlap of the different components in the hologram's spectrum (up to 70% between the real and conjugated orders). Moreover, the PS approach is robust in noisy conditions, and it is computationally efficient. Because of these advantages, we believe that this method presents a high likelihood for broad application because it jointly estimates the phase shifts and the complex amplitude distribution of the object wave accurately.

2. PHASE-SHIFTING DIGITAL HOLOGRAPHIC MICROSCOPY (PS-DHM)

DHM systems reconstruct the complex wavefield distribution (e.g., amplitude and phase) of a wave scattered by a microscopic sample after the cascade application of two processes [1,2,4]: the optical recording of the hologram and its reconstruction. In this section, we will briefly review these two processes and describe the reconstruction method used to retrieve the complex amplitude distribution in PS-DHM.

A. Optical Recording

The basic idea of the optical recording stage is the acquisition of an interference pattern, named a hologram, between the complex amplitude distribution of an object field and a reference wave. Note that in this stage, the only physics-based phenomena involved are diffraction and interference. A modified Mach–Zehnder interferometer is one of the most common optical configurations used in DHM [see Fig. 1(a)]. The light from a laser of wavelength λ_0 is collimated by a converging lens (CL), and the resultant plane beam impinges a cube beamsplitter (BS). The split beams are usually known as the object (O) and the reference (R) waves. The specimen is illuminated by a uniform plane wave and the wavefield scattered by it, of amplitude distribution $o(\boldsymbol{x})$, is imaged by a conventional optical microscope. Referring to Fig. 1, it is readily observable that the object arm of the interferometer incorporates an imaging system setup that includes an infinity-corrected microscope objective (MO) and an appropriately matched tube lens (TL). It is also important to note that this imaging system operates in the telecentric regime. Thus, the back-focal plane (BFP) of the MO (i.e., the plane located at the MO's aperture stop) is set at the front-focal plane (FFP) of the tube lens. The configuration produces a plane wave at the TL lens exit. The result is a shift-invariant DHM system. In other words, it is capable of providing accurate phase measurements of any object regardless of its position within the field of view (FOV) [16,17]. The image of the specimen under research is set at the BFP of TL. This position is commonly referred to as the image plane of the microscope. Assuming that the object is set at the FFP of the MO, the complex amplitude distribution of its image, $u_{\mathrm{IP}}(\boldsymbol{x})$, is given by

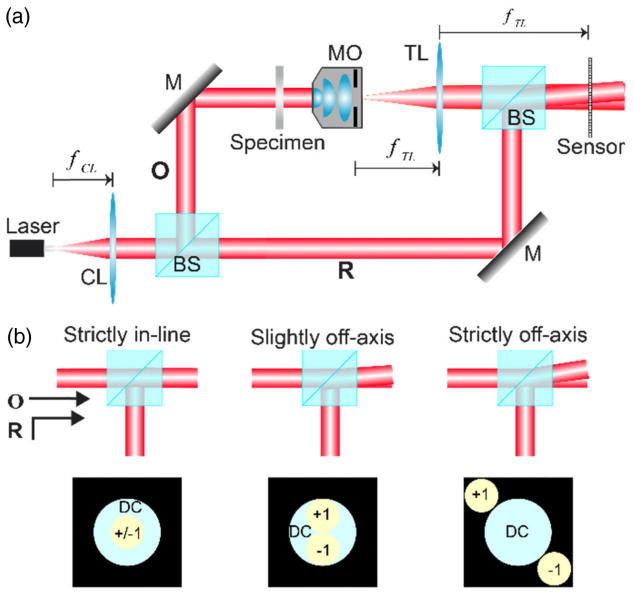

Fig. 1. (a) Optical configuration of a digital holographic microscope based on a Mach–Zehnder interferometer. (b) Illustration of the DHM performance through the Fourier transform of the digital hologram based on the angle between the object (O) and the reference (R) waves. Note that the size of the DC diffraction order (light blue) is always the double of the ±1 terms (yellow) if the DHM system operates in the telecentric regime (the aperture stop of the MO is located at the front focal plane of the TL). The remaining components of the system are denoted as: CL, converging lens; BS, beamsplitter; M, mirror; MO, microscope objective; TL, tube lens.

$$u_{\mathrm{IP}}(\boldsymbol{x}) = \frac{1}{M^2} e^{i2k_0(f_{\mathrm{MO}}+f_{\mathrm{TL}})} \left\{ o\left(\frac{\boldsymbol{x}}{M}\right) \otimes_2 P\left(\frac{\boldsymbol{x}}{\lambda_0 f_{\mathrm{TL}}}\right) \right\}, \quad (1)$$

where $\boldsymbol{x} = (x, y)$ are the transverse coordinates, $\otimes_2$ denotes the 2D convolution, $M = -f_{\mathrm{TL}}/f_{\mathrm{MO}}$ stands for the lateral magnification of the microscope system, and $P(\bullet)$ is the 2D Fourier transform of the MO's aperture stop. Equation (1) shows that the amplitude distribution in the image plane is obtained as the two-dimensional (2D) convolution between a scaled copy of the amplitude distribution of the object and the 2D amplitude point spread function of the imaging system.

In DHM systems, the term hologram refers to the recorded irradiance pattern that results from the interference between the complex object wavefield produced by the microscope at the image plane [Eq. (1)] and a plane wave, $r(\boldsymbol{x}) \propto \exp[ik_0(\sin\theta) \bullet \boldsymbol{x}]$, where $\boldsymbol{\theta} = (\theta_x, \theta_x)$ is the vector representation of the titled reference angle with respect to the optical axis, which also coincides with the center of the object wave O. The irradiance distribution of $h(\boldsymbol{x})$ is given by

$$h(\boldsymbol{x}) = |u_{\mathrm{IP}}(\boldsymbol{x})|^2 + |r(\boldsymbol{x})|^2 + u_{\mathrm{IP}}(\boldsymbol{x})r^*(\boldsymbol{x}) + u_{\mathrm{IP}}^*(\boldsymbol{x})r(\boldsymbol{x}), \quad (2)$$

where $|\cdot|^2$ represents the square modulus and * indicates the complex conjugate operation. Examination of Eq. (2) reveals that the hologram is composed of four terms. Whereas the first two terms do not carry any information about the phase of the object and the angle of the reference wave, the third and fourth terms encode the whole sample information. They generate the real and twin image of the object, respectively. The hologram of Eq. (2) is recorded on a surface of a discrete sensor (CCD or

CMOS) with $N \times N$ square pixels of Δx μm side. Without a loss of generality, the sensor is located at the image plane of the microscope, as shown in Fig. 1(a). This means that in-focus images [Eq. (1)] are recorded, and no numerical focusing step should be used *a-posteriori* in the reconstruction method.

B. Numerical Reconstruction Process

Equation (2) shows that the object information, $u_{\mathrm{IP}}(\cdot)$, (i.e., the desired information) is mixed with other undesired terms in the recorded hologram. The goal of the reconstruction stage is to remove those undesired terms from the object information and to provide well-contrasted images of the information of interest with the minimum noise possible. Let us describe the reconstruction process carefully. For this, it is interesting to analyze the hologram in the Fourier domain. The Fourier transform of Eq. (2) is

$$H(\boldsymbol{u}) = \mathrm{DC}(\boldsymbol{u}) + U_{\mathrm{IP}}(\boldsymbol{u} - \sin\theta/\lambda_0) + U^*_{\mathrm{IP}}(\boldsymbol{u} + \sin\theta/\lambda_0). \tag{3}$$

where $\boldsymbol{u} = (u, v)$ are the transverse spatial frequencies, $\mathrm{DC}(\boldsymbol{u}) = U_{\mathrm{IP}}(\boldsymbol{u}) *_2 U^*_{Ip}(\boldsymbol{u}) + R(\boldsymbol{u}) *_2 R^*(\boldsymbol{u})$ being $*_2$ the 2D cross-correlation operator. Remembering that the capital letters refer to the 2D Fourier transform distributions. Note that Eq. (3) has been derived using the convolution theorem. By noting that the Fourier transform of a plane wave is a Dirac delta function, the inherent multiplication by a complex exponential and subsequent application of the convolution theorem results in the shifted functions [18]. From this equation, it is evident that the Fourier transform of the hologram is composed by three distinguishable terms, as shown in Fig. 1(b). The first of these three terms correspond to the zero-order of the diffraction component. This is commonly known as the DC term and is always set at the center of the spectrum. Since it is a DC component, it does not carry any information about the phase of the object wave and the angle of the interference pattern. The other two terms of Eq. (3), identified as the ± 1 terms, encode the all required sample reconstruction information, both in amplitude and phase. It is important to mention that the three terms are compact support functions whose sizes are related to the resolution of the imaging system [19], $u_c = \mathrm{NA}/\lambda_0$ where NA is the numerical aperture of the MO lens. In fact, the size of the DC term and the ± 1 terms are, respectively, $2u_c$ and u_c. Equation (3) also highlights that whereas the DC terms are always placed at the center of the spectrum of the hologram, the frequencies of the ± 1 terms place these components at symmetric locations around the center with their positions, $(\sin\boldsymbol{\theta})/\lambda_0$, being proportional to the interference angle $\boldsymbol{\theta} = (\theta_x, \theta_y)$. In other words, the degree of overlap between the different components of the hologram spectrum is dependent upon the interference angle between both waves of the DHM recording system. Knowledge of the hologram's spectral composition is critical in the reconstruction stage because its content guides the selection of the reconstruction method. For example, if the angle between both object and reference wave is such as there is no overlap between the different terms, then the reconstruction of the object complex amplitude can be performed using a single-shot spatial filtering method [5]. This is the case of strictly off-axis DHM systems, such as those illustrated in Fig. 1(b). The other extreme case occurs when the angle between both waves is zero, and therefore no interference fringes are observed in the hologram. In this configuration, there is the maximum overlap between the three terms, and it is commonly referred to as strictly in-line DHM systems. Other system configurations lie between these two extremes. In these cases, there is an angle between both waves, but it is not enough to avoid overlapping between the different components of the spectrum. For the latter two cases (strictly in-line and slight off-axis systems), there is a need to record several images (e.g., multishot approaches) to produce the required interference pattern phase shift. These DHM systems are then known as PS-DHM systems. In PS-DHM techniques, there are different methods to generate the required hologram phase shift [6,20–24]. Mathematically, the phase-shifting can be viewed as a change in the phase of the reference wave, $r(\boldsymbol{x}) \propto \exp(\mathrm{i}\Delta\varphi_n)$ with $\Delta\varphi_n$ the specifying the phase shift of each hologram generated by any phase-shifting (PS) method. Once the phase-shifted holograms are recorded, the next step is the numerical reconstruction of the object's complex distribution via PS algorithms [6–15]. The main advantage of these algorithms is that the phase measurements are retrieved via simple mathematical operations, such as subtractions and divisions [3]; consequently, spatial noise is reduced overall. PS algorithms require a minimum of two measurements. On the other hand, most of these PS algorithms work exclusively as strictly in-line DHM systems. Because of the difficulty associated with perfectly aligning the object and reference waves to achieve a strictly in-line setup, one should consider the case of slightly off-axis DHM systems. Remember that slightly off-axis systems are those in which the tilt of one of the interfering waves is not large enough to separate the different terms in the Fourier spectrum [see Fig. 1(b)]. Note that in this case, the traditional PS algorithms cannot be applied to recover the object phase information correctly. For slightly off-axis systems, De Nicola *et al.* [25] proposed an alternative PS strategy. When the interference pattern is recorded using a slightly off-axis arrangement, the phase data can be retrieved from four shots ($n = 4$) in which the phase step between two consecutive holograms is equal to $\pi/2$, $\Delta\varphi_n = \{0, \pi/2, \pi, 3\pi/2\}$. In their approach, both the amplitude and phase distributions of the object under examination are reconstructed by computing a synthetic image, $\hat{u}_{\mathrm{synth}}$, using the recorded hologram, h_i, and generating synthetic reference waves $\hat{r}_i$ as

$$\hat{u}_{\mathrm{synth}}(\boldsymbol{x}) = \hat{r}_1 h_1 + \hat{r}_2 h_2 + \hat{r}_3 h_3 + \hat{r}_4 h_4. \tag{4}$$

To simplify the notations, we have neglected the variables' dependence in the holograms h_i, and the synthetic references $\hat{r}_i$. Equation (4) provides a complex amplitude distribution of the specimen without the presence of the DC term and the conjugate image (e.g., the -1 term). A quantitative phase image can be estimated by computing the angle of Eq. (4).

3. PROPOSED ITERATIVE METHOD FOR BLIND PS-DHM

Although PS approaches reconstruct the phase distribution using simple mathematical operations, many of these methods have strict requirements, including that accurate knowledge of the phase and/or the phase difference between the recorded

holograms must be constant. These two requirements can be experimentally difficult to achieve due to precision inaccuracies prevalent in most phase-shifting devices, particularly those based on mechanical movements. Some effort has been made in the case in which the phase shift between the acquisitions is unknown, leading to blind PS [8–15]. Blind PS approaches allow the phase recovery from a set of holograms through iterative algorithms. These algorithms consist of the cyclic evaluation of an error function to obtain the exact result of the unknown phase shift. The main disadvantage of these methods is the considerable computational load of the entire reconstruction process. In this paper we present a blind iterative PS-DHM algorithm for slightly off-axis DHM systems that is computationally efficient (e.g., reduced computational time), user friendly (e.g., results totally independent of user expertise), robust under noisy conditions, and functional for high-frequency objects without the requirement for frequency component removal (e.g., no spatial filtering is used).

Let us describe our approach framework. Assuming that the reference wave is a plane wave with an arbitrary phase shift $\Delta\varphi_n$, Eq. (2) can be rewritten as

$$h_n(\boldsymbol{x}) = d_0(\boldsymbol{x}) + \mathrm{e}^{-\mathrm{i}\Delta\varphi_n} d_1(\boldsymbol{x}) + \mathrm{e}^{\mathrm{i}\Delta\varphi_n} d_{-1}(\boldsymbol{x}), \tag{5}$$

where $d_0(\boldsymbol{x}) = 1 + |u_{\mathrm{IP}}|^2$ and $d_{\pm1}(\boldsymbol{x}) = \exp(\mp \mathrm{i} k_0 \sin\boldsymbol{\theta} \cdot \boldsymbol{x}) \bullet u_{\mathrm{IP}}$. Equation (5) shows that the recorded hologram is comprised of the linear combinations of three unknown components, d_0, d_{+1}, d_{-1}. Therefore, one only needs three recorded holograms, h_1, h_2, h_3 with the corresponding phase shifts $\Delta\varphi_1$, $\Delta\varphi_2$, $\Delta\varphi_3$, to estimate the three unknown components. For simplification, one can assume that the first phase shift is zero, $\Delta\varphi_1 = 0$, and therefore one must only introduce two-phase steps, $\Delta\varphi_2' = \Delta\varphi_2 - \Delta\varphi_1$ and $\Delta\varphi_3' = \Delta\varphi_3 - \Delta\varphi_1$. Using matrix notation, the estimated unknown components are computed by solving

$$\begin{pmatrix} d_0 \\ d_{+1} \\ d_{-1} \end{pmatrix} = \begin{pmatrix} 1 & 1 & 1 \\ 1 & \mathrm{e}^{-\mathrm{i}\Delta\varphi_2'} & \mathrm{e}^{\mathrm{i}\Delta\varphi_2'} \\ 1 & \mathrm{e}^{-\mathrm{i}\Delta\varphi_3^1} & \mathrm{e}^{\mathrm{i}\Delta\varphi_3^1} \end{pmatrix}^{-1} \begin{pmatrix} h_1 \\ h_2 \\ h_3 \end{pmatrix}. \tag{6}$$

This equation shows that the estimated values of the unknown components (d_{+1}, d_0, and d_{-1}) depends significantly on the value of the phase steps ($\Delta\varphi_2'$ and $\Delta\varphi_3'$). It is important to mention that Eq. (6) is applicable if: (1) the phase steps are different, '$\Delta\varphi_2' \neq \Delta\varphi_3'$; and (2) any of the phase steps is not an integer multiple of 2π, $\Delta\varphi_i' \neq 2m\pi$, where $i = \{1, 2\}$ and m is an integer number. In other words, one needs to ensure that the phase shifts are different between them and different from $2m\pi$. The impact of the correct phase step in the reconstruction algorithm is illustrated in Fig. 2. For this simulated result, we have generated a numerical object whose amplitude and phase distributions are shown in Fig. 2(a). The interference of the amplitude distribution of this object [u_{IP} in Eq. (1)] with a slightly tilted reference plane wave r produces the corresponding hologram h_n given by Eq. (2) and shown in Fig. 2(b). In this simulated case, we have considered that the phase steps of the reference wave were $\Delta\varphi_2' = 60$ deg and $\Delta\varphi_3' = 180$ deg. Figure 2(c) shows the Fourier transforms of the estimated three

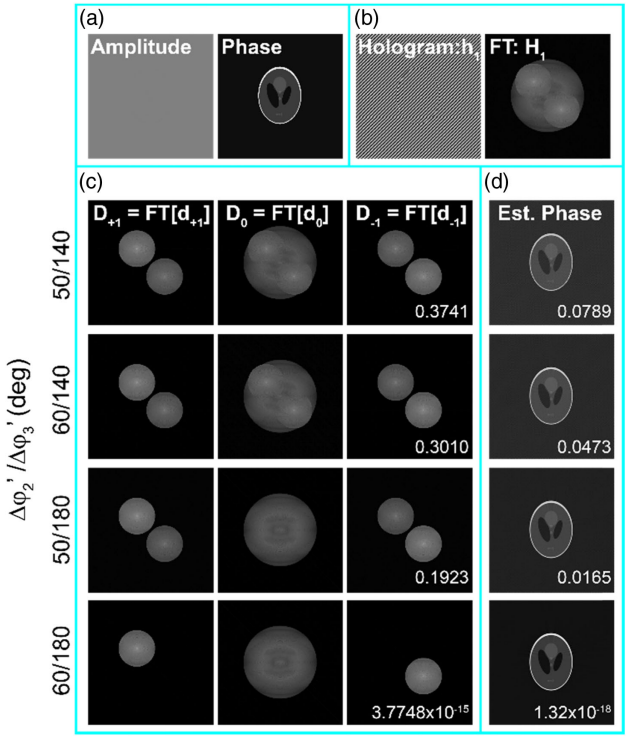

Fig. 2. Demonstration of the proposed cost minimization function in our approach. The panels are: (a) True complex (amplitude and phase) distributions of the simulated object. (b) Hologram and its Fourier transform using a reference slightly tilted. (c) Fourier transform of the demodulated components using Eq. (6) for different values of the phase steps ($\Delta\varphi_2'$ and $\Delta\varphi_3'$). (d) Quantitative phase image obtained from the demodulated component d_{+1}. The true phase steps were $\Delta\varphi_2' = 60$ and $\Delta\varphi_3' = 180$ deg, respectively. The values of the cost function and the MSE are shown in images of panel (c) and (d). Note that only when the phase steps coincide with the true ones, the demodulated components have a unique order, and the MSE error is almost null.

unknown components for different values of $\Delta\varphi_2'$ and $\Delta\varphi_3'$. Note that in our notation D_i is the 2D Fourier transform of d_i where $i = +1, 0, -1$. Observation of this figure shows that only when the phase steps $\Delta\varphi_2'$ and $\Delta\varphi_3'$ are equal to the ones of the reference waves can a perfect estimation of each Fourier component be achieved. This means that the spectrum of the estimated $d_{\pm1}$ component is composed of a unique order. Otherwise, one can observe two orders in the spectrums. The positions of these orders are a function of the tilt angle of the reference wave. Based on this observation, we have defined a cost function. The mathematical expression of the cost function is $J = (2i_{\mathrm{res}})/(i_{\mathrm{exp}} + i_{\mathrm{res}})$, where i_{exp} and i_{res} are the absolute value of the estimated Fourier component in the expected and residual positions, respectively. Therefore, it is clear that this cost function J quantifies the ratio difference between the expected order and the residual order in the estimated $D_{\pm1}$ components. For example, for the D_{+1} component, the expected order should be located at the frequency $\mathbf{u_m} = \sin(\boldsymbol{\theta})/\lambda_0$ and the residual order is at $\mathbf{u_m} = -\sin(\boldsymbol{\theta})/\lambda_0$. Therefore, the cost function for this particular case is computed as

$$J = \frac{2\,|D_{+1}(-\sin\boldsymbol{\theta}/\lambda_0)|}{|D_{+1}(\sin\boldsymbol{\theta}/\lambda_0)| + |D_{+1}(-\sin\boldsymbol{\theta}/\lambda_0)|}. \tag{7}$$

Similarly, the cost function can also be computed using the D_{-1} component, so

$$J = \frac{2\,|D_{-1}(\sin\boldsymbol{\theta}/\lambda_0)|}{|D_{-1}(-\sin\boldsymbol{\theta}/\lambda_0)| + |D_{-1}(\sin\boldsymbol{\theta}/\lambda_0)|}. \quad (8)$$

The value of the cost function obtained using the D_{+1} component, [Eq. (7)], is reported in the third column of Fig. 2(c). If the phase step used in Eq. (6) is the correct one, then $i_{\text{res}} = |D_{+1}(-\sin\boldsymbol{\theta}/\lambda_0)| = 0$, and the value of the cost function in Eq. (7) is equal to zero, $J = 0$. For the particular case shown in Fig. 2, the cost function for the correct phases [last row in Fig. 2(d)] is almost zero, $J = 3.77 \times 10^{-15}$. The utilization of any other different phase-step value produces a higher cost function value. Our approach is based on the minimization of this cost function using the Matlab *built-in* function *fminunc*. Figure 2(d) shows the estimated phase distribution for different phase values inputs. It is important to mention that the phase distribution is obtained by computing the angle of a synthetic image, $\hat{\phi} = \text{angle}(\hat{u}'_{\text{synth}}) = \text{angle}(\hat{r} \bullet d_{+1})$. This synthetic image is needed to compensate for the tilt angle introduced by the reference wave. The quality of the estimated phase is quantified by the mean square error (MSE) between the true and estimated phase maps. This error is reported in Fig. 2(d), and it was computed using the Matlab *built-in* function *immse*. Note that the minimum value of the MSE is 1.32×10^{-18}. The lower the cost function value, the lower the MSE value and, therefore, the more accurate the estimated phase distribution. The flowchart of the proposed algorithm is shown in Fig. 3.

Testing the validation of our approach (e.g., minimization of the cost function) was completed by estimating the MSE value between the true and estimated phase maps after running the proposed method 80 times. Note that the only difference between realizations is the initialization of the phase steps. In our algorithm, the initial values of the phase steps are random values between 0–360 deg generated using the Matlab *built-in* function *randi*. Figure 4 summaries this validation test. Again, the true phase steps in the holograms were {0, 60 deg, and 180 deg}. The estimated phase-step (mean ± standard deviation) values obtained by minimizing the proposed cost function were $(60.000000 \pm 1.3 \times 10^{-6})$ deg and $(179.999999 \pm 3 \times 10^{-6})$ deg. The high accuracy of the calculated phase-step values using our approach is clearly evident. This high precision leads us to well-estimated phase images quantified by really small values of the MSE error (mean $= 4 \times 10^{-16}$, red line in Fig. 3(c), and

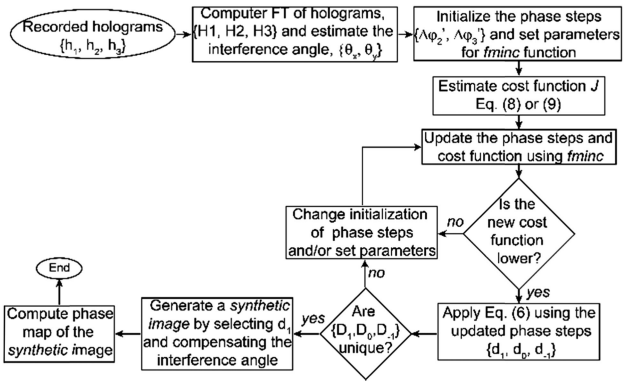

Fig. 3. Flowchart of the proposed algorithm.

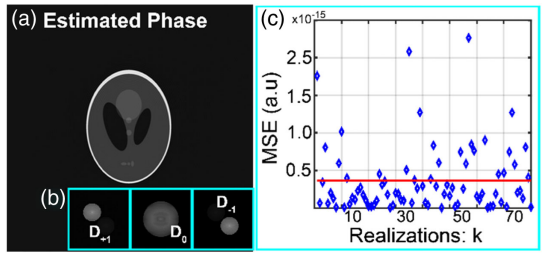

Fig. 4. Evaluation of the accuracy and the repeatability of our proposed method. The panels are: (a) Estimated quantitative phase image for a single realization. (b) Fourier transform of the demodulated components for the estimated phase steps ($\Delta\varphi'_2$ and $\Delta\varphi'_3$) provided by our approach. (c) MSE between the true and estimated phase maps for different realization. For each realization, initialization of the phase steps is different. The mean and standard deviation of the MSE values are 3.6×10^{-16} [red line in panel (c)] and 5×10^{-16}, respectively. The small values of the mean and standard deviation in the MSE values are correlated, respectively, with the accuracy and the repeatability of our method.

standard deviation $= 5 \times 10^{-16}$). Note that the small values of the standard deviation in the MSE values are correlated with the repeatability of our method. Processing times are also of note. The average computing time was 80 s (1.33 min) for a phase image of 1024 × 1024 pixels and a Windows-based i7-6700 CPU (3.40 GHz) 16.0 RAM desk computer.

To finalize this section, we investigate the sensitivity of the proposed PS algorithm for noisy conditions. For this study, we considered that a noisy phase map distorts the phase distribution. The noise was modeled by a white Gaussian distribution and added to the truth phase map [Fig. 4(a)]. For a particular signal-to-noise ratio (SNR) value, 15 noisy phase images were generated by the Matlab *built-in* function *awgn*. Table 1 shows the estimated phase steps provided by the proposed approach and the MSE value between the estimated phase image and the noisy truth map. For this study, the true phase-steps values were 40 deg and 150 deg. With our approach, the estimated phase values were (39.9925 ± 0.0007) deg and (150.0004 ± 0.0009) deg for all the studied SNR. Note that the percentage difference between the true and estimated phase-shift values were less than 0.019%. The root-mean-square error (RMSE) between our estimated phase shifts and the real ones is less than 0.007. Note that, to our knowledge, no currently reported technique cites

Table 1. Performance of the Proposed Algorithm Under Noise Conditions: SNR, $\Delta\varphi'_2$, $\Delta\varphi'_3$, and MSE[a]

SNR (dB)	$\Delta\varphi'_2$ (deg)	$\Delta\varphi'_3$ (deg)	MSE × 10^{-15} (a.u.)
5	$39.53 \pm 2 \times 10^{-6}$	$150.00 \pm 7 \times 10^{-6}$	0.1 ± 1.6
10	$39.99 \pm 7 \times 10^{-4}$	$150.00 \pm 4 \times 10^{-4}$	1.4 ± 1.4
15	$39.99 \pm 1.1 \times 10^{-6}$	$150.00 \pm 5 \times 10^{-6}$	1.3 ± 1.6
20	$39.99 \pm 1.7 \times 10^{-6}$	$150.00 \pm 6 \times 10^{-6}$	0.7 ± 1.6
25	$39.99 \pm 4 \times 10^{-5}$	$150.00 \pm 9 \times 10^{-4}$	2.0 ± 0.7
30	$39.99 \pm 7 \times 10^{-4}$	$150.00 \pm 7 \times 10^{-4}$	1.1 ± 2.0
35	$39.99 \pm 7 \times 10^{-4}$	$150.00 \pm 7 \times 10^{-4}$	0.9 ± 1.1
40	$39.99 \pm 3 \times 10^{-4}$	$150.00 \pm 5 \times 10^{-4}$	0.8 ± 1.3
45	$39.99 \pm 4 \times 10^{-4}$	$150.00 \pm 5 \times 10^{-4}$	0.9 ± 1.2

[a] Notation (mean ± standard deviation).

RMSE error this small. Additionally, the similarity between the true noisy phase map and the estimated phase map is still high, with an MSE value $< 1.5 \times 10^{-15}$. This result shows that we have demonstrated the robustness and accuracy of the approach under noisy conditions.

4. EXPERIMENTAL VERIFICATION

The proposed algorithm has been tested using experimental data obtained and recorded on a PS-DHM system implemented with the mechanical phase-shifting method. The robustness of the algorithm and the fact that we do not need accurate and precise phase shifts among the recorded holograms allows the use of simple methods to produce the needed holograms; a simple rotating cover glass inserted on the reference arm was used as phase shifter in this work. The PS-DHM setup follows a Mach–Zehnder architecture using an illuminating source, a laser diode emitting at 535 nm. The two interferometer arms are commonly referred to as the object and reference arms. The object arm consists of a regular microscopy imaging system that produces a magnified image of the specimen. To provide phase images with a shift-invariant property [16,17] (e.g., the measurement of the phase is independent of the position of the object within the field of view), the imaging system is composed by an infinity-corrected microscope objective [10× Plan Apo, 0.45 numerical aperture (NA) lens, Nikon] and a tube lens (TL) that operate in the telecentric regime [16,17]. It is important to mention that to ease the phase reconstruction process, the camera plane is located at the back focal plane of the TL. Therefore, in-focus holograms are recorded, which avoids the need for a-posteriori refocusing. The other interferometer arm, termed the reference arm, houses a glass slide mounted on a rotating stage. The three recorded holograms with the needed phase shifts have been recorded at 0°, 0.17°, and 0.28° of the glass slide [6] for a first experiment. A star target from the Benchmark Technologies QPI target with a nominal step high of 331.2 nm, according to the manufacturer, was used as an object.

Figure 5 shows the results of the application of the proposed method to recorded holograms of the said star target. In the left-hand side of panel (a) one of the recorded holograms is presented. The spectrum of its Fourier transform is shown in the right-hand side of the same panel. In this Fourier spectrum, the three partially overlapped orders D_{+1}, D_0, and D_{-1} are clearly evident. The slightly off-axis configuration of the DHM is also visible from the close location of the three orders occupying a reduced portion of the available space bandwidth. Panel (b) illustrates the three recovered orders by the proposed method. The dashed light blue lines in each figure indicate the center of the Fourier spectrum, which coincides with the center of the D_0 term. Using these lines as a reference it is clear the shifted location of the D_{+1} and D_{-1} recovered orders to the centered D_0 order. Once the different components of the hologram are estimated, we selected the D_{+1} component, we compensate the tilt between the reference and object beams and reconstruct the phase image. To recover these separated orders from the partially overlapped Fourier spectrum, we must compute the minimization of the cost function J mentioned in Section 3. From the results of the method, we find that the phase shifts among the recorded holograms are 112° and 188°.

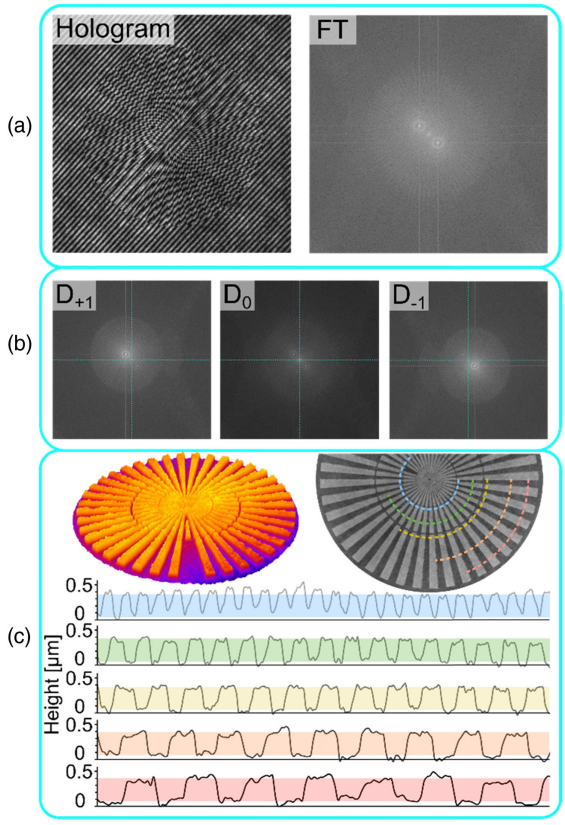

Fig. 5. Experimental validation of the proposed method. Panel (a) shows at left-hand side one of the recorded holograms; at right-hand side is the corresponding spectrum of the Fourier transform of (a). Panel (b) presents the three recovered Fourier orders D_{+1}, D_0, and D_{-1} from left- to right-hand side. Panel (c) shows a 3D rendering of the phase map of the reconstructed object and the height profiles measured at the line over the 3D phase map.

In panel (c), a 3D rendering of the reconstructed phase map of the object (left, top side) along with height profiles measured at different radius are presented. The 3D rendering shows the good quality of the reconstructed information. That quality is also verified by contrasting the measured heights at different spatial frequencies of the object (marked by dashed lines of different colors) with the nominal value reported by the manufacturer. In the right-hand side of panel (c) a set of height measurements for different spatial frequencies is shown. The profiles are all bounded inside a colored region that denotes the value of the nominal value reported by the manufacturer. Note that the color of the region is related to the spatial frequency (i.e., red color corresponds to the lower spatial frequency, and blue color denotes the highest spatial frequency). The agreement of the measured profiles with that nominal value supports the claim that the performance of the method is totally comparable to other methods where precise and accurate knowledge of the phase shifts is mandatory for the methods to work.

Finally, to illustrate the performance of the proposed algorithm in a more complex structure, we reconstruct the quantitative phase image of a transverse section of the head of a *Drosophila melanogaster* fly. The reconstructed quantitative phase image of this experimental sample is presented in Fig. 6. In

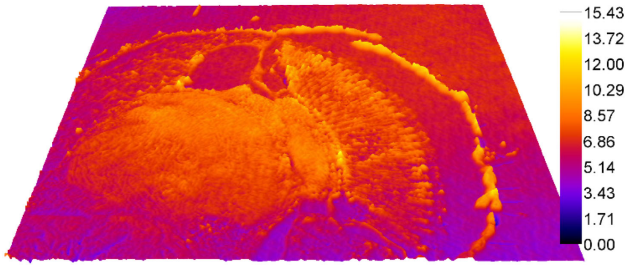

Fig. 6. Experimental verification of the proposed approach using a complex biological specimen: 3D rendering of the quantitative phase image of a section of the head of a Drosophila melanogaster fly.

the reconstructed phase image, we can identify some distinctive parts of the head of the *Drosophila melanogaster* fly. For this millimeter-sized complex sample, the proposed method is also well-suited.

5. CONCLUSIONS

In this work, we have presented a joint approach to estimate the phase shifts and the quantitative phase distribution in PS-DHM. This approach is based on the demodulation of the spectral components of the phase-shifted digital holograms. The principle of our approach is that well-estimated phase shifts guarantee that each demodulated component is unique in the Fourier spectrum, enabling the identification of the independent and separable orders. The proposed method is suitable for arbitrary unequal phase-shift values between the three recorded holograms. The only requirement of this approach is that the PS-DHM system should operate in a slightly off-axis regime. Thus, the angle between the reference and the object waves cannot be equal to zero, but the Fourier components can be partially overlapped. Although this work did not aim for a rigorous comparison between our method and previously reported noniterative and iterative methods, the speed of our algorithm is quite comparable to those previously reported. The computational time of high-precision, phase-shift estimations from an image of 256 × 256 pixels was 4 s; the code was implemented in Matlab running on an i7-6700 CPU 3.40 GHz 16.0 RAM desk computer. Our simulated and experimental results show that the proposed approach provides accurate quantitative phase images. Also, the proposed method, which was tested with simulations, is quite robust under noisy conditions.

Funding. The University of Memphis.

Acknowledgment. We thank Chrysanthe Preza for an interesting discussion about the cost function and its minimization.

REFERENCES

1. T. Kreis, *Handbook of Holographic Interferometry: Optical and Digital Methods* (Wiley, 2004).
2. M. K. Kim, "Principles and techniques of digital holographic microscopy," SPIE Rev. **1**, 18005 (2010).
3. G. Popescu, *Quantitative Phase Imaging of Cells and Tissues* (McGraw-Hill, 2011).
4. P. Picart and J.-C. Li, *Digital Holography* (Wiley, 2012).
5. E. Cuche, P. Marquet, and C. Depeursinge, "Spatial filtering for zero-order and twin-image elimination in digital off-axis holography," Appl. Opt. **39**, 4070–4075 (2000).
6. K. Creath, "Phase-measurement interferometry techniques," Prog. Opt. **26**, 349–393 (1988).
7. R. Sirohi and M. Kothiyal, *Optical Components, Systems, and Measurement Techniques*, 1st ed. (Marcel Dekker, 1991).
8. H. Guo, Y. Yu, and M. Chen, "Blind phase shift estimation in phase-shifting interferometry," J. Opt. Soc. Am. A **24**, 25–33 (2007).
9. X. F. Xu, L. Z. Cai, X. F. Meng, G. Y. Dong, and X. X. Shen, "Fast blind extraction of arbitrary unknown phase shifts by an iterative tangent approach in generalized phase-shifting interferometry," Opt. Lett. **31**, 1966–1968 (2006).
10. X. F. Xu, L. Z. Cai, Y. R. Wang, X. L. Yang, X. F. Meng, G. Y. Dong, X. X. Shen, and H. Zhang, "Generalized phase-shifting interferometry with arbitrary unknown phase shifts: direct wave-front reconstruction by blind phase shift extraction and its experimental verification," Appl. Phys. Lett. **90**, 121124 (2007).
11. F. Zeng, H. Gu, and Q. Tan, "Application of the blind signal separation method for phase-shifting interferometry with random phase shifts," Proc. SPIE **9046**, 90460R (2013).
12. F. Liu, J. Wang, Y. Wu, F. Wu, M. Trusiak, K. Patorski, Y. Wan, Q. Chen, and X. Hou, "Simultaneous extraction of phase and phase shift from two interferograms using Lissajous figure and ellipse fitting technology with Hilbert–Huang prefiltering," J. Opt. **18**, 105604 (2016).
13. D. Xie, D. Zhao, Y. Yang, and H. Zhai, "Phase-shift extraction algorithm for blind phase-shifting holography based on the quotient of inner products," Opt. Commun. **393**, 40–44 (2017).
14. C. Meneses-Fabian and N. Tejeda-Muñoz, "Self-calibrating phase-shifting interferometry of three unequal phase steps by fitting background light to a polynomial of degree K," Appl. Opt. **56**, 4278–4283 (2017).
15. G. A. Ayubi, I. Duarte, and J. A. Ferrari, "Optimal phase-shifting algorithm for interferograms with arbitrary steps and phase noise," Opt. Lasers Eng. **114**, 129–135 (2019).
16. A. Doblas, E. Sánchez-Ortiga, M. Martínez-Corral, G. Saavedra, P. Andrés, and J. Garcia-Sucerquia, "Shift-variant digital holographic microscopy: inaccuracies in quantitative phase imaging," Opt. Lett. **38**, 1352–1354 (2013).
17. A. Doblas, E. Sánchez-Ortiga, M. Martínez-Corral, G. Saavedra, and J. Garcia-Sucerquia, "Accurate single-shot quantitative phase imaging of biological specimens with telecentric digital holographic microscopy," J. Biomed. Opt. **19**, 046022 (2014).
18. J. D. Gaskill, *Linear Systems, Fourier Transforms and Optics* (Wiley, 1978).
19. E. Sánchez-Ortiga, A. Doblas, G. Saavedra, M. Martínez-Corral, and J. Garcia-Sucerquia, "Off-axis digital holographic microscopy: practical design parameters for operating at diffraction limit," Appl. Opt. **53**, 2058–2066 (2014).
20. I. Yamaguchi and T. Zhang, "Phase-shifting digital holography," Opt. Lett. **22**, 1268–1270 (1997).
21. C. Robledo-Sanchez, R. Juarez-Salazar, C. Meneses-Fabian, F. Guerrero-Sánchez, L. M. Arévalo Aguilar, G. Rodriguez-Zurita, and V. Ixba-Santos, "Phase-shifting interferometry based on the lateral displacement of the light source," Opt. Express **21**, 17228–17233 (2013).
22. M. Roy, P. Svahn, L. Cherel, and C. J. R. Sheppard, "Geometric phase-shifting for low-coherence interference microscopy," Opt. Lasers Eng. **37**, 631–641 (2002).
23. V. Micó, Z. Zalevsky, and J. Garcia, "Superresolved common-path phase-shifting digital inline holographic microscopy using a spatial light modulator," Opt. Lett. **37**, 4988–4990 (2012).
24. P. Slangen and B. Gautier, "Nematic liquid crystal light valve: application to phase shifting speckle interferometry," Proc. SPIE **6616**, 66162U (2007).
25. S. De Nicola, P. Ferraro, A. Finizio, and G. Pierattini, "Wave front reconstruction of Fresnel off-axis holograms with compensation of aberrations by means of phase-shifting digital holography," Opt. Lasers Eng. **37**, 331–340 (2002).

applied optics

Fast-iterative blind phase-shifting digital holographic microscopy using two images

Raul Castañeda,[1] Carlos Buitrago-Duque,[2] Jorge Garcia-Sucerquia,[2] and Ana Doblas[1,*]

[1]Department of Electrical and Computer Engineering, The University of Memphis, Memphis, Tennessee 38152, USA
[2]School of Physics, Universidad Nacional de Colombia—Sede Medellin, A. A.: 3840, Medellin 050034, Colombia
*Corresponding author: adoblas@memphis.edu

Received 22 May 2020; revised 18 July 2020; accepted 20 July 2020; posted 21 July 2020 (Doc. ID 398352); published 20 August 2020

Digital holographic microscopy (DHM) has consolidated as a tool for diagnosis and measuring in life sciences, thanks to its capability to perform quantitative phase imaging. The reduction of the acquisition and computation time has driven the development of diverse reconstruction methodologies using a single-shot and two-frame approach. Methods based on the Fourier transform, the Hilbert transform, and the phase derivative are counted among the most utilized. The sensitivity of those methods is highly dependent on the compensation of the phase step, which requires the accurate knowledge of the phase shift between the two recorded holograms. Here, an alternative fast-iterative method based on the demodulation of the different components of the recorded interferograms is presented. The novelties of the proposed two-frame approach are: minimum number of images, since it requires 2 recorded holograms; a minimum phase error of the order of 0.005% independently of the phase step ranging from 0 to 180 deg.; a maximum correlation coefficient equal to 1 between the phase and the retrieved phase image; and, finally, a reduced processing time compared with the previous three-frame approach. Experimental results demonstrate the goodness and feasibility of the proposed technique.

https://doi.org/10.1364/AO.398352

1. INTRODUCTION

Over the last decades, digital holographic microscopy (DHM) has become one of the most innovative and rapidly emerging quantitative phase imaging (QPI) modalities [1–3]. The hallmark of DHM is the accurate retrieval of the complex wavefield [4–6] (both amplitude and phase information) scattered by an object. DHM is an interferometric technique involving the optical recording of an interference pattern, commonly named as a hologram, between an object and a reference wave. The angle between these two waves determines the operation regimen of the DHM system; in-line versus off-axis systems. For example, in DHM operating in an off-axis regime, the angle between the reference wave and the object wave must be high enough that there is no overlap of the hologram components in the Fourier spectrum. Therefore, one can retrieve the complex object information using a single shot hologram and applying a spatial filter [7]. However, this condition of the nonoverlapping of the hologram components, is highly dependent on the spatial bandwidth of the camera.

Contrary to off-axis systems, in-line DHM systems are the most efficient ones based on the spatial bandwidth of the camera, since the angle between the reference and object waves is zero. Conventionally, the main drawback of in-line DHM systems is their applicability to the study of dynamic samples, since they require the recording of at least three phase-shifted holograms and the subsequent application of phase-shifting methods optimized for DHM (PS-DHM) to retrieve the complex object information. To increase the applicability of PS-DHM, the phase-shifting technique should be fast in both recording time and processing time. Over the years, different approaches have been developed to address these requirements. It has been proven that accurate results can be obtained with a minimum of two recorded holograms in in-line DHM systems with or without prior knowledge of the phase shifts [8–14]. Most of those approaches need precise knowledge of the phase step between both recorded holograms. However, such knowledge can be experimentally arduous without achieving accurate enough values. A rigorous study of two-frame algorithms in in-line DHM systems has been recently presented by Flores *et al.* [15], showing the potential of these approaches.

Alternatively, two-frame algorithms have been successfully demonstrated in slightly off-axis DHM systems. It is important to mention that slightly off-axis systems refer to those in which the DC term and the ± 1 diffracted terms partially overlap. While some research articles name slightly off-axis DHM systems as those in which there is no overlapping between the ± 1 terms, these terms still overlap with the DC order.

Several reconstruction methods have been proposed to reconstruct the phase map in slightly off-axis DHM systems in which there is no overlap between the ±1 terms. In 2011, Han *et al.* [16] proposed a multicolor slightly off-axis DHM system in which a color sensor recorded simultaneously a hologram within the red channel and the intensity of the object beam using the blue channel. The complex object distribution was then reconstructed after subtracting these two images, compensating the reference wave and the spatial filtering of the object frequencies.

Another widely used algorithm is the subtraction of two recorded phase-shifted holograms, which removes the DC term in the spectrum. Then, as in the previous approach, the complex object distribution is reconstructed after compensating the reference wave and filtering the object frequencies [17,18]. Note that the intensity of the reference wave needs to be measured in advance, and its intensity should not be less than 2 times the maximum intensity of the object wave [18]. An alternative approach has also been demonstrated using a Hilbert transform [19]. It is important to mention that these two approaches require the compensation of the global phase shift introduced between both holograms. If the interference fringes are horizontal or vertical, one can estimate the phase step by subtracting the phase value of each hologram. For each hologram, the phase is estimated by summing the fringe pattern columns or rows, depending on the direction of the fringes, and fitting the resulting vector to a sine wave [19]. Otherwise, this phase shift, which introduces a constant phase value, can be determined as the residual phase in the absence of sample and subtracting from the measured phase. In other words, the recorded holograms should exhibit an area free of the specimen such that the constant phase can be measured. This condition may reduce the usable field of view to provide accurate phase measurements. In Refs. [20–23], authors describe alternative two-frame reconstruction algorithms applied to slightly off-axis DHM systems that reconstruct the complex information of the object without prior knowledge of the hologram phase shift, namely blind PS methods. It is important to mention that some of these works also require the knowledge of the object and/or reference intensities, demanding a total of four images [20]. Also note that, whereas the method proposed by Meng *et al.* [20] is completely automatic, the optimal estimated phase step based on Hsieh's approximations have to be selected by trial and error, hiding the automatic feature of the method [21]. To finalize this brief review, in 2014, Guo *et al.* proposed a method based on a phase derivative approach [24]. The main limitation of that method is that it requires a hologram and the recording of the object and reference beams, namely three shots. However, an advantage of that phase derivative method is that it is a purely local method, not requiring any integral operation such as the Fourier transform or the Hilbert transform, which could significantly reduce the computing complexity and memory demands of the data processing system. Recently, a π-shifted spatially multiplexed interference microscopy has been proposed [25,26]. In that work, the authors record simultaneously in a single shot two holograms mutually phase-shifted by π radians. Reconstructed phase images of high quality were obtained by employing the Hilbert spiral transform on the π hologram.

In this work, an alternative blind PS-DHM algorithm that requires the use of two phase-shifted holograms is proposed. The algorithm has the features of recovering the complex object information without the necessity to have any knowledge of the phase shift in each recorded hologram. This algorithm is also based on the demodulation of the terms composing the Fourier transform of the hologram, as recently published [27]. The advantages of the proposed two-frame approach are: a minimum number of images needing only two recorded holograms, a minimum phase error of the order of 0.005% independently of the phase step ranging from 0 to 180 deg., a maximum correlation coefficient between the phase and the retrieved phase image equal to 1, and, finally, a reduced processing time compared with the previous three-frame approach [27]. It is predicted that the proposed algorithm will always work as far as one can distinguish the maximum peaks of the $D_{\pm 1}$ terms in the hologram spectrum. In addition, the proposed method could be used to determine the global phase step required in some previously-reported two-frame algorithms [17–19].

2. IMAGE FORMATION AND RECONSTRUCTION IN PHASE-SHIFTING DIGITAL HOLOGRAPHIC MICROSCOPY (PS-DHM)

In PS-DHM systems, the complex wavefield distribution and amplitude and phase of a microscopic sample is retrieved after the optical recording of multiple holograms and their reconstructions. As a hologram is the recorded irradiance pattern of the interference between the complex object wavefield of a microscopic sample produced by the microscope and a titled plane wave, its irradiance distribution, $h(\boldsymbol{x})$, can be written as [27]

$$h(\boldsymbol{x}) = d_0(\boldsymbol{x}) + \boldsymbol{e}^{-\mathrm{i}\Delta\varphi} d_1(\boldsymbol{x}) + \boldsymbol{e}^{\mathrm{i}\Delta\varphi} d_{-1}(\boldsymbol{x}), \tag{1}$$

where $d_0(\boldsymbol{x}) = 1 + |u_{\mathrm{IP}}(\boldsymbol{x})|^2$ being u_{IP} $(\mathbf{x})$ the complex amplitude distribution of the sample at the image plane of a microscope, and $d_{\pm 1} = \exp(\mp \mathrm{i} k_0 \sin\boldsymbol{\theta} \cdot \boldsymbol{x}) \cdot u_{\mathrm{IP}}$, where $k_0 = 2\pi/\lambda$ is the illumination wavenumber, and $\boldsymbol{\theta} = (\theta_x,\ \theta_y)$ is the vector representation of the titled reference angle to the optical axis, which represents the center of the object wave O. From Eq. (1), one realizes that the hologram is the linear combination between the three unknown components, $\{d_0,\ d_{+1},\ d_{-1}\}$. The weighting of each component depends on the phase shift $\Delta\varphi$. Thereby, three recorded holograms are needed, $\{h_1,\ h_2,\ h_3\}$ with the different phase shifts $\{\Delta\varphi_1,\ \Delta\varphi_2,\ \Delta\varphi_3\}$, to determine the unknown components:

$$\begin{pmatrix} d_0 \\ d_{+1} \\ d_{-1} \end{pmatrix} = \begin{pmatrix} 1 & 1 & 1 \\ 1 & \mathrm{e}^{-\mathrm{i}\Delta\varphi_2'} & \mathrm{e}^{\mathrm{i}\Delta\varphi_2'} \\ 1 & \mathrm{e}^{-\mathrm{i}\Delta\varphi_3'} & \mathrm{e}^{\mathrm{i}\Delta\varphi_3'} \end{pmatrix}^{-1} \begin{pmatrix} h_1 \\ h_2 \\ h_3 \end{pmatrix}. \tag{2}$$

Without a lack of generality, it is assumed that the first phase shift is 0, $\Delta\varphi_1' = 0$, and the other two-phase steps can be written as $\Delta\varphi_2' = \Delta\varphi_2 - \Delta\varphi_1$ and $\Delta\varphi_3' = \Delta\varphi_3 - \Delta\varphi_1$. This equation shows that the estimated values of the unknown components (d_{+1}, d_0, and d_{-1}) depend significantly on the value of the phase steps ($\Delta\varphi_2'$ and $\Delta\varphi_3'$). In particular, the spectrum of the estimated $d_{\pm 1}$ components is only composed of a unique order when the phase steps $\Delta\varphi_2'$ and $\Delta\varphi_3'$ used in Eq. (2) equal the ones introduced by the reference wave. Authors in Ref. [27] took advantage of this observation to estimate the phase steps

and the unknown components jointly. That estimation is based on the minimization of a cost function that quantifies the ratio difference between the expected order and the residual order in the spectrum of the estimated $d_{\pm 1}$ components. The lower the cost function value, the more accurate both the estimated phase steps and the unknown components. Once one has successfully estimated $\{d_0,\ d_{+1},\ d_{-1}\}$, the phase distribution is obtained by computing the angle of the d_{+1} component after the interference angle is compensated.

3. PROPOSED ITERATIVE METHOD FOR BLIND PS-DHM USING TWO IMAGES

In this paper, a blind iterative PS-DHM algorithm for slightly off-axis DHM systems that only requires the acquisition of two phase-shifted holograms is presented. The framework of the proposed algorithm is based on the linear combination of the recorded hologram, Eq. (1), as the sum of two unknown components, $\{d_0, d_3\}$, which reduces the computational load:

$$h_n(\boldsymbol{x}) = d_0(\boldsymbol{x}) + \mathrm{e}^{\mathrm{i}\Delta\varphi_n} d_3(\boldsymbol{x}), \tag{3}$$

where

$$d_3(\boldsymbol{x}) = d_{+1}(\boldsymbol{x}) + \mathrm{e}^{-i2\Delta\varphi_n} d_{-1}(\boldsymbol{x}). \tag{4}$$

From Eq. (3), one realizes that only two recorded holograms, $\{h_1,\ h_2\}$, with the corresponding phase shifts, $\{\Delta\varphi_1,\ \Delta\varphi_2\}$, are needed to estimate the two unknown components. Again, for simplicity, one can assume that the first phase shift is 0, $\Delta\varphi_1 = 0$, and therefore one must only introduce one phase step, $\Delta\varphi_2' = \Delta\varphi_2 - \Delta\varphi_1$. Using matrix notation, the estimated unknown components are computed by solving

$$\begin{pmatrix} d_0 \\ d_3 \end{pmatrix} = \begin{pmatrix} 1 & 1 \\ 1 & \mathrm{e}^{\mathrm{i}\Delta\varphi_2'} \end{pmatrix}^{-1} \begin{pmatrix} h_1 \\ h_2 \end{pmatrix}. \tag{5}$$

This equation shows that the estimated values of the unknown components (d_0 and d_3) depend significantly on the value of the phase step ($\Delta\varphi_2'$) used. It is important to mention that Eq. (5) is applicable if the phase step is not an integer multiple of 2π, $\Delta\varphi_2' \neq 2m\pi$, being m being an integer number. Figure 1 illustrates the impact of the correct phase step in the retrieval of the unknown components. For this simulation, a numerical pure phase object (i.e., amplitude distribution is equal to 1), whose phase distribution is shown in Fig. 1(a), was generated. The Fourier spectrum of the interference of the amplitude distribution of this object with a slightly tilted reference plane wave is shown in Fig. 1(b). In this simulated case, we have considered that the phase step of the reference wave was $\Delta\varphi_2' = 60$ deg. Figures 1(c) and 1(d) show the Fourier transforms of the estimated two unknown components [Fourier transform of Eq. (5)] for two different values of $\Delta\varphi_2'$. Note that in this notation, D_i is the 2D Fourier transform of d_i, where $i = 0,\ 3$. Observation of this figure shows that only when the phase step $\Delta\varphi_2'$ coincides with the real one of the reference waves [row named as *True* in Figs. 1(c) and 1(d)], the spectrum of the d_0 component is composed by two orders: one order is set at the center of the spectrum (D_0), and the other order is located at the frequency $\mathbf{u_m} = \sin(\boldsymbol{\theta})/\lambda_0$ (i.e., spatial frequencies proportional to the interference angle $\boldsymbol{\theta} = (\theta_x,\ \theta_y)$). When the phase step used in Eq. (5) is different from the real one, one can observe three orders in the D_0 component. The second row in Figs. 1(c) and 1(d) shows the spectrum of the unknown components when the phase step was $\Delta\varphi_2' = 80$ deg. The position of the additional order, which is a residual order, is located at $-\mathbf{u_m}$. Based on this observation, the following cost function was defined:

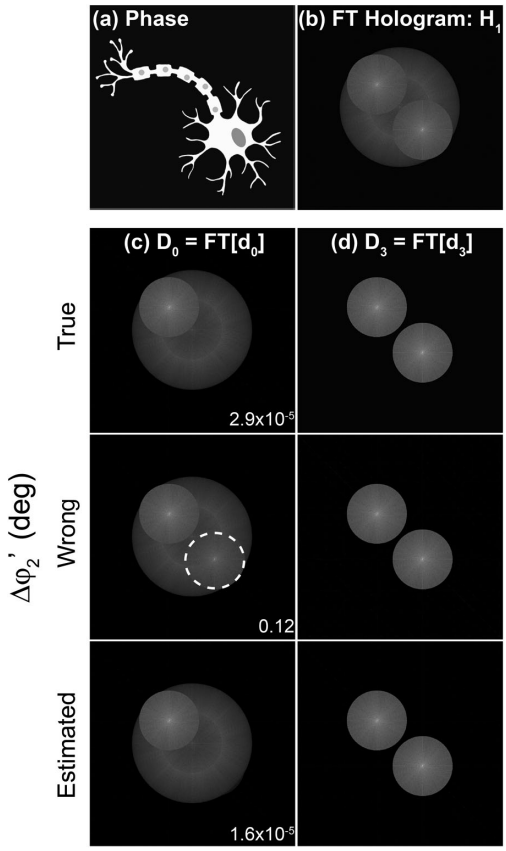

Fig. 1. Demonstration of the proposed algorithm based on the estimation of the spectral components D_0 and D_3 using two raw holograms. The panels are: (a) ground truth phase distribution of the simulated object; (b) Fourier transform of the hologram using a reference slightly tilted; (c) & (d) Fourier transform of the demodulated components using Eq. (5) for different values of the phase steps. The phase steps were 60 deg (True), 80 deg (Wrong), and 60.003 deg (Estimated), respectively. The MSE values between the D_0 components are shown in images in panel (c). Note that only when the phase step is wrong, it appears and additional order in the D_0 component.

$$J = \frac{2\,|D_0(-\boldsymbol{u}_m)|}{|D_0(\mathbf{0})| + |D_0(-\boldsymbol{u}_m)|}. \tag{6}$$

The cost function J quantifies the ratio difference between the expected central and the residual order in the estimated D_0 component. The value of the cost function Eq. (6) is reported in the first column of Fig. 1(c). If the phase step used in Eq. (6) is the correct one, then $D_0(-\boldsymbol{u}_m) = 0$, and the value of the cost function is equal to zero, $J = 0$. Note that for the particular case shown in Fig. 1(c), the cost function for the correct phases [first row in Fig. 1(d)] is almost zero, $J = 2.9 \times 10^{-5}$, whereas for $\Delta\varphi_2' = 80$ deg, the cost function is 0.12. Therefore, the utilization of a phase-step value different from the correct

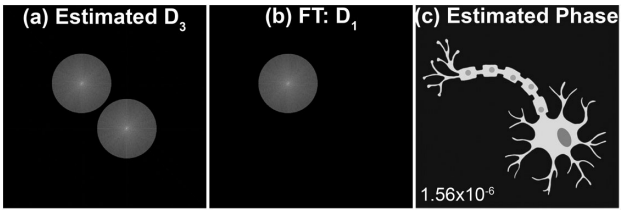

Fig. 2. Evaluation of the phase distribution estimated by the proposed method. The panels are: (a) estimated D_3 component from our method; (b) Fourier transform of the d_1 demodulated components by spatial filtering of D_3; (c) estimated phase image via inverse filtering D_1 after compensating the interference angle. The mean MSE between the true and the estimated phase images is 1.56×10^{-6}.

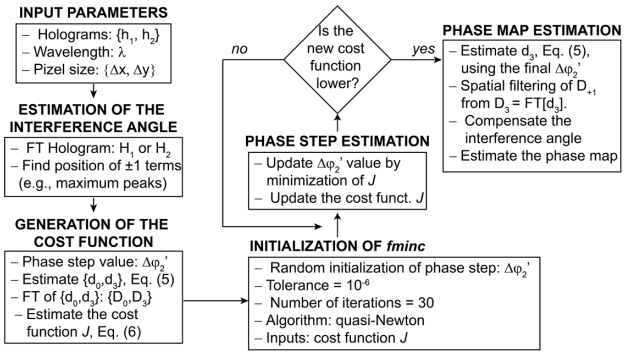

Fig. 3. Flowchart of the proposed algorithm.

one produces a higher cost function value. Note that there is a difference of the four orders of magnitude between both reported J values. This approach is based on the simultaneous estimation of both the phase step and the estimation of the unknown components by minimizing this cost function using the Matlab built-in function *fminunc*, which finds a local minimum of an unconstrained multivariable function using a quasi-Newton algorithm. The input parameters of the *fminunc* function are the cost function [Eq. (6)], an initial phase step, which is a random value between 0–360 deg generated using the Matlab built-in function *randi*, and a set of optimization options. In this algorithm, the input parameters of the cost function are the two recorded holograms and the positions of the expected and residual orders in the Fourier spectrum. The optimization options are the maximum number of iterations allowed and a termination tolerance on the cost function. The tolerance has been set up to 10^{-6}, which is the default value, since a lower tolerance value does not lead to improved results. Although up to 30 iterations were allowed, it did not take more than 8 iterations in the simulated data. Experimentally, the maximum number of iterations was 4. It is important to mention that this work does not provide a rigorous study of these optimization options, and the selection of a different algorithm and optimization options may yield better results. The last row in Fig. 1(c) shows the estimated unknown components provided by our method. The estimated phase step was $\Delta\varphi_2' = 60.003$ deg (difference error of 5×10^{-3}% compared with the real value) and the value of the cost function was almost zero, $J = 1.6 \times 10^{-5}$.

Once one has estimated both unknown components, one discards the d_0 component since the complex object information is only encoded on the d_3 component. In fact, the d_3 component contains both the real (d_{+1}) information and the virtual (d_{-1}) information of the object, as seen in Eq. (4). Figure 2 shows the steps to reconstruct the phase distribution of the object. These steps consist of the spatial filtering of the d_{+1} component, the compensation of the tilt angle introduced by the reference wave, and, finally, the computation of the angle of the resultant image. It is important to mention that this approach is suitable for slightly off-axis DHM systems in which the interference angle is such that there is no overlap between the $d_{\pm 1}$ components. The quality of the estimated phase is quantified by the mean-square error (MSE) between the true phase map and the estimated phase map. This error is reported in Fig. 2(c), and it was computed using the Matlab *built-in* function *immse*. Note that the value of the MSE is 1.56×10^{-6}. The flowchart of the proposed algorithm is shown in Fig. 3. Currently, upon request, the implementation of the proposed approach in Matlab and Python can be shared. In the future, these approaches will be publicly available.

Testing the validity of the proposed method using two holograms was completed by estimating the MSE value between the true and estimated phase maps after running the proposed method 20 times. The only difference between the realizations is the initialization of the phase steps, which is a random value between 0–360 deg. While the true phase step was 60 deg, the estimated phase-step (mean ± standard deviation) value obtained by minimizing the proposed cost function was (60.0028 ± 0.0004) deg, showing high accuracy of the calculated phase step. There is an error difference of 4.7×10^{-3} % between the estimated phase step and the ground truth. This accurate estimation of the phase-step results on well-estimated phase images, as quantified by the maximum value of the correlation coefficient (a value of 1 computed using the Matlab *built-in* function *corr2* between the true and estimated phase maps) and the small values of the MSE error (mean $= 1.6 \times 10^{-6}$; and standard deviation $= 2 \times 10^{-22}$). Note that the small value of the standard deviation in the MSE value is correlated with the repeatability of the proposed method. Regarding the processing time, the computing time was 9.3 ± 1.4 s (mean ± standard deviation) for a phase image of 1024×1024 pixels and a Windows-based i7-6700 CPU (3.40 GHz) 16.0 GBytes RAM desktop computer. By comparing with the previous three-hologram-based blind PS-DHM algorithm [27], the proposed method is 8.6 × faster in the processing time. The average computing time has been reduced from 80 s [27] to 9.3 s. It is important to mention that although the MSE error of the simulated-reconstructed phase image is smaller when one uses the algorithm of Ref. [27] (i.e., three instead of two recorded holograms), which is 3.87×10^{-12} compared to 1.6×10^{-6}, the experimental results of the following section show that this difference is not observable. In addition, a simulation study was conducted to investigate the influence of the phase step in the proposed two-frame blind PS algorithm. For this study, the true phase step was changed from 5 deg to 180 deg, in steps of 5 deg. The error difference between the calculated phase step and the true value was

Table 1. Performance of the Proposed Algorithm under Noise Conditions: SNR, $\Delta\varphi_2'$, $\Delta\varphi_3'$ and MSE.[a]

SNR (dB)	$\Delta\varphi_2'$ (deg)	MSE $\times 10^{-5}$ (a.u.)
5	$60.001 \pm 4 \times 10^{-3}$	2 ± 0.6
10	$60.002 \pm 1.7 \times 10^{-3}$	1.1 ± 0.3
15	$60.002 \pm 1.9 \times 10^{-3}$	0.61 ± 0.18
20	$60.003 \pm 6 \times 10^{-4}$	0.30 ± 0.09
25	$60.003 \pm 3 \times 10^{-4}$	0.24 ± 0.11
30	$60.003 \pm 1.8 \times 10^{-4}$	0.18 ± 0.02
35	$60.003 \pm 1.3 \times 10^{-4}$	0.157 ± 0.011
40	$60.003 \pm 7 \times 10^{-5}$	0.157 ± 0.009
45	$60.003 \pm 5 \times 10^{-5}$	0.157 ± 0.004

[a]Notation (mean ± standard deviation).

(0.0015 ± 0.0012) %, showing the high accuracy of the proposed approach to estimate the true phase step independently of its value. Again, this accurate estimation leads to well-estimated phase images with a reduced MSE value (mean $= 4.9 \times 10^{-7}$). The proposed approach was verified to work for a minimum phase step equal to 1 deg. The phase steps higher than 180 deg were not considered, since they behave the same.

Finally, the sensitivity of the proposed PS algorithm is evaluated for noisy conditions. For this study, it has been considered that the ground truth phase map [Fig. 1(a)] is distorted by noise that is described by a white Gaussian distribution. The resultant noisy phase image is generated by adding the noise map to the truth phase image. For a particular signal-to-noise ratio (SNR), 15 noisy phase images were generated by the Matlab built-in function *awgn*. Table 1 shows the estimated phase step provided by the proposed approach and the MSE value between the estimated phase image and the noisy truth map. The true phase step was again 60 deg. With the proposed approach, the lowest and highest error difference between the true and estimated phase shift was 0.0017% and 0.005%, respectively. The root-mean-square error (RMSE) between the estimated phase shift and the ground truth one is 0.0026. Based on these two values, one concludes that the proposed method is quite robust under noisy conditions. Note that the similarity between the true noisy phase map and the estimated phase map is still high, with an MSE value smaller than 2×10^{-5}.

4. EXPERIMENTAL VERIFICATION

The validation of the proposed method has been performed by reconstructing two QPI targets by Benchmark Technologies. Figure 4 illustrates the optical setup of the experimental DHM system. The employed PS-DHM system was a Mach–Zehnder interferometer using a laser diode emitting at a wavelength of 535 nm (CPS532, Thorlabs) as the illuminating source. The light emerging from the laser diode was split into the reference and object waves using a beam splitter. In the object arm, a telecentric imaging system was inserted composed of an infinity-corrected $4\times/0.1$ microscope objective (MO) (Olympus) and a tube lens of a focal length of 300 mm. The utilization of a telecentric imaging system in DHM ensures that the DHM is shift-invariant [28,29] without the need of compensating any spherical phase factor on the reconstructed phase image. This imaging system generates a magnified

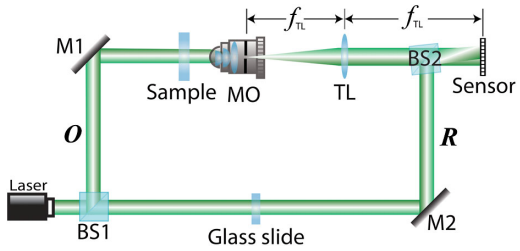

Fig. 4. Optical setup of a digital holographic microscope based on a Mach-Zehnder interferometer. The DHM system operates in the telecentric regime (the aperture stop of the MO is located at the front focal plane of the TL). The remaining components of the system are denoted as follows: BS, beam splitter; M, mirror; MO, microscope objective; TL, tube lens. The recorded holograms with the needed phase shift are recorded by rotating the glass slide, which is mounted on a rotational stage.

$6.67\times$ image of the sample under research; this lateral magnification is estimated by the ratio between the focal lengths of the TL and the MO, $M = -f_{TL}/f_{MO} = 6.67\times$. To ease the reconstruction stage, in-focus holograms were recorded by setting a CMOS camera (acA1920-25um, Basler) with 1920×1080 square pixels of a 2.4 μm pixel size at the image plane of the imaging system, which is the back focal plane of the TL. This sensor captures the optical interference between the object wave and the reference wave. It is important to mention that before the reference wave impinges on the camera, it has been reflected by a mirror (M2) and a second beam splitter (BS2). The tilt of these two elements controls the DHM configuration. These two elements were tilted to ensure that the real and virtual images of the hologram do not overlap in the Fourier domain, but these terms overlap with the D_0 component (i.e., our system operated in slightly off-axis). In the acquisition software, one can observe the effect of the tilt of these optical elements (M2 and BS2) by displaying the Fourier spectrum of the real-time hologram in the logarithmic scale. This visualization allows the adjustment of the reference angle in a time frame of 2–5 min, setting up the DHM configuration to operate in slightly off-axis mode. While the previously reported blind PS approach using three recorded holograms is suitable for any slightly off-axis DHM system [27], the proposed two-frame blind PS approach is suitable only for slightly off-axis DHM systems in which there is no overlapping between the $D_{\pm1}$ terms. However, these terms can overlap with the DC term. Experimentally, the needed arbitrary phase shift in the holograms was obtained by rotating a glass slide mounted on a rotating stage. This glass slide was inserted arbitrarily on the reference arm. The condition that the phase-shifting must differ from a multiple of 2π is experimentally satisfied by plotting a profile of the interference pattern and rotating the glass slide until the positions of the maximum intensity values have been laterally displaced. Note that one can implement different approaches to provide the required phase shifting of the holograms, such as beam splitters [26,30] or polarization elements [17,18].

In a first experiment, a USAF 1951 target was imaged. Figures 5(a) and 5(b) show one of the two holograms (h_1) needed in the algorithm and its Fourier spectrum (H_1), respectively. As the right-side panel in Fig. 5(a) shows, the holograms

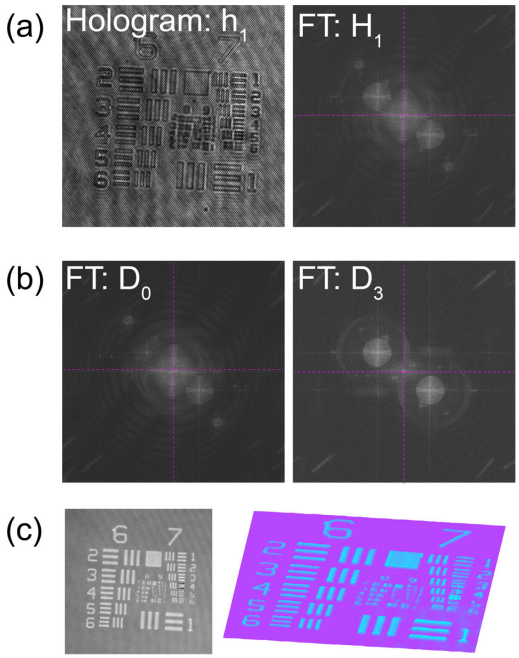

Fig. 5. Experimental validation of the proposed method. Panel (a) shows at the left-hand side of one of the recorded holograms; at the right-hand side is the corresponding spectrum of the Fourier transform of (a). Panel (b) illustrates the Fourier transforms of the two unknown components, D_0 and D_{-3}. Panel (c) shows the 2D reconstructed phase map and its 3D rendering.

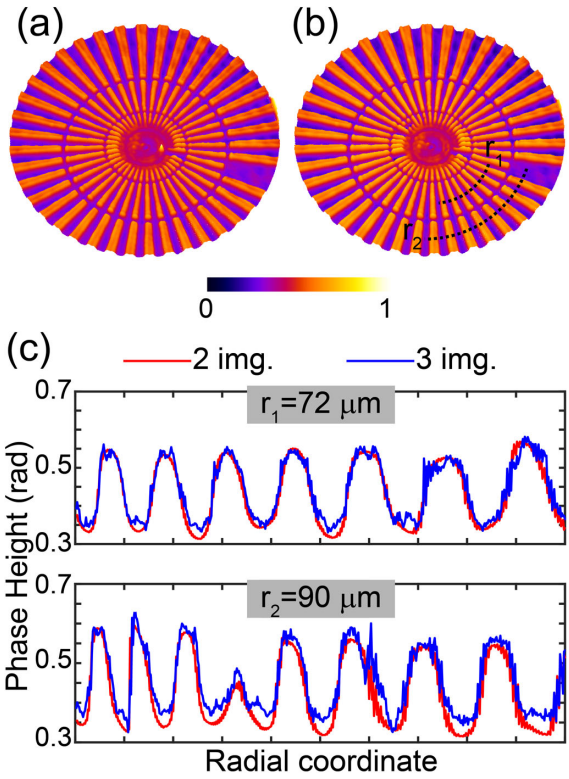

Fig. 6. Experimental comparison of the proposed method using a Star target. Panels (a) and (b) show the normalized phase image of the star using 2 holograms and 3 holograms, respectively. Panel (c) shows the phase-height profiles of the reconstructed phase maps at two different positions, $r_1 = 72$ μm and $r_2 = 90$ μm, radial positions measured from the center are marked in panel (b). In panel (c), the red and blue profiles correspond to the reconstructed phase profiles using 2 and 3 raw holograms, respectively. The area of the star is 358×358 μm^2.

were recorded by a PS-DHM system operating in slightly off-axis architecture. It was guaranteed that no overlapping occurred between the spectrum of d_{+1} and d_{-1}, so one can spatially filter the d_{+1} from the d_3 term without losing high spatial frequencies (i.e., high-resolution images should be reconstructed). Figure 5(b) shows the Fourier transforms of the estimated unknown components, D_0, and D_3, using the proposed method. It is important to mention that the algorithm only required a maximum of four iterations for successfully determining both D_0 and D_3. The dashed light-purple lines in each Fourier transform indicate the center of the Fourier spectrum. From the results of the method is found that the phase shift between both recorded holograms is 146.78°. Once one has estimated the D_3 component, one can filter the D_{+1} term and compensate for the interference angle introduced by the titled reference wave. After these two processes, the reconstructed 2D phase image and its 3D rendering are shown in Fig. 5(c). Clearly, Fig. 5(c) shows the good quality of the reconstructed information being able to distinguish up to the three vertical bars in element 5 of group 7, which corresponds to a separation of 2.461 μm, thus being the experimental resolution limit. Note that there is a high agreement between the experimental value and the Sparrow resolution limit of the experimental imaging system, defined by $0.47\lambda/\mathrm{NA} = 2.50$ μm being NA, the numerical aperture of the MO lens [31]. The resolution limit could be improved by using a MO lens with a higher NA. The goodness of the proposed blind two-frame PS algorithm is not affected by the choice of the MO lens. The performance of the proposed approach has been validated using a high-NA DHM system by reconstructing human red blood cells (RBCs) [32].

Finally, a second experiment is aimed to validate the accuracy of the proposed method of blind PS-DHM approach using two phase-shifted holograms, through the comparison of the recently published blind PS-DHM method that uses three phase-shifted holograms [27]. For this comparison, the QPI star target from Benchmark Technologies was selected. After applying the corresponding algorithms, the phase steps were estimated as: $\Delta\varphi_2' = 274.52°$ for the proposed method and $\Delta\varphi_2' = 273.89°$ and $\Delta\varphi_3' = 179.16°$ for the method reported in Ref. [27]. Note that the MSE value between both estimated $\Delta\varphi_2'$ is 0.4, corresponding to an error difference of 0.23%. Panels (a) and (b) in Fig. 6 show the reconstructed normalized phase images provided by both approaches. Note that each phase map has been normalized by each map's maximum and minimum values. Clearly, there is a high similarity between both retrieved phase maps. This high similarity is verified by the high correlation coefficient (correlation coefficient = 0.97) and the low value of the MSE (MSE value $= 4.3 \times 10^{-2}$) between both images. The high agreement of both methods is also verified by comparing the measured phase heights at different spatial distances of the object (marked by dashed black lines). The profiles for two different radial distances from the star's center (radii equal to 70 μm and 90 μm) are shown in Fig. 6(c). From an observation of these profiles, one can conclude that

there is a nearly perfect overlap between both estimated phase-height profiles regardless the object's frequency. Therefore, the accuracy of the proposed algorithm is demonstrated against the previous one that requires three phase-shifted holograms [27]. In addition, it is important to mention that the processing time has been reduced from 52 s [27] to 13 s, resulting in an experimental reduction of the processing time by a factor of 4. Thereby, the proposed method requires both a smaller number of phase-shifted holograms and less processing time, becoming a PS-DHM approach more suitable for live imaging and video-rate QPI visualization. Finally, the phase map of the star target was estimated using the approach described in Ref. [17] and the estimated phase step from this method as the global phase value. The correlation coefficient between the estimated phase map presented here [Fig. 6(a)] and the one obtained by Ref. [17] was 0.99, verifying the high similarity of the phase step.

5. CONCLUSIONS

In this work, a fast-iterative PS-DHM method based on the demodulation of the different components of phase-shifted holograms was presented. The proposed blind method only uses two-frame holograms with arbitrary phase shift. The main advantage of the proposed method is the reduction in both the acquisition and computation time; the final phase image is restored using 33% fewer data since only two phase-shifted holograms are needed, as opposed to the standard three-frame PS algorithms. The processing time of the proposed approach was compared to the previous three-frame approach reported in Ref. [27]. The simulated and experimental results show that the processing time has been improved by a factor of 8.6 and 4 times, respectively, without reducing the phase reconstruction accuracy. The only requirement of this approach is that the PS-DHM system should operate in slightly off-axis regime without overlapping of the spectrum of the ± 1 terms. Regarding the limitation of the proposed algorithm in terms of the intensity between the object and reference beams, it is predicted that the proposed algorithm will always work as far as the maximum peaks of the $D_{\pm 1}$ terms in the hologram spectrum are distinguishable. Some preliminary simulated results (not shown here) confirm that the proposed blind PS approach is suitable for an amplitude difference of $20\times$ between the object and reference beams, which provides a hologram with fringes' contrast as low as 0.1. A more detailed investigation of this difference will be reported in future work. The simulated and experimental results show that the proposed approach provides accurate quantitative phase images paving the route for video-rate PS-DHM in live and material sciences.

Funding. University of Memphis.

Disclosures. The authors declare no conflicts of interest.

REFERENCES

1. G. Popescu, *Quantitative Phase Imaging of Cells and Tissues* (McGraw Hill Professional, 2011).
2. M. K. Kim, *Digital Holographic Microscopy. Principles, Techniques, and Applications* (Springer, 2011).
3. A. Asundi, *Digital Holography for MEMS and Microsystem Metrology* (Wiley, 2011).
4. E. Cuche, F. Bevilacqua, and C. Depeursinge, "Digital holography for quantitative phase-contrast imaging," Opt. Lett. **24**, 291–293 (1999).
5. E. Cuche, P. Marquet, and C. Depeursinge, "Simultaneous amplitude-contrast and quantitative phase-contrast microscopy by numerical reconstruction of Fresnel off-axis holograms," Appl. Opt. **38**, 6994–7001 (1999).
6. U. Schnars and W. Jüptner, "Direct recording of holograms by a CCD target and numerical reconstruction," Appl. Opt. **33**, 179–181 (1994).
7. E. Cuche, P. Marquet, and C. Depeursinge, "Spatial filtering for zero-order and twin-image elimination in digital off-axis holography," Appl. Opt. **39**, 4070–4075 (2000).
8. J.-P. Liu and T.-C. Poon, "Two-step-only quadrature phase-shifting digital holography," Opt. Lett. **34**, 250–252 (2009).
9. T. Tahara, R. Otani, Y. Arai, and Y. Takaki, "Multiwavelength digital holography and phase-shifting interferometry selectively extracting wavelength information: phase-division multiplexing (PDM) of wavelengths," in *Holographic Materials and Optical Systems* (2017), p. 205.
10. M. Rivera, O. Dalmau, A. Gonzalez, and F. Hernandez-Lopez, "Two-step fringe pattern analysis with a Gabor filter bank," Opt. Lasers Eng. **85**, 29–37 (2016).
11. J. Vargas, J. A. Quiroga, T. Belenguer, M. Servín, and J. C. Estrada, "Two-step self-tuning phase-shifting interferometry," Opt. Express **19**, 638–648 (2011).
12. J. Vargas, J. A. Quiroga, C. O. S. Sorzano, J. C. Estrada, and J. M. Carazo, "Two-step interferometry by a regularized optical flow algorithm," Opt. Lett. **36**, 3485–3487 (2011).
13. J. Vargas, J. A. Quiroga, C. O. S. Sorzano, J. C. Estrada, and J. M. Carazo, "Two-step demodulation based on the Gram–Schmidt orthonormalization method," Opt. Lett. **37**, 443–445 (2012).
14. J. Deng, H. Wang, F. Zhang, D. Zhang, L. Zhong, and X. Lu, "Two-step phase demodulation algorithm based on the extreme value of interference," Opt. Lett. **37**, 4669–4671 (2012).
15. V. H. Flores, A. Reyes-Figueroa, C. Carrillo-Delgado, and M. Rivera, "Two-step phase shifting algorithms: where are we?" Opt. Laser Technol. **126**, 106105 (2020).
16. J. Han, P. Gao, B. Yao, Y. Gu, and M. Huang, "Slightly off-axis interferometry for microscopy with second wavelength assistance," Appl. Opt. **50**, 2793–2798 (2011).
17. P. Gao, B. Yao, J. Min, R. Guo, J. Zheng, T. Ye, I. Harder, V. Nercissian, and K. Mantel, "Parallel two-step phase-shifting point-diffraction interferometry for microscopy based on a pair of cube beamsplitters," Opt. Express **19**, 1930–1935 (2011).
18. P. Gao, B. Yao, I. Harder, J. Min, R. Guo, J. Zheng, and T. Ye, "Parallel two-step phase-shifting digital holograph microscopy based on a grating pair," J. Opt. Soc. Am. A **28**, 434–440 (2011).
19. N. T. Shaked, Y. Zhu, M. T. Rinehart, and A. Wax, "Two-step-only phase-shifting interferometry with optimized detector bandwidth for microscopy of live cells," Opt. Express **17**, 15585–15591 (2009).
20. X. F. Meng, L. Z. Cai, Y. R. Wang, X. L. Yang, X. F. Xu, G. Y. Dong, X. X. Shen, and X. C. Cheng, "Wavefront reconstruction by two-step generalized phase-shifting interferometry," Opt. Commun. **281**, 5701–5705 (2008).
21. W. T. Hsieh, M. K. Kuo, H. F. Yau, and C. C. Chang, "A simple arbitrary phase-step digital holographic reconstruction approach without blurring using two holograms," Opt. Rev. **16**, 466–471 (2009).
22. C.-C. Chang, W. T. Hsieh, and M. K. Kuo, "Digital holography with arbitrary phase-step reconstruction using multiple holograms," Proc. SPIE **7358**, 735813 (2009).
23. X. Yu, R. Song, X. Li, P. Jiang, K. Wang, Z. Zhang, and T. Shen, "Accurate blind extraction of arbitrary unknown phase shifts by an improved quantum-behaved particle swarm optimization in generalized phase-shifting interferometry," OSA Continuum **2**, 3404–3414 (2019).
24. C.-S. Guo, B.-Y. Wang, B. Sha, Y.-J. Lu, and M.-Y. Xu, "Phase derivative method for reconstruction of slightly off-axis digital holograms," Opt. Express **22**, 30553–30558 (2014).
25. M. Trusiak, J.-A. Picazo-Bueno, K. Patorski, P. Zdańkowski, and V. Mico, "Single-shot two-frame π-shifted spatially multiplexed interference phase microscopy," J. Biomed. Opt. **24**, 096004 (2019).

26. J. A. Picazo-Bueno, M. Trusiak, and V. Micó, "Single-shot slightly off-axis digital holographic microscopy with add-on module based on beamsplitter cube," Opt. Express **27**, 5655–5669 (2019).
27. A. Doblas, C. Buitrago-Duque, A. Robinson, and J. Garcia-Sucerquia, "Phase-shifting digital holographic microscopy with an iterative blind reconstruction algorithm," Appl. Opt. **58**, G311–G317 (2019).
28. A. Doblas, E. Sánchez-Ortiga, M. Martínez-Corral, G. Saavedra, P. Andrés, and J. Garcia-Sucerquia, "Shift-variant digital holographic microscopy: inaccuracies in quantitative phase imaging," Opt. Lett. **38**, 1352–1354 (2013).
29. A. Doblas, E. Sánchez-Ortiga, M. Martínez-Corral, G. Saavedra, and J. Garcia-Sucerquia, "Accurate single-shot quantitative phase imaging of biological specimens with telecentric digital holographic microscopy," J. Biomed. Opt. **19**, 046022 (2014).
30. M. León-Rodríguez, J. A. Rayas, R. R. Cordero, A. Martínez-García, A. Martínez-Gonzalez, A. Téllez-Quiñones, P. Yañez-Contreras, and O. Medina-Cázares, "Dual-plane slightly off-axis digital holography based on a single cube beam splitter," Appl. Opt. **57**, 2727–2735 (2018).
31. A. Lipson, S. G. Lipson, and H. Lipson, *Optical Physics* (Cambridge University, 2010).
32. C. Trujillo, A. Doblas, G. Saavedra, M. Martínez-Corral, and J. García-Sucerquia, "Phase-shifting by means of an electronically tunable lens: quantitative phase imaging of biological specimens with digital holographic microscopy," Opt. Lett. **41**, 1416–1419 (2016).

Research Article Vol. 58, No. 34 / 1 December 2019 / Applied Optics G11

Non-approximated Rayleigh–Sommerfeld diffraction integral: advantages and disadvantages in the propagation of complex wave fields

Carlos Buitrago-Duque and Jorge Garcia-Sucerquia*

School of Physics, Universidad Nacional de Colombia—Sede Medellin, A.A: 3840, Medellin 050034, Colombia
**Corresponding author: jigarcia@unal.edu.co*

Received 19 June 2019; revised 28 July 2019; accepted 29 July 2019; posted 29 July 2019 (Doc. ID 370601); published 4 September 2019

Advantages and disadvantages of the non-approximated numerical implementation of the Rayleigh–Sommerfeld diffraction integral (RSD) are revisited. In this work, it is shown that as trade-off for its large computation load, the non-approximated RSD removes any limitation on the propagation range and does not introduce any artifact in the computed wave field. A non-approximated GPU implementation of the RSD is contrasted with the angular spectrum, the Fresnel transform, and a fast Fourier transform implementation of the RSD. The forecasted phase shift introduced in the propagated wave fields as light is diffracted on complementary apertures and utilized as a metric to quantify the performance of the tested methods. An application to numerical reconstructions with arbitrary shape and size of digital recorded holograms from digital lensless holographic microscopy is presented.

https://doi.org/10.1364/AO.58.000G11

1. INTRODUCTION

The most striking current applications of optics rely on the numerical propagation of wave fields. Numerical reconstruction of digitally recorded holograms, coined digital holography [1,2], digital holographic microscopy (DHM) [3,4], Fourier ptychographic imaging [5,6], compressive sensing [7], optical encryption [8,9], computer-generated holograms [10], and numerical compensation of aberrations in optical systems [11], can be named as examples. For these types of applications, the numerical propagation of complex wave fields takes place in isotropic and homogeneous media, hence a scalar theory fully describes the physical phenomenon.

The Helmholtz equation encompasses the scalar theory of wave fields propagation [12]. In ideal problems, the Helmholtz equation is analytically solved by using different assumptions that lead to the methods of angular spectrum (AS) [13], Rayleigh–Sommerfeld and Fresnel–Kirchhoff diffraction formulae [12], to name some of them. For real applications, as those mentioned in the above paragraph, it is necessary to resort to numerical implementations to compute the propagation of wave fields. These numerical propagation methods are made technologically attractive by casting them into the form of discrete Fourier transforms, which can be computed via a fast Fourier transform algorithm [14]. Similarly, as for the case of the analytical solutions, the numerical propagation methods are meant to provide a tool for propagating wave fields from the very aperture to infinity. However, due to the use of Fourier's formalism, the correct sampling of the terms involved in the computation has to be guaranteed, which introduces limitations on the range of validity of the different methods of numerical propagation [15–18].

Among the multiple methods of numerical propagation of wave fields, up to the best knowledge of the authors, there is no reported use of the non-approximated, non-Fourier implemented Rayleigh–Sommerfeld diffraction (RSD) integral. Most of the publications that make use of the RSD, utilize its convolution implementation [15,19–21], which bounds the pixel size at the input and output planes to be equal, and limits its applicability range; a different approach utilizes an innovative sampling scheme to remove the said limitation in the computation of non-paraxial scalar diffracted wave fields [22]. In this paper, the use of the non-approximated, non-Fourier implemented RSD for the numerical calculation of propagated wave fields is revisited. Despite its large computational complexity, it is shown that its implementation under the GPGPU programing paradigm makes its use technologically feasible, providing a limitless propagation range between the very aperture and infinity, along with the capability of using input and output planes with arbitrary and independent shape, size, and orientation.

2. PROPAGATION OF WAVE FIELDS

The propagation of vector wave fields is fully described by means of the wave equation [12]. When the electromagnetic wave propagates through an isotropic and homogeneous medium, at low numerical apertures (NAs) with no coupling

of the energy from different polarization states, and the technique of separation of variables is used to derive the time-independent solution to the wave equation, the latter turns into the Helmholtz equation:

$$\left(\frac{\partial^2}{\partial x^2}+\frac{\partial^2}{\partial y^2}+\frac{\partial^2}{\partial z^2}+k^2\right)U(x,y,z)=0, \tag{1}$$

where $k=2\pi/\lambda$ is the wavenumber, with λ the wavelength of the electromagnetic scalar wave field $U(x,y,z)$. This equation can be solved with different methods [13]; the AS and RSD formula are some of the possible solutions to describe the propagation of scalar wave fields. Although both approaches can be utilized to describe the propagation of wave fields, only in very few cases it is possible to find a fully analytical solution; therefore, the finding of propagated wave fields mainly relies on numerical results from a diffraction integral that is derived from the Helmholtz equation [2,23].

The approach to solve Helmholtz equation via the AS is supported on considering a decomposition of the scalar wave field $U(x,y,z)$ in terms of plane waves traveling with cosine directors $\alpha_x=\lambda f_x$, $\alpha_y=\lambda f_y$, and $\alpha_z=\sqrt{1-\lambda^2(f_x^2+f_y^2)}$, where f_x and f_y are the corresponding spatial frequencies. Hence, by understanding the Fourier transform as the weighting factor of a set of plane waves that synthetize a given function, the likelihood of expressing a propagated wave field within the Fourier transform framework can be indicated. Specifically, a propagated scalar wave field $U(x,y,z)$ is the result of the propagation of an input scalar wave field $U(x_0,y_0,0)$ at the input plane $(x,y,0)$. The AS of the input wave field,

$$A(f_x,f_y,0)=\int_{-\infty}^{\infty}\int_{-\infty}^{\infty}U(x_0,y_0,0)\times\exp(-i2\pi(f_xx_0+f_yy_0))\mathrm{d}x_0\mathrm{d}y_0, \tag{2}$$

is weighted by the transfer function of the free space to reach the output plane (x,y,z), yielding the AS of the propagated wave field:

$$A(f_x,f_y,z)=A(f_x,f_y,0)\exp\left(ikz\sqrt{1-\lambda^2(f_x^2+f_y^2)}\right). \tag{3}$$

Equation (3) indicates that the only waves that can be propagated to the far field are those whose spatial frequencies fulfill the condition $1/\lambda^2\geq f_x^2+f_y^2$; waves with spatial frequencies outside of this circle with radius $1/\lambda$ in the spectrum domain constitute the set of evanescent waves [13]. From Eq. (3) the propagated wave field can be therefore computed through an inverse Fourier transform,

$$U(x,y,z)=\int_{-\infty}^{\infty}\int_{-\infty}^{\infty}A(f_x,f_y,z)\exp(-2\pi(f_xx+f_yy))\mathrm{d}x\mathrm{d}y, \tag{4}$$

which in terms of the Fourier transform operator $\boldsymbol{F}\{\bullet\}$ can be readily written as

$$U(x,y,z)=\boldsymbol{F}^{-1}\left\{\boldsymbol{F}\{U(x_0,y_0,0)\}\exp\left(ikz\sqrt{1-\lambda^2(f_x^2+f_y^2)}\right)\right\}. \tag{5}$$

A different approach to solve the Helmholtz equation is to consider expressing the wave field $U(x,y,z)$ in terms of spherical wavefronts. The simplest approach to this method is the Huygens principle [12], expressing the propagated wavefront as the amplitude superposition of the spherical wavelets produced by any point on the input wavefront. A more elegant way to express the propagated wave fields in terms of spherical wavefronts is the use of Green functions and the appropriated boundary conditions [12,13]; Fresnel–Kirchhoff and Rayleigh–Sommerfeld diffraction integrals are two solutions of the Helmholtz equation within this framework with equivalent performance in terms of accuracy in the far field. The latter expresses the propagated wave field as

$$U(x,y,z)=-\frac{1}{2\pi}\int_{-\infty}^{\infty}\int_{-\infty}^{\infty}U(x_0,y_0,0)\left(ik+\frac{1}{r}\right)\times\frac{\exp(ikr)}{r}\cos\chi\mathrm{d}x_0\mathrm{d}y_0, \tag{6}$$

with $r=\sqrt{(x-x_0)^2+(y-y_0)^2+z^2}$ being the distance from one point on the input plane $(x_0,y_0,0)$ to the point on the output plane where one computes $U(x,y,z)$; χ denotes the angle between the outward normal to output plane containing (x,y,z) and the position vector directed from the point $(x_0,y_0,0)$ to the point (x_1,y_1,z), such that $\cos\chi=z/r$. On considering the explicit form of the distance r, Eq. (6) allows the understanding of the free space propagation as a linear space-invariant operation [13,24]. Hence, the convolution theorem can be used to compute the propagated wave field via Fourier transforms [20,21]:

$$U(x,y,z)=-\frac{1}{2\pi}\boldsymbol{F}^{-1}\left\{\boldsymbol{F}\{U(x_0,y_0,0)\}\boldsymbol{F}\left\{\left(ik+\frac{1}{r'}\right)\frac{\exp(ikr')}{r'}\frac{z}{r'}\right\}\right\}, \tag{7}$$

with $r'=\sqrt{x^2+y^2+z^2}$; this approach can be named the convolution RSD (CRSD). On comparing Eqs. (5) and (7) the reader can realize the direct equivalence between AS and CRSD, because the analytical expression of the last Fourier transform of Eq. (7) is exactly the propagation kernel of the AS in Eq. (5). This analytical equivalence, derived from the convolutional approach of both methods, is not evident in the numerical performance of them. This difference in performance of the AS and CRSD is due to the fact that while in the former an analytical expression of the amplitude transfer function is used, in the latter the amplitude transfer function is the numerical Fourier transform of the impulse response. This numerical Fourier transform of the impulse response introduces numerical artefacts, inherited, for instance, from data truncation, which lead to an overall different numerical performance of the analytically equivalent AS and CRSD.

A widely used method to compute propagated wave fields is the Fresnel–Fraunhofer (FF) paraxial approximation [13,23]. This approach considers a Taylor expansion of the distance r, limiting its range of application to the paraxial region where the distance z between the input and output planes fulfills the condition $z^3\gg\frac{\pi}{4\lambda}[(x_0-x)^2+(y_0-y)^2]^2_{\mathrm{MAX}}$. The propagated wave field can be computed as

$$U(x,y,z) = \frac{-i\exp(ikz)}{\lambda z}\exp\left(\frac{ik}{2z}(x^2+y^2)\right) \times \int_{-\infty}^{\infty}\int_{-\infty}^{\infty} U(x_0,y_0,0)\exp\left(\frac{ik}{2z}(x_0^2+y_0^2)\right) \times \exp\left(\frac{-ik}{z}(x_0x+y_0y)\right)\mathrm{d}x_0\mathrm{d}y_0, \quad (8)$$

where one can recognize the computation of the propagated wave field as a scaled Fourier transform:

$$U\left(\frac{x}{\lambda z},\frac{y}{\lambda z},z\right) = \frac{-i\exp(ikz)}{\lambda z}\exp\frac{ik}{2z}(x^2+y^2) \times \boldsymbol{F}\left\{U(x_0,y_0,0)\exp\frac{ik}{2z}(x_0^2+y_0^2)\right\}. \quad (9)$$

The equations presented above to compute the propagated wave fields must be numerically implemented to their practical use.

3. NUMERICAL CALCULATION OF WAVE FIELDS PROPAGATION

The numerical calculation of the wave fields propagation requires the complete discretization of the expression for its computation; input and output planes, either in spatial or spatial frequency coordinates, the known input wave field $U(x_0,y_0,0)$, and the propagation kernels that can include the Fourier transform operator, have to be discretized. The set of constraints on data sampling and propagation kernels are analyzed elsewhere [22,25–27].

The procedure is illustrated with the discretization of the numerical computation of the propagated wave fields via the AS, namely Eq. (5). The continuous spatial coordinates at the input plane are discretized on a rectangular grid with pixel size $\Delta x_0 \times \Delta y_0$, such that $x_0 = m\Delta x_0$ and $y_0 = n\Delta y_0$, m and n being integer numbers; correspondingly for the output plane $x = p\Delta x$ and $y = q\Delta y$, with p and q integer numbers. Accordingly, the spatial frequencies are also discretized as $f_x = r\Delta f_x$ and $f_y = s\Delta f_y$. By introducing these discretizations on Eq. (5), the propagated wave field is computed as

$$U(p\Delta x,q\Delta y,z) = \sum_{r=1}^{R}\sum_{s=1}^{Q} A(r\Delta f_x,s\Delta f_y,0)\exp(i\mu z) \times \exp\, i2\pi(p\Delta x r\Delta f_x + q\Delta y s\Delta f_y)\Delta f_x\Delta f_y, \quad (10)$$

with $\mu = 2\pi/\lambda\sqrt{1-\lambda^2((r\Delta f_x)^2+(s\Delta f_y)^2)}$ being the transfer function, R and Q the number of pixels along each direction of the output plane, and the AS of the input wave field

$$A(r\Delta f_x,s\Delta f_y,0) = \sum_{m=1}^{M}\sum_{n=1}^{N} U(m\Delta x_0,n\Delta y_0,0) \times \exp -i2\pi(m\Delta x_0 r\Delta f_x + n\Delta y_0 s\Delta f_y)\Delta x_0\Delta y_0, \quad (11)$$

where M and N are the number of pixels along each direction of the input plane. For the particular case of square input and output planes, the computation complexity of Eq. (10) is $\bigcirc(M^2\times R^2)$. The casting of the Fourier transform operator $\boldsymbol{F}\{\bullet\} = \sum_m\sum_n \bullet \exp -i2\pi(m\Delta x_0 r\Delta f_x + n\Delta y_0 s\Delta f_y)$ into a discrete Fourier transform kernel $\mathrm{DFT}\{\bullet\} = \sum_m\sum_n \bullet \exp -i2\pi(mr/M + ns/N)$, reduces that computational complexity to $\bigcirc(2\times M\log M\times R\log R)$. This casting imposes $\Delta x_0\Delta f_x = 1/M$ and $\Delta y_0\Delta f_y = 1/R$ such that the propagated wave field via the AS yields

$$U(p\Delta x,q\Delta y,z) = \frac{1}{MR}\mathrm{DFT}^{-1}\left[\begin{array}{l}\mathrm{DFT}[U(m\Delta x_0,n\Delta y_0,0)] \\ \times\exp\left(iz\frac{2\pi}{\lambda}\sqrt{1-\lambda^2\left(\left(\frac{r}{M\Delta x_0}\right)^2+\left(\frac{s}{N\Delta y_0}\right)^2\right)}\right)\end{array}\right]. \quad (12)$$

The use of the formalism of the AS imposes that the size of the pixels at the output plane equals that of the input plane. This feature limits the possibility of producing a magnification of the propagated wave field with respect to the input one. As for providing the AS with magnification, variations to the description above presented can be found in the literature, which include, for instance, zero padding [28–30] or the use of a chirp z transform operation [22].

In particular interest for the present work is the discretization of the RSD Eq. (6); the direct discretization leads to

$$U(p\Delta x,q\Delta y,z) = -\frac{1}{2\pi}\sum_{m=1}^{M}\sum_{n=1}^{N} U(m\Delta x_0,n\Delta y_0,0)\left(ik+\frac{1}{r}\right) \times \frac{\exp(ikr)}{r}\frac{z}{r}\Delta x_0\Delta y_0, \quad (13)$$

with $r = \sqrt{(p\Delta x - m\Delta x_0)^2 + (q\Delta y - r\Delta y_0)^2 + z^2}$. This equation shows the possibility of computing one point of the propagated wave field by means of $\mathrm{O}(M\times N)$ complex-valued operations. It follows that for an output plane of $R\times Q$ pixels, the total of the complex-valued operations is $\mathrm{O}(M\times N\times R\times Q)$; this number is too large for most practical uses, rendering it to non-practical elapsed times of computing of the order of hours, which has discouraged its use in the present way. Despite this negative feature, the expression of the propagated wave field as a direct summation allows its computation over areas with size and shape chosen completely at will, which can sensibly reduce the computation elapsed time.

As was already pointed out in the result of Eq. (7), the distance between the output and the input points of calculation allows the computation of the propagated wave fields via a convolution operation [15,19,20]. Indeed, this approach to the computation of the propagated wave field is quite similar to the AS, with the difference that in this case the transfer function is numerically computed via a Fourier transform. Consequently, the complete calculation can be casted to discrete Fourier transforms to use FFTs and therefore the size of the input and output planes has to be equal:

$$U(p\Delta x,q\Delta y,z) = -\frac{1}{2\pi MR}\mathrm{DFT}^{-1}\left[\begin{array}{l}\mathrm{DFT}[U(m\Delta x_0,n\Delta y_0,0)] \\ \times\mathrm{DFT}\left[\left(ik+\frac{1}{r}\right)\frac{\exp(ikr)}{r}\frac{z}{r}\right]\end{array}\right]. \quad (14)$$

With respect to the AS approach, this convolution method exhibits a larger computational complexity of $\circ(3\times M\log M\times R\log R)$. Also, as is the case for the AS, different methods have been proposed in the literature to allow the propagated wave fields to have a different scale size than those of the input wave fields [31,32].

A similar procedure of discretization can be applied to the calculation of the propagated wave fields by means of the FF, Eq. (9). The details can be read elsewhere [15,23], with the result being

$$U\left(\frac{p\Delta x}{\lambda z},\frac{q\Delta y}{\lambda z},z\right)=\frac{-i\exp(ikz)}{\lambda z}\exp\frac{ik}{2z}\left(\left(\frac{p\lambda z}{M\Delta x_0}\right)^2+\left(\frac{q\lambda z}{N\Delta y_0}\right)^2\right)\times\mathrm{DFT}[U(m\Delta x_0,n\Delta y_0,0)\times\exp\frac{ik}{2z}[(m\Delta x_0)^2+(n\Delta y_0)^2]\Delta x_0\Delta y_0]. \tag{15}$$

Equation (15) has the particular feature that the pixel size at the output plane is determined by the experiment conditions such that $\Delta x=\lambda z/M\Delta x_0$ and $\Delta y=\lambda z/N\Delta y_0$. The last figures mean that for a given propagation distance z, there is a fixed size relation between the input and output planes; this limitation has been alleviated by different approaches [33–35]. In terms of its computational complexity for square input and output planes it is reduced to $\circ(M\log M\times R\log R)$, approximately the half of that required for the AS method.

4. RANGE OF VALIDITY FOR NUMERICAL IMPLEMENTATIONS OF SCALAR DIFFRACTION

In terms of the propagation distance, the analytical formulae for computing propagated wave fields presented in Section 2 are valid from the very aperture placed at the input plane to the infinity. However, as their numerical implementations are computed via the formalism of the Fourier transform, the sampling theorem for all the involved terms has to be fulfilled [15]. The correct sampling introduces constrains that relate the illuminating wavelength, the size and number of pixels at the input plane, and the propagation distance. In turn, the latter is no longer valid from the very aperture to the infinity; rather the range of validity of the propagation distance is restricted for the different methods to guarantee the correct sampling. By examining the number of pixels required to sample a π-phase jump at the largest spatial frequency in all the methods, one can find a critical distance that splits the range of valid use of each approach. This condition of the phase jump sampling is expressed for the largest spatial frequency as

$$\frac{\lambda}{2Z_c}\geq\left[\sqrt{1-\lambda^2\left(\frac{1}{2\Delta x_0}\right)^2}-\sqrt{1-\lambda^2\left(\frac{M/2-1}{M\Delta x_0}\right)^2}\right], \tag{16}$$

where M is the number of pixels along the x-direction and Δx_0 its pixel size. Considering the Taylor's expansion of the square root and some direct algebra, one arrives to the result that constitutes an upper limit for the AS and a lower limit for FF and the CRSD. This result that provides the critical propagation distance Z_c is given by [16,17,36]

$$Z_c=\frac{M\Delta x_0^2}{\lambda}. \tag{17}$$

For the two-dimensional case a similar expression is obtained for the y-direction. Despite the wide acceptance of the former limit, it has been shown that this figure must be finely tuned. The revisited approach, obtained by sampling a 2π-phase jump with 3 pixels, leaves a gap between the application limits for the AS and the FF and CRSD [18]. The non-overlapping of the valid propagation distances supposes an additional difficulty for numerical diffraction applications, as the accuracy of the results cannot be trusted with either method inside this critical region. Owing to the non-approximated non-convolution RSD not using computation through the Fourier formalism, it is envisioned not to have the formerly said limits for the other propagation methods.

To test the range of validity of the presented methods in this work, a metric for evaluating their limits of application has been set by using Babinet's principle for complementary apertures. This principle states that the sum of the amplitudes of the diffracted wave fields produced by an obstacle $U_1(x_1,y_1,z)$ and its complementary aperture $U_2(x_1,y_1,z)$ equals that recorded when the wave field propagates in the free space $U_0(x_1,y_1,z)$ [12]. If the complementary apertures are taken in such a way that their superposition represents a circular aperture subtending an even number of Fresnel's zones in the observation plane [12], their amplitude sum in the optical axis will yield $U_1(0,0,z)+U_2(0,0,z)=0$. This last relation translates into an analytical prediction that reads $U_1(x_1,y_1,z)=-U_2(x_1,y_1,z)$; that is, the corresponding diffracted wave fields will have identical magnitude and a π-phase difference in the optical axis, regardless of the screen shape. This relation is summarized in Fig. 1 using a superposition circle with a radius of 1 mm and an intricate internal shape for the complementary apertures, as presented in the three left upper panels. The lower panels represent the wave field amplitude diffracted by each aperture illuminated by plane waves with a wavelength of 405 nm and propagated to 100 mm using a numerical implementation of FF. The amplitude superposition matches the propagation of the circular aperture and displays the expected dark spot in the optical axis, zoomed-in in the right-most panel in the upper row.

The fulfilling of the aforementioned predicted phase shift can thus be taken as the metric for the range of validity of the presently studied methods. To do so, the phase difference between the numerically propagated wave fields of the complementary apertures is measured in the optical axis while the propagation distance is changed. The radius of the circular aperture is consequently modified for each distance to ensure that an even number of Fresnel's zones are being subtended. A more detailed description of this testing method can be read elsewhere [18].

This predicted phase difference is used to evaluate the range of validity of the AS, FF, RSD, and CRSD propagation methods. The results are summarized in Fig. 2, with the normalized distance against the limit proposed in literature, as presented in Eq. (17), and the phase difference normalized to the expected value (π).

The highlighted regions in Fig. 2 emphasize the ranges where negligible disturbances respect to the forecasted phase shift are achieved with each method. Unlike the others,

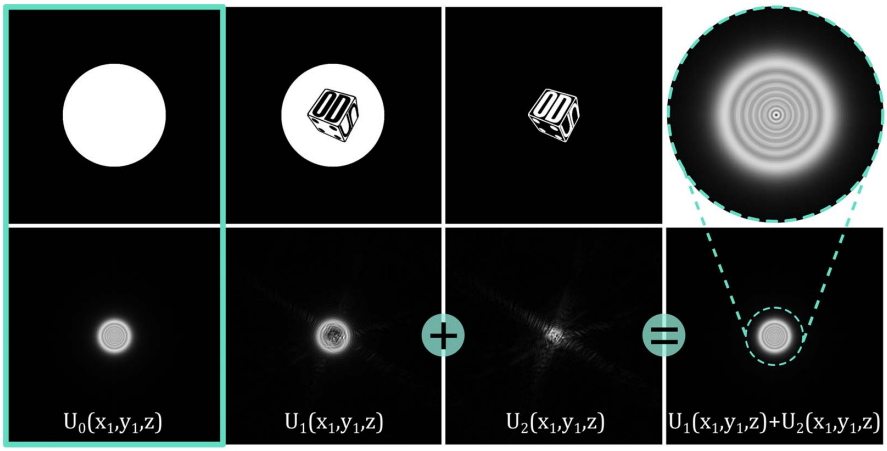

Fig. 1. Babinet's principle of complementary apertures using a circle of 1 mm as free space. The apertures in the left-most upper panels were illuminated with plane waves of 405 nm and propagated to 100 mm using Fresnel–Fraunhofer diffraction, such that the circle subtended an even number of Fresnel's zones. The sum of the obstacle's wave field U_1 and the aperture's wave field U_2 appropriately matches the free space propagation U_0 and present the expected dark spot in the optical axis shown in the right-most upper panel.

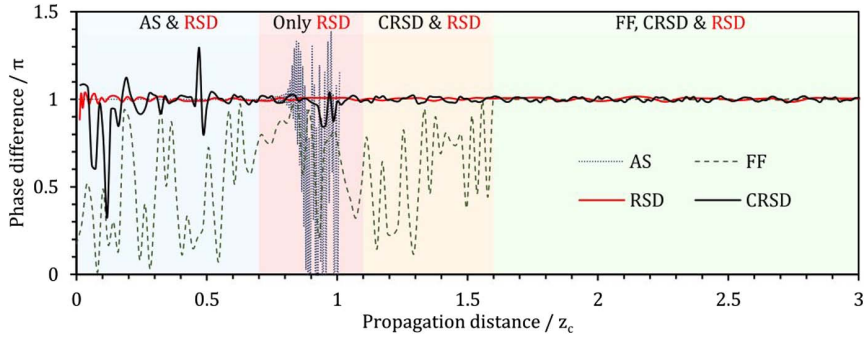

Fig. 2. Normalized phase difference of the propagated wave fields of the aperture and its complement as the propagation distance changes, with $Z_c = M\Delta x_0^2/\lambda$. The highlighted distance ranges emphasize the methods with negligible disturbances. The RSD shows an even behavior all over the propagation distance.

the RSD has no major deviations from the expected value at any point over the complete propagation distance, from the very aperture to the far field. This unique feature shows that, despite its long-elapsed time of computation, the RSD is the only propagation method that can be used all over the propagation range with no major distortion of its accuracy.

To further explore the accuracy of the propagation methods in phase retrieval, an optical pure phase wave field was numerically modeled. It was propagated near to Z_c, and backpropagated to the initial plane using each of the studied methods. Figure 3 shows the results; the modeled pure phase wave field with 1024 × 1024 pixels is illustrated in Fig. 3(a). The utilized propagation distance was $z = 61.2$ mm with $\lambda = 405$ nm and $\Delta x_0 = 5.2$ μm. The results for the AS, FF, CRSD, and RSD are shown in Figs. 3(b), 3(c), 3(d), and 3(e), respectively. All the evaluated methods but the RSD introduce distortions in the recovered phase map. The AS highly distorts the map, ruining any possibility of phase measurement. FF introduces a sort of phase tilt, and strong corruptions in the smaller details. The CRSD recovers the overall shape of the original map, but it introduces a great number of local distortions. The retrieved phase map via the use of the RSD shown in Fig. 3(e) confirms that it can recover the information entirely and to an excellent extent. No phase distortion is introduced by the RSD as it can be further seen by comparing the insets of each panel, in which a surface plot of the region bounded by the yellow square is shown.

Despite its accurate calculations and full-range applicability, the RSD has a computational complexity $O(N^4)$ for input and output planes of $N \times N$. This becomes its main setback, as even a medium-sized image needs more processing time than most practical applications may allow. It has been shown in this work that the attempts to overcome this difficulty via its implementation as a convolution CRSD present difficulties inhered from the Fourier formalism. However, to keep the calculation completely free of approximations, which renders full accuracy and range of propagations, the complexity order cannot be reduced. Nonetheless, a GPGPU implementation of the RSD can be used to increase the effective throughput and reduce the elapsed processing time. Taking advantage of the installed power in a regular computer hosting a Graphics Processing Unit GeForce GTX 580 by NVIDIA, the parallelization of the

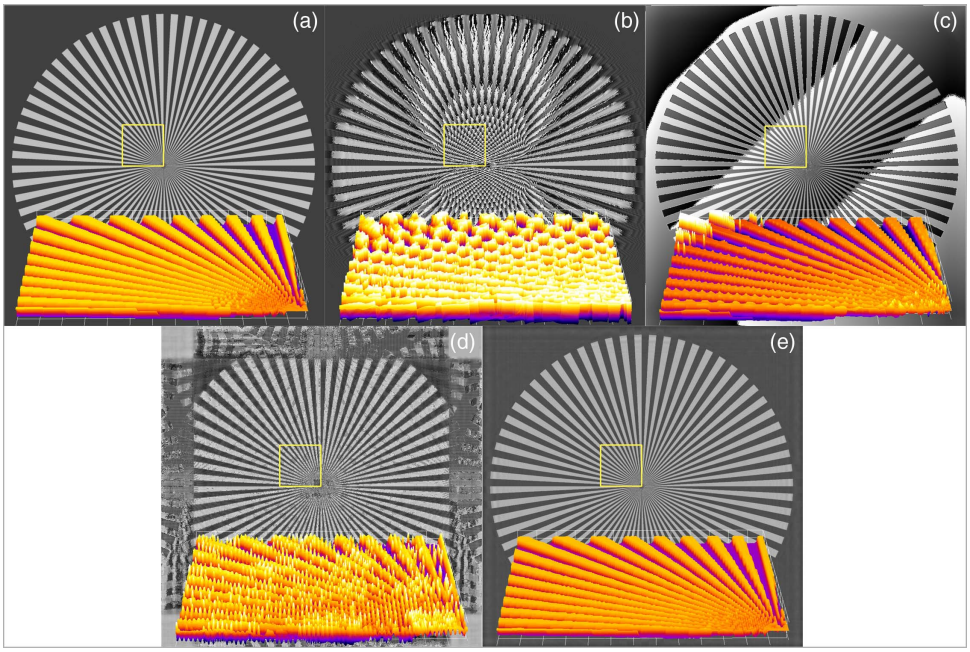

Fig. 3. Recovering of a phase object at a given distance. (a) Initial phase distribution. Recovered phase after propagating near to $Z_c = M\Delta x_0^2/\lambda$ and back using (b) angular spectrum, (c) Fresnel–Fraunhofer transform, (d) convolution Rayleigh–Sommerfeld, (e) Rayleigh–Sommerfeld diffraction integral. The insets in each panel plot the region bounded by the yellow square.

RSD can achieve a 170-time reduction of computation time compared with a regular CPU-based calculation on an Intel Core i7-2600. With this GPU-based implementation of the RSD, it turns into a full-range, full-accurate way of numerical computing diffraction integrals within technologically attractive timeframes, as can be shown in the application to numerical reconstruction of digitally recorded holograms from digital lensless holographic microscopy.

5. APPLICATION TO NUMERICAL RECONSTRUCTION OF DIGITALLY RECORDED HOLOGRAMS

Digital holographic microscopy has powered science and technology with the capability of accessing the amplitude and phase at microscopic scale. The simplest architecture available for DHM is that supported by the microscopy principle proposed by Gabor [37] implemented in the digital world. In digital lensless holographic microscopy (DLHM) [38,39] the sample is illuminated by a spherical wavefront to record on a digital camera the amplitude superposition of the unperturbed portion of the spherical wave and the light scattered by the specimen. To ensure a high spatial resolution, the holograms must be recorded with high NAs [4], which introduces an unavoidable technical difficulty for the backpropagation process that is required to retrieve the specimen information; most of the numerical propagation algorithms, as previously stated, cannot modify at will the size of the propagated wave field limiting their application to high-NA propagations.

The use of the RSD, due to its lack of approximations, allows the reconstruction of DLHM holograms without further modifications to the algorithm or the input field. For testing the use of the RSD on the reconstruction of DLHM holograms, a self-assembled monolayer of micrometer-sized polystyrene spheres was illuminated with a point-source of $\lambda = 405$ nm at a distance of 149 μm from it. On a square complementary metal–oxide–semiconductor sensor with side length of 12.3 mm located 15 mm away from the illumination source, the DLHM hologram was recorded. The reconstruction of the full-size 1024 × 1024 hologram in a CPU-based implementation of the RSD could take an overwhelming 6 days and a half of processing time, which is far from being technologically feasible. However, introducing the GPU-based implementation achieves an effective 170-fold reduction for the full-size reconstruction, diminishing the total computation time to 45 min. This resulting reconstruction in intensity is displayed in Fig. 4(a).

A further improvement in the processing time is inherited from the complete independence that the RSD allows between the size and number of points of the input and output planes. If one has a prior knowledge of the spatial distribution of the reconstructed object, gained, for instance, from a faster but approximated method, it is possible to limit the computation to a region of interest (ROI) which can be of arbitrary shape, orientation, and even contain multiple propagation distances. Taking advantage of this unique feature of the RSD, the total processing time would be proportional to the amount of points contained within the ROI, with each point being calculated in just a couple of milliseconds. Applying this idea, an unevenly shaped ROI in the destination plane was selected in the area outlined in yellow in Fig. 4(a). With the input image being 1024 × 1024 pixels in size, the individual computation of each data point in the destination plane takes around 3.5 ms; thus, for the selected ROI containing 8.6 thousand pixels, the reconstruction can be obtained in 30 s,

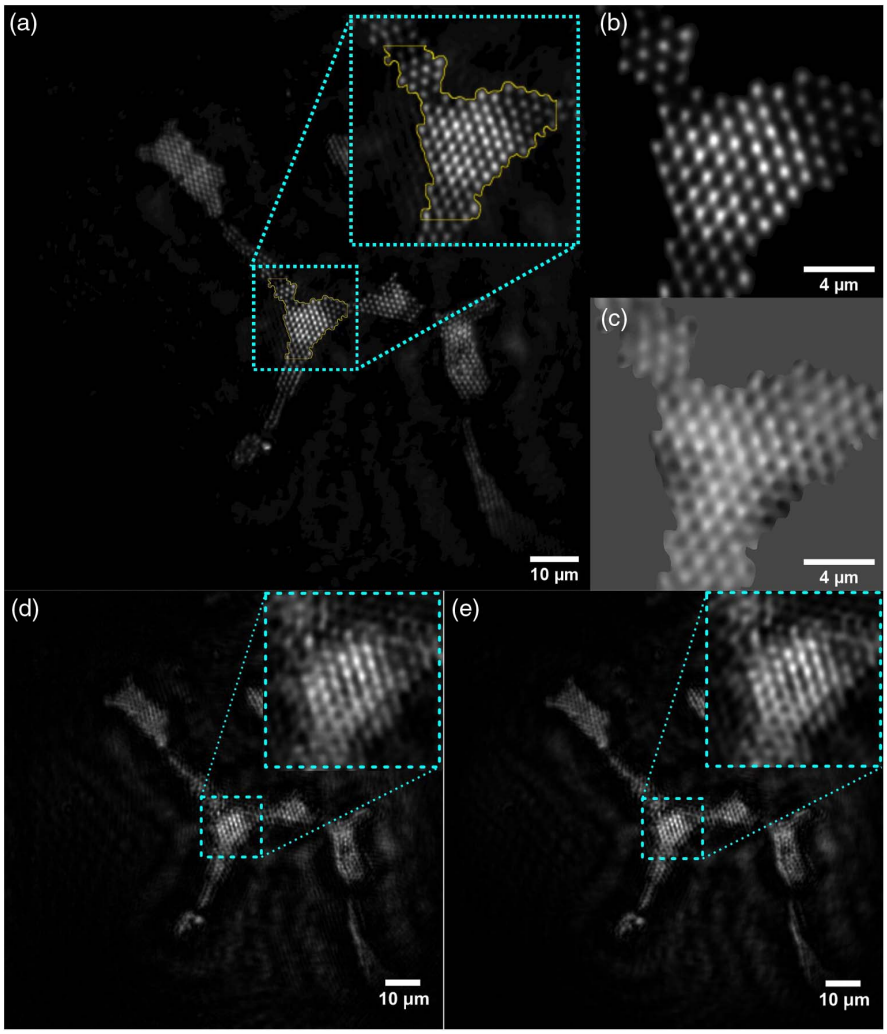

Fig. 4. Reconstruction of a DLHM hologram of a self-assembled monolayer of micrometer-sized polystyrene spheres. (a) Full-size intensity reconstruction of 1024 × 1024 hologram. The region outlined in yellow, originally bounded by 141 × 141 pixels, was independently reconstructed into a 512 × 512 image in (b) intensity and (c) phase. The same full-size DLHM hologram has been reconstructed via the AS in panel (d) and by CRSD in panel (e).

which is a technologically attractive time. Additionally, as the output plane discretization is completely independent from the input parameters in the RSD, it is possible to reconstruct this same ROI into a higher pixel count to improve the visualization quality. Figures 4(b) and 4(c) show the reconstruction in intensity and phase, respectively, in an extended version of the aforementioned ROI now containing 120 thousand pixels whose computation takes a total of approximately 4 min; as reference, the resulting image is of 512 × 512 pixels while the original ROI was bounded by a box of 141 × 141 pixels, showing another example of the freedom of computation that the RSD provides for the propagation of wave fields. To compare the performance of the RSD on the reconstruction of DLHM holograms with the results provided by the AS and CRSD, Figs. 4(d) and 4(e) present the corresponding full-size 1024 × 1024 intensity reconstructions, respectively. Contrasting panels (a), (d), and (e), one can see the superior performance of the RSD over the AS and CRSD in terms of the quality of the reconstructed images. Furthermore, the possibility of choosing at will the reconstruction area is not available for the two latter methods, indicating an extra reason to use the RSD approach for the reconstruction of this type of hologram, when the computation time has no importance.

6. CONCLUSIONS

The Rayleigh–Sommerfeld diffraction integral has been revisited within the framework of the numerical calculation of propagation of wave fields. The angular spectrum, direct non-approximated integration, convolution method, and Fresnel–Fraunhofer diffraction formula have been presented as possible solutions of the scalar Helmholtz equation. The numerical implementation of the above-said methods has also been shown to discuss some of their particular features.

An emphasis has been focused on studying the range of valid computation for each method. Based on the analysis of the correct sampling of the propagation kernel for each method, its range of use has been recalled. The validation of the range has been done by testing the Babinet´s forecasted phase shift

introduced in the diffraction patterns of complementary apertures. The results indicate that among the tested methods, the only one that reproduces the forecasted phase shift from the input to the output plane with no error is the non-approximated Rayleigh–Sommerfeld diffraction integral.

In addition to the exact calculation of the propagated wave fields, the non-approximated Rayleigh–Sommerfeld diffraction integral enables the computation between input and output planes with arbitrary size, shape, and orientation. The trade-off for all the here-mentioned features is the large computational complexity it exhibits. The use of the GPGPU programming paradigm eases the elapsed time of computing, setting the option of numerical calculation of propagated wave fields with the non-approximated Rayleigh–Sommerfeld diffraction integral within a technologically attractive framework.

The non-approximated Rayleigh–Sommerfeld diffraction integral has been applied to numerical reconstruction of digitally recorded holograms from digital lensless holographic microscopy. The reconstructed images have spatial resolution in the micrometer-size range at variable reconstruction fields of view, showing some of the versatility provided by this method of computing propagated wave fields.

Funding. Universidad Nacional de Colombia—Sede Medellin.

REFERENCES

1. U. Schnars, "Direct phase determination in hologram interferometry with use of digitally recorded holograms," J. Opt. Soc. Am. A **11**, 2011–2015 (1994).
2. P. Picart and L. Juan-chang, *Digital Holography* (Wiley, 2012).
3. E. Cuche, F. Bevilacqua, and C. Depeursinge, "Digital holography for quantitative phase-contrast imaging," Opt. Lett. **24**, 291–293 (1999).
4. M. K. Kim, *Digital Holographic Microscopy. Principles, Techniques, and Aplications* (Springer, 2011).
5. K. Giewekemeyer, M. Beckers, T. Gorniak, M. Grunze, T. Salditt, and A. Rosenhahn, "Ptychographic coherent x-ray diffractive imaging in the water window," Opt. Express **19**, 1037–1050 (2011).
6. G. Zheng, R. Horstmeyer, and C. Yang, "Wide-field, high-resolution Fourier ptychographic microscopy," Nat. Photonics **7**, 739–745 (2013).
7. P. Clemente, V. Durán, E. Tajahuerce, P. Andrés, V. Climent, and J. Lancis, "Compressive holography with a single-pixel detector," Opt. Lett. **38**, 2524–2527 (2013).
8. E. Tajahuerce and B. Javidi, "Encrypting three-dimensional information with digital holography," Appl. Opt. **39**, 6595–6601 (2000).
9. T. Nomura and B. Javidi, "Securing information using a digital holographic technique," Opt. Comput. **4089**, 619–624 (2000).
10. W. Dallas, "Computer-generated holograms," in *The Computer in Optical Research*, B. R. Frieden, ed. (Springer-Verlag, 1980), Vol. 41, pp. 291–366.
11. K. W. Seo, Y. S. Choi, E. S. Seo, and S. J. Lee, "Aberration compensation for objective phase curvature in phase holographic microscopy," Opt. Lett. **37**, 4976–4978 (2012).
12. M. Born and E. Wolf, *Principles of Optics*, 7th ed. (Cambridge University, 2005).
13. J. W. Goodman, *Introduction to Fourier Optics*, 3rd ed. (Roberts and Company Publishers, 2005).
14. M. Frigo and S. G. Johnson, "FFTW: an adaptive software architecture for the FFT," in *Proceedings of the 1998 IEEE International Conference On Acoustics, Speech and Signal Processing* (1998), Vol. **3**, pp. 1381–1384.
15. J. Li and P. Picart, "Calculating diffraction by fast Fourier transform," in *Digital Holography* (Wiley, 2012), pp. 77–114.
16. D. Mendlovic, Z. Zalevsky, and N. Konforti, "Computation considerations and fast algorithms for calculating the diffraction integral," J. Mod. Opt. **44**, 407–414 (1997).
17. D. Mas, J. Garcia, C. Ferreira, L. M. Bernardo, and F. Marinho, "Fast algorithms for free-space diffraction patterns calculation," Opt. Commun. **164**, 233–245 (1999).
18. R. Castañeda, W. Toro, and J. Garcia-Sucerquia, "Evaluation of the limits of application for numerical diffraction methods based on basic optics concepts," Optik **126**, 5963–5970 (2015).
19. J. A. C. Veerman, J. J. Rusch, and H. P. Urbach, "Calculation of the Rayleigh-Sommerfeld diffraction integral by exact integration of the fast oscillating factor," J. Opt. Soc. Am. A **22**, 636–646 (2005).
20. V. Nascov and P. C. Logofătu, "Fast computation algorithm for the Rayleigh-Sommerfeld diffraction formula using a type of scaled convolution," Appl. Opt. **48**, 4310–4319 (2009).
21. F. Shen and A. Wang, "Fast-Fourier-transform based numerical integration method for the Rayleigh-Sommerfeld diffraction formula," Appl. Opt. **45**, 1102–1110 (2006).
22. M. Hillenbrand, D. P. Kelly, and S. Sinzinger, "Numerical solution of nonparaxial scalar diffraction integrals for focused fields," J. Opt. Soc. Am. A **31**, 1832–1841 (2014).
23. O. K. Ersoy, *Diffraction, Fourier Optics and Imaging* (Wiley, 2006).
24. U. Schnars and W. Juptner, "Digital recording and numerical," Inst. Phys. Publ. **13**, 17 (2002).
25. D. G. Voelz and M. C. Roggemann, "Digital simulation of scalar optical diffraction: revisiting chirp function sampling criteria and consequences," Appl. Opt. **48**, 6132–6142 (2009).
26. D. P. Kelly, "Numerical calculation of the Fresnel transform," J. Opt. Soc. Am. A **31**, 755–764 (2014).
27. L. Onural, "Sampling of the diffraction field," Appl. Opt. **39**, 5929–5935 (2000).
28. T. Shimobaba, K. Matsushima, T. Kakue, N. Masuda, and T. Ito, "Scaled angular spectrum method," Opt. Lett. **37**, 4128–4130 (2012).
29. T. Shimobaba, Y. Nagahama, T. Kakue, N. Takada, N. Okada, Y. Endo, R. Hirayama, D. Hiyama, and T. Ito, "Calculation reduction method for color digital holography and computer-generated hologram using color space conversion," Opt. Eng. **53**, 24108 (2014).
30. T. Shimobaba, J. Weng, T. Sakurai, N. Okada, T. Nishitsuji, N. Takada, A. Shiraki, N. Masuda, and T. Ito, "Computational wave optics library for C++: CWO++ library," Comput. Phys. Commun. **183**, 1124–1138 (2012).
31. M. Leclercq and P. Picart, "Method for chromatic error compensation in digital color holographic imaging," Opt. Express **21**, 26456–26467 (2013).
32. D. Claus and J. M. Rodenburg, "Pixel size adjustment in coherent diffractive imaging within the Rayleigh–Sommerfeld regime," Appl. Opt. **54**, 1936–1944 (2015).
33. J. F. Restrepo and J. Garcia-Sucerquia, "Magnified reconstruction of digitally recorded holograms by Fresnel-Bluestein transform," Appl. Opt. **49**, 6430–6435 (2010).
34. F. Zhang, I. Yamaguchi, and L. P. Yaroslavsky, "Algorithm for reconstruction of digital holograms with adjustable magnification," Opt. Lett. **29**, 1668–1670 (2004).
35. T. Shimobaba, T. Kakue, N. Okada, M. Oikawa, Y. Yamaguchi, and T. Ito, "Aliasing-reduced Fresnel diffraction with scale and shift operations," J. Opt. **15**, 075405 (2013).
36. M. Sypek, C. Prokopowicz, and M. Gorecki, "Image multiplying and high-frequency oscillations effects in the Fresnel region light propagation simulation," Opt. Eng. **42**, 3158–3164 (2003).
37. D. Gabor, "Microscopy by reconstructed wave-fronts," Proc. R. Soc. London A **197**, 454–487 (1949).
38. W. Xu, M. H. Jericho, I. A. Meinertzhagen, and H. J. Kreuzer, "Digital in-line holography for biological applications," Proc. Natl. Acad. Sci. U. S. A. **98**, 11301–11305 (2001).
39. J. Garcia-Sucerquia, W. Xu, S. K. Jericho, P. Klages, M. H. Jericho, and H. J. Kreuzer, "Digital in-line holographic microscopy," Appl. Opt. **45**, 836–850 (2006).

Optics and Lasers in Engineering 134 (2020) 106176

Contents lists available at ScienceDirect

Optics and Lasers in Engineering

journal homepage: www.elsevier.com/locate/optlaseng

Sizing calibration in digital lensless holographic microscopy via iterative Talbot self-imaging

Carlos Buitrago-Duque, Jorge Garcia-Sucerquia*

Universidad Nacional de Colombia sede Medellín, School of Physics, A.A: 3840-Medellín-050034, Colombia

ARTICLE INFO

Keywords:
Digital lensless holographic microscopy
Length calibration
Talbot self-imaging
Monolayer
Polystyrene spheres

ABSTRACT

In this work, an iterative method to calibrate the length measurements in digital lensless holographic microscopy (DLHM) is presented. In DLHM, the correct sizing is controlled by the accurate knowledge of the illumination wavelength, the digital camera specifications, and the source-to-screen distance. While the two formers are provided by the manufacturers, the latter has to be somehow measured, usually by mechanical means. As an alternative for performing that key measurement in DLHM, the Talbot self-imaging effect, and hence the Talbot distance, is used as a measurement tool in this work. Amplitude reconstructions of a monolayer of self-organized spheres of polystyrene produce the self-imaging phenomenon, with the Talbot distance controlled by the illuminating wavelength, the reconstruction distance, and the period of the monolayer. As the latter can be varied in DLHM by changing the source-to-screen distance while keeping fixed the wavelength and the camera specifications, the source-to-screen distance is iteratively varied until the correct Talbot distance is found. The proposed method has the advantages of i) increased sensitivity because of the axial quadratic dependency on transversal measurements, ii) not requiring in-focus images that demand the use of focusing criteria, and iii) can use non-approximated propagation methods to produce axial intensity profiles to determine the correct source-to-screen distance. The feasibility of the calibration method is tested by reconstructing a USAF 1951 test of resolution.

1. Introduction

The precise and accurate sizing in microscopy is an essential feature for the screening and diagnosis of different diseases. For instance, in the detection of malaria, the quantification of the parasitemia in microscopic blood slides is a key factor that demands an accurate sizing of the microscopic structures [1]. When the imaging tool is an optical microscope, the size of the produced image of the sample is simply determined by the optical magnification of the device, leading to a direct way to measure accurately in the micrometer-sized range. The use of opto-digital imaging methods, like digital holographic microscopy [2–4] (DHM), that provide the versatility of the digital manipulation of the information demands an alternative definition of the magnification concept from the classical one, where it's simply understood as the ratio of the size of the image to that of the sample. In some architectures of DHM, like image-plane DHM [5,6] where an in-focus image of the sample is produced over the digital sensor with magnification controlled by the optical imaging system and the numerical reconstruction does not change the size of the reconstructed image, it is possible to trust the sizing reported by the imaging architecture. However, in other approaches of DHM where the numerical reconstruction stage can modify the size of the produced image, the sizing of the method has to be standardized employing calibrated samples.

Digital lensless holographic microscopy [7] (DLHM) is a DHM method in which the size of the produced image is strongly determined by the numerical reconstruction stage. While for the recording the sample is illuminated by a spherical wavefront, the reconstruction stage is the numerical diffraction process that an arbitrary illuminating wavefront undergoes on the recorded hologram. As the wavefront illuminating the hologram is not necessarily equal to the spherical one utilized in the recording stage in curvature, radius, and location, the reconstructed image of the sample has a magnification and in-focus position given by the holography equations [8,9]. Those equations are greatly simplified by using identical wavelengths for the recording and reconstruction stages and by guessing the location of the origin of the spherical wavefront in the recording. The former can be accurately fulfilled, but the approximate guessing of the latter introduces a nonunitary magnification and makes the reconstructed image to not be located at the true sample plane. In summary, in DLHM the correct sizing is controlled by the number and the size of the pixels of the digital screen that records the in-line hologram, the illuminating wavelength utilized, and the distance from the point source to the digital screen that records the hologram, being this last one the responsible of producing the spherical wavefront

* Corresponding author.
E-mail address: jigarcia@unal.edu.co (J. Garcia-Sucerquia).

https://doi.org/10.1016/j.optlaseng.2020.106176
Received 2 November 2019; Received in revised form 17 April 2020; Accepted 6 May 2020

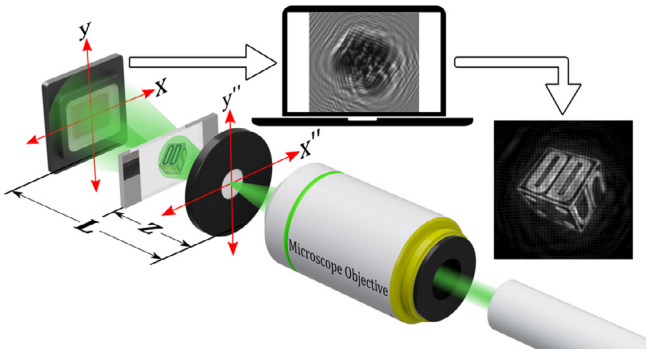

Fig. 1. Illustration of a digital lensless holographic microscope (DLHM). L source-to-screen distance and z source-to-sample distance.

to illuminate the sample. The digital screen specifications and the illuminating wavelength can be accurately known; however, the point source-to-screen distance has to be somehow measured. This measurement is regularly done by mechanical means, which renders to a bad estimation of the said distance and introduces an inaccurate sizing in DLHM.

The need for a better sizing calibration of the DLHM has been already recognized and a method to improve it presented [10]. In this work, the method proposed in the just quoted reference is analyzed, with a special focus on the spatial resolution issue by them reported. Furthermore, an alternative method to iteratively calibrate the sizing is DLHM is proposed. The proposed method uses the Talbot self-imaging [11] phenomenon by studying the Talbot's distance produced by a monolayer of spheres of polystyrene of 1.09 μm in diameter. The accuracy of the calibration method is then validated by imaging a USAF 1951 resolution test.

2. Digital lensless holographic microscopy

Digital lensless holographic microscopy (DLHM) [7] is the simplest label-free imaging method for micrometer-sized objects. DLHM follows the same imaging principle envisioned by D. Gabor [12] composed of two stages: recording and reconstruction.

2.1. Recording in DLHM

For the recording, a transmissive sample is illuminated by a spherical wavefront. Said wavefront is usually produced by focusing down laser light onto the surface of a pinhole with its diameter in the order of the illuminating wavelength λ. The sample is placed at a distance z from the pinhole. The diffraction pattern of the sample is magnified by the propagation in the free space until it reaches a recording screen, the center of which is located at a distance L from the pinhole. The recording plate used by Gabor in its original setup is replaced in DLHM by a digital camera that records what is called a digital in-line hologram [7] and transfers it to a computer for its processing. Fig. 1 illustrates this setup. From the geometrical arrangement utilized in the recording, one can realize that the magnification of the diffraction pattern is $M = L/z$. The magnification has to be large enough to guarantee that the sampling theorem [13] for the largest spatial frequency of the diffraction pattern is fulfilled. At this point, it is important to emphasize that this M is not the magnification of the DLHM, and must not be confused with the magnification in optical microscopy. In the latter, it is defined as the size ratio of the image to the sample; such ratio has no sense in DLHM since in this imaging method the final image can have whatever size is allowed for the digital processing of the information.

To mathematically model the recording stage, one can recur to Gabor's proposal. According to his idea, the digital in-line hologram can be understood as the amplitude superposition of a reference wave $R(x, y)$ with an object wave $O(x, y)$ over the surface of the digital camera. $R(x, y)$ follows the analytical expression of a spherical wavefront and $O(x, y)$ is the diffraction pattern produced by illuminating the sample with the reference wave; thus, $O(x, y)$ gathers the information of the sample. The recorded digital in-line hologram is, therefore:

$$\begin{aligned} H(x,y) &= |R(x,y) + O(x,y)|^2 \\ &= R^2(x,y) + O^2(x,y) + R(x,y)O^*(x,y) + R^*(x,y)O(x,y). \end{aligned} \tag{1}$$

For DLHM to work properly, the sample has to behave as a weak scatter, such that in Eq. (1) $O^2(x, y) \approx 0$. In the said equation, the term $R^2(x, y)$ carries no information about the sample; it represents what is called the zeroth-order of diffraction [13] and can be removed from the digital in-line hologram by pixel-wise subtracting the recorded intensity without the sample present. This latter procedure leads to the contrast digital in-line hologram

$$\tilde{H}(x,y) \approx R(x,y)O^*(x,y) + R^*(x,y)O(x,y). \tag{2}$$

The contrast hologram carries the information of the object wave and its complex conjugate. These terms in Eq. (2) are recognized as the twin images [13]; their deleterious effects in the original Gabor´s experiments are not present in DLHM, as it has been studied elsewhere [7]. The contrast hologram is finally stored in the memory of a computer to perform the reconstruction stage.

2.2. Reconstruction in DLHM

The reconstruction stage in DLHM follows the original recipe to recover the complex-valued object wavefront [13]: the recorded hologram, understood as a diffraction grating, is illuminated with the complex conjugate of the reference wavefront utilized in the recording stage. A replica of the object wavefront is obtained over the sample plane, as a result of the backpropagation of the diffracted wavefront from the hologram to the said plane. In DLHM, a complex-valued object wavefront is numerically produced by evaluating the diffraction that the complex-conjugated reference wave undergoes as it illuminates the contrast digital in-line hologram. This wavefront propagation expressed in terms of the Kirchhoff-Helmholtz diffraction formula gives:

$$\begin{aligned} O(x',y') = -\frac{i}{2\lambda} \underset{\substack{\text{Digital}\\ \text{camera}}}{\iint} \tilde{H}(x,y)R*(x,y) \frac{\exp\left[ik\sqrt{(x-x')^2+(y-y')^2+z^2}\right]}{\sqrt{(x-x')^2+(y-y')^2+z^2}} \\ \times(1+\cos\chi)\mathrm{d}x\mathrm{d}y \end{aligned} \tag{3}$$

being $(1 + \cos \chi)$ the inclination factor [13]. The numerical computation of Eq. (3) is so extremely time-consuming, that its direct calculation has no sense for a technologically viable implementation of DLHM. To overcome this limitation, Prof. H.J. Kreuzer developed a numerical strategy to convert Eq. (3) into a circular convolution that can be solved via fast Fourier transforms [14,15]. This development embraces a change of coordinates, which includes the point-source-to-screen distance L and the point-source-to-reconstruction plane distance Z, into a modified and discretized contrast hologram $\tilde{H}'[m, n]$, being m,n integer numbers. As the information of the complex-conjugated reference wavefront and the geometry of the recording setup are included in the numerical calculation of Eq. (3), to obtain an identical replica of the complex-valued object wavefront placed at the exact sample plane, the number and size of the pixels of the recording camera have to be known, the recording illumination wavelength of the sample has to be used in the reconstruction stage, the reconstruction distance Z has to be equal to z, and the numerically utilized point-source-to-screen distance L_0 in the reconstruction stage has to be identical to that used to record the digital in-line hologram L. The specifications of the camera and the illuminating wavelength are known from the manufacturer's information of the camera and the laser source, respectively; therefore, these figures can be introduced accurately in the reconstruction algorithm. In principle, the $Z = z$ condition

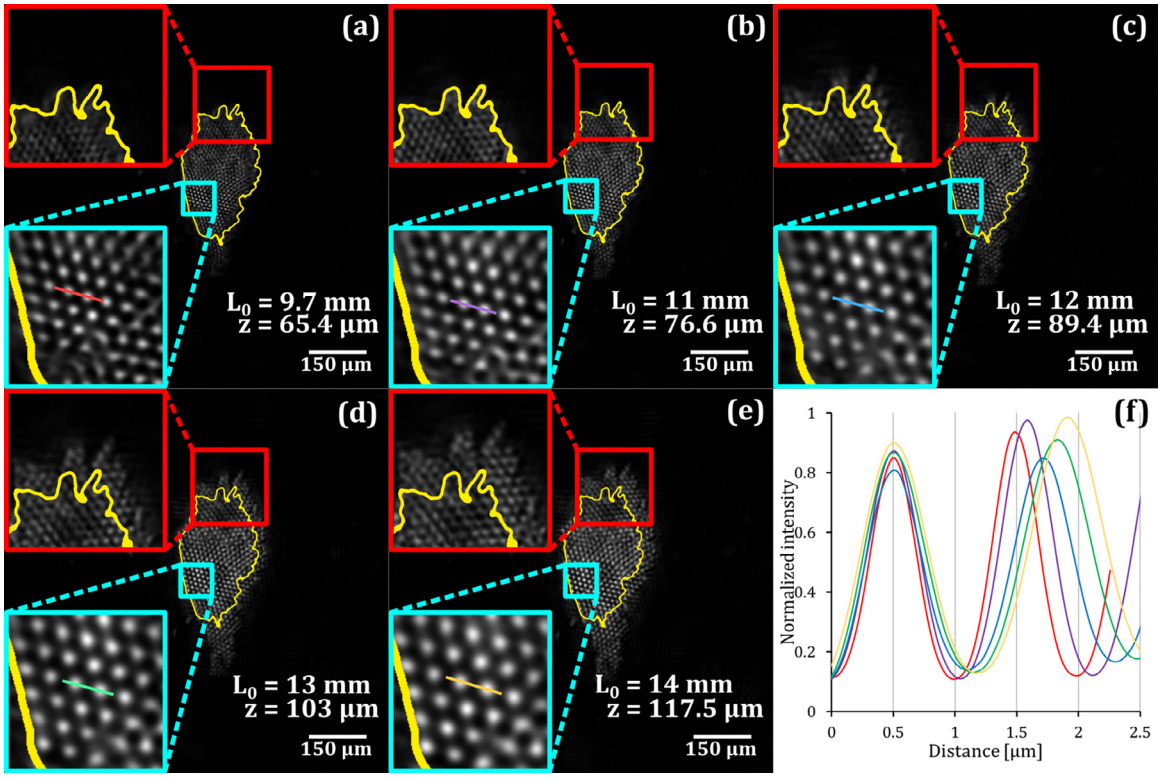

Fig. 2. Reconstructions of a digital in-line hologram of a monolayer of polystyrene spheres of 1.09 µm in diameter for different point source-to screen distances. Reconstructions for L_0 varied from 9.7 mm to 14 mm are shown in panels from (a) to (e). The zoomed-in red- and cyan-bounded areas show the preservation of spatial resolution for all the L_0 distances. Panel (f) shows profiles along the colored line inside the cyan-bounded zoomed-in areas.(For interpretation of the references to color in this figure legend, the reader is referred to the web version of this article.)

is reached when the reconstructed object wavefront is in perfect focus, something that can be determined by using focusing methods applicable to DLHM, like the modified enclosed energy or any other [16,17]. However, if the introduced point-source-to-screen distance L_0 is not identical to that used in the recording stage L, the in-focus object wavefront is found in a different plane from that located at a distance z away from the point source, and the size of the reconstructed sample is not the real one; therefore, for the correct sizing in DLHM, it is mandatory to have an accurate knowledge of the point-source-to-screen distance L, to be introduced in the reconstruction algorithm as $L_0 = L$. Regularly, the distance L is measured with a ruler or caliper, imposing the need for mechanical intervention in the setup. A precise measurement would require the fragile surfaces of the pinhole and the camera to be touched; this inadequate, when not impossible, practice leads to just an approximate measurement which introduces a distortion on the sizing of the DLHM that has to be accounted for. To solve this limited sizing derived from the rough measurement of the point source-to-screen distance L, a self-calibrating method, which uses reference marks on the sample holders, has been previously introduced [10]. In that work, the authors, beyond the sizing issue, report a loss of spatial resolution inherited from the same limited measurement, even in the range of tens of micrometers; our group has also recognized the lack of accurate sizing but not the loss of spatial resolution. To test the reported resolution issue, we have conducted reconstructions for different point source-to-screen distances L_0 of a recorded digital in-line hologram of a monolayer of polystyrene spheres of 1.09 µm in diameter; Fig. 2 shows the results.

The hologram was recorded in a complementary metal-oxide-semiconductor (CMOS) camera with 2048 × 2048 pixels, each with a size of 6 µm. The monolayer was illuminated with the spherical wavefront produced by focusing down the light from a 405 nm laser onto the surface of a 500 nm pinhole in diameter. The rough measurement of L is 12 mm. However, to test the reported loss of spatial resolution, we have reconstructed the digital in-line hologram for L_0 varying from 9.7 mm to 14 m; the reconstructed images are shown in panels from (a) to (e) of Fig. 2. The insets in each panel show zoomed-in areas revealing that, for the different values of L_0, the spatial resolution is kept while the sizing of the reconstructed monolayer varies. The sizing change with the same spatial resolution is highlighted in the profiles of panel (f); such plots are obtained along the lines in the cyan square bounded areas in panels from (a) to (e). In summary, the results in Fig. 2 show that the use of a point source-to-screen distance L_0 in the reconstruction stage not equal to the distance L in the recording stage leads to wrong sizing of the sample but without affecting the spatial resolution. Perhaps the perturbation on the spatial resolution previously reported [10] was due to the reconstruction algorithm that those authors utilized [18], which is different from the one used in the present work. The just-mentioned finding justifies the search for a method for correcting the sizing in DLHM as shown in the following section.

3. Sizing calibration in DLHM via iterative Talbot Self-imaging

3.1. Description of the iterative Talbot self-imaging method

Having shown that the appropriate selection of the point-source-to-screen distance L_0 conditions the correct sizing and measurements in the sample reconstruction but does not affect the spatial resolution, an iterative method to achieve calibration of this distance is proposed. Making use of the self-imaging properties of periodic objects illuminated by a coherent source, known as Talbot effect [11], one can predict that the intensity distribution along the axial distance is composed of a set of replicas of the object, periodically located along the propagation direction. Such a prediction is controlled by the Talbot distance, which, for the DLHM architecture, only depends on the illumination wavelength λ

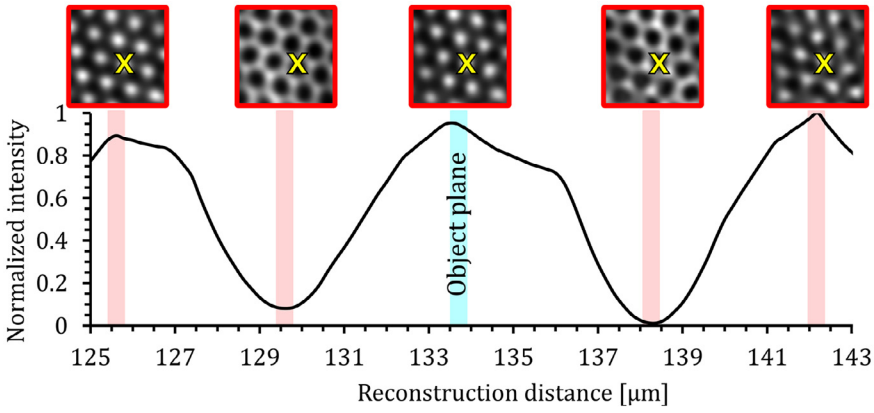

Fig. 3. Normalized axial intensity profile for a monolayer of polystyrene microspheres taken over the X-marked spot in the upper insets. The highlighted distances identify the Talbot's fractional planes, with the central one corresponding to the object plane.

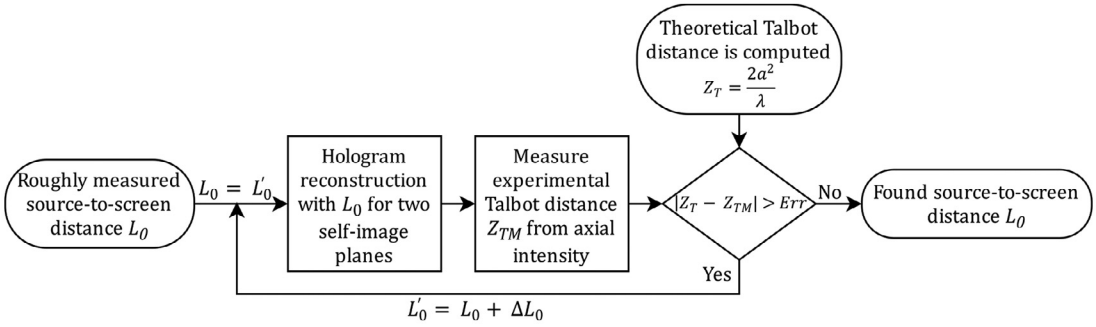

Fig. 4. Illustration of the iterative method to calibrate length measurements of DLHM. a is the monolayer pitch, and *Err* the user-set error limit of the calibration method.

and the pitch a of the periodic sample as [19]

$$Z_T = \frac{2a^2}{\lambda} \tag{4}$$

Given a known periodic sample meant to be used as the calibration element, the pitch a is precisely known as well as the corresponding illumination wavelength; thus, the Talbot distance is completely determined and can be used as a control metric. An erroneous value of the point-source-to-screen distance in the reconstruction stage L_0would produce an alteration in the sizing of the reconstructed sample, yielding a modified pitch of the periodic structure; this modification would thus greatly change the measured Talbot distance because of the quadratic dependence on the pitch, allowing a more precise optimization to be pursued.

The calibration of the point-source-to-screen distance starts with the approximate value of L_0obtained by the traditional methods, namely using a ruler or caliper. Using this rough value, the hologram is reconstructed near the object plane and numerically propagated until the first self-image plane is found. An axial analysis of the intensity profile leads to the expected periodic behavior [11], as illustrated in Fig. 3 for a monolayer of microspheres over the X-marked point; in the figure, the highlighted distances are the Talbot's fractional planes, with the central one being the object plane. The axial distance between the object plane and the first self-image is taken as the experimental measurement of the Talbot distance Z_{TM}, and compared to the control value Z_T as given by Eq. (4). If the measured difference $|Z_{TM} - Z_T|$ is greater than the user-defined allowable error *Err*, the distance estimation L_0 is modified in a small amount ΔL_0, either positive or negative, yielding a new point-source-to-screen distance prediction $L_0' = L_0 + \Delta L_0$. The process is then repeated using the new value L_0' in the reconstructions, which will be consequently modified as many times as needed until the desired threshold in the measured difference $|Z_{TM} - Z_T|$ is reached. The final value of $L_0' = L_0$ will correspond to the calibrated measurement of the point-source-to-screen distance. The above-described procedure is summarized as a flowchart in Fig. 4.

3.2. Direct sizing calibration via standard test target versus proposed Talbot-based method

The size calibration in DLHM could also be performed as in any other regular microscopy technique: a calibrated test target is imaged and the parameters that control the sizing of microscope adjusted to obtain the true measurement of the target. Following this idea, provided that the illumination wavelength is accurately known, one could consider a calibrated USAF 1951 test target as the object to image in DLHM, and use its known-size features to iteratively calibrate the reconstruction distance L_0 measuring only in the x-y direction. This method would follow a similar procedure to the one described for the calibration using the Talbot effect: i) The process starts by a rough measurement of the distance $L_0 = L_0´$; ii) for the given $L_0´$ distance, a reconstruction of the calibrated test target is performed to the in-focus object plane; iii) on the reconstructed image, the measurement Δ_M of a feature of the test, say an element of a given group, is obtained and compared to its standard size Δ_T; iv) if the absolute difference between these measurements is greater than the user-defined allowable error *Err*, $|\Delta_M - \Delta_T| > Err$, the distance L_0' is varied $L_0' = L_0 + \Delta L_0$ with ΔL_0 being a small positive or negative distance; and, finally, v) the steps ii) to iv) are iteratively executed until the condition $|\Delta_M - \Delta_T| \leq Err$ is reached.

The above-described method would be equivalent to the previously reported methodology in ref. [10], but making use of a standard target rather than reference structures in the sample holder. In either case, the main difference between those methods and the one proposed in the present work is the evaluated variable during the iterative process; while the Talbot-based method proposes a measurement in the propagation direction, the former methods act only in the object plane with measurements in the x-y direction. However, this seemingly simple difference gives the method three features that, when combined, set the Talbot-based method as an attractive alternative for calibrating the point-source-to-screen distance in DLHM systems: First, unlike the traditional approach where the measurements would be done directly

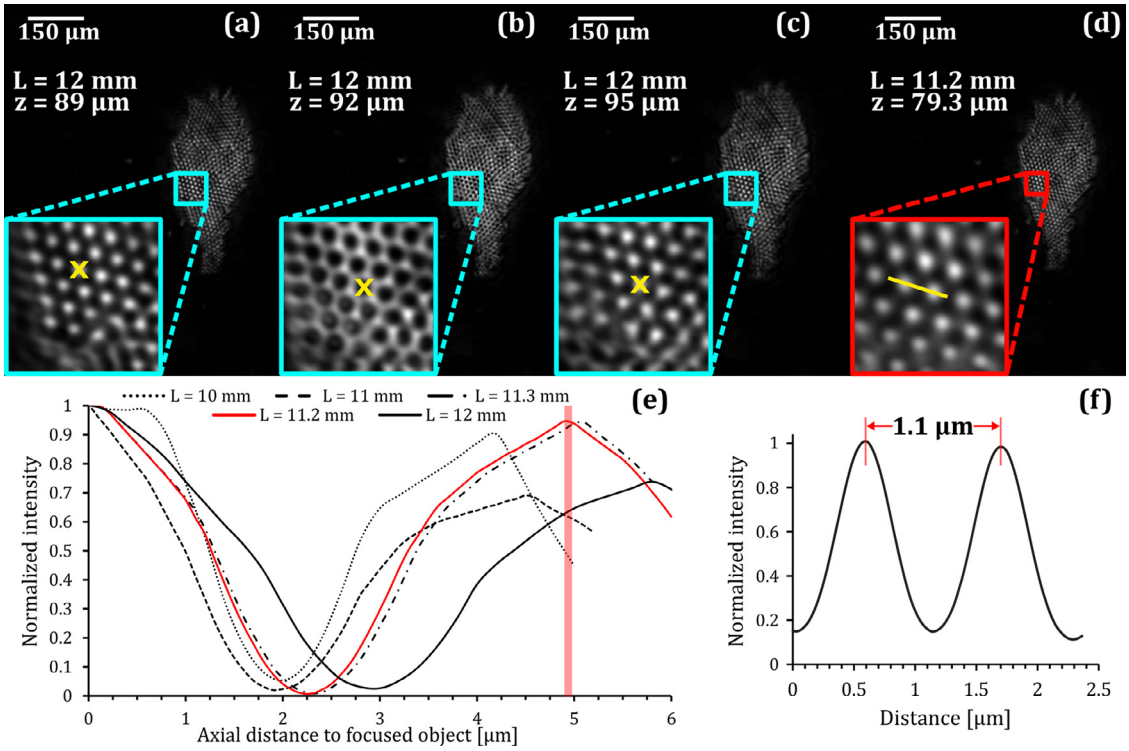

Fig. 5. Sizing calibration using the iterative method. In (a) to (c) intensity reconstructions using a rough estimate of the point-source-to-screen distance L in the first three Talbot planes. (d) Intensity reconstruction using the corrected L. (e) Axial intensity distribution for iterative variations of L measured over a single bead, as shown in the region marked by the yellow cross in panels (a) to (c). The red vertical line marks the theoretical Talbot distance. (f) Intensity profile taken over the yellow line in panel (d).

on the modified features over the in-focus x-y plane, the consideration of the Talbot's distance sets the control metric on the propagation direction, which has increased sensitivity to the scale changes due to the quadratic dependence portrayed in Eq. (4). Second, because the measurements would be done based on an intensity profile taken over the propagation direction, the need for a high-precision knowledge of the in-focus position of the object is waived; rather, as seen in Fig. 3, approximate knowledge of the object plane suffices to apply the calibration strategy, allowing the removal of the focusing step in each iteration that is otherwise needed to ensure an adequate x-y measurement. Finally, as the proposed analysis requires the propagation of a single point on the x-y plane, there is no need to calculate the reconstruction of the whole image in each iteration, opening the possibility of implementing non-approximated reconstruction approaches; for instance, ref. [20] shows that the full Rayleigh-Sommerfeld formalism could be implemented in such a way that 280 different axial data points could be calculated in less than a second for a 1024 × 1024 input image; this consideration allows to perform measurements with enhanced accuracy without time penalties and could prevent the introduction of any numerical artifact derived from the propagation method.

4. Experimental results

To verify the proposed iterative algorithm, the method has been utilized to calibrate a DLHM composed of a 405 nm laser source focused on a pinhole with 500 nm in diameter, and a CMOS camera with 2048 × 2048 square pixels with a side length of 6 µm. As the calibration sample, a self-assembled monolayer of polystyrene beads of 1.09 µm in diameter was used; after Eq. (4), the Talbot distance is thus $Z_T \approx 4.94\,\mu$m. The whole calibration process is summarized in Fig. 5.

A mechanical rough estimate of the point-source-to-screen distance L yielded, approximately, 12 mm. As seen in panels (a), (b) and (c) of Fig. 5, where intensity reconstructions in the object plane, first fractional-plane, and first self-image plane are respectively shown, the experimental Talbot distance $Z_{TM} \approx 6\,\mu$m exceeds the expected value. The distance L is then iteratively calibrated using the proposed method until the measured error $|Z_{TM} - Z_T|$ is less than $\lambda/10$. Some excerpts from the algorithm execution are presented in panel (e) in the form of intensity profiles; each was measured along the propagation direction over a single sphere, as illustrated in panels (a) to (c) by the yellow cross inside the insets. As expected, small modifications to the point-source-to-screen distance have noticeable effects in the period of the Talbot self-images. The red vertical line marks the correct Talbot distance. The value of L that finally minimizes the error below the allowable limit is found to be $L \approx 11.2$ mm with a Talbot distance of $Z_{TM} \approx 4.90\,\mu$m. The result is shown in panel (d), where an intensity reconstruction in the object plane using the calibrated distance L is presented. To further emphasize the effectivity of this calibration, panel (f) shows an intensity profile taken over the yellow line inside the inset of panel (d); a measurement between the maximums yields 1.1 µm, which adequately matches the diameter of the polystyrene beads used in the monolayer assembly. Even though, for illustration purposes, the whole sample plane was reconstructed for each Talbot's image in Fig. 5, the profiles in panel (e) were produced for a single pixel at each distance. Each raw profile was done with 70 points along the axial direction, obtained in less than 0.8 seconds in total by propagating the complex-valued wavefield with the non-approximated Rayleigh–Sommerfeld diffraction integral [20]; from these profiles, the illustrated excerpt was taken. This application highlights that no focusing criteria are needed for the method to work properly, and that it is possible to avoid the introduction of numerical artifacts associated with approximated propagation algorithms without time penalties.

Finally, the calibrated microscope was used to image the groups 6 and 7 from a USAF 1951 resolution test target. The results are shown in Fig. 6. In panel (a), an intensity reconstruction of the corresponding hologram using the rough estimation of 12 mm for the point-source-to-

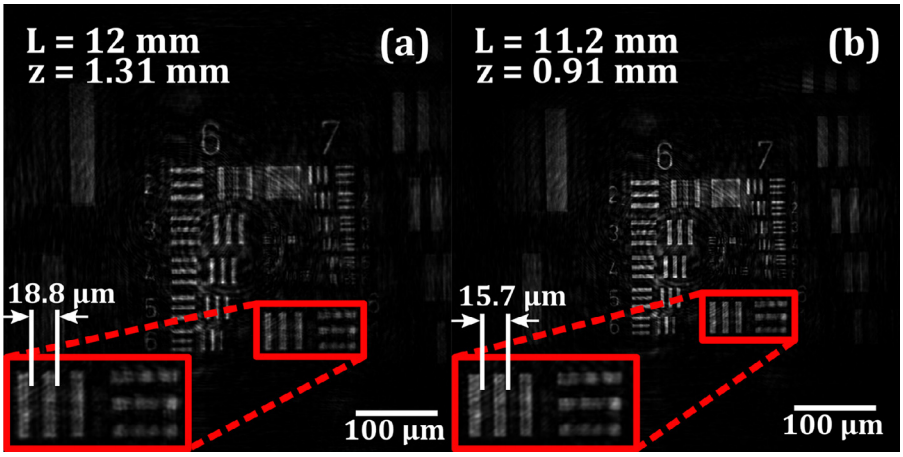

Fig. 6. Application of the calibrated distance to verify correct sizing and measuring. (a) Intensity reconstruction using the original rough estimate of the point-source-to-screen distance L. (b) Intensity reconstruction using the calibrated L.

screen distance is presented. If the first element from group 6 is measured, it yields 18.8 µm; this value is far from the correct value of 15.6 µm for a standard USAF 1951 Target. However, as shown in panel (b), once the calibrated value of 11.2 mm for L is utilized, the measurement on the same element yields 15.7 µm. The good agreement in the resulting measurements after the calibration process is applied serves as experimental verification of its validity and feasibility for DLHM applications.

5. Conclusions

A method to calibrate a digital lensless holographic microscope (DLHM) based on an iterative digital Talbot self-imaging method has been presented. In this microscopy technology, the correct sizing of the imaged samples is supported in the accurate knowledge of the illuminating wavelength, the camera dimensions, and the pinhole-to-screen distance. The two former parameters are provided by the manufacturers of the lasers and the cameras, in that order. The measurement of the pinhole-to-screen distance could be performed by means of a ruler or with greater accuracy by using a regular caliper; both measuring tools imply a mechanical interference in the microscope structure, which could be not desirable, or even impossible, in many applications. The method presented in this work allows the accurate determination of the point-source-to-screen distance using an iterative digital Talbot self-imaging approach. The self-images are produced by the numerical reconstruction of a DLHM hologram of a periodic sample illuminated coherently. Because the proposed method starts from the precise knowledge of the pitch of the periodic sample, the accurate determination of the Talbot distance is subject to the correct finding of the reconstruction distance which depends on the measurement of the point source-to-screen distance. The latter is therefore varied iteratively until the correct Talbot distance, determined by the illuminating wavelength, the period of the sample, and the reconstruction distance, is achieved. The proposed method has the advantages of having an increased sensitivity to scale changes, the waived need for focusing at each iteration, and allowing the use of non-approximated reconstruction approaches for enhanced accuracy. The method has been illustrated by numerically reconstructing a DLHM hologram produced by a self-organized monolayer of 1.1 μm beads of polystyrene illuminated by a 405 nm laser, and later applied to a USAF 1951 Test Target in the same system.

Disclosures

The authors declare no conflicts of interest associated with the present work.

Declaration of Competing Interests

None

CRediT authorship contribution statement

Carlos Buitrago-Duque: Software, Validation, Writing - review & editing. **Jorge Garcia-Sucerquia:** Conceptualization, Methodology, Writing - original draft, Writing - review & editing.

Acknowledgments

The present work was done thanks to the funding by Universidad Nacional de Colombia Sede Medellin.

Supplementary materials

Supplementary material associated with this article can be found, in the online version, at doi:10.1016/j.optlaseng.2020.106176.

References

[1] Wongsrichanalai C, Barcus MJ, Muth S, Sutamihardja A, Wernsdorfer WH. A review of malaria diagnostic tools: microscopy and rapid diagnostic test (RDT). Am J Trop Med Hyg 2007;77:119–27.
[2] Cuche E, Bevilacqua F, Depeursinge C. Digital holography for quantitative phase-contrast imaging. Opt Lett 1999;24:291–3. https://doi.org/10.1364/OL.24.000291.
[3] Kreuzer HJ, Fink HW, Schmid H, Bonev S. Holography of holes, with electrons and photons. J Microsc 1995;178:191–7.
[4] Kim MK. Digital holographic microscopy. Principles, techniques, and Aplications. New York City: Springer; 2011.
[5] Langehanenberg P, Ivanova L, Bernhardt I, Ketelhut S, Vollmer A, Dirksen D, et al. Automated three-dimensional tracking of living cells by digital holographic microscopy. J Biomed Opt 2009;14:014018. https://doi.org/10.1117/1.3080133.
[6] Sánchez-Ortiga E, Doblas A, Saavedra G, Martínez-Corral M, Garcia-Sucerquia J, Saavedra G, et al. Off-axis digital holographic microscopy: practical design parameters for operating at diffraction limit. Appl Opt 2014;53:2058–66. https://doi.org/10.1364/ao.53.002058.
[7] Garcia-Sucerquia J, Xu W, Jericho SK, Klages P, Jericho MH, Kreuzer HJ. Digital in-line holographic microscopy. Appl Opt 2006;45:836–50.
[8] Leith EN, Upatnieks J. Microscopy by wavefront reconstruction. J Opt Soc Am 1965. https://doi.org/10.1364/josa.55.0569_1.
[9] Repetto L, Pellistri F, Piano E, Pontiggia C. Gabor's hologram in a modern perspective. Am J Phys 2004. https://doi.org/10.1119/1.1652041.
[10] Riesenberg R, Kanka M. Self-calibrating lensless inline-holographic microscopy by a sample holder with reference structures. Opt Lett 2014. https://doi.org/10.1364/ol.39.005236.
[11] Patorski K. I The self-imaging phenomenon and its applications. In: Prog. Opt.. Elsevier; 1989. p. 1–108.
[12] Gabor D. A New Microscopic Principles. Nature 1948;161:777–8.
[13] Goodman JW. Introduction to fourier optics. Greenwood Village. 3rd Editio. USA: Roberst & Company Publishers; 2005 https://doi.org/10.1117/1.601121.
[14] Jericho MH, Kreuzer HJ. Point source digital in-line holographic microscopy. In: Ferraro P, Wax A, Zalevvsky Z, editors. Coherent Light Microsc.. Berlin Heidelberg: Springer-Verlag; 2011. p. 3–30.
[15] Garcia-Sucerquia J., Trujillo C., Restrepo Agudelo J. Microscopio holográfico digital sin lentes (MHDSL) y método para visualizar muestras. 14258943 0 0, 2018.
[16] Trujillo CA, Garcia-Sucerquia J. Automatic method for focusing biological specimens in digital lensless holographic microscopy. Opt Lett 2014;39:2569–72. https://doi.org/10.1364/OL.39.002569.

[17] Trujillo C, Garcia-Sucerquia J. Cooperative execution of auto-focusing metrics in digital lensless holographic microscopy for internal-structured samples. Appl Opt 2017;56:5877–82. https://doi.org/10.1364/AO.56.005877.
[18] Kanka M, Wuttig A, Graulig C, Riesenberg R. Fast exact scalar propagation for an in-line holographic microscopy on the diffraction limit. Opt Lett 2010;35:217–19. https://doi.org/10.1364/ol.35.000217.
[19] Garcia-Sucerquia J, Alvarez-Palacio DCC, Kreuzer HJJ. High resolution Talbot self-imaging applied to structural characterization of self-assembled monolayers of microspheres. Appl Opt 2008;47:4723–8. https://doi.org/10.1364/AO.47.004723.
[20] Buitrago-Duque C, Garcia-Sucerquia J. Non-approximated Rayleigh–Sommerfeld diffraction integral: advantages and disadvantages in the propagation of complex wave fields. Appl Opt 2019. https://doi.org/10.1364/ao.58.000g11.

Carlos Buitrago-Duque is a graduate student from the School of Physics of the Universidad Nacional de Colombia, Medellin, Colombia, where he also received his degree in Engineering Physics. His research interests include digital holography, computational modeling and numerical processing of physical systems, and optical metrology.

Jorge Garcia-Sucerquia is an Associate Professor with the School of Physics, Universidad Nacional de Colombia, Medellin, Colombia, where he serves in the program of Engineering Physics. He received his B.Sc., M.Sc. and PhD in Physics from the Universidad de Antioquia, Medellin, Colombia. His research interests include digital holography, optical metrology and optical coherence, fields in which he is author of more than 200 journal papers.

Research Article Vol. 60, No. 4 / 1 February 2021 / Applied Optics A205

applied optics

Open-source, cost-effective, portable, 3D-printed digital lensless holographic microscope

Heberley Tobon-Maya, Samuel Zapata-Valencia, Erick Zora-Guzmán, Carlos Buitrago-Duque, and Jorge Garcia-Sucerquia*

School of Physics, Universidad Nacional de Colombia—Sede Medellin, A.A: 3840, Medellin 050034, Colombia
**Corresponding author: jigarcia@unal.edu.co*

Received 19 August 2020; revised 16 October 2020; accepted 17 October 2020; posted 20 October 2020 (Doc. ID 405605); published 17 November 2020

In this work, the design, construction, and testing of the most cost-effective digital lensless holographic microscope to date are presented. The architecture of digital lensless holographic microscopy (DLHM) is built by means of a 3D-printed setup and utilizing off-the-shelf materials to produce a DLHM microscope costing US$52.82. For the processing of the recorded in-line holograms, an open-source software specifically developed to process this type of recordings is utilized. The presented DLHM setup has all the degrees of freedom needed to achieve different fields of view, levels of spatial resolution, and 2D scanning of the sample. The feasibility of the presented platform is tested by imaging non-bio and bio samples; the resolution test targets, a section of the head of a Drosophila melanogaster fly, red blood cells, and cheek cells are imaged on the built microscope.

https://doi.org/10.1364/AO.405605

1. INTRODUCTION

Simple and affordable 3D-printing systems have driven the development of cost-effective, portable, and lightweight devices in different fields of science and technology. In particular, the field of microscopy has been greatly benefited because 3D printers have made it possible to achieve cost-effective, compact, robust, field-portable, and lightweight imaging systems with high throughput for different modalities of microscopy. From the very large list of 3D-printed microscopes, one can start by mentioning the OpenFlexure project [1]. This 3D-printed microscope is based on a regular microscope objective, a tube lens, and an 8MP CMOS sensor (Raspberry Pi camera V2) to offer different microscopy modes of operation; bright-field trans-illumination, bright-field epi-illumination, polarization-contrast imaging, and fluorescence imaging are the modalities in which this microscope can operate. However, because of the utilized imaging principle, it is not possible to make quantitative imaging of transparent samples in this system. To this aim, the 3D-printed microscope should resort to mainly interferometric principles of microscopic imaging [2].

There are different modalities of microscopes based on interferometric principles that have been developed using 3D-printing technology. Initially, one could mention those based on off-axis digital holographic microscopy [3]. In general, this methodology needs to record the interference of two waves with a given degree of inclination between them. The fringe pattern resulting from this amplitude superposition constitutes the carrier information that is modulated by the imaged sample. The recovery of the sample information, both in amplitude and phase, can be done by a regular spatial filtering approach [4,5]. Currently, off-axis 3D-printed digital holographic microscopes based on the interference of two point-sources [6,7], on side illumination and analog hologram gratings [8], on shearing digital holography [9,10], and on slide holographic microscopy [11] are available.

An alternative option for interferometric imaging in microscopy is the in-line configuration [12]. In this configuration, the information of the sample is gathered by the propagation of the illuminating wavefront through the micrometer-sized specimen. The minimum needed components for the architecture of in-line holographic microscopy are an illumination source and a digital recording device. When the illumination is provided by a point source, the recorded intensity can be understood as a magnified diffraction pattern from which the information of the specimen can be somehow retrieved. This simplicity of hardware sets the digital in-line holographic microscopy architecture as a noteworthy candidate to the production of compact, robust, cost-effective, and 3D-printed digital holographic microscopes. Indeed, numerous developments that take advantage of this architecture can be found in the literature. Some of the earliest reports on cost-effective digital holographic microscopes based on the in-line architecture come from Ozcan's group [13–16]. In these works, Ozcan proposed the use of point-source illumination with the sample very close to the digital camera to achieve, employing multiple shots and intensive computational effort, an enormous field of view of around 8 cm^2, and micrometer-sized spatial resolution. Another set of notable works of digital in-line holographic microscopy that reported

compact and cost-effective setups can be read in [17,18]; in these references, the building price ranges from US$1000 to US$250, and the reported spatial resolutions are about 3 μm. Further development in this direction, explicitly including the use of substantially cost-effective light sources, was reported by Micó's group [19,20]. In this multiframe single-shot in-line architecture, micrometer-sized spatial resolution and observation of dynamic events are reported. Following the path to push for price reduction in making digital in-line holographic microscopes, researchers of the Institute of Applied Physics at Technische Universität Darmstadt in Germany have presented an open-source 3D-printed digital in-line holographic microscope for low-cost cellular imaging [21]. In this work, the researchers use laser diode and LED illumination to offer two different microscopes with a varied optical performance. For the geometry of their microscopes, the nominal field of view and spatial resolution is fixed, yielding the spatial resolution controlled by the light source; while for the laser diode a spatial resolution of 1.55 μm is obtained, for the LED illumination 3.91 μm is claimed. The price reported for the making of the LED-based digital in-line holographic microscope, the less expensive of the two, is US$190.

In the present work, the design, construction, and testing of an open-source, cost-effective, portable, 3D-printed digital lensless holographic microscope, are reported. The presented microscope is based on the digital lensless holographic microscopy (DLHM) [22–24] technology. DLHM is a digital in-line holographic microscopy technique that provides micrometer-sized spatial resolution by using spherical wavefront illumination light sources with numerical apertures above 0.4. The proposed open-source, cost-effective, portable, 3D-printed digital lensless holographic microscope offers the full set of degrees of freedom to vary the field of view of the microscope at different levels of spatial resolution. For the easy 2D scanning of the sample, the body of the microscope has been equipped with a slide holder. As compared with the most cost-effective digital holographic microscope to date [21], the one presented in this work is almost 4 times less expensive, provides full access to a varying field of view and spatial resolution, and provides accurate 2D scanning of the sample. A fully open-source processing software joins the 3D-printed microscope to access the said optical features from software. The capabilities of the constructed open-source, cost-effective, portable, 3D-printed digital lensless holographic microscope have been tested on imaging resolution test targets, a section of the head of a Drosophila melanogaster, red blood cells, and cheek cells.

2. FUNDAMENTALS

DLHM [22–24] is a realization of the original invention of Gabor's invention [25] with modern technology. A point source illuminates a weakly scattering sample placed at a distance z from the said source. A digital camera, located L apart from the point source, records the intensity resulting from the diffraction of the spherical wavefronts emitted by the point source on the sample. Figure 1 illustrates a DLHM setup.

The diffraction pattern, known as in-line hologram, is magnified by the free-space propagation from the sample to the digital camera. The value of such magnification $M = L/z$ must be such

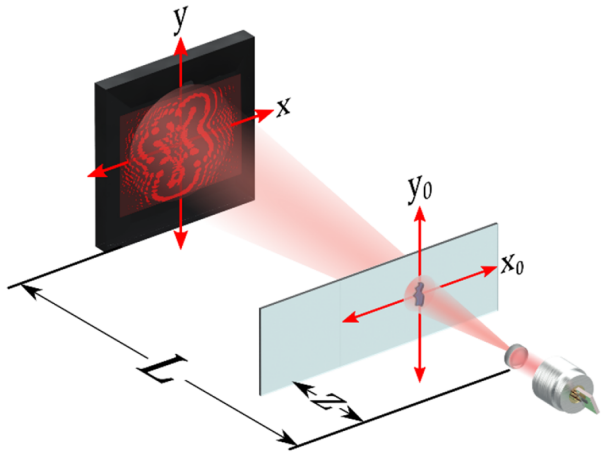

Fig. 1. Illustration of the recording setup of a digital lensless holographic microscope.

that the recording of the in-line hologram fulfills the sampling requirements [26,27]. Also, the value of M can be utilized to categorize the two types of microscopy without lenses [16,19,20]: while $M < 1$, the sample close to the digital camera, denotes what is mainly known as computational microscopy [28–30], values of $M > 1$, the sample close to the point source, apply for methods of lensless microscopy such as multi-illumination single-holographic-exposure lensless Fresnel (MISHELF) [19,31,32] or DLHM [24,33,34]. As inherited from Gabor's idea of holography, the very first understanding of the in-line hologram of DLHM is modeled as the amplitude superposition of a reference $U_{\text{ref}}(\vec{r})$ with an object wave $U_{\text{scat}}(\vec{r})$ on the plane of the digital camera, where the position vector $\vec{r} = (x, y, L)$ is measured from the point source to denote a point on the digital camera plane. The former is the portion of the spherical wave that propagates from the point source to the digital camera with no perturbation, regularly assumed to be the diverging spherical wave that illuminates the sample $U_{\text{ref}}(\vec{r}) = \exp[ik\vec{r}]/|\vec{r}|$; the object wave is the portion of the spherical wavefront that, after undergoing a diffraction process on the sample, propagates to the said digital camera. In this framework, the in-line hologram can be read as

$$I(\vec{r}) = \left[U_{\text{ref}}(\vec{r}) + U_{\text{scat}}(\vec{r})\right]\left[U_{\text{ref}}(\vec{r}) + U_{\text{scat}}(\vec{r})\right]^* \approx U_{\text{ref}}(\vec{r})\, U^*_{\text{ref}}(\vec{r}) + U_{\text{ref}}(\vec{r})\, U^*_{\text{scat}}(\vec{r}) + U^*_{\text{ref}}(\vec{r})\, U_{\text{scat}}(\vec{r}). \quad (1)$$

In Eq. (1), the * superscript denotes the complex conjugate, and the intensity of the object wave $U_{\text{scat}}(\vec{r})U^*_{\text{scat}}(\vec{r})$ is negligible, as for DLHM to work the sample must be a weak scatterer [25]. The first term of the equation corresponds to the intensity of the reference wave, and the last two terms are the twin images, whose effects on the performance of DLHM can be read elsewhere [24,35].

Upon the understanding that in the DLHM architecture it is not possible to have a reference wave fairly described as a diverging spherical wavefront, an alternative model for the in-line hologram based on a simple diffraction phenomenon has been proposed [34,36]. The recorded in-line hologram is, therefore, the resulting single-shot intensity of the diffraction process that

undergoes a diverging spherical wavefront $\exp[ik\vec{r}]/|\vec{r}|$ and the sample with a given transmittance $S(\vec{r}_0)$. With the sample placed at a distance z from the point source that produces the diverging spherical wavefront, the in-line hologram can be correctly described through the Rayleigh–Sommerfeld diffraction formula [26] as

$$I(\vec{r}) = \left| \int_{\text{Sample}} S(\vec{r}_0) \frac{\exp[ik\vec{r}_0]}{|\vec{r}_0|} \frac{\exp[ik(\vec{r}-\vec{r}_0)]}{|\vec{r}-\vec{r}_0|} \mathrm{d}\vec{r}_0 \right|^2. \quad (2)$$

In Eq. (2), $|\bullet|^2 = (\bullet)(\bullet)^*$, the position vector $\vec{r}_0 = (x_0, y_0, z)$ denotes a point on the sample plane measured from the point source, $i = \sqrt{-1}$, and $k = 2\pi/\lambda$ is the wavenumber with λ the illumination wavelength.

In either representation, Eq. (1) or Eq. (2), the in-line hologram is a single-shot intensity recorded in the digital camera with a magnification factor of $M = L/z$. From the said magnified intensity, the complex-valued wavefield scattered by the sample can be recovered in the experiment volume contained from the point source to the digital camera. The different planes within this recovering volume are composed of points denoted by position vectors $\vec{r}_r = (x_r, y_r, z_r)$, such that $z \le z_r \le L$; the retrieved complex-value wavefield for $z_r = z$ corresponds to the in-focus image of the sample transmittance.

The use of a digital camera to record the in-line hologram provides DLHM with the power and versatility of the digital world. The recovery of the complex-valued wavefield scattered by the sample can be done by means of a fully numerical approach. The recorded in-line hologram $I(\vec{r})$ is pixelwise multiplied by a converging spherical wavefront $\exp[-ik\vec{r}]/|\vec{r}|$, and the complex-valued wavefield resulting from this multiplication is propagated towards the reconstruction plane. This propagation is computed by evaluating the diffraction process of the converging spherical wavefront as it illuminates the in-line hologram. This process can be numerically described by means of a scalar diffraction formula [26]:

$$U(\vec{r}_r) = \int_{\text{Digital Camera}} I(\vec{r}) \frac{\exp[-ik\vec{r}]}{|\vec{r}|} \frac{\exp[-ik(\vec{r}-\vec{r}_r)]}{|\vec{r}-\vec{r}_r|} \mathrm{d}\vec{r}. \quad (3)$$

When $\vec{r}_0 = \vec{r}_r$, the complex-valued wavefield resulting from Eq. (3) represents the wavefield scattered by the sample. From it, one can compute its intensity $U(\vec{r}_0)U^*(\vec{r}_0)$ or phase $\phi(\vec{r}_0) = \arctan(\mathrm{Im}[U(\vec{r}_0)]/\mathrm{Re}[U(\vec{r}_0)])$, with Im and Re being the imaginary and real parts, respectively. As said before, Eq. (3) can be computed for different values of $\vec{r}_r$ within the experiment volume to produce a stack of reconstructed images that could be used to produce a 3D recreation of the sample volume, within the axial resolution limits of DLHM [24]. The numerical implementation of Eq. (3) follows a coordinate remapping and change of variables proposed by Kreuzer, aimed to cast this equation into a fast Fourier transform formalism; the detailed process is described in [35].

As in any other microscopy system, the precise control of the spatial resolution and the field of view (FOV) is essential. The spatial resolution in DLHM and related methods has been extensively studied [24,37–41]. For the practical interest of the present work, one can state that two point objects can be distinguished in DLHM if the distance between them Δr is such that

$$\Delta r \ge \frac{\lambda}{2\mathrm{NA}}. \quad (4)$$

In Eq. (4) NAis the effective numerical aperture, which is taken to be the smallest between that of the illuminating point source and that of the recording setup. The NA of the illuminating point source is set by the method used to produce the said source. Conventionally in DLHM, the point source is produced by focusing down the light of a laser onto the surface of a metallic pinhole with a diameter in the order of λ, to render to a maximum illuminating NA of 0.77 [24]; however, alternative developments have been proposed with engineered optical fibers to produce point sources valid for DLHM with NA of 0.88 [42,43]. Similarly, the NA of the recording setup of DLHM is given by the geometry of the arrangement

$$\mathrm{NA} = \frac{W}{2\sqrt{\left(\frac{W}{2}\right)^2 + L^2}} \quad (5)$$

with W the width of the digital camera. In the common practice of DLHM, the NA of the illuminating point source is set up as the upper limit. Hence, the effective NA of the DLHM microscope is usually the one given by the geometry of the recording arrangement, provided that it is always smaller than the one of the illuminating point source.

The FOV of the DLHM microscope is also controlled by the geometry of the recording setup. Upon the condition stated in the last paragraph, imposing the condition that a full illumination of the width W of the camera must be guaranteed, the FOV of DLHM is a circle whose area is given by

$$\mathrm{FOV} = \pi\left(\frac{Wz}{2L}\right)^2. \quad (6)$$

In summary, Eq. (5) and Eq. (6) state that a DLHM microscope could operate at all the theoretically available ranges of spatial resolution and FOV, only if the distances between the point source and the sample and between the point source and the digital camera can be varied independently. This crucial condition has been considered in the design and construction of the open-source, cost-effective, 3D-printed DLHM to be presented in the sections to follow.

3. DESIGN AND CONSTRUCTION OF THE OPEN SOURCE, COST-EFFECTIVE, 3D-PRINTED DLHM

The recognized parameters of the DLHM architecture that determine its performance were taken into account to drive an open-source, cost-effective, and 3D-printable design of a DLHM microscope. The point source, the digital camera, the body of the microscope, and the processing software are the elements that were integrated in a coordinated way to produce a design that can fulfill the expected features in terms of open reproducibility, price, and manufacturability.

A. Point-Source Module

The point source has been recognized as a key element in the overall performance of the DLHM microscopes [34,42,43] and similar architectures [19]. As stated before, in conventional DLHM microscopes, the point source is produced by focusing down the light from a laser or a LED upon the surface of a metallic pinhole with a diameter in the order of the illuminating wavelength. This method, which can produce point sources with NA = 0.77 at most [24], is highly demanding in the required optomechanics, leading to a costly and bulky source with limited mechanical stability [34]. As a response to these unwanted features for a key element of the DLHM microscopes, different options have been explored. Optical pick-up units, particularly those for Blu-ray technology [44], can produce writing/reading spots with a diameter in the order of 300 nm, which, for an illuminating wavelength of 405 nm, imposes NA ≈ 0.85. This figure sets the optical pick-ups as a desirable point source for DLHM or related architectures [19]; however, the reverse engineering needed for its appropriate use hinders a wide range of applications. A very attractive point source for DLHM, supported on engineered optical fibers, has also been developed [34,42,43]; nonetheless, despite the outstanding results achievable with this also cost-effective point source, this development presently lacks the mechanical robustness needed for being the most solid candidate for the point source of DLHM.

Gradient-index (GRIN) lenses [45] and aspheric lenses [20] have also been presented as alternative methods for producing point sources. The former exhibits an excellent optical performance with a reasonable NA, but its price and the needed fine optomechanics for its assembly conceal the possibility of them being utilized in the present work. Aspheric lenses are also available at a wide range of NA, but at a much lower entry price, with easy optomechanical implementation and the possibility of being purchased as a plug-and-play device to be coupled with cost-effective laser diodes; these characteristics rank the aspheric lenses as the most appropriate element to produce a cost-effective, robust, and easy-to-assemble point-source module for DLHM.

Figure 2 shows a 3D rendering of the point source developed for the present microscope. A 5 mW laser diode, costing US$1.03 and operating at 4 VDC, shines 650 nm light; see ① in Fig. 2. The laser light is collected by a NA = 0.65 plug-and-play aspheric lens ②, with a cost of US$4.70; this price includes the retaining holders denoted by ③ in Fig. 2. The laser diode with the assembled aspheric lens is hosted in the 3D-printed housing indicated by ④ in Fig. 2. An effective NA = 0.65 of the built point source was measured following the regular procedure proposed by Mandel *et al*. [46], which assumes a Gaussian beam propagation. According to this method, the NA is related to the change of the full width at half-maximum (FWHM) along a propagation distance ΔZ by

$$\mathrm{NA} = \mathrm{Sin}\left[\mathrm{Tan}^{-1}\left(\frac{\Delta \mathrm{FWHM}}{\sqrt{2\ln 2}\Delta Z}\right)\right], \tag{7}$$

where the FWHM is related to the radius of the beam's spot $w(Z)$ at a distance Z from the aspherical lens by

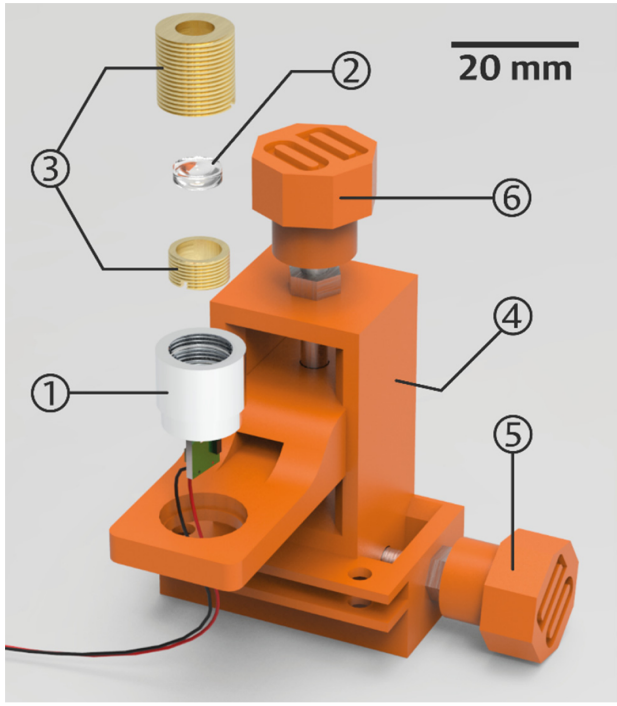

Fig. 2. Point source module for DLHM based on an aspheric lens. ① Laser diode. ② Aspheric lens. ③ Retaining holders. ④ 3D-printed housing. ⑤ Alignment screw. ⑥ Distance control screw.

$$w(Z) = \frac{\mathrm{FWHM}}{\sqrt{2\ln 2}}. \tag{8}$$

In summary, the point-source module developed for this DLHM microscope has a NA = 0.65, allows its alignment with screw ⑤ in Fig. 2, and sets its distance to the sample with screw ⑥ in the same figure. The total cost of the designed and built point source is US$5.79.

B. Digital Camera Module

One of the most expensive materials to build a lensless microscope is the digital camera. In the case of computational microscopy [16], digital cameras with a sensitive area in the order of 8 cm^2 are used to have a FOV in that same order. In DLHM and related architectures [24,32], scientific-grade digital cameras at board level are regularly utilized. In both cases, the cost of these cameras is above the US$1000 mark.

With the aim of developing a cost-effective DLHM microscope, a surveillance camera manufactured by ELP (ELP-USB500W05G-FD100), shown as ① in Fig. 3, is used for the recording of the in-line holograms. This camera has 2592 × 1944 square pixels with 2.2 μm of side length; however, to prevent anisotropies in the parametrization of the system, the sensing area can be cropped to its lower limit of 1944 × 1944 pixels. These dimensions of the sensitivity area indicate that, for the given NA = 0.65 of the built point source, the minimum distance point-source camera that can be utilized is 2.5 mm. This board-level camera has hardware dimensions of 38 mm × 38 mm. A 3D-printed housing, shown as ② in Fig. 3, is attached to two screws, marked as ③ and ④ in the same

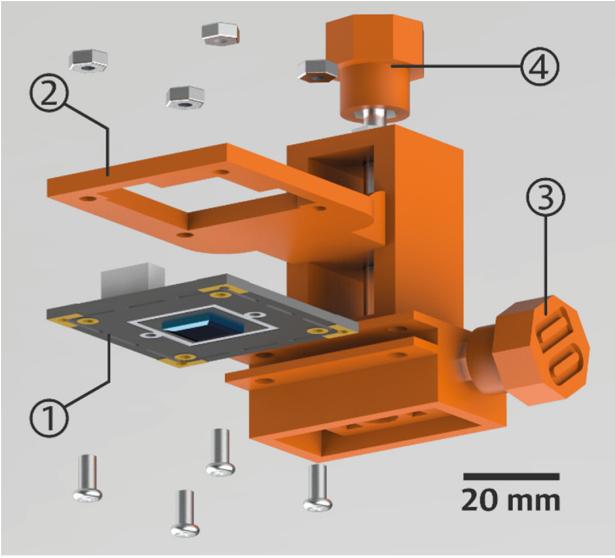

Fig. 3. Digital camera module. ① Digital camera. ② 3D-printed housing. ③ Alignment screw. ④ Height control screw.

figure, that allow the alignment and the height control, in that order; the operation of these screws is detailed in the body of the DLHM microscope section. The cost of the chosen digital camera for this work is US$43.04.

C. Body of the DLHM Microscope

Figure 4 shows the designed and 3D-printed body of the DLHM microscope and the point-source and digital camera modules; see ①,②, and ③ in Fig. 4. The design of the body of the DLHM microscope was done considering all the needed degrees of freedom to make mechanically accessible the limit FOV and spatial resolution dictated by the produced point source and the assembled digital camera. To this aim, the modules attached to the body of the microscope have been equipped with the screws ④ and ⑤. Each of these screws has a 19 mm total travel along the z direction; therefore, the point-source-to-sample distance can be varied from 0 to 19 mm, and the point-source-to-digital-camera distance from 2.5 to 21.5 mm. For the limiting NA = 0.65 set by the built point source, the body of the microscope offers to the user a FOV from 0.023 to 11.24 mm^2 and a spatial resolution from 0.5 to 6.5 µm. For the alignment of the DLHM, an imaginary line perpendicular to the center of the digital camera must cross by the center of the spherical lens, where the point source is produced. To do this alignment, the body of the microscope is also equipped with the screws ⑥ in Fig. 4. The stage of the microscope, marked as ⑦ in Fig. 4, has 50 cm^2 to allow the free and controlled displacement of the microscope slide. This $x - y$ displacement is done through the spring-loaded slide holder, shown as ⑧ in Fig. 4, which offers a travel distance of 7.1 mm along the x axis and 15 mm along the y axis.

The assembled body of the presented DLHM microscope weights less than 280 grams, and the 102 grams of polylactic acid (PLA) needed for its printing cost approximately US$1.60.

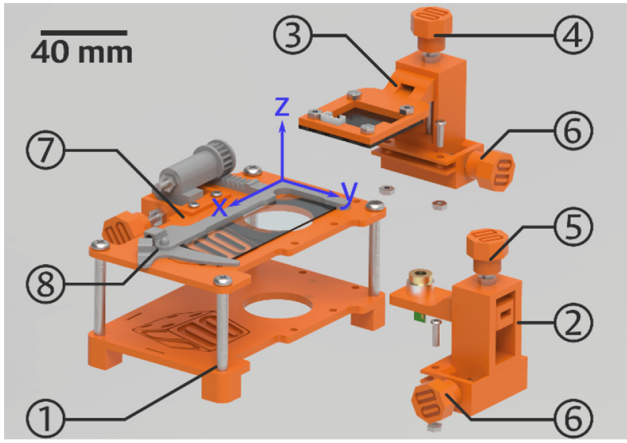

Fig. 4. 3D-printed body of the DLHM microscope. ① Microscope body. ② Point source module. ③ Digital camera module. ④ Screw to change the height of the camera. ⑤ Screw to control de distance of the point source. ⑥ Alignment screws. ⑦ Stage of the microscope. ⑧ Slide holder.

D. Processing Software

The processing of the recorded in-line holograms is done with an open-source ImageJ [47] plugin developed in our group [36]; Fig. 5 shows the graphical user interface of the developed plugin. In group ① of the controls, the user sets up the parameters to perform the reconstruction of the in-line hologram; the names of the images for the hologram and reference can be chosen in the first two drop-drown lists. The wavelength, reconstruction distance, distance from the point source to the camera, and dimensions of the hologram are introduced in the following entry boxes, in that order. The selected parameters are logged into the text field shown in ② of Fig. 5. The processing software offers the user the option of choosing, with the check boxes in group ③ of controls, the type of reconstruction performed, namely, phase, amplitude, intensity, and real or imaginary part of the complex-valued reconstructed wavefield. Group ④ of the controls in Fig. 5 offers the opportunity of running batch reconstructions, moving between reconstruction distances with a fixed step, and changing the plugin settings, which include the input units, the type of scaling for the results, the type of

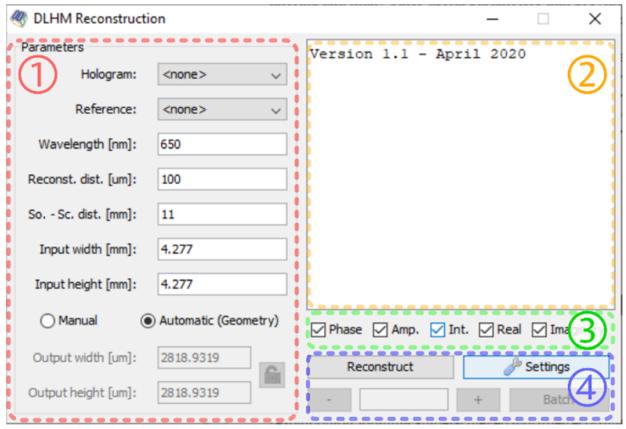

Fig. 5. Graphical user interface of the reconstruction software for the in-line holograms.

optional preprocessing filtering, and many other useful parameters that provide the user with the tools to produce results according to their specific needs. Additionally, the fact that this plugin has been developed for the solid environment of the image processing software of ImageJ [47] powers the processing of the in-line holograms with the full set of useful built-in tools for the representation of the obtained results; for instance, 3D-rendering with a wide set of tunable features like the ones used in this paper. For a complete and detailed description of the processing software, the reader is referred to [36].

4. RESULTS

Following the described design and construction guidelines, a real picture of the manufactured microscope is shown in Fig. 6. The resulting device measures 148.8 mm × 112.3 mm × 121.6 mm (W × L × H) and weighs less than 300 grams; it has an imaging system composed of a 650 nm laser illumination collected by a NA = 0.65 aspherical lens and projected into a CMOS camera with a sensing area of 1944 × 1944 square pixels of 2.2 μm of side length. The microscope has freedom of movement in both the illumination and camera position, allowing adaptation of the FOV and resolution values to the conditions that best suit each specific use case. However, the current implementation does not achieve a complete use of the designed usability ranges; instead, the travel range of the illumination source had to be restricted to stop 2 mm away from the sample stage due to undesirable distortions of the wavefront produced by the aspherical lens in the closest distances. This change limits the maximum achievable resolution and FOV, offering the user an effective FOV from 0.023 to 10 mm^2 and an effective spatial resolution ranging from 1.15 to 6.3 μm.

The differences from the experimental values to the design ones are due to the compensation required to prevent distortions from the aspherical lens used as the illumination source and mechanical differences in the resulting 3D-printed device. These impasses, especially the aspherical illumination distortions near its focal plane, require further research and development that fall beyond the scope of the present work. Nonetheless, the proposed and constructed microscope is capable of producing high-quality images of microscopic objects, even pure-phase ones, at the lowest cost available in the literature for such a system.

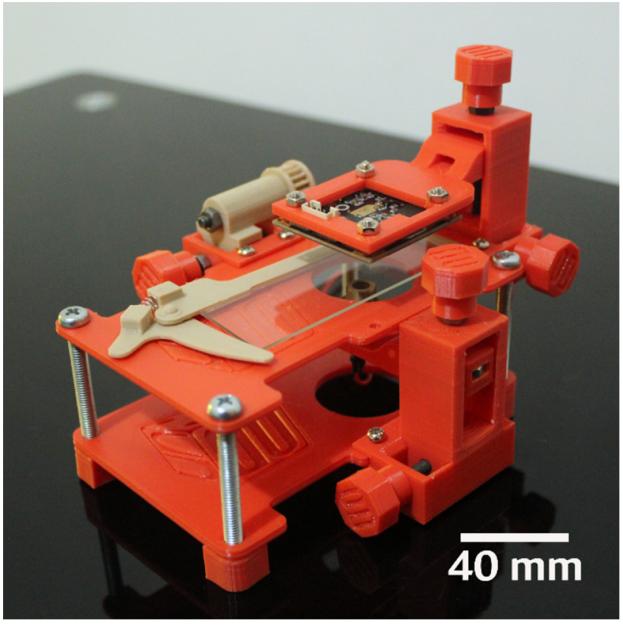

Fig. 6. Picture of the open-source, cost-effective, 3D-printed DLHM microscope.

To test the performance of the open-source, cost-effective, 3D-printed DLHM microscope, spatial resolution and FOV evaluations were done over intensity and phase reconstructions using standardized test targets and a biological sample. To improve the visualization of the results, two recordings were made in each case: one with the diffraction pattern of the sample illuminated by the spherical wavefront, as described in Eqs. (1) and (2), and one with the irradiance distribution of the illuminating wavefront without the sample present. The intensity reconstructions were obtained by backpropagating the contrast hologram, which is calculated as the pointwise difference between the two aforementioned recordings; from Eq. (1), it follows that this subtraction removes the $U_{\mathrm{ref}}(\vec{r})U^{*}_{\mathrm{ref}}(\vec{r})$ term that would otherwise introduce a constant value into the reconstructed field. Similarly, for the phase reconstructions, the recovered fields were divided by the backpropagation of their corresponding reference before computing the phase map; this operation, which is equivalent to the pointwise subtraction of the associated phases, allows compensation of the phase distortion introduced by the carrier wavefront. All these operations, and all the needed processing for the reconstruction of the experimental results, were done with the cited open-source ImageJ plugin and the associated software tools of this same image processing software [36].

A. Spatial Resolution

The evaluation of the spatial resolution of the built microscope was done by imaging a star test target with a nominal height of 150 nm and a USAF 1951 resolution target with a nominal height of 350 nm. Both samples are made of acrylate polymer on glass, allowing them to be considered pure phase objects

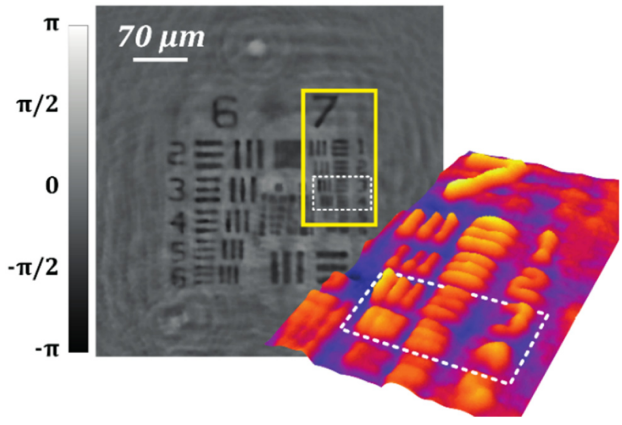

Fig. 7. Phase reconstruction of a pure-phase USAF 1951 target. The accompanying inset shows a 3D representation of the yellow-bounded region of group 7. The test shows a resolution capability between 2.76 and 3.10 μm.

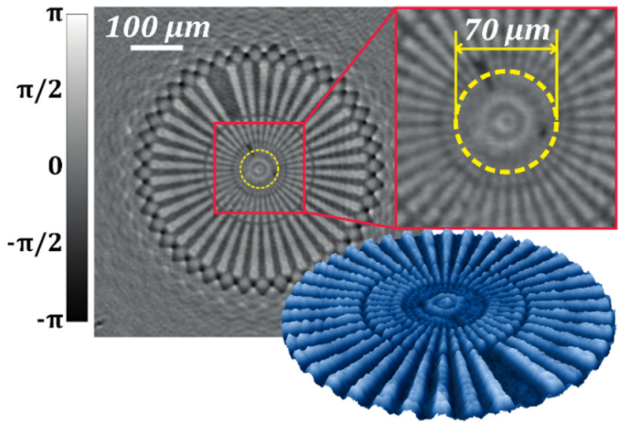

Fig. 8. Phase reconstruction of a pure-phase star test target. The dashed yellow line marks the minimum resolvable circumference, which, for this 40-spoke test, sets the resolution limit at 2.75 μm.

and thus fulfilling the weak scattering condition [25]. Initially, the system was configured with an illumination distance of 10.56 mm, measured from the point source to the digital camera; placing the USAF-1951 resolution target 2.36 mm away from the source of spherical wavefronts, two recordings were made: the hologram and its associated reference as previously described. Figure 7 shows the corresponding phase reconstruction, in which all the features up to element 3 of group 7 can be fully resolved, while element 4 of this same group is only partially resolved. These observations are further supported by the 3D-height profile calculated over the yellow-bounded region of group 7; despite the phase irregularities inherited from the twin-image presence and some coherent noise, the reconstructed image produces an overall good recreation of the USAF-1951 features. From the resolved elements, the resolution capability of the recording geometry can be expected to lie between 2.76 and 3.10 μm.

Similar results are achieved using the star test target while keeping the same illumination distance of 10.56 mm and a point-source-to-sample distance of 2.36 mm. Figure 8 shows the phase reconstruction obtained by the described two-shot experimental procedure. Once again, despite the unavoidable phase distortions, the results show high reconstruction quality and fidelity to the morphology of the sample. According to the manufacturer's information, the employed target has a 400 μm external diameter and 40 identical spokes; therefore, the smallest resolvable circumference, marked by the yellow dashed circle that has a 70 μm diameter, sets the resolution limit for the recording geometry at approximately 2.75 μm, which is consistent with the previous result on the USAF-1951 test.

Finally, if a uniform refraction index of 1.52 is assumed for both samples; as reported by the manufacturer of the target, the average phase delays introduced by the USAF 1951 and the star test correspond to an estimated height of 378 nm and 156 nm, respectively. These values, measured over the features of each test against the mean background value, are in agreement with the nominal values of 350 nm and 150 nm.

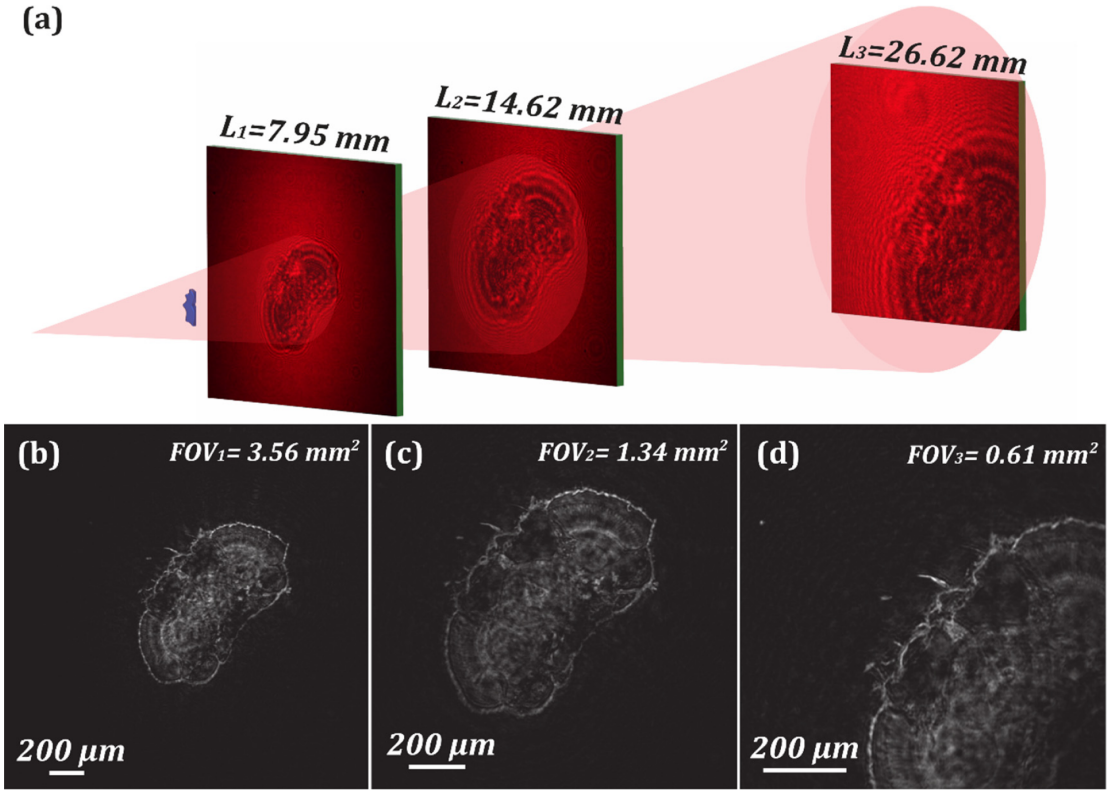

Fig. 9. Intensity reconstructions of a thin section of the head from a Drosophila melanogaster fly with different field of view values. (a) Hologram recording setup for three camera positions and, thus, variable illumination distances. (b),(c),(d) Intensity reconstruction for illumination distances of 7.95,16.62, and 26.62 mm, respectively.

B. Field of View

To test the constructed microscope capability of adjusting the available FOV and achieving different magnifications of the diffraction pattern, a thin section of the head of a Drosophila melanogaster fly has been imaged at different camera positions. Following the description in Eq. (6), by modifying the distance between the sample and the camera, different values of FOV are obtained. Panel (a) of Fig. 9 shows three example positions of the sensor and the hologram that is registered at each illumination distance. Panels (b), (c), and (d) of the same figure show the intensity reconstructions for these three positions, corresponding to illumination distances of 7.95, 14.62, and 26.62 mm, respectively. Each panel, and thus each camera position, has an increasing diffraction pattern magnification due to the larger propagation distance; consequently, as the sensor remains the same size, there is a reduction of the FOV, namely, 3.56, 1.34, and 0.61 mm^2 are obtained for the three considered positions in the same order as before.

C. Common Biological Specimens

As a final usability verification of the open-source, cost-effective, 3D-printed DLHM, two biological samples of common interest were imaged, namely, buccal cells and human blood cells. To demonstrate the label-free imaging capabilities of DLHM over micrometric translucent objects [24,25], these samples were subjected to neither a special preparation process nor any sort staining.

Initially, the microscope was configured with the point source at a distance of 22.51 mm to the camera, and the sample was placed approximately 3 mm away from the source; these specifications set the observable FOV at 0.25 mm^2 and a maximum resolution of 3.3 μm, allowing the effortless visualization of the buccal cells, whose transversal size is typically between 50 and 60 μm. With this configuration, a freshly taken buccal swab sample was imaged in two different regions using the two-shot procedure described at the beginning of this section. The resulting phase reconstructions are shown in Fig. 10, with each panel representing one of the imaged regions. The insets of both panels allow the observation of fine inner details in the cells, including their nuclei as marked by the white arrows.

The illumination distance was then changed to 7.18 mm, and the human blood smear sample was placed as close as possible to the point source to observe the unstained blood cells. Figure 11 summarizes the resulting reconstructions in intensity and phase, taken from two different regions of the sample that were imaged using the aforementioned two-shot procedure. In panel (a), the intensity reconstruction of the first region is shown, containing two red blood cells. The FOV in this reconstruction is wide enough to allow the easy visualization of the erythrocytes, which are magnified in the accompanying insets. Panel (b) shows the phase reconstruction of a second region of the human blood smear sample, clearly including an erythrocyte and a neutrocyte. These two specimens can be further inspected in the 3D renders included as insets of this last panel. Of special interest is the

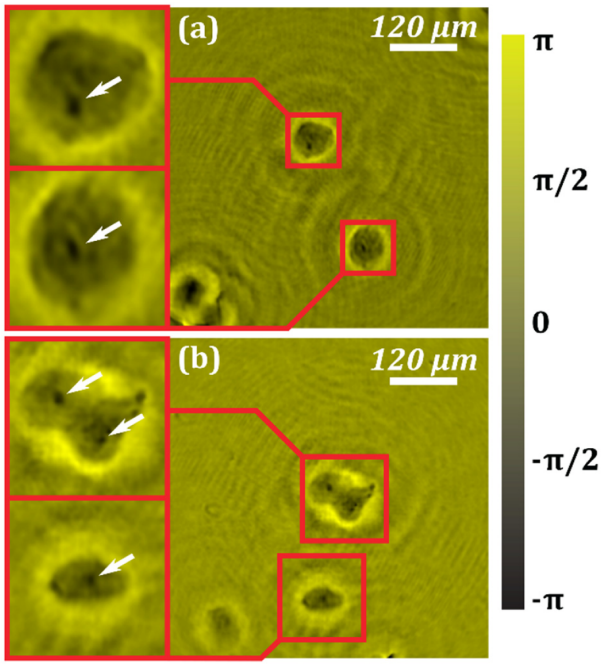

Fig. 10. Phase reconstructions from two different regions of an unstained buccal swab sample. The white arrows in the insets mark the nucleus position of each cell. The color scale bar applies to phase values in both panels.

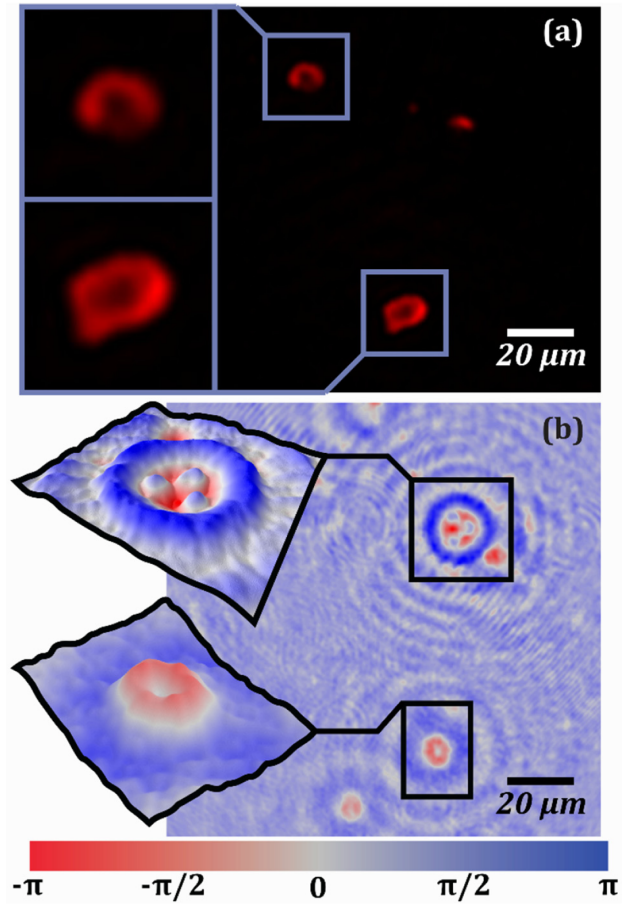

Fig. 11. Reconstruction of an unstained human blood smear sample. (a) Intensity reconstruction of erythrocytes. (b) Phase reconstruction, in a different region of the sample, showing an erythrocyte and a neutrocyte.

neutrocyte, whose characteristic multisegmented nucleus can be seen in both the phase map and the 3D plot.

The results in both Figs. 10 and 11 portray the ability of the open-source, cost-effective, 3D-printed DLHM to achieve trustable visualizations of microscopic objects and biological specimens without any special sample preparation nor labeling process. The high quality of the experimental results and the versatility of the designed and constructed system position the proposed microscope as the most cost-effective digital lensless holographic microscope to date with proven applicability to common interest areas of DLHM.

5. CONCLUSIONS

The design, construction, and testing of the most cost-effective digital lensless holographic microscope to date have been presented. For digital lensless holographic microscopy (DLHM) to work, a point source produces spherical wavefronts that illuminate a sample placed close to the said point source. The diffracted wavefield propagates through the free space to reach a digital camera. The distance between the sample and the digital camera is set in such a way that the free-space propagation guarantees the magnification of the diffracted wavefield to be correctly recorded in the digital camera. The only needed hardware in DLHM is, therefore, a point source and a digital camera. To make the most cost-effective DLHM microscope up to date, the design and building of the body of the microscope via an optimized 3D-printable model have been presented; the said design and building encompass all the needed degrees of freedom to achieve a DLHM setup with variable FOV and spatial resolution that can be utilized in different applications. All the CAD files for the 3D printing and the list of materials with a supplier company will be fully available by request to the authors. The point source has been made by coupling a US$1.03 laser diode to a US$4.70 aspherical lens. This simple setup produces an illuminating point source with a numerical aperture (NA) of 0.65; with this NA at the 650 nm operating wavelength, a maximum theoretical spatial resolution of 500 nm can be achieved. For the recording of the in-line holograms, a surveillance digital camera costing US$43.40 is utilized. The 3D printing of the DLHM microscope body and the slide holder needs, approximately, 102 grams of polylactic acid (PLA), which costs around US$1.60. For the assembly and operation of the DLHM microscope, 20 screws are needed with a joint cost of US$1.00. The former values set an overall price for the materials needed to build the cost-effective DLHM microscope presented in this work at just US$52.82, which thus renders this design the most cost-effective DLHM microscope to date. Optimized software for the recording and processing of the in-line holograms has also been made available in an open-source philosophy, to set up a complete platform of DLHM accessible for everyone, with a special focus on low-resource settings. The proposed platform embraces the state-of-art technology available of DLHM with variable spatial resolutions reaching the micrometer-sized range and FOVs ranging from 0.023 to 11.2 mm^2.

The cost-effective state-of-the-art DLHM microscope has been tested on imaging pure phase resolution test targets and a Drosophila melanogaster head section in phase and intensity, respectively, showing its feasibility on the two modalities of any digital holographic approach to microscopy and evaluating its spatial resolution and variable FOV. Additionally, to show its usability in traditional microscopy imaging applications, human blood cells and buccal cells were imaged; these samples were used without special preparations nor staining, proving the label-free capabilities of DLHM in the designed and constructed system. While the constructed version of the microscope could not reach full-range access to the design parameters, the results support the claimed micrometer-sized spatial resolution and the variable FOV achievable with the US$52.82 DLHM microscope while maintaining high-quality reconstructions of microscopic objects and even pure phase ones.

The presented development of this DLHM microscope shows great promise as a disposable state-of-the-art microscopy tool to be used in remote areas as a point-of-care diagnosis tool, as a teaching tool for modern technologies of microscopy, and/or as a research tool for laboratories with limited resources.

Funding. Universidad Nacional de Colombia (Hermes 49282, Hermes 50210).

Acknowledgment. The authors of this paper acknowledge all the former and present members of the Optics and Opto-digital Processing Group of the Universidad Nacional de Colombia Sede Medellin who have historically contributed to the development of the extremely cost-effective DLHM microscope presented in this work.

Disclosures. The authors declare no conflicts of interest.

REFERENCES

1. J. T. Collins, J. Knapper, J. Stirling, J. Mduda, C. Mkindi, V. Mayagaya, G. A. Mwakajinga, P. T. Nyakyi, V. L. Sanga, D. Carbery, L. White, S. Dale, Z. J. Lim, J. J. Baumberg, P. Cicuta, S. McDermott, B. Vodenicharski, and R. Bowman, "Robotic microscopy for everyone: the openflexure microscope," Biomed. Opt. Express **11**, 2447–2460 (2020).
2. E. Cuche, F. Bevilacqua, and C. Depeursinge, "Digital holography for quantitative phase-contrast imaging," Opt. Lett. **24**, 291–293 (1999).
3. E. Cuche, P. Marquet, and C. Depeursinge, "Simultaneous amplitude-contrast and quantitative phase-contrast microscopy by numerical reconstruction of Fresnel off-axis holograms," Appl. Opt. **38**, 6994–7001 (1999).
4. M. Takeda, H. Ina, and S. Kobayashi, "Fourier-transform method of fringe-pattern analysis for computer-based topography and interferometry," J. Opt. Soc. Am. **72**, 156–160 (1982).
5. E. Cuche, P. Marquet, and C. Depeursinge, "Spatial filtering for zero-order and twin-image elimination in digital off-axis holography," Appl. Opt. **39**, 4070–4075 (2000).
6. J. K. Wallace, S. Rider, E. Serabyn, J. Kühn, K. Liewer, J. Deming, G. Showalter, C. Lindensmith, and J. Nadeau, "Robust, compact implementation of an off-axis digital holographic microscope," Opt. Express **23**, 17367–17378 (2015).
7. T. Beckmann, M. Fratz, A. Schiller, A. Bertz, and D. Carl, "Digital holographic microscopy for 200 € using open-source hard- and software," in *Opt. InfoBase Conf.* (2019), pp. 7–8.
8. M. Rostykus and C. Moser, "Compact lensless off-axis transmission digital holographic microscope," Opt. Express **25**, 16652–16659 (2017).

9. S. Rawat, S. Komatsu, A. Markman, A. Anand, and B. Javidi, "Compact and field-portable 3D printed shearing digital holographic microscope for automated cell identification," Appl. Opt. **56**, D127–D133 (2017).
10. T. O'Connor, A. Doblas, and B. Javidi, "Structured illumination in compact and field-portable 3D-printed shearing digital holographic microscopy for resolution enhancement," Opt. Lett. **44**, 2326–2329 (2019).
11. T. Cacace, V. Bianco, B. Mandracchia, V. Pagliarulo, E. Oleandro, M. Paturzo, and P. Ferraro, "Compact off-axis holographic slide microscope: design guidelines," Biomed. Opt. Express **11**, 2511–2532 (2020).
12. M. K. Kim, *Digital Holographic Microscopy: Principles, Techniques, and Applications* (Springer, 2011).
13. O. Mudanyali, D. Tseng, C. Oh, S. O. Isikman, I. Sencan, W. Bishara, C. Oztoprak, S. Seo, B. Khademhosseini, and A. Ozcan, "Compact, light-weight and cost-effective microscope based on lensless incoherent holography for telemedicine applications," Lab Chip **10**, 1417–1428 (2010).
14. D. Tseng, O. Mudanyali, C. Oztoprak, S. O. Isikman, I. Sencan, O. Yaglidere, and A. Ozcan, "Lensfree microscopy on a cellphone," Lab Chip **10**, 1787–1792 (2010).
15. M. Lee, O. Yaglidere, and A. Ozcan, "Field-portable reflection and transmission microscopy based on lensless holography," Biomed. Opt. Express **2**, 2721–2730 (2011).
16. E. McLeod and A. Ozcan, "Microscopy without lenses," Phys. Today **70**, 50–56 (2017).
17. T. G. Dimiduk, E. A. Kosheleva, D. Kaz, R. McGorty, E. J. Gardel, and V. N. Manoharan, "A simple, inexpensive holographic microscope," in *Biomedical Optics and 3-D Imaging*, OSA Technical Digest (CD) (Optical Society of America, 2010), paper JMA38.
18. T. Shimobaba, Y. Taniguchi, A. Shiraki, N. Masuda, and T. Ito, *Portable and low-cost digital holographic microscopy using web camera, point light source LED and open-source libraries* (2012), paper JM3A.50.
19. M. Sanz, J. Á. Picazo-Bueno, L. Granero, J. Garciá, and V. Micó, "Compact, cost-effective and field-portable microscope prototype based on MISHELF microscopy," Sci. Rep. **7**, 43291 (2017).
20. M. Sanz, M. Trusiak, J. García, and V. Micó, "Variable zoom digital in-line holographic microscopy," Opt. Laser Eng. **127**, 105939 (2020).
21. S. Amann, M. von Witzleben, and S. Breuer, "Open-source 3D-printed digital inline holographic microscope for low-cost cellular imaging," Proc. SPIE **11306**, 113060B (2020).
22. H. J. Kreuzer, H. W. Fink, H. Schmid, and S. Bonev, "Holography of holes, with electrons and photons," J. Microsc. **178**, 191–197 (1995).
23. W. Xu, M. H. Jericho, I. A. Meinertzhagen, and H. J. Kreuzer, "Digital in-line holography for biological applications," Proc. Natl. Acad. Sci. USA **98**, 11301–11305 (2001).
24. J. Garcia-Sucerquia, W. Xu, S. K. Jericho, P. Klages, M. H. Jericho, and H. J. Kreuzer, "Digital in-line holographic microscopy," Appl. Opt. **45**, 836–850 (2006).
25. D. Gabor, "A new microscopic principle," Nature **161**, 777–778 (1948).
26. J. W. Goodman, *Introduction to Fourier Optics*, 3rd ed. (Roberts & Company, 2005).
27. S. K. K. Jericho, J. Garcia-Sucerquia, W. Xu, M. H. H. Jericho, and H. J. J. Kreuzer, "Submersible digital in-line holographic microscope," Rev. Sci. Instrum. **77**, 043706 (2006).
28. S. Seo, T. W. Su, A. Erlinger, and A. Ozcan, "Multi-color LUCAS: Lensfree on-chip cytometry using tunable monochromatic illumination and digital noise reduction," Cell. Mol. Bioeng. **1**, 146–156 (2008).
29. S. Seo, T.-W. Su, D. K. Tseng, A. Erlinger, and A. Ozcan, "Lensfree holographic imaging for on-chip cytometry and diagnostics," Lab Chip **9**, 777–787 (2009).
30. W. Bishara, T.-W. Su, A. F. Coskun, and A. Ozcan, "Lensfree on-chip microscopy over a wide field-of-view using pixel super-resolution," Opt. Express **18**, 11181–11191 (2010).
31. M. Sanz, J. A. Picazo-Bueno, J. García, and V. Micó, "Improved quantitative phase imaging in lensless microscopy by single-shot multi-wavelength illumination using a fast convergence algorithm," Opt. Express **23**, 21352–21365 (2015).
32. M. Sanz, J. Á. Picazo-Bueno, L. Granero, J. García, and V. Micó, "Multi-illumination single-holographic-exposure lensless Fresnel (MISHELF) microscopy using 4 channels," in *Imaging and Applied Optics (COSI, IS, MATH, PcAOP)*, OSA Technical Digest (Optical Society of America, 2019), paper JW2A.1.
33. J. Garcia-Sucerquia, "Color lensless digital holographic microscopy with micrometer resolution," Opt. Lett. **37**, 1724–1726 (2012).
34. B. Patiño-Jurado, J. F. Botero-Cadavid, and J. Garcia-Sucerquia, "Cone-shaped optical fiber tip for cost-effective digital lensless holographic microscopy," Appl. Opt. **59**, 2969–2975 (2020).
35. M. H. Jericho and H. J. Kreuzer, "Point source digital in-line holographic microscopy," in *Coherent Light Microscopy*, P. Ferraro, A. Wax, and Z. Zalevvsky, eds. (Springer-Verlag, 2011), pp. 3–30.
36. C. Trujillo, P. Piedrahita-Quintero, and J. Garcia-Sucerquia, "Digital lensless holographic microscopy: numerical simulation and reconstruction with ImageJ," Appl. Opt. **59**, 5788–5795 (2020).
37. J. Garcia-Sucerquia, D. C. Alvarez-Palacio, and H. J. Kreuzer, "High resolution Talbot self-imaging applied to structural characterization of self-assembled monolayers of microspheres," Appl. Opt. **47**, 4723–4728 (2008).
38. M. Kanka, R. Riesenberg, P. Petruck, and C. Graulig, "High resolution (NA=0.8) in lensless in-line holographic microscopy with glass sample carriers," Opt. Lett. **36**, 3651–3653 (2011).
39. P. Petruck, R. Riesenberg, and R. Kowarschik, "Optimized coherence parameters for high-resolution holographic microscopy," Appl. Phys. B **106**, 339–348 (2012).
40. V. Micó and Z. Zalevsky, "Superresolved digital in-line holographic microscopy for high-resolution lensless biological imaging," J. Biomed. Opt. **15**, 046027 (2010).
41. J. Garcia-Sucerquia, W. Xu, S. K. K. Jericho, M. H. H. Jericho, P. Klages, and H. J. J. Kreuzer, "Resolution power in digital in-line holography," Proc. SPIE **6027**, 60272H (2006).
42. B. Patiño-Jurado, J. F. Botero-Cadavid, and J. Garcia-Sucerquia, "Step-index optical fibers with 0.88 numerical aperture," J. Lightwave Technol. **37**, 3734–3739 (2019).
43. B. Patiño-Jurado, J. F. Botero-Cadavid, and J. Garcia-Sucerquia, "Optical fiber point-source for digital lensless holographic microscopy," J. Lightwave Technol. **37**, 5660–5666 (2019).
44. E. E. Te Hwu and A. Boisen, "Hacking CD/DVD/Blu-ray for biosensing," ACS Sens. **3**, 1222–1232 (2018).
45. E. Serabyn, K. Liewer, C. Lindensmith, K. Wallace, and J. Nadeau, "Compact, lensless digital holographic microscope for remote microbiology," Opt. Express **24**, 28540–28548 (2016).
46. L. Mandel, E. Wolf, and P. Meystre, "Optical coherence and quantum optics," Am. J. Phys. **64**, 1438 (1996).
47. C. A. Schneider, W. S. Rasband, and K. W. Eliceiri, "NIH image to ImageJ: 25 years of image analysis," Nat. Methods **9**, 671–675 (2012).

Single-shot pseudostochastic speckle noise reduction in numerical complex-valued wavefields

Carlos Buitrago-Duque,[a] Raúl Castañeda,[a,b] and Jorge Garcia-Sucerquia[a,*]
[a]Universidad Nacional de Colombia Sede Medellín, School of Physics, Medellín, Colombia
[b]The University of Memphis, Department of Electrical and Computer Engineering, Memphis, Tennessee, United States

Abstract. A single-shot procedure to reduce speckle noise in numerically computed complex-valued wavefields is presented. The method is supported by the possibility of numerically producing multiple speckle realizations of a calculated complex-valued wavefield to reduce the speckle noise through a noncoherent superposition of the produced realizations. Although the method is applied to digital holographic microscopy, it could be utilized in other techniques where a numerical representation of the complex-valued wavefield of interest can be obtained. Experimental results with nonbiological and biological samples are presented to support the feasibility of the method. © *2020 Society of Photo-Optical Instrumentation Engineers (SPIE)* [DOI: 10.1117/1.OE.59.7.073107]

Keywords: speckle; digital holographic microscopy; image enhancement; coherent imaging.

Paper 20200519 received May 3, 2020; accepted for publication Jul. 17, 2020; published online Jul. 31, 2020.

1 Introduction

Coherent imaging has pros and cons that should be weighed at the time of deciding on its use. Among the pros, one can consider that the use of coherent light sources to produce steady interference patterns makes possible the quantitative label-free imaging of phase objects[1,2] and/or the contactless surface imaging of reflective samples;[1,3,4] while transparent objects code their refractive index and topography into the phase information of a complex-valued wavefield that propagates through, the height maps of reflective objects are coded into the phase of a complex-valued wavefield reflected on the surface of the sample.[1,4] In either case, the phase information can be retrieved through different approaches that analyze, for instance, in digital holographic microscopy (DHM), the steady interference pattern produced by the coherent superposition of a reference wave, and the wavefield propagating through or reflected from the sample. Unfortunately, among the cons, one must consider that the use of coherent light sources to produce steady interference patterns introduces coherent noise known as speckle.[5] The speckle noise results from the interference of the multiple wavefields with random phases emitted by scatterers that compose the specimens.[5] Although the speckle phenomenon has been utilized in diverse metrological methods such as digital speckle pattern interferometry,[6] it can be a ruining factor in the performance of coherent imaging systems. Knowing the importance of coherent imaging and recognizing the perturbations introduced by the speckle noise, multiple approaches have been proposed in the literature to diminish its deleterious effects. Overall, the methods can be classified into three main categories: (i) numerical[7–11] for those that use a wide type of image processing tools to enhance the quality of the recovered images from the coherent imaging system; (ii) physical[12–14] for those that use the knowledge of the underlying physics that produces the speckle noise to introduce variations in the optical set ups aimed to reduce the unwanted effects, for instance, the reduction of the spatial coherence of the light source to diminish the contrast of the speckle noise;[15] and (iii) those that combine (i) and (ii).[16–20]

Among the great number of proposals to reduce the speckle noise in numerical coherent imaging, those that use a single-shot image have received special interest due to their applicability to the imaging of dynamical processes with enhanced signal-to-noise ratios.[7,10,20,21] In this

*Address all correspondence to Jorge Garcia-Sucerquia, E-mail: jigarcia@unal.edu.co

paper, a method to reduce the speckle noise in numerically recovered complex-valued wavefields that use a single-shot image as input is presented. Even though the feasibility of the method is shown in complex-valued wavefields retrieved from DHM, its principle can be applied to complex-valued wavefields numerically recovered from any other coherent imaging method. The speckle noise is reduced using the proposed method in coherent images of a reflective United States Air Force (USAF) 1951 test target, a vegetal cell of *Borojoa patinoi*, and red blood cells (RBCs).

2 Pseudostochastic Speckle Reduction in Complex-Valued Wavefields

Let us consider a numerically retrieved complex-valued wavefield $\psi(x, y)$ for the point (x, y) of the form

$$\begin{aligned}\psi(x, y) &= A(x, y)\exp[i\phi(x, y)]\\ \psi(x, y) &= \mathrm{Re}[\psi(x, y)] + i\mathrm{Im}[\psi(x, y)],\end{aligned} \tag{1}$$

where $A(x, y)$ and $\phi(x, y)$ are the amplitude and phase, respectively; Re and Im are the real and imaginary parts of the complex-valued wavefield, respectively. While the amplitude is proportional to the transmittance or reflectance of the imaged sample, the phase codes the refractive index and topographic map for transmissive samples and the height map for reflective samples. When such a sample is coherently imaged, either by transmission or by reflection, the phase $\phi(x, y)$ can be understood to be composed of a deterministic and random portions, such that one can write

$$\phi(x, y) = \phi_{\mathrm{DET}}(x, y) + \phi_{\mathrm{RAN}}(x, y). \tag{2}$$

The deterministic portion $\phi_{\mathrm{DET}}(x, y)$ is introduced in the wavefield by the object itself due to the refractive index and topography if the object is imaged by transmission, or the height map if the object is imaged by reflection. The random portion $\phi_{\mathrm{RAN}}(x, y)$ can be then linked to the speckle noise produced by the steady interference of the wavefields emitted by randomly distributed scatterers in or over the sample for the transmissive or reflective samples, respectively. Within this context, the methods that reduce the speckle noise by the superposition of multiple images of the same scene with uncorrelated speckle noise can be understood as a superposition of images that carry the same deterministic phase $\phi_{\mathrm{DET}}(x, y)$ but different random phases $\phi_{\mathrm{RAN}}(x, y)$. Therefore, if a numerically retrieved complex-valued wavefield $\psi(x, y)$ affected by speckle noise is understood in the way described above, one can computationally generate a partially uncorrelated complex-valued wavefield $\psi'(x, y)$ by saving the deterministic component while the random portion is numerically modified. To produce the partially uncorrelated complex-valued wavefield, one can, for instance, save the deterministic portion in the imaginary part while introducing a numerical realization of the speckle noise in the real part modeled as a random set of numbers. The reduction of the speckle noise is, therefore, achieved by the uncorrelated superposition of N numerically generated complex-valued wavefields, such that the n'th realization of those wavefields can be written as

$$\psi'_n(x, y) = \{\mathrm{Re}[\psi(x, y)] + r_n(x, y)\} + i\mathrm{Im}[\psi(x, y)], \tag{3}$$

where $r_n(x, y)$ is a set of random numbers representing a pseudospeckle realization. The N realizations are then superimposed and averaged to produce a synthetic reconstruction with reduced speckle noise, either in amplitude,

$$|\psi_{\mathrm{NR}}(x, y)| = \frac{1}{N}\sum_{n=1}^{N}|\psi_n(x, y)|, \tag{4}$$

or phase,

$$\phi_{\mathrm{NR}}(x, y) = \frac{1}{N}\sum_{n=1}^{N}\mathrm{atan}\,2\left\{\frac{\mathrm{Im}[\psi_n(x, y)]}{\mathrm{Re}[\psi_n(x, y)]}\right\}, \tag{5}$$

with the function atan2 providing a 2π-module phase map. As $\psi_{\mathrm{NR}}(x,y)$ includes the complete information introduced by the object in the deterministic phase and multiple realizations of the speckle noise in the random phase, any feature of the complex-valued wavefield computed from it, namely its amplitude as in Eq. (4) or phase as in Eq. (5), reproduces the overall information of the sample with reduced speckle noise because of the incoherent superposition of the partially correlated numerically generated complex-valued wavefields. Two questions can arise regarding this description: (i) is it equivalent to add the random set of numbers to either the real or imaginary part of the complex-valued wavefield? and (ii) what values should the random noises take for the method to work? To answer both questions, the amplitude and phase can be computed after adding the random set of numbers to either the real or imaginary part of the complex-valued wavefield. If the random set of number is added to the real part, the amplitude of the n'th realization is calculated as

$$\begin{aligned} A'_n(x,y) &= \sqrt{\{\mathrm{Re}[\psi(x,y)] + r_n(x,y)\}^2 + \{\mathrm{Im}[\psi(x,y)]\}^2} \\ &= A(x,y)\sqrt{2\frac{r_n(x,y)}{A(x,y)}\ \cos[\phi(x,y)] + \frac{r_n^2(x,y)}{A^2(x,y)}}. \end{aligned} \tag{6}$$

The corresponding phase is calculated as

$$\begin{aligned} \phi'_n(x,y) &= \mathrm{atan2}\left(\frac{\mathrm{Im}[\psi(x,y)]}{\mathrm{Re}[\psi(x,y)] + r_n(x,y)}\right) \\ &= \mathrm{atan}\,2\left(\frac{\sin[\phi(x,y)]}{\cos[\phi(x,y)] + \frac{r_n(x,y)}{A(x,y)}}\right). \end{aligned} \tag{7}$$

If the random set of number is added to the imaginary part of the complex-valued wavefield instead, the amplitude of the n'th realization is calculated as

$$\begin{aligned} A''_n(x,y) &= \sqrt{\{\mathrm{Re}[\psi(x,y)]\}^2 + \{\mathrm{Im}[\psi(x,y) + r_n(x,y)]\}^2} \\ &= A(x,y)\sqrt{2\frac{r_n(x,y)}{A(x,y)}\ \sin[\phi(x,y)] + \frac{r_n^2(x,y)}{A^2(x,y)}}. \end{aligned} \tag{8}$$

The corresponding phase is given by

$$\begin{aligned} \phi'_n(x,y) &= \mathrm{atan}\,2\left(\frac{\mathrm{Im}[\psi(x,y)]}{\mathrm{Re}[\psi(x,y)] + r_n(x,y)}\right) \\ &= \mathrm{atan}\,2\left(\frac{\sin[\phi(x,y)] + \frac{r_n(x,y)}{A(x,y)}}{\cos[\phi(x,y)]}\right). \end{aligned} \tag{9}$$

Therefore, by comparing the corresponding equations from Eqs. (6)–(9), the two former questions can be answered: (i) the effect of the random noise addition to the complex-valued wavefield is completely equivalent whether it is done on the real or imaginary part. When there is a contrast shifting in the amplitude, the resulting phase evolution is inverted as the difference between the real or imaginary noise addition is reflected on the numerator or denominator of the function. In both cases, the amplitude and phase information are intertwined and mutually dependent on each other. (ii) From Eqs. (7) and (9), the valid values for $r_n(x,y)$ can be studied. As both the sine and cosine in these equations may vary between -1 and 1, the added noise should be a small fraction of the original amplitude such that the resulting phase is not far deviated from that of the object information; that is, $r_n(x,y) \ll A(x,y)$. Thus, the random numbers should be such that $r_n(x,y) = \mathrm{rand}[0, K \times A(x,y)]$ for $K \ll 1$. If such a condition is met, the last term of Eq. (6) becomes negligible, and the amplitude reduces to $A'_n(x,y) \approx A(x,y)\sqrt{2\frac{r_n(x,y)}{A(x,y)}\ \cos[\phi(x,y)]}$; consequently, the resulting amplitude is a scaled

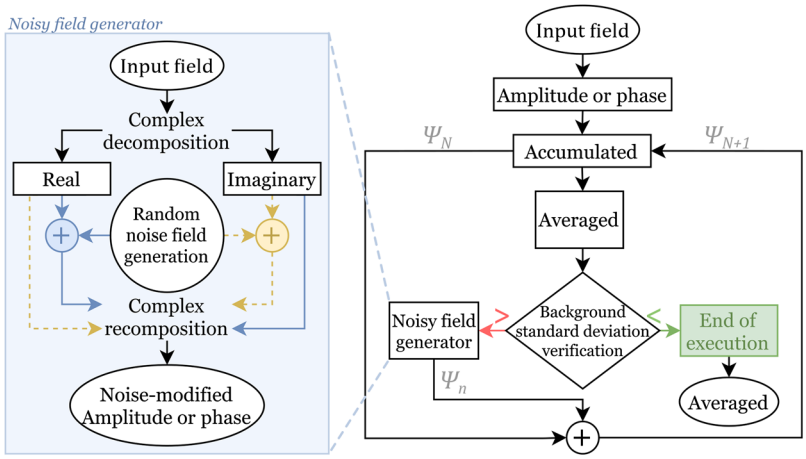

Fig. 1 Flowchart of the proposed method for speckle reduction by averaging pseudostochastic noisy wavefields.

version of the original amplitude with the scaling factor depending on both the original value of the amplitude and its associated phase value. The same reasoning is valid starting from Eq. (8).

In Fig. 1, the flowchart of the proposed method is presented. From the numerically produced complex-valued wavefield, an input field, either its amplitude or phase, is computed to apply the speckle reduction method. The chosen feature of the wavefield is stored in an accumulated variable from which its average is calculated. The standard deviation is measured on the background of the averaged wavefield to use its value as the criterion to stop the application of the process. If the said standard deviation is greater than the sought value, a new noisy wavefield is produced from which the chosen feature of the wavefield is computed to be accumulated and averaged to follow the process just described. The noisy wavefield generator in each iteration takes the input field to decompose it into its real and imaginary parts; to either of these parts, a random noise field with pointwise values ranging from 0 to $KA(x, y)$ is added to produce a new noisy wavefield through the complex recomposition of the modified part with the nonmodified one. The chosen feature of the wavefield is computed to be inputted to the accumulated variable. The possibility of modifying either the real or imaginary part is shown in the flowchart by means of the dashed and solid lines. If the random noise field is added to the real part, the imaginary part is kept with no modification; the complex recomposition is, therefore, done with the modified real part with the nonmodified imaginary part (see solid lines in the flowchart). The noisy wavefield can also be produced by modifying the imaginary part and retaining no modification the real part (see dashed lines in the flowchart).

In the following section, the proposed method is applied to nonbiological and biological samples to show its feasibility on diminishing the speckle noise in experimentally computed complex-valued wavefields.

3 Experimental Results

The proposed method has been tested with complex-valued wavefields retrieved from an off-axis DHM operating in dual mode, that is, reflection and transmission, following the schematic in Fig. 2. The DHM microscope was implemented to operate at an illumination wavelength of $\lambda = 633$ nm produced from a laser manufactured by Uniphase and coupled to a patch cable of SM600 optical fiber. The holograms were recorded in a Thorlabs CMOS camera with 1280×1024 square pixels of 6-μm side lengths, connected to a midrange laptop via universal serial bus (USB) 2.0. The complete optical set up was built based on the Cage System by Thorlabs to ensure enhanced mechanical stability and simplicity of hardware. For imaging the nonbiological reflective samples, the DHM was configured in reflection mode[4] (see the dashed-line arrows in Fig. 2), and the biological transmissive samples were imaged in transmission mode[22,23] (see the solid-line arrows in Fig. 2). For both modes, the DHM was set up in an afocal-telecentric

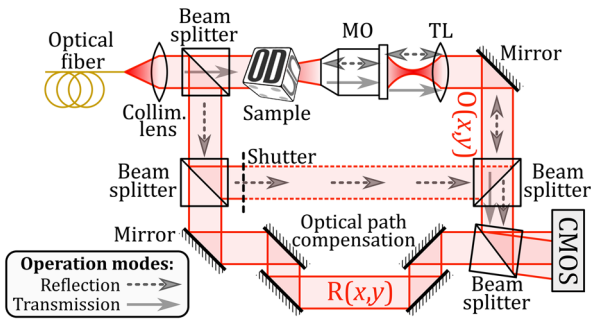

Fig. 2 Experimental layout of off-axis DHM for operation in either reflection or transmission mode. The lower-left convention applies to the optical path for the object wave in each mode.

architecture, such that any phase perturbation is minimized[24,25] and the tilt off-axis phase is eliminated accordingly.[26]

In a first experiment, a reflective USAF 1951 test target was imaged using a $40\times/0.65$ infinity-corrected microscope objective and a 200-mm focal length tube lens. The directly reproduced phase map is shown in Fig. 3(a). Despite the overall good quality of the reproduced phase map and the possibility of resolving the complete target, the enlarged area of the square bounded elements of group number 7 shows a significant amount of noise surrounding the features. The apparently small amount of coherent noise exhibited by these results is due to the object utilized in this experiment and the refinement of the set up. The former was made by depositing a thin aluminum film on a regular USAF 1951 test target, resulting in a "flat" mirror whose features have heights in the order of 80 nm; the low roughness of this object, added to the very clean surfaces of all the optical elements in the set up, produces the very small speckle noise observed in the reproduced image of the USAF.

For this sample, the proposed method was then iteratively applied. The standard deviation, measured over the background region bounded by the green square in the upper-left corner of the object, was used as the control metric with 0.12 rad set as the desired threshold. A 6-nm uncertainty, which corresponds to the phase standard deviation of 0.12 rad, is consistent with the possibility of providing interferometric-based measurements with uncertainties of the order of $\lambda/100$.[27] Figure 3(c) shows the evolution of the standard deviation and some interim results over the same region enlarged in Fig. 3(a). The sought value is finally reached after superposing 36 uncorrelated wavefields whose average produced the phase map shown in Fig. 3(b).

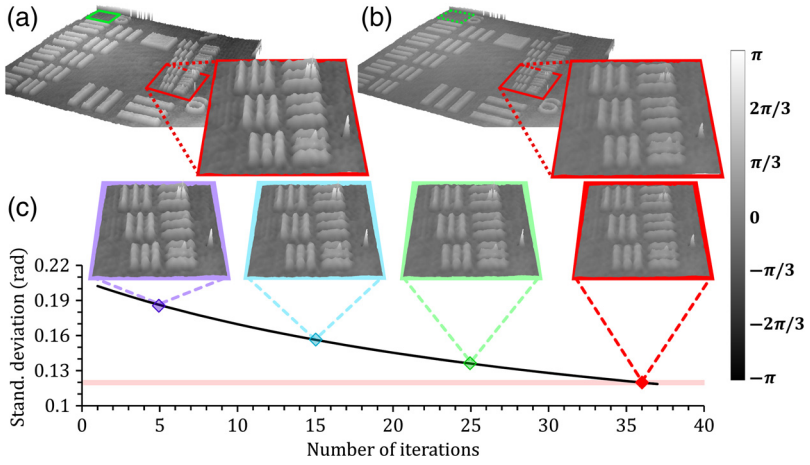

Fig. 3 Denoising process with the proposed method over height maps of the reflective USAF 1951 test target. Phase map obtained (a) before and (b) after the reduction of speckle noise. The enlarged areas bounded by red squares in these panels show the elements 4 to 6 of group 7 before and after the reduction of speckle noise. (c) Standard deviation evolution measured in the background region bounded by the green square in the upper-left corner in (a) and (b); the insets show interim results. Color scale bar applies to the three-dimensional images in all panels.

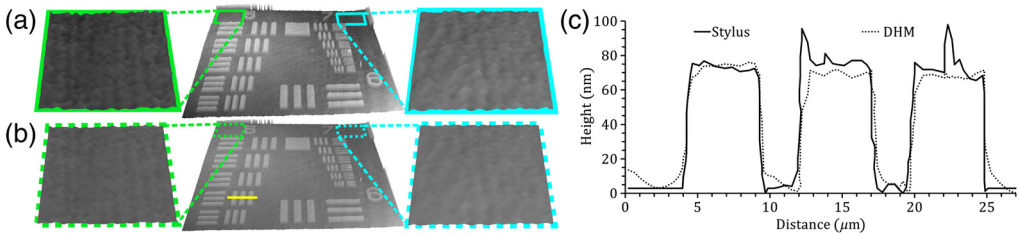

Fig. 4 Verification of the denoising result of the reflective USAF 1951 test target. Phase map obtained (a) before and (b) after the reduction of speckle noise; the enlarged areas show the background noise before and after the reduction of speckle noise. (c) Profiles along the yellow line over element 5 of group 6 in (b), measured with the profilometer (solid line) and with the DHM (dotted line) after the reduction of the speckle noise.

The corresponding enlarged area of elements 3 to 6 of group number 7 presented in the inset shows a more uniform background, as is to be expected from a flat mirror.

The effective reduction in the speckle noise can be further seen in Fig. 4, with enlarged areas over two different background regions for the original phase map, in Fig. 4(a), and the denoised map, in Fig. 4(b). Additionally, to compare the height measurements obtained from the phase map, which were computed from the corresponding phase maps via $H(x,y) = \lambda\phi(x,y)/4\pi$,[28] and ensure that the results of the method can still be used as quantitative phase information, the height $H(x,y)$ was measured with a calibrated stylus profilometer along the yellow line over element 5 of group number 6. The stylus measurement is represented by the solid line in Fig. 4(c) and compared with the corresponding profile over the phase map, as shown by the dotted line in Fig. 4(c). The height measurement of the profilometer averaged 73 ± 3 nm; the anomalous peaks observed in the measured profile are due to mechanical instabilities of the tabletop device utilized to make the measurement. The height of the target's bars, as obtained from the phase map, measured a global value of 223 nm, against a background of 151 nm, leading to an overall height of 72 ± 6 nm. The agreement between both measurements of the height, with the profilometer and the phase map, indicates the suitability of the proposed method to reduce the speckle noise in quantitative phase imaging systems.

With the same control parameter of 0.12 rad measured in the background region of its corresponding phase map, the proposed method to reduce the speckle noise was applied to image a cell of *Borojoa patinoi*. This biological sample was imaged in the afocal-telecentric DHM operating in transmission mode at a wavelength of 633 nm, with a microscope composed of a $40\times/0.65$ infinity-corrected microscope objective and a 200-mm focal length tube lens. In Fig. 5, the quantitative phase images before and after the reduction of the speckle noise are shown in Figs. 5(a) and 5(b), respectively. For this sample, the sought 0.12-rad uncertainty is reached after the superposition of 50 images. Intensity images can also be computed from the resulting complex-valued wavefield with reduced speckle noise, as shown in Figs. 5(c) and 5(d) before and after, respectively, and the application of the proposed method to reduce the coherent noise. The visual appearance of these intensity images reveals the improvement attributed to the application of the method. That improvement can be quantified by measuring the contrast of the speckle noise, computed as $C = \sigma_I/\overline{I}$. Here, σ_I is the standard deviation and $\overline{I}$ is the average of the intensity.[5] The image in Fig. 5(c), for which the contrast of the speckle noise can be assumed to be unitary, has a limited visualization of the cell details. After the application of the proposed method to reduce the speckle noise, the contrast of the speckle is reduced to 0.5, easing the visualization of details of the sample, such as the cell wall in the enlarged areas of the figure.

The method to reduce the speckle noise has also been applied to phase images of RBCs made in the afocal-telecentric DHM operating with a $40\times/0.65$ infinity-corrected microscope objective and a 200-mm focal length tube lens. Figure 6 shows the phase maps of the RBCs before [Fig. 6(a)] and after [Fig. 6(b)] the application of the method. The sought 0.12-rad standard deviation on the phase map over an area with no sample, used as the control parameter, is reached in this experiment after the superposition of 42 uncorrelated complex-valued wavefields. Before the application of the noise reduction method, the phase map of the RBCs looks quite

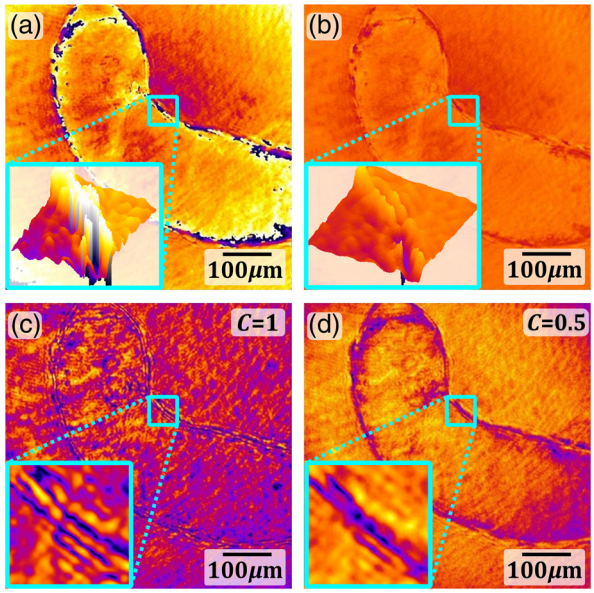

Fig. 5 Images of a cell of *Borojoa patinoi*. (a)–(c) Before and (b)–(d) after the application of the proposed method to reduce the speckle noise. (a) and (b) Quantitative phase images and (c) and (d) intensity images. In this experiment, 26 uncorrelated wavefields are superimposed. The enlarged areas show the cell wall.

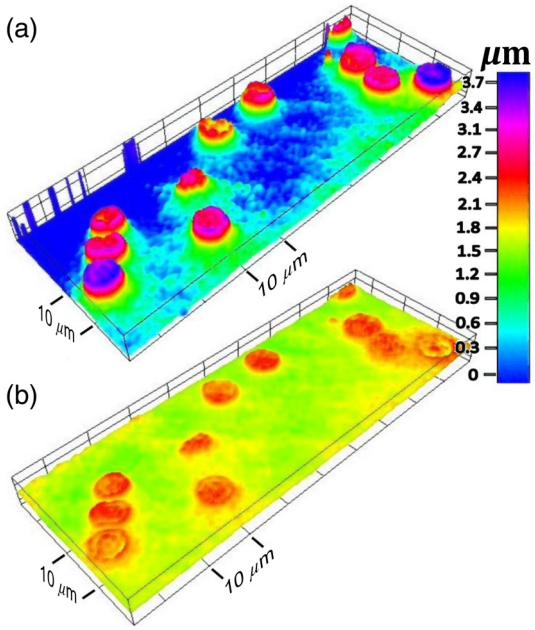

Fig. 6 RBCs imaged with transmission DHM. (a) Phase map of the RBCs prior to the application of the noise reduction proposed method. (b) Phase map after noise reduction. Color scale bar applies to both (a) and (b). To reduce the speckle noise in this experiment, we have superimposed 14 uncorrelated wavefields.

inhomogeneous, especially in the background area with no RBCs where variations on the phase of the order of 0.73 rad can be measured. After the application of the noise reduction method, the evenness of the same areas is sensibly improved. Considering a mean index of refraction for the RBCs of 1.406,[29] the average measurement of the optical thickness of the RBCs is $\sim$1.2 μm, which is in good agreement with the value regularly reported for normal RBCs.

4 Conclusions

In summary, a single-shot method to reduce the speckle noise in numerically computed complex-valued wavefields has been presented. The speckle noise, originated from the use of coherent light sources in imaging systems to gather the information of the sample, can be understood as the random component of the total phase of the complex-valued wavefield that joins the deterministic phase introduced by the specimen itself. Within the framework of this idea, the methods that reduce speckle noise by superimposing uncorrelated complex-valued wavefields can be understood as the addition of multiple complex-valued wavefields that carry the same deterministic phase but different random-phase realizations. The performance of the proposed method is, therefore, supported by the possibility of numerically expressing a set of random realizations of the speckle noise, either in the real or imaginary part of the numerical complex-valued wavefield. The deterministic phase of the recovered complex-valued wavefield is saved in the part where no realizations of the speckle noise are performed. The random realizations are performed over the complex-valued wavefield obtained from a single-shot experiment. The resulting complex-valued wavefields are added uncorrelatedly, leading to a new complex-valued wavefield with reduced speckle noise from which amplitude or phase images with reduced speckle noise can be computed. Although the method has been validated in this work with experimental data from DHM, it can be applied to any other coherent imaging technique where a numerical representation of the complex-valued wavefield of interest can be obtained. The method has been tested with images of a reflective USAF 1951 test target, and with complex-valued wavefields of a *Borojoa patinoi* cell and RBCs. For all the cases, the images before and after the application of the method to reduce the speckle noise are compared. The main advantages of the proposed technique are its single-shot nature and its suitability for systems where a noisy image of the sample is already recorded, as is the case of in-focus DHM.

Acknowledgments

This research did not receive any specific grant from funding agencies in the public, commercial, or nonprofit sectors. The authors declare no conflicts of interest associated with this work.

References

1. E. Cuche, F. Bevilacqua, and C. Depeursinge, "Digital holography for quantitative phase-contrast imaging," *Opt. Lett.* **24**(5), 291–293 (1999).
2. G. Popescu, *Quantitative Phase Imaging of Cells and Tissues*, McGraw Hill Professional, New York (2011).
3. P. Ferraro et al., "Controlling image size as a function of distance and wavelength in Fresnel-transform reconstruction of digital holograms," *Opt. Lett.* **29**(8), 854–856 (2004).
4. R. Castañeda and J. Garcia-Sucerquia, "Single-shot 3D topography of reflective samples with digital holographic microscopy," *Appl. Opt.* **57**(1), A12–A18 (2018).
5. J. W. Goodman, "Some fundamental properties of speckle," *J. Opt. Soc. Am.* **66**(11), 1145 (1976).
6. O. Lekberg, "Electronic speckle pattern interferometry," *Phys. Technol.* **11**, 16 (1980).
7. J. Maycock et al., "Reduction of speckle in digital holography by discrete Fourier filtering," *J. Opt. Soc. Am. A* **24**(6), 1617 (2007).
8. V. Bianco et al., "Random resampling masks: a non-Bayesian one-shot strategy for noise reduction in digital holography," *Opt. Lett.* **38**(5), 619–621 (2013).
9. A. Uzan, Y. Rivenson, and A. Stern, "Speckle denoising in digital holography by nonlocal means filtering," *Appl. Opt.* **52**(1), A195 (2013).
10. D. Hincapie, J. Herrera-Ramírez, and J. Garcia-Sucerquia, "Single-shot speckle reduction in numerical reconstruction of digitally recorded holograms," *Opt. Lett.* **40**(8), 1623–1626 (2015).
11. K. Dabov et al., "Image denoising by sparse 3-D transform-domain collaborative filtering," *IEEE Trans. Image Process.* **16**(8), 2080–2095 (2007).

12. T. Baumbach et al., "Improvement of accuracy in digital holography by use of multiple holograms," *Appl. Opt.* **45**(24), 6077 (2006).
13. J. Garcia-Sucerquia et al., "Incoherent recovering of the spatial resolution in digital holography," *Opt. Commun.* **260**(1), 62–67 (2006).
14. L. Rong et al., "Speckle noise reduction in digital holography by use of multiple polarization holograms," *Chin. Opt. Lett.* **8**(7), 653–655 (2010).
15. J. Garcia-Sucerquia, "Noise reduction in digital lensless holographic microscopy by engineering the light from a light-emitting diode," *Appl. Opt.* **52**(1), A232–A239 (2013).
16. F. Le Clerc, M. Gross, and L. Collot, "Synthetic-aperture experiment in the visible with on-axis digital heterodyne holography," *Opt. Lett.* **26**(20), 1550–1552 (2001).
17. T. M. Kreis, M. Adams, and W. P. O. Jueptner, "Aperture synthesis in digital holography," *Proc. SPIE* **4777**, 69–76 (2002).
18. Y. Park et al., "Speckle-field digital holographic microscopy," *Opt. Express* **17**(15), 12285–12292 (2009).
19. V. Bianco et al., "Quasi noise-free digital holography," *Light Sci. Appl.* **5**, e16142 (2016).
20. M. Haouat et al., "Reduction of speckle noise in holographic images using spatial jittering in numerical reconstructions," *Opt. Lett.* **42**(6), 1047–1050 (2017).
21. T. Fukuoka, Y. Mori, and T. Nomura, "Speckle reduction by spatial-domain mask in digital holography," *J. Disp. Technol.* **12**(4), 315–322 (2016).
22. E. Cuche, P. Marquet, and C. Depeursinge, "Simultaneous amplitude-contrast and quantitative phase-contrast microscopy by numerical reconstruction of Fresnel off-axis holograms," *Appl. Opt.* **38**(34), 6994–7001 (1999).
23. B. Kemper et al., "Modular digital holographic microscopy system for marker free quantitative phase contrast imaging of living cells," *Proc. SPIE* **6191**, 61910T (2006).
24. E. Sánchez-Ortiga et al., "Off-axis digital holographic microscopy: practical design parameters for operating at diffraction limit," *Appl. Opt.* **53**(10), 2058 (2014).
25. J. Garcia-Sucerquia and R. Castañeda, "3D topography of reflective samples by single-shot digital holographic microscopy (Conference Presentation)," *Proc. SPIE* **10666**, 106660V (2018).
26. C. Trujillo et al., "Automatic full compensation of quantitative phase imaging in off-axis digital holographic microscopy," *Appl. Opt.* **55**(36), 10299–10306 (2016).
27. D. Malacara, M. Servín, and Z. Malacara, *Interferogram Analysis for Optical Testing*, Front Matter, 2nd ed., p. 440, CRC Press (2005).
28. E. Hecht, *Optics*, 4th ed., Addison Wesley Publishing Company, Boston, Massachusetts (2001).
29. J. He et al., "Light scattering by multiple red blood cells," *J. Opt. Soc. Am. A* **21**(10), 1953 (2004).

Carlos Buitrago-Duque is a graduate student from the School of Physics of the Universidad Nacional de Colombia, Medellin, Colombia, where he also received his degree in engineering physics. His research interests include digital holography, computational modeling and numerical processing of physical systems, and optical metrology. He is a member of SPIE.

Raúl Castañeda received his BS degree in physics engineering and his MS degree from the Universidad Nacional de Colombia. He is currently pursuing his PhD in electrical and electronic engineering at the University of Memphis. His research interests include digital holography and DHM, focusing in the reduction of speckle noise and improvement of the capability of imaging resolution.

Jorge Garcia-Sucerquia is an associate professor at the School of Physics, Universidad Nacional de Colombia, Medellin, Colombia, where he serves in the program of engineering physics. He received his BSc, MSc, and PhD degrees in physics from the Universidad de Antioquia, Medellin, Colombia. His research interests include digital holography, optical metrology, and optical coherence. He is the author of more than 200 journal papers in these fields. He is a member of SPIE.

Optics and Lasers in Engineering 137 (2021) 106365

Contents lists available at ScienceDirect

Optics and Lasers in Engineering

journal homepage: www.elsevier.com/locate/optlaseng

Pointwise phasor tuning for single-shot speckle noise reduction in phase wave fields

Carlos Buitrago-Duque[a], Raul Castañeda[a,b], Jorge Garcia-Sucerquia[a,*]

[a] Universidad Nacional de Colombia sede Medellín, School of Physics, A.A: 3840-Medellín-050034, Colombia
[b] Department of Electrical and Computer Engineering, The University of Memphis, Memphis, TN 38152, USA

ARTICLE INFO

Keywords:
Speckle reduction: Digital holographic microscopy
Image enhancement
Coherent imaging

ABSTRACT

A single-shot procedure to reduce speckle noise in numerically computed unwrapped phase maps is proposed. The method is supported on the possibility of expressing the computed phase maps as phasors in the complex plane to understand the phase denoising as a pointwise iterative operation of phasor tuning. Notwithstanding in this work the method is applied in digital holographic microscopy, it could be utilized in any other technique where an unwrapped phase map can be obtained. Numerical modeling and experimental results with non- and –biological samples are presented to support the feasibility of the method.

1. Introduction

Coherent imaging has advantages and disadvantages that should be weighted at the time of deciding on its utilization. For instance, the use of coherent light sources to produce interference patterns makes possible the quantitative label-free imaging of phase objects [1,2] and/or the contact-less surface imaging of reflective samples [1,3]. While transparent objects code their refractive index and topography into the phase information of a complex wavefield that propagates through, reflective objects code their height maps on the phase of a wave reflected on the surface of the sample. The phase information, in either case, can be retrieved by means of different approaches that analyze, as in digital holographic microscopy (DHM), the interference pattern produced by the coherent superposition of a reference wave and the wavefield propagating through or reflected from the sample. The price to be paid by the use of coherence light sources is the introduction of coherent noise known as speckle [4]. Speckle noise is an unavoidable feature in wavefield optics inherited from the roughness that most real-world materials have in the optical scale [4]; while the speckle is useful in some metrological applications [5], it can ruin the retrieved information from the coherent imaging systems. This difficulty has been extensively reported for many years in a wide range of disciplines like ultrasound imaging [6,7], synthetic aperture radar [8,9], optical coherence tomography [10,11], optical astronomy [12,13], optical [14] and digital [15] holography, among many others. Therefore, multiple approaches have been proposed in the literature to diminish its deleterious effects. All the methods can be classified into three main categories: i) numerical [16–18] ii) physical [19,20], and iii) those that combine i) and ii) [21–23]; for a comprehensive review of the state of the art of speckle noise reduction, the reader is referred to [15]. Among the great number of proposals to reduce the speckle noise in numerical coherent imaging, those that use a single-shot image have received special interest for its applicability to the imaging of dynamical process with enhanced signal-to-noise ratio. In response to this interest, in this work, a method to reduce the speckle noise in numerically recovered unwrapped phase wavefields that uses a single-shot image as input is presented, thus corresponding to the first category of the aforementioned classification. Even though the feasibility of the method is shown in experimental wavefields retrieved from DHM, it can be applied to unwrapped phase maps obtained from complex wavefields numerically recovered by any other technique.

2. Pointwise phasor tuning for speckle reduction

Let us consider a numerically retrieved complex-valued wavefield $\psi(x, y)$ for the point (x, y) of the form

$$\psi(x, y) = A(x, y) \exp[i\phi(x, y)] \tag{1}$$

with $A(x, y)$ and $\phi(x, y)$ its amplitude and phase, respectively. The amplitude is proportional to the transmittance or reflectance of the imaged sample, being essentially unitary for pure phase samples, as in the case studied in this work. As such sample is coherently imaged, either by transmission or by reflection, the phase $\phi(x, y)$carries multiplicative speckle noise $\phi_{NOI}(x, y)$ [24]

$$\phi(x, y) = \phi_{SAM}(x, y) + \phi_{NOI}(x, y) \tag{2}$$

* Corresponding author.
E-mail address: jigarcia@unal.edu.co (J. Garcia-Sucerquia).

https://doi.org/10.1016/j.optlaseng.2020.106365
Received 2 April 2020; Received in revised form 10 August 2020; Accepted 31 August 2020

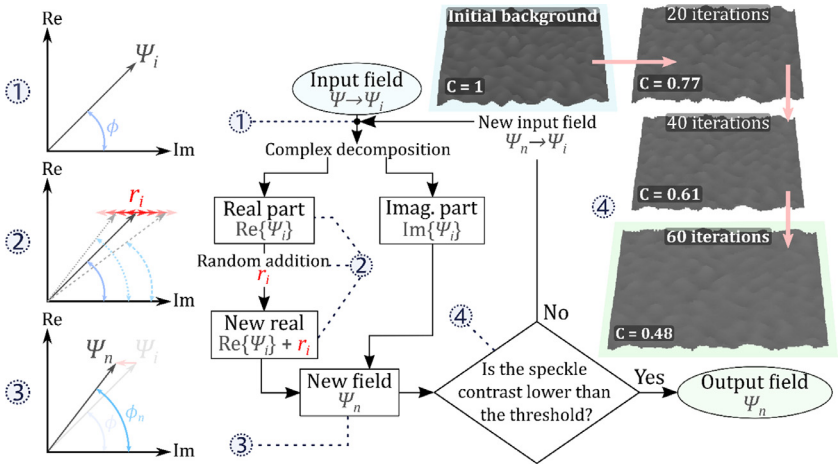

Fig. 1. Flowchart of the proposed PPT method for speckle reduction. The circled numbers associate the steps with its corresponding inset. ① Phasor representation of an input point. ② Phase tuning by random modification in the real component. ③ Phasor representation of the new field. ④ Denoising process example over the 3D render of a background area.

being $\phi_{SAM}(x, y)$ introduced in the wavefield by the object itself; while it corresponds to refractive index and topography if the object is imaged by transmission, it codes the height map of the object as imaged by reflection. The speckle noise $\phi_{NOI}(x, y)$, produced by the interference of the randomly scattered wavefields in or over the sample, is normally distributed over the range $-\pi$ to $+\pi$ with zero mean for each plane over which the complex wavefield is computed [4]. The complex wavefield in Eq. (1), with $A(x, y) = 1$ for pure phase objects, can be represented as a unitary phasor in the complex plane, subtending an angle $\phi(x, y)$ with its real axis. According to Eq. (2), the phase map $\phi(x, y)$ of the phasor $\psi(x, y)$ is the result of the superposition of the $\phi_{SAM}(x, y)$and $\phi_{NOI}(x, y)$ phase maps. Within this context, the denoising of the phase map can be understood as a pointwise tuning process meant to keep the phase map $\phi_{SAM}(x, y)$ while the contribution of $\phi_{NOI}(x, y)$ to the phasor $\psi(x, y)$ is diminished. In this method, the denoising is therefore done through a pointwise iterative process in the complex plane. After decomposing the input phasor $\psi(x, y)$ into its real and imaginary components, a set of uniformly distributed random numbers are added to either one of them in each iteration. The phase is thus modified, with the net effect that these additions slightly move the phasor around the phase angle $\phi(x, y)$. The complex wavefield is given, after each iteration, by

$$\begin{aligned}
\psi_0(x,y) &= \left[\mathrm{Re}\{\psi_0(x,y)\} + i\mathrm{Im}\{\psi_0(x,y)\}\right] \\
\psi_1(x,y) &= \left[\mathrm{Re}\{\psi_0(x,y)\} + r_1(x,y) + i\mathrm{Im}\{\psi_0(x,y)\}\right] \\
&\vdots \\
\psi_i(x,y) &= \left[\mathrm{Re}\{\psi_{i-1}(x,y)\} + r_i(x,y) + i\mathrm{Im}\{\psi_{i-1}(x,y)\}\right]
\end{aligned} \tag{3}$$

where the $r_i(x, y)$ are the set of random numbers to be added in the i-th iteration. After each iteration, the speckle contrast of the phase map is computed as $C = \sigma_P/\bar{P}$, with σ_p the standard deviation and $\bar{P}$ the average of the phase over a fixed background region in the new wavefield. If the resulting speckle contrast is lower than the set threshold, the process stops, and the last realization of the complex field becomes the output. Although in this work only the real component is modified, similar results could be attained if the random additions are made over the imaginary component. The proposed denoising process, hereafter referred to as PPT, is illustrated in the flowchart of Fig. 1. In this figure, the circled numbers associate the main steps of the process with its corresponding inset; ① is a representation of the phasor of an arbitrary input point, ② illustrates the phase tuning by random modifications in the real component. The resulting phasor, after the random addition is done, is shown in ③. In ④, an example denoising over a background constant-phase region is shown using 3D renders; the speckle contrast is assumed to be unitary in the initial state, and a reduction to 48% of its original value is achieved after 60 iterations. This process will be further illustrated and detailed with the numerical and experimental results in the following sections.

3. Numerical modeling

To verify the feasibility of this idea, the method has been applied to a numerically-modeled phase map with a simulated roughness distribution added, as shown in panel (a) of Fig. 2. To a pure phase map with values between $-\pi/2$ and $\pi/2$, a Gaussian distributed surface roughness with values in the range of $\lambda/3$, with λ being the illumination wavelength, has been added. The rough phase map, shown in panel (a), is then illuminated by a plane wave of unitary amplitude. The resulting complex wavefront is imaged through a numerically simulated microscope composed by an infinity-corrected microscope objective 40X/0.65 and a tube lens of 200 mm focal length in telecentric-afocal architecture. As a result of the imaging process, the imaged phase map, shown in panel (b), is now corrupted by the speckle noise resulting from the interference of the random wavefields scattered by the roughness distribution of the modeled sample. The obtained denoised phase map with the PPT method is shown in panel (c) of Fig. 2. The performance of the denoising proposal is quantified via the speckle contrast and the signal to distortion ratio (*SDR*) [24,25]; the latter is computed as $SDR = \|S\|_2/\|S - D\|_2$, where S is the input noisy image, D the output denoised one, and $\|\|_2$ the Euclidean norm. These metrics can be applied without prior knowledge of the noise or the ideal noise-free image, which is the case for the subsequent experimental results. For comparison purposes, the speckle contrast of the initial phase map in panel (b) is taken as unitary in the background region bounded by the yellow square. After applying 60 iterations, the resulting phase image has a reduced speckle contrast of 0.48 in that same area and a resulting *SDR* of 10.1 dB. The 3D renders in inset ④ of **Fig. 1** were taken from this application case in the same area where the metrics were computed. As for performance comparison, panel (d) shows the obtained denoised phase map using the state-of-the-art method of Block-Matching and 3D Filtering (BM3D) [26]. For the parameters utilized in this comparison, a 0.55 speckle contrast and 17.4 dB *SDR* are reached. Below each panel, the two insets show a close-up, from the corresponding phase map, of the second element from the rightmost group in the USAF 1951 test and the center of the star target pattern; the insets are extracted from the bounded region by the red rectangles. The dashed circle present in the latter, has the same size and location in each panel, indicating the preservation of the details at that given spatial frequency.

The method shows a clear improvement in the visualization of the height map, quantified by the considerable reduction in the speckle contrast value in 52% for 60 iterations. Comparing panels (c) and (d), BM3D achieves a greater overall smoothness inside the features and background. However, due to the pointwise effect of the PPT method, a correction of the extremal values and local perturbations of the phase is attained; this effect is seen by comparing the right inset of panels (c)

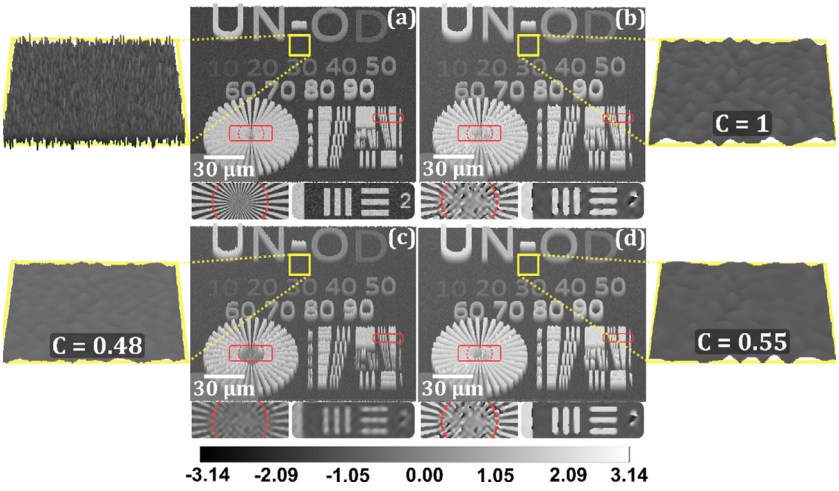

Fig. 2. 3D rendering of the phase maps from the noisy numerical modeling and subsequent denoising. (a) Numerically modeled pure phase map with variations between $-\pi/2$ and $\pi/2$ and a surface roughness in the order of $\lambda/3$ added. (b) Noisy map obtained from imaging the phase map through a simulated microscope composed by a microscope objective 40X/0.65 and tube lens of 20 cm focal length in telecentric-afocal architecture. (c) Denoised phase map by PPT. (d) Denoised phase map by BM3D. Bellow each panel, two insets show a close-up from the corresponding phase map on the second element from the rightmost group of the USAF 1951 test and the center of the star target; the dashed circle in the latter has the same diameter for all the panels. The scale bar indicates the phase value for all panels.

and (d). Additionally, the detail retention performance of the method can be directly verified from the star target pattern. Comparing the left inset of panels (b) to (d), the dashed circle shows that there is no further loss of higher spatial frequency components after the application of the method. The apparent reduction in resolution seen in the height map is a misleading representation due to the local phase perturbations.

4. Experimental results

The proposed method has been tested with experimental wavefields retrieved from off-axis DHM. A regular DHM microscope was implemented operating at a wavelength of 533 nm in transmission mode. The DHM was set up in telecentric-afocal architecture, such that any phase perturbation introduced by the imaging system is minimized [27] and the tilt off-axis phase eliminated accordingly [28]. Additionally, the microscope was configured such that the sample was sharply imaged into the digital-recording sensor, where the superposition with the reference wave takes place. From the resulting interferogram, the complex-valued wavefield $\psi(x, y)$ of the sample can be retrieved by means of a spatial filter in the Fourier domain to eliminate the zero-order intensity and the twin image [29]. However, the aforementioned architecture allows an accelerated reconstruction process because no propagation is required as the image plane coincides with the hologram recording plane [30]. From the complex-valued retrieved wavefield, the phase map is numerically calculated as customary via $\phi(x, y) = \arctan[\mathrm{Im}(\psi(x, y))/\mathrm{Re}(\psi(x, y))]$. All the computations, both for the reconstruction of the holograms and the denoising processing, were done on a mid-range laptop equipped with a 6-core 2.2 GHz CPU and 16 GB of RAM, using standard MATLAB implementations without performance enhancements nor GPU acceleration to ensure a fair comparison of the computation times.

As first instance, a star test target with a nominal height of 150 nm, was imaged. The target is made of acrylate polymer on glass, making it a pure-phase object. In Fig. 3 the resulting phase maps are presented; before the application of the PPT method to reduce the speckle noise in panel (a), and after its application in panel (b). As a comparison with the state-of-the-art algorithms, the phase map was also denoised using Two-Dimensional Windowed Fourier Transform Filtering (WFT2F) [31], in panel (c), and BM3D, in panel (d). Considering the speckle contrast in panel (a) as unitary in a background region bounded by the yellow square, the resulting phase map in panel (b) has a 0.55 speckle contrast after 30 iterations measured in that same region; in comparison, WFT2F and BM3D obtain, respectively, 0.86 and 0.81. On the other hand, measurement of the *SDR* yields comparable results of 13.2 dB for PPT against the 11.6 dB and 15.8 dB achieved by WFT2F and BM3D, in that order. This reduction can be further seen from the 3D surface plots taken over the background area bounded by the blue polygon between the test's spokes in all panels. As for the computation time, the proposed

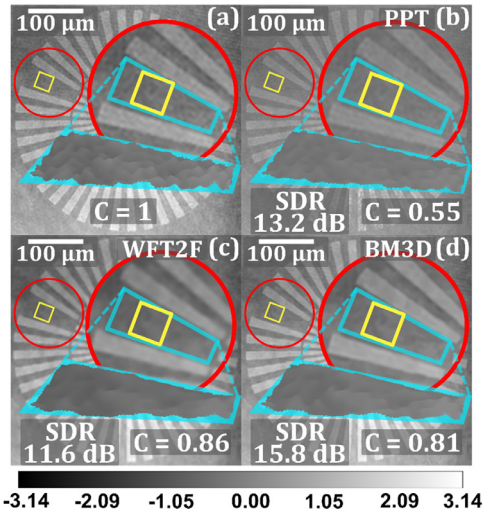

Fig. 3. Phase maps of a pure phase, height-calibrated, star test target obtained (a) before and (b) after the reduction of speckle noise using PPT. As a comparison, phase maps denoised using (c) WFT2F and (d) BM3D. Scale bar applies to phase values in all panels.

PPT method required a total execution time of 8.1 s, while WFT2F and BM3D took 4.3 s and 8.8 s, respectively, to converge in the presented results.

Due to its design as a benchmarking target, the star test is a highly-controlled sample with small deviations on its surface. This feature can be seen by the minimal, albeit notorious, changes in the details after the application of the method; see the red encircled regions in both panels. Nonetheless, the background areas, which were initially quite inhomogeneous, show a reduction of 45% of the speckle contrast after 30 iterations.

The proposed pointwise method to reduce the speckle noise was also applied to the recovered phase map of a thin transversal section of the head of a *Drosophila Melanogaster* fly. This biological sample is of special interest due to the intricate structures present in its interior. In panel (a) of Fig. 4, the phase map directly recovered from the complex-valued wavefield is shown. In panel (b), the resulting phase map after the application of the PPT is presented. For this sample, the speckle contrast is reduced to 0.52 after 30 iterations in the region indicated by the yellow square, as that region is taken to have unitary speckle contrast in the noisy image. In comparison, WFT2F and BM3D produce a reduction to 0.47 and 0.74, respectively. Furthermore, the measurement of *SDR* in the same bounded region yields 13.2 dB for PPT, to be compared with 19.1 dB and 21.6 dB achieved by WFT2F and BM3D, respectively.

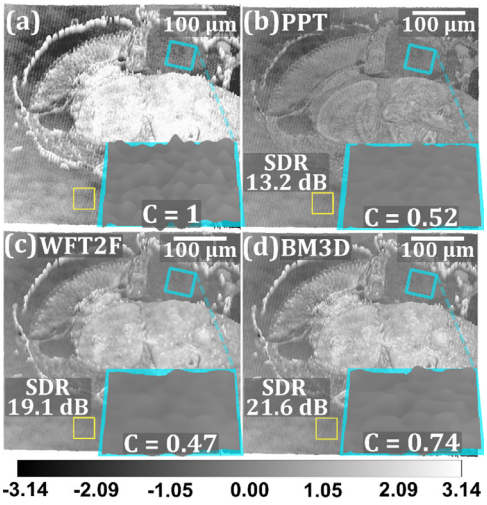

Fig. 4. Biological specimen with complex internal structure: section of the head of a *Drosophila Melanogaster* fly. (a) Height map of the head section prior to the application of the PPT method. (b) Height map after noise reduction. (c) Height map denoised using WFT2F. (d) Height map denoised using BM3D. Scale bar applies to all panels indicating the nominal phase value.

Similarly, the noise reduction effect can also be seen from the 3D surface plots taken in the background blue-bounded region in each panel which would, ideally, have a near-constant phase value. The direct comparison between panels (a) and (b) of Fig. 4 shows the great quality enhancement that the PPT method produces in the phase maps. This improvement is represented in the ease of visualization of the finer details and complex structures inside the sample that cannot be seen in the directly computed phase map. For these results, the application of the PPT method took 7.5 s to converge, while WFT2F and BM3D required 5.6 s and 9.0 s, respectively.

In all cases, both modeled and experimental, the resulting value of the speckle contrast after the PPT application is inversely related to the number of iterations. A complete dependence analysis on the evolution of the metrics with the number of iterations and the selected threshold is set aside for future work, due to the length constraints of the present work. Nonetheless, the resulting computation times show that the convergence rate of the proposed method is comparable with the state-of-the-art approaches, being almost equal to BM3D in this regard.

5. Conclusions

In summary, an iterative pointwise method to reduce the speckle noise in numerically computed unwrapped phase maps has been presented. The method is supported by the possibility of expressing the computed phase maps as a phasor in the complex plane. The speckle noise can be understood as a phase angle added to the angle representation of the phase introduced by the specimen itself. Within the framework of this idea, the denoising of phase maps can be understood as an iterative pointwise tuning process in the complex plane to reduce the angle representing the noise while preserving the one representing the sample. The iterative pointwise method has been initially tested with fully controlled numerically modeled phase maps; in this modeled experiment the method reported a reduction of 48% in the speckle contrast after 60 iterations. Notwithstanding the method has been validated with experimental data from digital holographic microscopy, it can be applied to any other imaging technique where a numerically computed unwrapped phase map can be obtained. The method has been applied to a phase-only star test target and a section of the head of a *Drosophila Melanogaster* fly. In both cases, notorious improvements, quantified on the reduction of the speckle contrast in the regions without sample and comparable signal to distortion ratios to what is achieved with state-of-the-art methodologies, have been obtained. For all the experiments, the images before and after the application of the iterative pointwise method to reduce the speckle noise are compared via the change of the speckle contrast and *SDR*. The proposed technique presents the advantages of being single-shot and suitable for systems where a noisy image of the phase sample is already recorded, without the need for additional special preparations during the recording.

Declaration of Competing Interest

The authors declare that they have no known competing financial interests or personal relationships that could have appeared to influence the work reported in this paper.

CRediT authorship contribution statement

Carlos Buitrago-Duque: Software, Validation, Writing - review & editing. **Raul Castañeda:** Software. **Jorge Garcia-Sucerquia:** Conceptualization, Methodology, Writing - original draft, Writing - review & editing.

Acknowledgment

The present work was done thanks to the funding by Universidad Nacional de Colombia Sede Medellin (Grant no. 49282).

References

[1] Cuche E, Bevilacqua F, Depeursinge C. Digital holography for quantitative phase-contrast imaging. Opt Lett 1999;24:291–3. doi:10.1364/OL.24.000291.
[2] Popescu G. Quantitative phase imaging of cells and tissues. McGraw Hill Professional; 2011.
[3] Ferraro P, De Nicola S, Coppola G, Finizio A, Alfieri D, Pierattini G. Controlling image size as a function of distanceand wavelength in Fresnel-transformreconstruction of digital holograms. Opt Lett 2004;29:854–6.
[4] Goodman JW. Some fundamental properties of speckle. J Opt Soc Am 1976;66:1145. doi:10.1364/JOSA.66.001145.
[5] Goodman JW. Speckle phenomena in optics: theory and applications. Second Ed. SPIE; 2020. Second Ed. doi:10.1117/3.2548484.
[6] Tay PC, Garson CD, Acton ST, Hossack JA. Ultrasound despeckling for contrast enhancement. IEEE Trans Image Process 2010;19:1847–60. doi:10.1109/TIP.2010.2044962.
[7] Mateo JL, Fernández-Caballero A. Finding out general tendencies in speckle noise reduction in ultrasound images. Expert Syst Appl 2009;36:7786–97. doi:10.1016/j.eswa.2008.11.029.
[8] Lee Jong-Sen, Grunes MR, de Grandi G. Polarimetric SAR speckle filtering and its implication for classification. IEEE Trans Geosci Remote Sens 1999;37:2363–73. doi:10.1109/36.789635.
[9] Lee JS, Jurkevich L, Dewaele P, Wambacq P, Oosterlinck A. Speckle filtering of synthetic aperture radar images: a review. Remote Sens Rev 1994;8:313–40. doi:10.1080/02757259409532206.
[10] Bouma BE, Tearney GJ. Handbook of optical coherence tomography. New York: Marcel Dekker; 2002.
[11] Schmitt JM, Xiang SH, Yung KM. Speckle in optical coherence tomography. J Biomed Opt 1999;4:95. doi:10.1117/1.429925.
[12] Roddier F. V the effects of atmospheric turbulence in optical astronomy, 1981, p. 281–376. doi:10.1016/S0079-6638(08)70204-X.
[13] Michael CR, Byron MWImaging, bulence. CRC Press; 2018. doi:10.1201/9780203751282.
[14] Caulfield HJ. Special problems: speckle. Handb. Opt. Hologr. 1979:367–71.
[15] Bianco V, Memmolo P, Leo M, Montresor S, Distante C, Paturzo M, et al. Strategies for reducing speckle noise in digital holography. Light Sci Appl 2018;7:48. doi:10.1038/s41377-018-0050-9.
[16] Maycock J, Hennelly BM, McDonald JB, Frauel Y, Castro A, Javidi B, et al. Reduction of speckle in digital holography by discrete Fourier filtering. J Opt Soc Am A 2007;24:1617. doi:10.1364/JOSAA.24.001617.
[17] Bianco V, Paturzo M, Memmolo P, Finizio A, Ferraro P, Javidi B. Random resampling masks: a non-Bayesian one-shot strategy for noise reduction in digital holography. Opt Lett 2013;38:619–21. 10.1364/OL.38.000619.
[18] Haouat M, Garcia-Sucerquia J, Kellou A, Picart P. Reduction of speckle noise in holographic images using spatial jittering in numerical reconstructions. Opt Lett 2017;42:1047–50. doi:10.1364/OL.42.001047.
[19] Baumbach T, Kolenovic E, Kebbel V, Jüptner W. Improvement of accuracy in digital holography by use of multiple holograms. Appl Opt 2006;45:6077. doi:10.1364/AO.45.006077.

[20] Rong L, Xiao W, Pan F, Liu S, Li R. Speckle noise reduction in digital holography by use of multiple polarization holograms. Chinese Opt Lett 2010;8:653–7. doi:10.3788/COL20100807.0653.
[21] Le Clerc F, Gross M, Collot L. Synthetic-aperture experiment in the visible with on-axis digital heterodyne holography. Opt Lett 2001;26:1550–2. doi:10.1364/OL.26.001550.
[22] Park Y, Choi W, Yaqoob Z, Dasari R, Badizadegan K, Feld MS. Speckle-field digital holographic microscopy. Opt Express 2009;17:12285–92. doi:10.1364/OE.17.012285.
[23] Bianco V, Memmolo P, Paturzo M, Finizio A, Javidi B, Ferraro P. Quasi noise-free digital holography. Light Sci Appl 2016;5:e16142. doi:10.1038/lsa.2016.142.
[24] Memmolo P, Esnaola I, Finizio A, Paturzo M, Ferraro P, Tulino AM. SPADEDH: a sparsity-based denoising method of digital holograms without knowing the noise statistics. Opt Express 2012;20:17250–7. doi:10.1364/OE.20.017250.
[25] Montresor S, Picart P. Quantitative appraisal for noise reduction in digital holographic phase imaging. Opt Express 2016;24:14322. doi:10.1364/OE.24.014322.
[26] Dabov K, Foi A, Katkovnik V, Egiazarian K. Image denoising by sparse 3-D transform-domain collaborative filtering. IEEE Trans Image Process 2007;16:2080–95. 10.1109/TIP.2007.901238.
[27] Sánchez-Ortiga E, Doblas A, Saavedra G, Martínez-Corral M, Garcia-Sucerquia J. Off-axis digital holographic microscopy: practical design parameters for operating at diffraction limit. Appl Opt 2014;53:2058. doi:10.1364/AO.53.002058.
[28] Trujillo C, Castañeda R, Piedrahita-Quintero P, Garcia-Sucerquia J. Automatic full compensation of quantitative phase imaging in off-axis digital holographic microscopy. Appl Opt 2016;55:10299–306. doi:10.1364/AO.55.010299.
[29] Cuche E, Marquet P, Depeursinge C. Spatial filtering for zero-order and twin-image elimination in digital off-axis holography. Appl Opt 2000;39:4070. doi:10.1364/AO.39.004070.
[30] Kemper B, von Bally G. Digital holographic microscopy for live cell applications and technical inspection. Appl Opt 2008;47:A52. doi:10.1364/AO.47.000A52.
[31] Kemao Q. Windowed Fourier transform for fringe pattern analysis. Appl Opt 2004;43:2695–702. doi:10.1364/AO.43.002695.

Heliyon 7 (2021) e06098

Contents lists available at ScienceDirect

Heliyon

journal homepage: www.cell.com/heliyon

Research article

Physical pupil manipulation for speckle reduction in digital holographic microscopy

Carlos Buitrago-Duque, Jorge Garcia-Sucerquia *

Universidad Nacional de Colombia sede Medellín, School of Physics, A.A: 3840, Medellín 050034, Colombia

ARTICLE INFO

Keywords:
Speckle
Digital holography
Image enhancement
Quantitative phase imaging

ABSTRACT

The reduction of speckle noise by physically changing the pupil of the imaging system, as first envisioned in optical holography, is experimentally applied to a digital holographic microscope (DHM). The imaging pupil of a DHM, operating in image plane telecentric-afocal architecture, is changed in a controlled way between successive recordings, allowing the shooting of multiple partially-decorrelated holograms. Averaging the numerically reconstructed holograms yields amplitude and/or phase images with reduced speckle noise. Experimental results of biological specimens and a phase-only resolution test show the feasibility to recover micron-sized features in images with reduced speckle noise.

1. Introduction

Speckle noise, the granular pattern that arises from coherently-illuminated objects, is an unavoidable condition inherited from the roughness that most real-world materials have in the optical scale [1]. Although this phenomenon is widely used in metrological applications [2], in coherent imaging it is considered an annoyance that must be reduced or eliminated [3]. Holography is one field of application where speckle effects are especially deleterious. The suppression of speckle noise in holographic techniques is a particularly difficult problem due to their dependence on the light coherence to produce the images [4]; in consequence, multiple methods have been envisioned since the very onset of the field to reduce its incidence, and it continues to be a widely active field of research. In particular, in digital holography (DH), the problem has been lengthily studied; Ref. [5, 6, 7] present comprehensive reviews of the available methods, both optical and numerical, to deal with speckle noise.

Among the optical methods to reduce the effects of speckle noise in holographic techniques, the most common approach is averaging multiple images of the same scene that have been acquired with different random noises [4]. In these methods, known as multi-look approaches, the multiple realizations of the noise can be obtained by an ample range of procedures that include the use of a rotating diffuser [8, 9, 10], changing the wavelength [11] or the polarization state [12] of the illumination, and using different angles of recording [13, 14]. Most of these techniques have been successfully applied both on optical and digital holography, either in the recording or the reconstruction stage.

In this work, an optical multi-look method in which the multiple speckle fields are obtained by physically altering the pupil function of the imaging system is implemented in Digital Holographic Microscopy (DHM). The manipulation of the imaging pupil is a denoising strategy that has been widely reported in optical holography [15, 16, 17, 18, 19, 20, 21], and also numerically implemented in its digital counterpart [22, 23]; however, the existing literature has been mostly interested in the denoising of intensity reconstructions. The digital world has given holography the ability to directly access the phase information of the samples, enabling the development of label-free quantitative phase imaging (QPI) techniques [24]; DHM directly benefits from this capability as it allows an ample range of applications, for instance in the biological sciences, where most samples are both of micrometric dimensions and translucent [25], thus encoding their parameters in the phase information. Therefore, in this work, the denoising method by pupil manipulation is applied in the observation of biological samples and a phase-only resolution test, validating its feasibility to recover micron-sized features of translucent samples with enhanced contrast in numerically reconstructed phase maps, and also showing the validity of the optically-inspired methods to reduce the speckle noise in the digital-based techniques. For guiding the reader about the performance of the present method in comparison with other multi-look denoising approaches, the imaged biological samples are also denoised by means of

* Corresponding author.
E-mail address: jigarcia@unal.edu.co (J. Garcia-Sucerquia).

https://doi.org/10.1016/j.heliyon.2021.e06098
Received 8 September 2020; Received in revised form 7 December 2020; Accepted 22 January 2021

the rotating diffuser method; some conclusions about the comparative performance are also stated.

2. Speckle reduction by pupil control in optical holography

The idea of reducing speckle noise in image-plane holograms by introducing moving pupils into the experimental setup was first proposed by Dainty and Welford in 1971 [15]. Their work, applied in the reconstruction stage of an optical hologram, shows that an aperture, smaller than the pupil, moving rapidly in the pupil plane of the reconstructing objective can reduce the speckle in the image plane, at the expense of the resolution and the available light. Figure 1 shows the experimental setup required for such a proposal.

The process of physically moving the aperture in the pupil plane, and then integrating the resulting intensity over time, was then understood as a filtering process over the spatial frequencies of the object; as such, its denoising effect was mathematically and experimentally described by Hariharan and Hegedus in terms of the power spectrum of the associated speckle patterns [17]. The following mathematical description is a summary of their results; to avoid unnecessary work duplication, the reader is referred to the corresponding reference for a complete treatment of the problem.

As illustrated in Figure 2, a circular aperture, smaller than the pupil of the imaging system, is assumed to be displaced in the pupil plane between successive exposures. If N exposures are done with different positions of the aperture, the resulting irradiance will be the sum of the corresponding contributions $I(\vec{r}) = \sum_{i}^{N} |g_i(\vec{r})|^2$, where the impinging field at the i-th position of the aperture in the pupil plane

$$g_i(\vec{r}) = f(\vec{r}) \otimes h_i(\vec{r}) \tag{1}$$

is given by the convolution between the reconstructed object information, $f(\vec{r})$, and the impulse response of the system for that position of the aperture, $h_i(\vec{r})$.

It was shown that the average power spectrum of the image irradiance is given by the sum of the power spectrum of a spatially incoherent object, having the same radiance as the noise-free object information, and the speckle power spectrum. The latter is shown to be given, for the case under consideration, by

$$\Omega_2(\vec{u}) = |R_{tt}(0)|^2 \sum_{ij} \left[H_i(\vec{u}) H_j^*(\vec{u}) \right] \otimes \left[H_i^*(-\vec{u}) H_j(\vec{u}) \right] \tag{2}$$

where $H_i(\vec{u})$ and $H_j(\vec{u})$ are the transfer functions of the system in the i-th and j-th positions, respectively, as given by the aperture, and $R_{tt}(0)$ is the autocorrelation of the noise-free object information and thus constant. If, for convenience, only two exposures are considered, $|R_{tt}(0)|^2$ is assumed to be unitary, and the pupil is taken to be aberration-free, Eq. (2) becomes

$$\Omega_2(\vec{u}) \approx 2|H(\vec{u})|^2 \otimes |H(-\vec{u})|^2 + 2[H(\vec{u})H(\vec{u}-\Delta\vec{u})] \otimes [H(-\vec{u}) H(\Delta\vec{u}-\vec{u})] \tag{3}$$

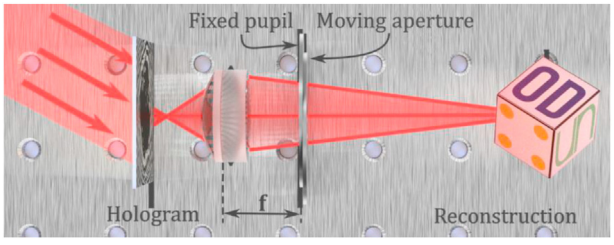

Figure 1. Speckle reduction by moving aperture in the reconstruction stage of plane-image optical holography. Based on the setup diagram in [15].

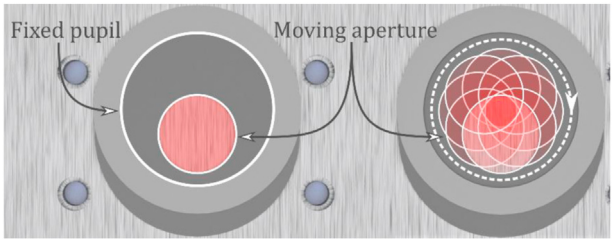

Figure 2. Relation between the fixed and moving pupil for multi-look speckle reduction in optical holography. Based on the diagram in [15].

with $\Delta\vec{u}$ being the displacement between the positions of the aperture in each exposure. Therefore, for a given displacement of the aperture, the speckle power spectrum would be determined by the sum of the incoherent transfer function of the system with an aperture $H(\vec{u})$ two times: one for a spatial frequency $\vec{u}$, as given by the first term to the right in Eq. (3), and one for a spatial frequency $\vec{u} + \Delta\vec{u}$, as given by the second term to the right in Eq. (3).

Within this framework, one can envision the reduction of speckle noise by superimposing reconstructions with varied speckle wavefields produced by a variety of pupil functions with different sizes, shapes, and positions. This observation led to further implementations with different geometries and movements of the filter mask [18, 19, 20, 21]. As will be presented in the next section, the experimental conditions of DHM present a direct parallel with these results, allowing the pursual of an implementation of this speckle reduction method to be sought.

3. Speckle reduction by pupil control in DHM

DHM can be implemented with multiple architectures. In the case of translucent samples, the most common one corresponds to a transmission DHM setup, as illustrated in Figure 3. In this setup, a digital camera, usually a charge-coupled device (CCD) or complementary metal-oxide semiconductor (CMOS), records the amplitude superposition of a reference $R(x,y)$ and an object wave $O(x,y)$, which produces a steady interference pattern if both waves are generated from the same coherent optical light source, like a laser. $R(x,y)$ is set to travel directly to the digital camera, while $O(x,y)$ propagates through the sample, gathering its information. The object wave is, thus, the propagation of the complex-valued wavefield at the sample plane $S(x',y')$ through the imaging system composed of the microscope objective (MO) and the tube lens (TL).

To ensure that any curvature-phase perturbation is removed from $O(x,y)$, and to guarantee the obtention of trustable QPI maps, the MO and TL must be configured in a telecentric-afocal architecture [26, 27, 28, 29]. The fulfillment of this condition allows the complex-valued object wavefield at the recording plane to be written as

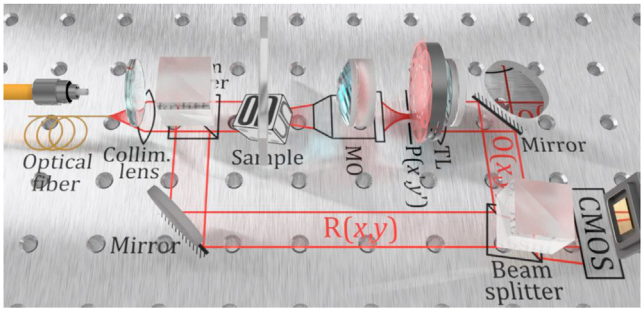

Figure 3. Configuration diagram of a Digital Holographic Microscope operating in transmission mode.

$$O(x,y)=\frac{1}{|M|}S\left(\frac{x}{M},\frac{y}{M}\right)\otimes_2\tilde{h}\left(\frac{x}{\lambda f_{TL}},\frac{y}{\lambda f_{TL}}\right), \tag{4}$$

with $M=-f_{TL}/f_{MO}$ being the overall magnification of the microscope given by the focal lengths of the TL and the MO, respectively, $\otimes_2$ denoting the 2D convolution operation, and λ the illumination wavelength. In Eq. (4), $\tilde{h}(x,y)$ is the diffraction pattern of the pupil function $P(x',y')$ of the microscope at the digital camera plane:

$$\tilde{h}\left(\frac{x}{\lambda f_{TL}},\frac{y}{\lambda f_{TL}}\right)=\int_{-\infty}^{\infty}\int_{-\infty}^{\infty}P(x',y')\exp\left[-i\frac{2\pi}{\lambda f_{TL}}(x'x+y'y)\right]dx'dy'. \tag{5}$$

The reconstruction of the complex-object wavefield from the hologram can be done by following any interferometry method [30]. In particular, for the afocal-telecentric configuration operating at diffraction limit [28] utilized in this work, the retrieval of $O(x,y)$ is done directly by numerical spatial filtering [31, 32] with no further propagation; allowing the obtention of a non-distorted wavefield like that in Eq. (4). This means that all the features of the digitally-recovered $O(x,y)$ are expressed in the just said equation, in direct analogy to the optical holography case of an image-plane hologram, like the one used in Ref. [15]. The speckle noise, inherited from the use of coherent illumination to gather the sample information [1] must also be present in $O(x,y)$. In Eq. (4), $1/|M|S()$ is the geometrical image of the sample because the sample plane and the camera plane are conjugated; therefore, all the diffractive effects, including the speckle noise, are left to the point spread function in Eq. (5) [33]. Just like in optical holography, the light spots that compose the geometrical image of $O(x,y)$ have their size, position and shape controlled, likewise, by the size, position and shape of the pupil function $P(x',y')$. Under this understanding of the imaging process, it is reasonable to expect that the results from optical holography can be directly applied to the experimental conditions of DHM by physically modifying the imaging pupil in the object arm during the recording stage.

3.1. Experimental setup

A transmission DHM, operating in an afocal-telecentric configuration and the diffraction limit, is set up as illustrated in Figure 3. If the effective focal length of the MO is not enough for the optomechanical components of the moving aperture to be properly positioned at its pupil plane, a relay lens can be used to project the pupil plane further away from the objective. The physical manipulation of the aperture can be easily achieved with off-the-shelf components by using, for instance, an iris diaphragm mounted into an X–Y displacer, giving control over both the size and position; however, if the use of customized components is possible, faster experimental results can be obtained by using a rotation mount coupled to either a linear displacer with an iris diaphragm or a pair of pupils, like those of Ref. [15] illustrated in Figure 2. With the setup completed, the aperture can be freely manipulated while registering a hologram for each different realization. Once all the desired digital exposures are completed, their numerical processing follows the same process as any other multi-look denoising methodology; namely, each of the holograms is numerically reconstructed for the desired information, either phase or intensity, and latter averaged to finally obtain a denoised image. Figure 4 presents a summary of this approach.

For the experiments in this work, the microscope was configured using an illumination wavelength of 533 nm and a CMOS camera with 1024 × 1024 square pixels with a side length of 5.2 μm. The object arm was composed of an infinity-corrected 10x/0.25 MO, and a TL with 200 mm of focal length; the changing aperture was created using an iris diaphragm, larger than the system's pupil size, mounted on an X–Y displacement cage. This configuration, located at the pupil plane of the MO as shown in Figure 5, allowed the manipulation of the aperture size from its fully open configuration to 20% of the pupil size, while keeping the possibility of scanning the entire original pupil. Examples of the different positions that the modified aperture can take are shown in panels (b), (c), and (d) of Figure 5 for an aperture whose size has been reduced to 80%, 50%, and 30% of the original pupil's diameter, respectively, and displaced in a circular path concentric to the system's pupil.

In these displacement paths, the different realizations of speckle are expected to be only partially uncorrelated due to the overlap in the aperture positions. As most denoising methods based on multiple exposures require the superposed fields to be uncorrelated [7], the expected performance of the method is intrinsically related to how much of a decorrelation can be introduced with the selected degrees of freedom. Therefore, to predict the degree of correlation for the aforementioned configuration, the system was numerically simulated using a realistic representation of the speckle noise for the experimental conditions of DHM [34]; the sample was assumed to be a diffuser with superficial roughness in the order of λ/4, imaged with multiple aperture positions and sizes. The correlation between a pair of consecutive speckle intensity realizations, denoted A and B with respective means $\overline{A}$ and $\overline{B}$, was measured using the discrete form of the Pearson's correlation coefficient [35].

$$R_{AB}=\frac{\sum_i\sum_j\left(A_{ij}-\overline{A}\right)\left(B_{ij}-\overline{B}\right)}{\sqrt{\left(\sum_i\sum_j\left(A_{ij}-\overline{A}\right)^2\right)\sum_i\sum_j\left(B_{ij}-\overline{B}\right)^2}}. \tag{6}$$

The results are summarized in Figure 6 for the two available degrees of freedom. Panel (a) shows the variation in the correlation coefficient against the displacement of the aperture, with the latter being measured in its radius units. Three aperture positions are shown in panel (b), taken with displacements of 0.5, 0.6, and 0.95 times the aperture radius, for the red (dashes), green (dots), and blue (dash-and-dot) lines, in that order. In this same panel, the white circle represents the original pupil of the system, spatially centered in the pupil plane, and the crosses indicate the center position for each pupil displacement.

Panel (c) shows the variation in the correlation coefficient against the percentual aperture radius reduction. Panel (d) shows the three reduction cases of Figure 5; namely, 80%, 50%, and 30% of the original pupil radius for the red (dashes), green (dots), and blue (dash-and-dot) lines, respectively. In this panel, the white circle represents the original pupil of the system and the yellow cross indicates the spatial center of the pupil plane.

The behavior seen in Figure 6 is consistent with the expectation of only partially uncorrelated speckle fields for the illustrated displacements. This condition limits the method's efficiency if only small modifications to the pupil are considered. Nonetheless, it was shown in Ref. [17] that, under such conditions of low-decorrelation, a noise-reduction effect is still to be found in the object intensity; therefore,

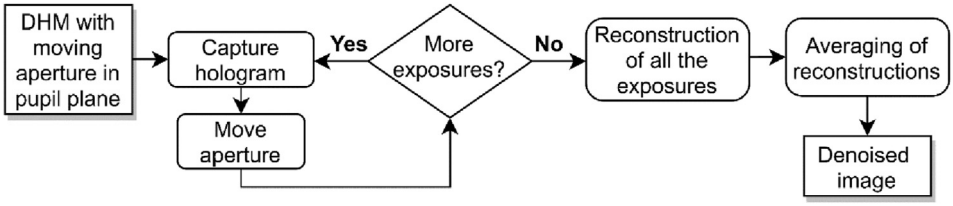

Figure 4. Flowchart of the method for speckle noise reduction by physical manipulation of the pupil function.

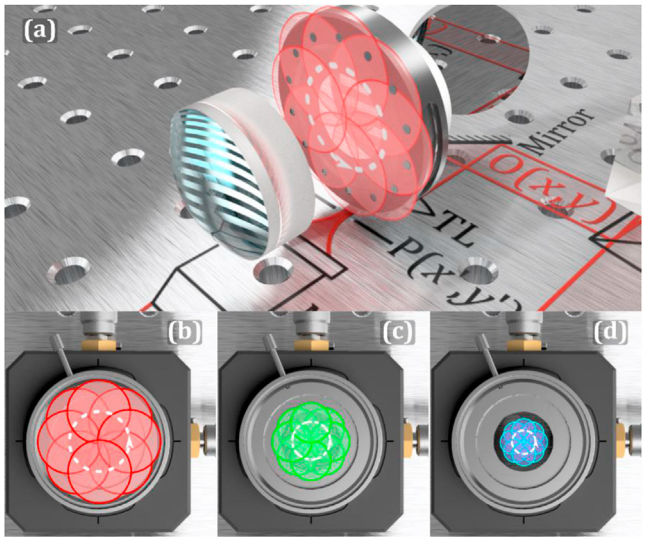

Figure 5. Movements and sizes of the aperture used for speckle noise reduction. (a) The moving aperture is located at the pupil plane of the object arm of the DHM. (b/c/d) Movement path of the aperture with 0.8/0.5/0.3 times the original pupil diameter.

it is reasonable to expect that a similar filtering effect holds for the phase information. This was corroborated with a phase-only resolution test and later applied to a biological specimen.

3.2. Experimental results

The experimental setup described in the previous section was used to image a calibrated star test resolution target, over which the described speckle noise reduction method was applied. As the target was made of acrylate polymer on glass, allowing it to be considered as a pure phase object, all the resulting images are quantitative phase maps. For each aperture configuration, the improvement of the image quality was measured using the well-known metric of speckle contrast [4]; it was computed over a background region between the spokes of the target as $C = \sigma_P/\overline{P}$, where σ_p is the standard deviation and $\overline{P}$ the average of the phase values in the selected region. Additionally, according to the manufacturer's information, the used target has a 400 μm external diameter and 40 identical spokes; therefore, by measuring the minimum resolvable circumference in the denoised phase map, the resulting resolution power (RP) can be found. From these two values, the resolution penalty associated with the application of the proposed method can be measured and compared to the denoising performance for different aperture configurations. To ease the comparison, both the speckle contrast and the resolution power measurements were normalized against the original noisy image, such that their initial values are unitary.

Initially, the performance of the method when the imaging pupil is only modified displacing the aperture while its original size is kept was evaluated. Figure 7 shows the behavior of the two aforementioned metrics for this case, where each point represents the measurements over the averaged phase map from 8 different positions of the aperture, following the paths illustrated in Figure 5. As is expected from the partial correlation of the speckle fields predicted in Figure 6, the speckle contrast steadily decreases as the displacement of the aperture increases. This behavior can be seen in the dot-marked dashed-line series of the graph. The resolution power, represented by the diamond-marked solid-line series in Figure 7, remains essentially unaffected by the increasing alteration of the pupil function; thus, one can seek the maximum achievable improvement in the image quality without an evident resolution loss. Such condition is attained when the aperture is displaced 0.95 times the pupil radius (r_p), producing a reduction of the speckle contrast by approximately 25%.

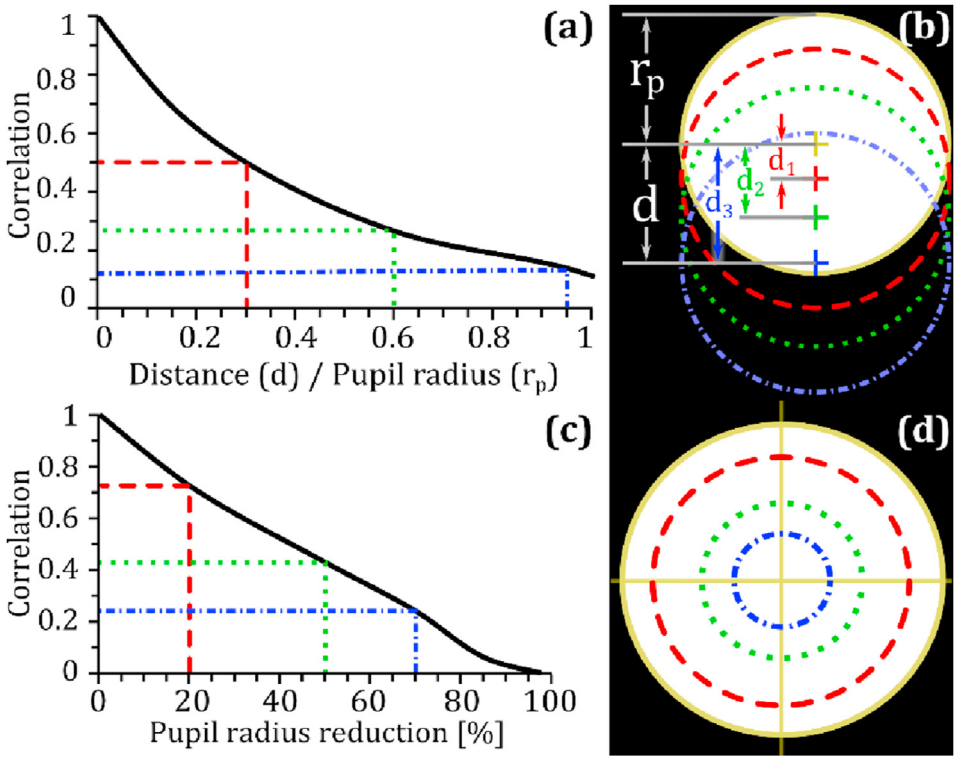

Figure 6. Correlation factor between consecutive speckle realizations. (a) Change of the correlation coefficient against the aperture displacement from the center measured in its radius units. (b) Illustration of the three different displacements highlighted in panel (a). (c) Correlation coefficient change against the aperture radius reduction percentage. (d) Illustration of the three different radii highlighted in panel (c). The color and dashing coding are shared between each pair of panels.

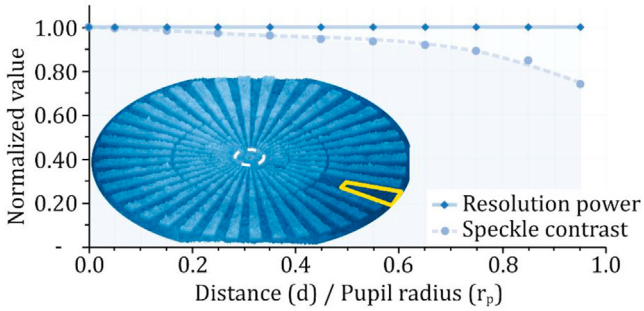

Figure 7. Relation between speckle-noise reduction with the proposed method and the resulting spatial resolution for multiple displacements of the aperture. The diamond-marked-solid-line series shows the resolution power in the denoised image, while the dot-marked dashed-line series shows the speckle contrast measured in a background area. Both curves are measured following the paths indicated in Figure 5 after averaging 8 phase reconstructions with a given displacement in units of the original pupil radius. The values are normalized against the corresponding measurements of the original phase map.

It is possible to further enhance the denoising effect of the method by introducing the size changes as a second freedom degree into the pupil's manipulation. To evaluate the performance of this case, the two metrics were measured over the averaged phase map resulting from 8 different positions of the aperture with a reduced size and displaced 0.95 times its radius, once again following the paths illustrated in Figure 5. The results are summarized in Figure 8 using the same conventions as the previous figure. As predicted by the correlation measurements in Figure 6, a further reduction in the aperture size allows the obtention of a more decorrelated speckle field, which in turn leads to a higher degree of noise reduction when the average is taken. Unlike the previous case, however, the resolution power is affected. This is expected, as the reduction in aperture diameter must be associated with a rejection of higher-order spatial frequencies during the recording stage. For the small size reductions, the effect is partially compensated by the scanning of multiple positions of the aperture, whose superposition behaves as the effective imaging pupil, although it must be noted that it will *never* be larger than the original pupil size. Therefore, a trade-off must be sought between the degree of denoising and the required resolution when the method is applied.

When considering a displacement of 0.95 times the aperture radius, a maximum reduction of 30% of the pupil size can be applied without significantly degrading the resolution; this limit configuration allowed a total reduction of the speckle contrast to 0.7 times its original value.

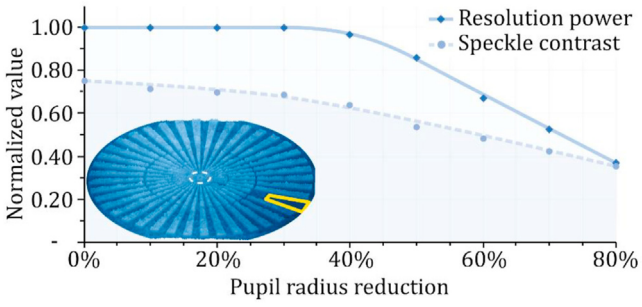

Figure 8. Relation between speckle-noise reduction with the proposed method and the resulting spatial resolution for multiple sizes of the aperture. The diamond-marked solid-line series shows the resolution power in the denoised image, while the dot-marked dashed-line series shows the speckle contrast measured in a background area. Both curves are measured following the paths indicated in Figure 5 after averaging 8 phase reconstructions with a given aperture radius, displaced 0.95 times the resulting radius. The values are normalized against the corresponding measurements of the original phase map.

Above this limit, the scanning is not enough to fully compensate for the higher-order spatial frequency rejections, and thus the resolution is inevitably affected. Nonetheless, if the application allows the resolution penalty to be taken, further decreasing the aperture radius may yield speckle contrast reductions of up to 65% with only 8 exposures.

Finally, to visualize the results of the above-studied behavior, Figure 9 illustrates 3 denoising cases. Panel (a) shows a 3D rendering of the initial noisy phase map obtained with the original pupil of the system. Panels (b), (c), and (d), show the renders of the averaged phase maps obtained after the aperture was manipulated using the sizes and movement paths previously illustrated in Figure 5, taking 8 different exposures in each case. As before, the speckle contrast (C) of each averaged phase map is taken over the background region highlighted between the spokes of the target, and the resulting resolution power (RP) is measured from the minimum resolvable circumference; additionally, both values were normalized against those of panel (a) to ease the comparison.

The original noisy phase map, in panel (a) of Figure 9, yields a maximum resolution of 1.26 μm. This value, which is consistent with the theoretical expectation for the 10x/0.25 microscope objective employed, is also obtained for panel (b) of the same figure when the aperture is reduced to 80% of its original size. In this latter panel, the average achieved a reduction of 29% in the speckle contrast. In panel (c), where the aperture diameter was only half of the original pupil size, a speckle contrast reduction of 48% was achieved, while the effective resolution decreased to 1.46 μm. Finally, when the aperture had a diameter of only 30% of the original pupil's, as shown in panel (d), a total reduction in the speckle contrast of 60% was reached, but the resolution dropped to 2.39 μm. The accompanying insets of each panel show a close-up on the central region of the test, where the inner dashed circle marks the resolution limit for the corresponding reconstruction. The penalty on the final resolution of the system when the described method is taken to its limits can be directly seen by comparing these panels.

While the application of the presented method in the resolution target in Figure 9 shows great promise in the desired noise reduction, this sample has a relatively simple morphology and, due to its benchmarking nature, a highly controlled roughness; in consequence, having verified the feasibility of the denoising capabilities of physically controlling the imaging pupil in quantitative phase images, and having identified its resolution trade-off, the methodology is applied to a biological specimen: a thin section taken from the head of a *Drosophila Melanogaster* fly. This sample has intricate structures present in the interior of its features, thus representing a challenging application case.

The denoising results are shown in Figure 10; panel (a) presents the phase map acquired with the original pupil of the system fully opened, and panel (b) shows the final averaged phase image resulting from 8 different positions of an aperture reduced to 0.4 times its original diameter. If the speckle contrast inside the rectangle-bounded region in panel (a) is assumed to be unitary, the denoising method achieves a total reduction of 65% in the speckle contrast when measured in that same region in panel (b). This improvement can be further seen in the close-up circular insets, where the finer details of the sample acquire increased visibility.

This result was finally compared to the well-known multi-look speckle denoising technique of using a rotating diffuser [10]; the comparison is summarized in Figure 11, with panel (a) showing the same denoising result of Figure 10, and panel (b) the result of using the rotating diffuser. Overall, a similar improvement is noticed in both approaches; the region bounded by the yellow square, which is magnified in the lower left inset in both panels, shows that the background information reaches a comparable smoothness, with a further reduction of the speckle contrast for the method proposed in this work. However, the region bounded by the red circle, magnified in the lower right inset of both panels, shows again the trade-off of the described technique: due to the reduction in the effective aperture size, and consequent rejection of higher-order spatial frequencies, the internal structure of the sample loses sharpness, thus reducing the contrast of its smallest features.

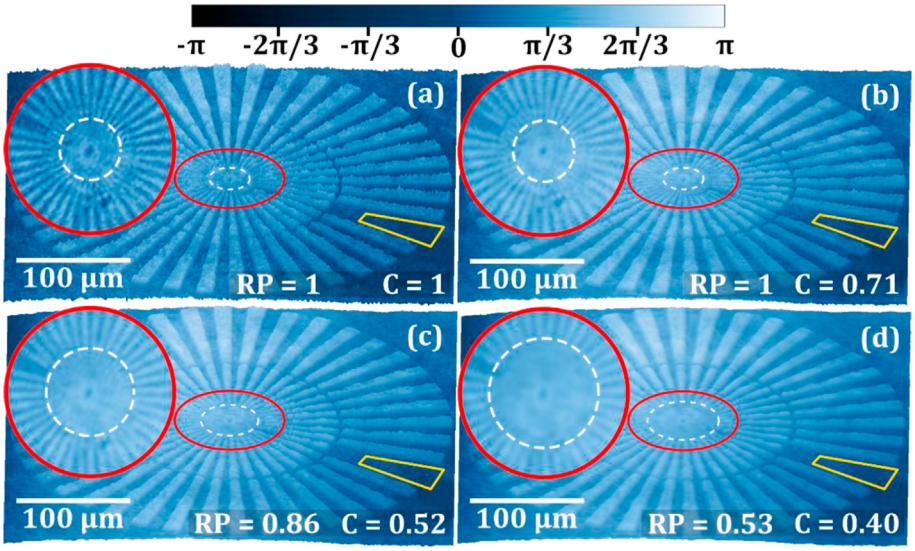

Figure 9. Speckle denoising by physically moving an aperture at the imaging pupil. (a) Noisy phase map obtained with a fully open and centered pupil. (b/c/d) Denoised image after averaging the reconstruction of 8 different displacements of an aperture with 0.8/0.5/0.3 times the original pupil diameter. The speckle contrast is measured in the yellow-bounded region. The close-ups on the red-encircled regions attest to the loss in resolution. The color scale bar applies to phase values in all panels. *RP* is the resolution power and *C* the speckle contrast, both normalized against the corresponding values of panel (a).

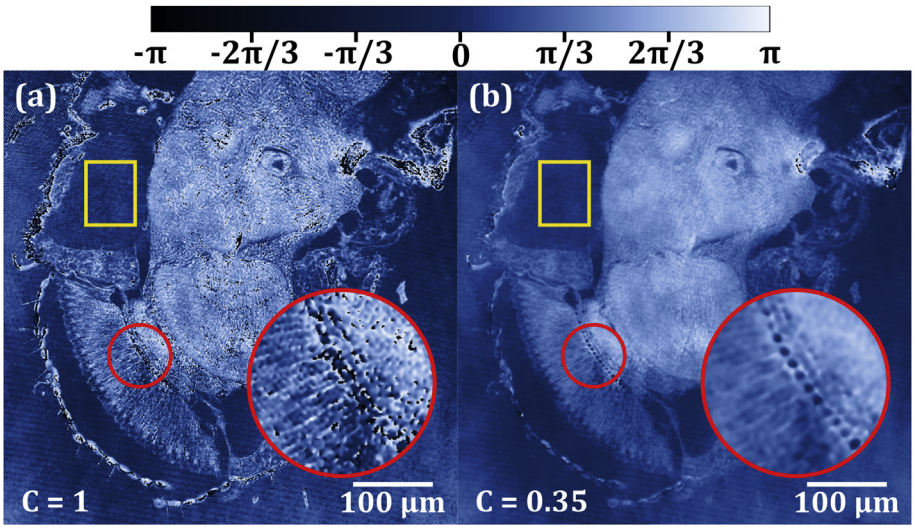

Figure 10. Speckle denoising of a thin section from the head of a Drosophila Melanogaster fly. (a) Phase reconstruction obtained without modifying the system's pupil. (b) Image with reduced speckle noise after averaging the reconstructed fields from 8 different displacements of an aperture reduced to 40% of the original pupil radius. The circle-bounded region is three times magnified. The speckle contrast is measured in the rectangle-bounded region. The color scale bar applies to phase values in both panels..

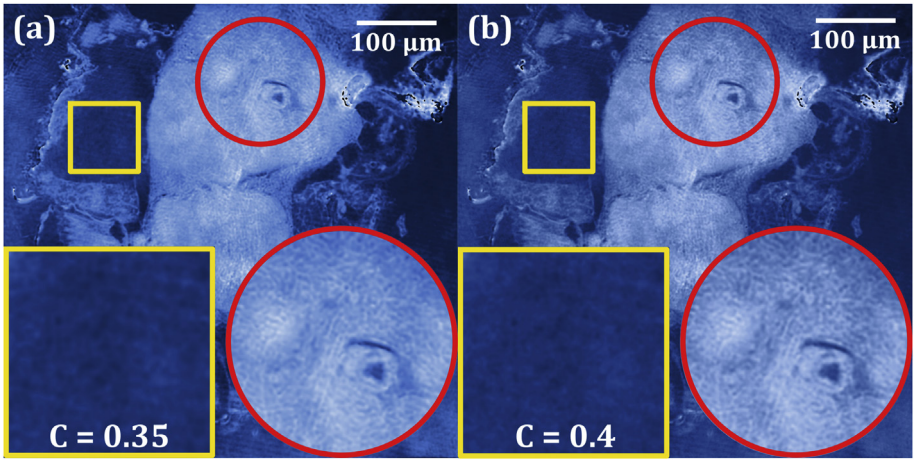

Figure 11. Speckle denoising in phase map by averaging multiple recordings obtained by (a) physically varying the system's pupil, and (b) rotating a diffuser. The square-bounded region shows an equally denoised background region. The circle-bounded region shows better preservation of higher spatial frequencies in the result of panel (b).

Because the multi-look method based on the rotating diffuser preserves the size of the imaging pupil, the above-mentioned spatial resolution trade-off does not occur.

Both the resolution test and biological sample results show that the described method of physically modifying the pupil function is a viable alternative to reduce speckle noise in phase images obtained from DHM architectures. Furthermore, despite the resolution trade-off, the experimental result with the biological sample shows that the described methodology is even suitable for complex internal structures, whose visualization is prone to be highly affected by the deleterious effects of speckle noise.

4. Conclusion

By understanding the coherent imaging system in the object arm of a Digital Holographic Microscope (DHM) as linear in amplitude, all its diffraction-derived effects, like speckle noise, can be directly attributed to the impulse response of the system. A denoising approach for the recovered object wavefield, which can be described as the convolution between this impulse response and a geometrical image of the sample, can thus be sought by manipulating the imaging pupil to obtain multiple partially uncorrelated fields to be statistically averaged. This denoising methodology, initially envisioned for the reconstruction stage of optical holography, was implemented in the object arm of a DHM operating in a telecentric-afocal architecture during the recording stage. With the controlled variation in size and displacement of an aperture in the pupil plane of the microscope objective, whose correlation degree was numerically measured, phase reconstructions with enhanced contrast and reduced noise levels were achieved.

The method was successfully applied to a phase-only resolution test target and a thin section from the head of a *Drosophila Melanogaster* fly. The former allowed the visualization of the resolution trade-off associated with the described method due to the reduction in the effective aperture of the system, while the latter showed promising results in the improvement of the visualization of micron-sized details in quantitative phase images (QPI).

The biological sample result was then compared with the denoising achieved via a rotating diffuser, showing similar outcomes. This comparison highlighted the possibility of applying optically-envisioned multi-look methods in the digital realm, which eases the data manipulation as the multiple configurations are not limited to the exposure time of the analog recording medium, and allow each exposure to be handled separately. Both methods may allow obtaining similar denoising results; however, due to the only-partial decorrelation introduced by the pupil approach, the configurations that allow the same improvement to be achieved involve a penalty in the effective resolution. To serve as a guide to the reader at the time of deciding which method to implement according to the particular application needs, this difference in the performance of both methods, particularly regarding the trade-off between the spatial resolution and the speckle reduction, is illustrated for the different configurations of the moving aperture.

These results show that the physical control of the pupil in the object arm of a DHM is worth considering among the set of tools available to researchers for reducing the deleterious effects that speckle noise introduces in QPI recovered in this technique.

Declarations

Author contribution statement

Jorge Garcia-Sucerquia: Conceived and designed the experiments; Contributed reagents, materials, analysis tools or data; Wrote the paper.

Carlos Buitrago-Duque: Performed the experiments; Analyzed and interpreted the data; Wrote the paper.

Funding statement

Jorge Garcia-Sucerquia was supported by the Universidad Nacional de Colombia (HERMES 50210).

Data availability statement

Data will be made available on request.

Declaration of interests statement

The authors declare no conflict of interest.

Additional information

No additional information is available for this paper.

Acknowledgements

The authors thank the Optics Laboratory for the use of their equipment.

References

[1] J.W. Goodman, Some fundamental properties of speckle, J. Opt. Soc. Am. 66 (1976) 1145.
[2] T. Kreis, Handbook of Holographic Interferometry: Optical and Digital Methods, WILEY-VCH GmbH & Co, Weinheim, 2005. https://www.wiley.com/en-us/Handbook+of+Holographic+Interferometry%3A+Optical+and+Digital+Methods-p-9783527405466.
[3] J.M. Artigas, M.J. Buades, A. Felipe, Contrast sensitivity of the visual system in speckle imagery, J. Opt. Soc. Am. A. 11 (1994) 2345.
[4] J.W. Goodman, Speckle Phenomena in Optics: Theory and Applications, second ed., SPIE, 2020.
[5] S. Montresor, P. Picart, Quantitative appraisal for noise reduction in digital holographic phase imaging, Optic Express 24 (2016) 14322.
[6] V. Bianco, P. Memmolo, M. Leo, S. Montresor, C. Distante, M. Paturzo, P. Picart, B. Javidi, P. Ferraro, Strategies for reducing speckle noise in digital holography, Light Sci. Appl. 7 (2018) 48.
[7] V. Bianco, P. Memmolo, M. Paturzo, A. Finizio, B. Javidi, P. Ferraro, Quasi noise-free digital holography, Light Sci. Appl. 5 (2016) e16142–e16142.
[8] J. Garcia-Sucerquia, J.H. Ramírez, R. Castaneda, J. Herrera-Ramírez, R. Castaneda, Incoherent recovering of the spatial resolution in digital holography, Opt. Commun. 260 (2006) 62–67.
[9] T. Baumbach, E. Kolenovic, V. Kebbel, W. Jüptner, Improvement of accuracy in digital holography by use of multiple holograms, Appl. Opt. 45 (2006) 6077.
[10] Y. Park, W. Choi, Z. Yaqoob, R. Dasari, K. Badizadegan, M.S. Feld, Speckle-field digital holographic microscopy, Optic Express 17 (2009) 12285–12292.
[11] N. George, A. Jain, Speckle reduction using multiple tones of illumination, Appl. Opt. 12 (1973) 1202.
[12] L. Rong, W. Xiao, F. Pan, S. Liu, R. Li, Speckle noise reduction in digital holography by use of multiple polarization holograms, Chin. Optic Lett. 8 (2010) 653–655.
[13] J. Herrera-Ramirez, D.A. Hincapie-Zuluaga, J. Garcia-Sucerquia, Speckle noise reduction in digital holography by slightly rotating the object, Opt. Eng. 55 (2016) 121714.
[14] F. Pan, W. Xiao, S. Liu, F. Wang, L. Rong, R. Li, Coherent noise reduction in digital holographic phase contrast microscopy by slightly shifting object, Optic Express 19 (2011) 3862–3869.
[15] J.C.C. Dainty, W.T.T. Welford, Reduction of speckle in image plane hologram reconstruction by moving pupils, Opt. Commun. 3 (1971) 289–294.
[16] W.T.T. Welford, Time-averaged images produced by optical systems with time-varying pupils, Opt. Commun. 4 (1971) 275–278.
[17] P. Hariharan, Z.S. Hegedus, Reduction of speckle in coherent imaging by spatial frequency sampling, Opt. Acta (Lond) 21 (1974) 345–356.
[18] P. Hariharan, Z.S. Hegedus, Reduction of speckle in coherent imaging by spatial frequency sampling - II. Random spatial frequency sampling, Opt. Acta (Lond) 21 (1974) 683–695.
[19] Y. Kawagoe, N. Takai, T. Asakura, Speckle reduction by a rotating aperture at the fourier transform plane, Optic Laser. Eng. 3 (1982) 197–218.
[20] R.W. Lewis, Speckle reduction by spatial sampling, Opt. Eng. 15 (1976) 274–275.
[21] D. Kermisch, Speckle reduction by spatial sampling, Appl. Opt. 13 (1974) 1000.
[22] J. Maycock, B.M. Hennelly, J.B. McDonald, A. Castro, T.J. Naughton, Y. Frauel, A. Castro, B. Javidi, T.J. Naughton, Reduction of speckle in digital holography by discrete Fourier filtering, J. Opt. Soc. Am. A. 24 (2007) 1617–1622.
[23] T. Fukuoka, Y. Mori, T. Nomura, Speckle reduction by spatial-domain mask in digital holography, J. Disp. Technol. 12 (2016) 315–322.

[24] E. Cuche, F. Bevilacqua, C. Depeursinge, Digital holography for quantitative phase-contrast imaging, Opt. Lett. 24 (1999) 291–293.
[25] G. Popescu, Quantitative Phase Imaging of Cells and Tissues, McGraw Hill Professional, 2011.
[26] E. Sánchez-Ortiga, P. Ferraro, M. Martínez-Corral, G. Saavedra, A. Doblas, Digital holographic microscopy with pure-optical spherical phase compensation, J. Opt. Soc. Am. A. Opt. Image Sci. Vis. 28 (2011) 1410–1417.
[27] A. Doblas, E. Sánchez-Ortiga, M. Martínez-Corral, G. Saavedra, P. Andrés, J. Garcia-Sucerquia, Shift-variant digital holographic microscopy: inaccuracies in quantitative phase imaging, Opt. Lett. 38 (2013) 1352–1354.
[28] E. Sánchez-Ortiga, A. Doblas, G. Saavedra, M. Martínez-Corral, J. Garcia-Sucerquia, Off-axis digital holographic microscopy: practical design parameters for operating at diffraction limit, Appl. Opt. 53 (2014) 2058.
[29] A. Doblas, E. Sánchez-Ortiga, M. Martínez-Corral, G. Saavedra, J. Garcia-Sucerquia, Accurate single-shot quantitative phase imaging of biological specimens with telecentric digital holographic microscopy, J. Biomed. Optic. 19 (2014) 46022.
[30] T. Kreis, Holographic Interferometry: Principles and Methods, Akademie Verlag, 1996.
[31] M. Takeda, H. Ina, S. Kobayashi, Fourier-transform method of fringe-pattern analysis for computer-based topography and interferometry, J. Opt. Soc. Am. 72 (1982) 156.
[32] E. Cuche, P. Marquet, C. Depeursinge, Spatial filtering for zero-order and twin-image elimination in digital off-axis holography, Appl. Opt. 39 (2000) 4070–4075.
[33] J.W. Goodman, Introduction to Fourier Optics, third ed., Roberts & Company Publishers, 2005.
[34] C. Buitrago-Duque, J. Garcia-Sucerquia, Realistic modeling of digital holographic microscopy, Opt. Eng. 59 (2020) 1.
[35] K. Pearson, On the measurement of the influence of "Broad categories" on correlation, Biometrika 9 (1913) 116.